Cranfield UNIVERSITY

MARIE-LAURE PERVIER

MECHANICS OF ICE DETACHMENT APPLIED TO TURBOMACHINERY

SCHOOL OF ENGINEERING
department of Power and Propulsion
Phd Thesis (full time) - 2012
supervisor: D.W. Hammond

This thesis is submitted in the fulfilement of the requirements for the Degree of PhD.

Contents

List of Figures

List of Tables

Nomenclature

α_i	thermal expansion coefficient of ice	
β	local catch efficiency	
ΔS	surface	m^{-2}
ΔT	thermal shock resistance	°C
$\dot{m}$	mass flux of water impinging the surface per unit of time	$\mathrm{kg.m}^{-2}.\mathrm{s}^{-1}$
$\dot{m}_e$	mass flux of water which evaporates	$\mathrm{kg.m}^{-2}.\mathrm{s}^{-1}$
$\dot{m}_i$	mass flux of ice which form on the surface	$\mathrm{kg.m}^{-2}.\mathrm{s}^{-1}$
$\dot{m}_s$	mass flux of ice which sublime to vapor	$\mathrm{kg.m}^{-2}.\mathrm{s}^{-1}$
$\dot{m}_{rb}$	mass flux of runback water	$\mathrm{kg.m}^{-2}.\mathrm{s}^{-1}$
ϵ	emissivity of the object	
Λ_f	latent heat of fusion	$\mathrm{J.kg}^{-1}$
Λ_s	latent heat of sublimation	$\mathrm{J.kg}^{-1}$
Λ_v	latent heat of evaporation	$\mathrm{J.kg}^{-1}$
μ_a	viscosity of air	$\mathrm{kg.m}^{-1}.\mathrm{s}^{-1}$
ν	Poisson's ratio	
ν_i	Poisson's ratio of ice	
ω	rotational speed	$\mathrm{rad.s}^{-1}$
ρ_a	density of air	$\mathrm{kg.m}^{-3}$
ρ_i	density of ice	$\mathrm{kg.m}^{-3}$

ρ_w	density of water	$kg.m^{-3}$
σ_t	tensile strength	Pa
σ_{SB}	Stefan-Boltzmann constant	$W.m^{-2}.K^{-4}$
τ	shear strength	Pa
Θ	absolute temperature	K
A_c	surface of contact between the ice and the substrate	m^2
a_g	average grain size	m
A_p	surface of the plunger applying the force to the ice	m^2
A_{cp}	accumulation parameter	
c	radius of the flaw	m
Cp_a	specific heat of air	$J.kg^{-1}.K^{-1}$
Cp_{is}	specific heat of ice	$J.kg^{-1}.K^{-1}$
Cp_{ws}	specific heat of water on model surface	$J.kg^{-1}.K^{-1}$
d	characteristic length	m
D_v	diffusivity of water vapor in air	$m^2.s^{-1}$
E	Young's modulus	Pa
E_i	Young's modulus of ice	Pa
E_i^f	energy to form an interstitial	J
E_M	total collection efficiency	
E_v^f	internal energy that must be added to move a molecule from the interior of a crystal to its surface	eV
F_b	body force applied on ice	$N.m^{-3}$
FE	fracture energy	$J.m^{-2}$
G	shear modulus	Pa
h	ice thickness	m

h_c	heat transfer coefficient	$\mathrm{W.m^{-2}.K^{-1}}$
h_G	gas-phase mass transfer coefficient	$\mathrm{kg.s^{-1}.m^{-2}}$
k_a	thermal conductivity of air	$\mathrm{W.m^{-1}.K^{-1}}$
k_B	Boltzmann's constant	
K_{Ic}	fracture toughness in mode I	$\mathrm{kPa}\sqrt{\mathrm{m}}$
K^*_{IIc}	equivalent of the fracture toughness in mode II	$\mathrm{kPa}\sqrt{\mathrm{m}}$
K^*_{II}	"stress intensity factor" in mode II	$\mathrm{kPa}\sqrt{\mathrm{m}}$
l_g	length of the line drawn for the determination of the grain size	mm
LWC	liquid water content	$\mathrm{g.m^{-3}}$
m_i	mass of the ice piece	kg
MVD	Mean Volume Diameter	μm
n	freezing fraction	
n_g	number of grain intersected by the line drawn on the picture of the ice microstructure	
Nu_a	Nusselt number of air	
P_c	critical pressure	Pa
p_w	vapor pressure in the atmosphere	Pa
p_{tot}	total pressure	Pa
p_{ww}	vapor pressure at the surface	Pa
Pr_a	Prandtl number of air	
q_c	heat flux due to the convection from the surface to the boundary layer	$\mathrm{W.m^{-2}}$
q_e	heat flux lost from the evaporation of water	$\mathrm{W.m^{-2}}$
q_f	heat flux due to the release of latent heat of fusion from the freezing water	$\mathrm{W.m^{-2}}$

q_i	hat flux due to the decrease of temperature of ice from freezing temperature to surface temperature	$\mathrm{W.m^{-2}}$
q_k	heat flux due to the kinetic energy of water drop impinging the surface	$\mathrm{W.m^{-2}}$
q_r	heat flux due to radiation from the surface	$\mathrm{W.m^{-2}}$
q_s	heat flux due to the sublimation of ice	$\mathrm{W.m^{-2}}$
q_w	heat flux due to the rise of temperature of impinging water to freezing point	$\mathrm{W.m^{-2}}$
q_{cond}	heat flux due to the conduction through the ice	$\mathrm{W.m^{-2}}$
q_{rb}	heat flux due to runback water	$\mathrm{W.m^{-2}}$
r	radial position on the airfoil	m
r_d	radius of the droplets	μm
r_f	recovery factor	
Re_a	Reynolds number of air	
S_i	extra entropy per interstitial module	J
S_v	extra entropy associated with each vacancy	J
Sc_a	Schmidt number of air	
T	free-stream temperature	K
t	time of accretion	s
T_f	freezing temperature	K
T_{bl}	temperature in the boundary layer	K
T_{film}	film temperature	K
T_{st}	static temperature	K
T_s	surface temperature	K
T_{tot}	total temperature	°C
V	tunnel air velocity	$\mathrm{m.s^{-1}}$

v_0	droplet impact velocity	$\mathrm{m.s^{-1}}$
V_i	volume of the piece of ice	$\mathrm{m^3}$

Abstract

Flying in icing conditions is a real hazard for aircraft as they can undergo potential disastrous increase in drag, reduction in maximum lift which lead to an increase in fuel consumption. Additionally pitot tubes and other sensors can become blocked or their operation compromised. Ice shed from other parts of the aircraft can enter the engine and lead to blade damage. Whilst ice protection systems are comonly used on propellers, the potential benefit of applying them to a fan have not, as yet, been considered sufficient to offset the cost and energy penalties of such system. As engines become larger, it is more difficult to contain ice and self-shedding becomes an increasing hazard for the nacelle and other parts downstream of the fan.
The main objectives of the project were to determine the mechanical properties of ice such as might form on an engine fan, in order to help Rolls-Royce in building a finite elements model able to simulate ice shedding from fan blades. Lots were written about ice however only little information about the mechanical properties of impact ice was available in the literature and the values which were, were generally not applicable in the case of aeroengine in icing conditions. According to the literature and from Rolls-Royce photos and films of ice shedding from fan blades, self-shedding mechanisms were ruled by adhesive shear strength and tensile strength. Therefore, the experimental part of the project consisted of measuring these two mechanical properties as well as the density, the stiffness and the grain size of ice grown on titanium substrate.
Two test rigs were used to measure the mechanical properties: the "mode I" and the "shear" test rig. The mode I test rig was already available and was only modified in order to test more specimens during each run. This test allowed to measure the pressure needed to remove the ice from the substrate in a running icing tunnel. Using equations from the literature, fracture energy, fracture toughness and tensile strength were calculated. The influence of ambient total temperature, cloud liquid water content and tunnel wind speed were investigated. Tensile strength was found to be increasing as the total temperature is decreasing, decreasing as the LWC is increasing and going trough a maximum as the tunnel wind speed is increasing. Values obtained lied in the

range from 0.6 to 1.5 J.m^{-2} (corresponding to between 2 and 10 MPa) which is, in general, higher than the ones reported by other authors. This difference can be explained by the fact that the mode I test was conducted in a running icing tunnel while the previous authors have conducted the mechanical test after the tunnel has been stopped. In parallel, finite element models have been developed and results similar to the experiments were obtained.
The shear test rig was designed as part of the project. It allowed to measure the pressure needed to push the ice along a substrate surface. A finite element model was developed to view the shear stress distribution at the ice/substrate interface and to determine a value of shear strength along the edge on which the ice was pushed. The influence of the ambient total temperature, the cloud LWC, the tunnel wind speed and the surface roughness were investigated. Shear strength values have been found to increase as the ambient total temperature is decreasing, to increase with the LWC, the tunnel wind speed and the substrate roughness. Values obtained, between 2 and 14 MPa, were higher than the ones reported by previous authors. However, similarly to the mode I test, the shear test was conducted in a running icing tunnel and the values obtained were not an average value of the shear strength but the actual values at the edge were the load is applied.
An attempt has been made to model the shear test with finite element using a layer of cohesive elements between the ice and the substrate. This model was successful in a way that it could predict the pressure at which the ice will be removed from the substrate but the shear stress distribution was then unrealistic.
Measurements of the density, the stiffness and the average grain size have been carried out. Impact ice was found to have a lower density at lower temperature. Its stiffness was found to decrease as the temperature decreases as well as the average grain size. The grain size was found to be, in general, smaller at the interface than at the top surface. Investigation of the influence of the cloud LWC and the tunnel wind speed have been carried out but the trends were not clear.
A preliminary finite element model simulating the ice shedding from a rotating bar has been successfully developed. The model used basic geometries for the blade and the ice, and a layer of cohesive elements at the interface ice/substrate. A centrifugal load was progressively applied on the ice. At a certain load, the cohesive elements started to break off and the ice to slide. This model was developed to show the abilities of the software to simulate ice shedding.

Chapter 1

Introduction

Aircraft can suffer from icing conditions in various parts of their flight: on ground, during climb, hold and descent. Water can be present in the clouds as supercooled droplets which can freeze on any surface of the aircraft, especially on the wings and on the engine's blades (figure 1.1). As a consequence, the

Figure 1.1: *Icing on fan blades (courtesy of Rolls-Royce)*

weight and the drag of the aircraft will increase, leading to an increase in fuel consumption. The flow over the wings will be disrupted causing a decrease in lift. Instruments like pitot tube can be obstructed leading to a misreading of information. Ice formation in engine's blades will reduce the flow passage and pieces of ice can fall into the engine resulting in damage of the blades and the casing, compressor surge and in some case engine flame-out.

This project, sponsored by Rolls-Royce, is focusing on ice shedding from fan blades. Rolls-Royce's particular interest is on the change in ice shedding piece dimension when the blade dimension or material is modified. The objective of the PhD is to understand the ice shedding process quantitatively and provide impact ice properties values in order to build a finite elements model (FEM) allowing the estimation of the size of the ice piece which could shed from the blades.
Generally fan blades are not protected from ice. It is just required as a certification process that the ice build up on fan blades should shed by itself and that the engine components placed downstream are strong enough to handle the passage of ice blocks.
From Rolls-Royce pictures and films and from the information found in the literature, it is believed that ice shedding from fan blade is mainly due to centrifugal forces. Other sources of stress in rotating blades, like Scavuzzo et al. (1996) reported, exist including thermal stresses caused by the phase change of accreted ice, vibration, aerodynamic forces, flexion and twist of the blades. However the main cause of shedding seems to be due to centrifugal forces and it will be the principal cause investigated in the present work.
Figure 1.2 shows the process of ice shedding from a fan blade (Scavuzzo et al., 1990). As ice accretes on the blade, at constant rotational speed, the shear

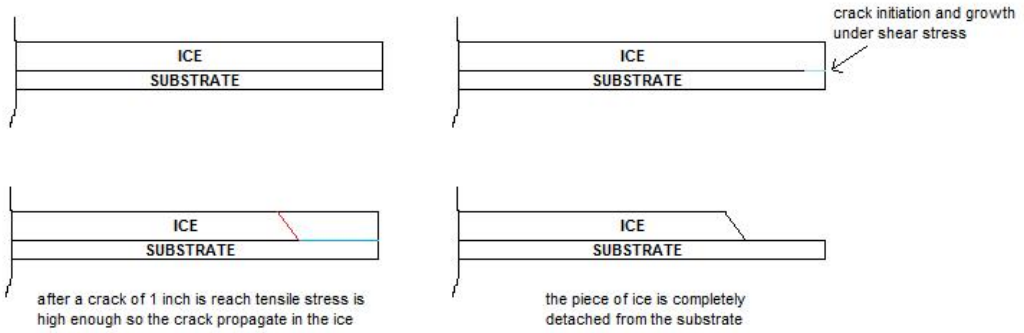

Figure 1.2: *Schematic view of how ice is shedding from the blade*

stress due to centrifugal force is increasing (equation 1.1) with a higher value at the tip than at the hub.

$$\tau = \rho_i \omega^2 r h \tag{1.1}$$

where ρ_i is the ice density, ω the rotational speed, r the radial position on the airfoil and h the ice thickness.
At some point, the value of the shear stress at the tip of the blade will become greater than the shear strength and a crack will initiate (figure 1.2). As ice

accretion continue, the crack will grow in the direction of the hub. After the crack has propagated to a certain length, 1 inch according to Scavuzzo et al. (1996), tensile stress inside the ice will start to increase. This increase in tensile strength is believed to be due to the fact that the piece of ice at the tip is detached from the substrate but still attached to the rest of ice. The piece of ice from the tip wants to detach from the blade and then pull on the remaining piece of ice resulting in an increase in tensile stress. At some point the tensile stress reaches the tensile strength and a tensile crack will initiate and propagate until fracture occurs.
Hence, in order to simulate ice shedding accurately, mechanical properties of ice, like tensile and shear strength, need to be known. On top of these, more common properties like the density, the Young's modulus and the grain size needs to be determined as these properties vary with the ice growth conditions and have not been widely reported in the literature.
The present work aims to test ice in a running icing tunnel to get values as close as possible to the ones encountered by an aircraft in icing condition. Two test rigs will be used:

- a mode I test rig to measure the fracture energy in mode I and in order to determine the tensile strength of a bulk of impact ice
- a shear test rig to determine the adhesive shear strength of ice

During most of the experiments, samples of ice were taken off and used to measure the density and the stiffness and for microstructure observations.
General theoretical background are presented in chapter 2 including a presentation of the ice and more especially impact (atmospheric) ice, detailed explanation about the freezing fraction and some mechanical background.
Chapter 3 describes the facilities used at Cranfield University and the work done prior to the test to calibrate the tunnel.
Chapter 4 is dedicated to the physical properties of ice, the density, the stiffness and the grain size, while chapter 5 presents the mechanical properties of ice including experimental results and finite elements analysis of both mode I and shear tests.
To finish, chapter 6 reports works done on ice shedding due to centrifugal force. It includes the work done by previous authors, a description of certification tests done by Rolls-Royce and ice shedding observations, and a preliminary finite elements model on a rotating arm.

Chapter 2

Background knowledge

2.1 Ice

2.1.1 Structure of ice Ih

Ice can exist in twelve known crystalline and two amorphous forms. Only two of these forms are stable at ordinary pressures: hexagonal ice Ih and cubic ice Ic. The ice present naturally on earth is the ice Ih. The ice Ic is obtained by depositing water vapor at temperature lower than -130°C.
The crystalline structure of ice Ih is presented on figure 2.1. The oxygen

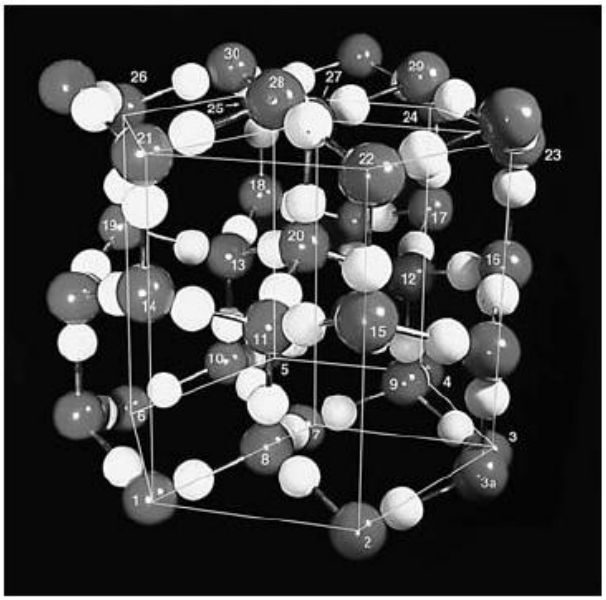

Figure 2.1: *Crystal structure of ice Ih (Schulson and Duval, 2009)*

atoms are represented by large spheres and the hydrogen atoms by small white spheres. Each oxygen atoms has four nearest neighbours. The oxygen atom of each molecule is linked to the hydrogen atoms by a strong covalent bonds whereas the oxygen atoms from two different molecules are linked by a weak hydrogen bonds.

At -20°C, the length of the cell's side is a=0.4510 nm and the height of the cell is c=0.7357 nm. The values are changing with temperature but the ratio c/a is constant and equal to 1.628 (the value for hard spheres closely packed is 1.633). The fact that the c/a ratio does not vary with temperature implies that thermal expansion is isotropic.
The thermal expansion coefficient near the melting point is relatively high (5.3×10^{-5} at -20°C). The Young's modulus and the tensile strength are relatively low (∼10 GPa and ∼1 MPa respectively) which means that the thermal shock resistance is quite low

$$\Delta T \sim \frac{\sigma_t}{E_i \alpha_i} \sim 2^\circ C$$

To compare concrete has a thermal shock resistance of ∼10°C and diamond of ∼1000°C.

2.1.2 Point defects

Point defects are atomic sized featured that form in the ice lattice. There are five sorts of point defects: three are also found within crystal of metals and compounds

- vacancies
- interstitials
- solutes

and two are specific to ice

- ionic
- Bjennum

2.1.2.1 Vacancies

A vacancy can be defined as an empty molecular site. The vacancy concentration in a crystal can be estimated from the Boltzmann relationship (Schulson, 2001)

$$C_v = exp(S_v/k_B)\ exp(-E_v^f/k_B\Theta) \tag{2.1}$$

where S_v is the extra entropy associated with each vacancy, E_v^f is the internal energy that must be added to move a molecule from the interior of a crystal to its surface, k_B is the Boltzmann's constant and Θ is the absolute temperature . E_v^f has been estimated as 0.5 eV, hence, assuming $S_v \sim 0$, the equilibrium vacancy concentration is about 10^{-10} at the melting point. This value is quite low compared to those for metals and alloys near their melting point (between 10^{-3} and 10^{-4}) however it is large enough to account for the formation of vacancy-type prismatic dislocation loops upon rapid cooling from the melting point (Schulson and Duval, 2009).

2.1.2.2 Interstitials

An interstitial is formed when a molecule moves into the open space of the crystal lattice. The equilibrium interstitial concentration can be calculated from the relation (Schulson, 2001)

$$C_i = exp(S_i/k_B)\ exp(-E_i^f/k_B\Theta) \tag{2.2}$$

where S_i is the extra entropy per interstitial module and E_i^f is the energy to form an interstitial. Assuming $S_i = 4.9k_B$ and $E_i^f = 0.40$eV, the interstitial concentration is $\sim 10^{-6}$ for temperature near melting point. This value is several order higher than the one for metals and alloys and also several order higher than the equilibrium vacancy concentration in ice Ih, hence there will probably be a greater tendency for the formation of interstitial dislocation loops when ice is subject to rapid cooling from near melting point.

2.1.2.3 Solutes

The solubility of foreign species within the ice crystal lattice is very low. However, impurities may be found in the solid as liquid inclusions.

2.1.2.4 Ionic and Bjerrum defects

These defects are the consequences of violation of the Bernal-Fowler rules which creates protonic defects. A ionic defect is created when a hydrogen atom moves from one position to an other along a 0-0 bond. One oxygen atom will have three hydrogen atoms around it, H_3O^+, while the other will only have one, OH^-, (violation of the first principle). Bjerrum defects are created when a proton moves around the oxygen atom in a way that on one O-O bond there is no hydrogen atom, L-type, and on the other O-O bond there are two hydrogen atoms, D-type, (figure 2.2).

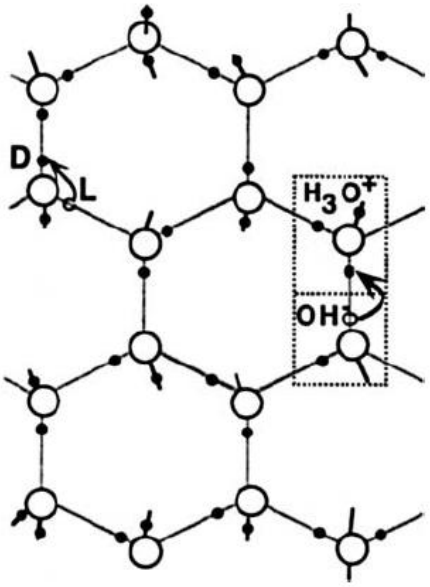

Figure 2.2: *Schematic sketch of ionic (H_3O^+ and OH^-) and Bjerrum (L and D) point defects (Schulson and Duval, 2009)*

The equilibrium concentration of ionic and Bjerrum defects can be estimated from the following relations

$$C_- = C_+ = exp(S_\pm/k_B)\ exp(-E_\pm/2k_BT) \tag{2.3}$$

$$C_L = C_D = exp(S_{LD}/k_B)\ exp(-E_{LD}/k_BT) \tag{2.4}$$

Protonic defects contribute to the electric conductivity of ice and also affect dislocation mobility and creep.

2.1.3 Planar defects

Planar defects relevant to creep and fracture are grain boundaries and free surfaces.
Grain boundaries are regions, about several nanometers in thickness, which separate the individual grains or crystals in polycrystalline ice. Near the melting point, they contains liquid water. Amongst other functions, grain boundaries serve as a source of point defects. They are, also, preferential sites for impurities, sites from which dislocations are generated and sites of crack nucleation (Schulson and Duval, 2009). Therefore, grain boundaries can be considered as the largest "defect" that can initiate cracks.

2.1.4 Volumetric defects

Pores and hard particles are the main volumetric defects in ice. Pores are the result of rejecting oxygen and nitrogen from water during the ice formation. The shape and distribution of porosity depend on the thermal-mechanical history of the ice. Hard particles are common in ice: atmospheric particulates in glacier ice, salts in sea ice, etc... Pores and hard particles have a significant effect on creep deformation and crack propagation (Schulson and Duval, 2009).

2.1.5 Different sort of ice

Ice, even if it has the same internal structure, can have different appearances due to its mechanical history. Glacier ice is formed by compaction of snow. Hence its density and aspect depends on the depth. Snow gradually changes to firn, which have a density of 600 $kg.m^{-3}$ (as compared to a density of 917 $kg.m^{-3}$ for ice made from freezing water in a freezer). Closed pores progressively form, leading to bubbly ice. The evolution of microstructure with depth depends on temperature, strain rate, presence of impurities, grain growth and recrystallisation. The grain size of this type of ice is typically between one millimeter and several centimeters. The microstructure will evolve with age and plastic deformation over periods of hundreds to thousands years.
Floating ice sheet forms from the solidification of water over period of weeks to months. It includes sea ice, lake ice, river ice and reservoir ice. The process initiates on or near the surface and continues downward. The cover layer is made of polycrystalline ice composed of columnar shape grains of 5 to 10 mm in diameter (Schulson and Duval, 2009).
Hailstones are formed by the accretion of supercooled water droplets on ice nuclei in the clouds. Their size can grow over 50 mm in diameter. Their microstructure is constituted of finely grained polycrystalline layers within entrapped air bubbles.
Atmospheric ice, also known as impact ice, is formed when supercooled water droplets hit a cold surface and freeze on contact. This kind of ice has a polycrystalline form with fine grains (< 1 mm). Depending on the meteorological conditions and on impact speed, different type of atmospheric ice can be obtained:

- glaze ice which is hard and transparent in appearance and has a smooth surface

- hard rime ice which is hard, opaque or translucent and has a smooth or scaled surfaces

- soft rime ice which is white and opaque and has a granular or needled surface

Rime ice (figure 2.3) is produced when the supercooled droplets freeze rapidly

Figure 2.3: *Rime ice*

on contact with the substrate surface. All the liquid water become ice and bubbles of air are trapped resulting in the white and opaque appearance. On the contrary, glaze ice (figure 2.4) is obtained while the water freeze very slowly

Figure 2.4: *Glaze ice*

and usually a film of liquid water can be seen at the ice surface. It results in transparent ice as the air can escape during the freezing process.

2.1.6 Ice classification

A classification was suggested by Michel and Ramsier (Eskandarian, 2005) to distinguish the different type of ice according to their crystallographic structure. There are two main types: granular and columnar ice. In granular ice, the c-axes are randomly oriented (figure 2.5) which results in an isotropic mechanical behaviour of ice. Granular ice is produced by the freezing of snow or other ice particles saturated in water,eg snow layer on a river, a lake or

an ocean, or the upper sections of glaciers (Sinha, 1989). Columnar ice have been divided in 3 subcategories: S1, S2 and S3 ice. In S1 ice, the c-axes are predominantly vertical. It is characteristic of ice from glaciers, lakes, reservoirs and rivers with low flow velocities. S1 ice is a transversely isotropic material. S2 ice has its c-axes randomly oriented in the horizontal plane (figure 2.5).

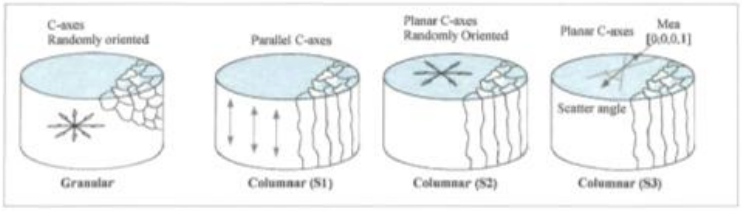

Figure 2.5: *Different type of ice with their c-axes orientation (Eskandarian, 2005)*

It usually occurs when the water is near freezing point and when the surface is seeded (Eskandarian, 2005). The grains grow in columnar shape in the direction of the heat flow and the c-axis are randomly distributed in the plane perpendicular to the columns. S2 ice is also a transversely isotropic material. S3 ice has its c-axes in the horizontal plane but aligned in a particular direction (figure 2.5). It usually forms in the presence of strong currents (river and sea ice). S3 ice is an orthotropic material.
Our main interest here is about atmospheric ice. The grains are mainly columnar with c-axes aligned perpendicularly to the growth front (Schulson, 2001).

2.2 Mechanics

By definition "fracture is the separation of a body under stress into two or more parts" (Jayatilaka, 1979). Two kinds of fracture can happen: a ductile fracture or a brittle fracture. In the first one, the material is subject to extensive plastic deformation before its fracture. The crack propagation is quite slow and results from the formation and the coalescence of voids (figure 2.6). While, brittle fracture is mainly controlled by the presence of cracks in the material which can be in the form of point defects, dislocations, pores, inclusions, segregations or even grain boundaries in the case of polycrystalline materials.

2.2.1 Statistics

It has been observed that brittle materials exhibit a scatter of failure strengths. In ductile material, in which plastic deformation takes place, the scatter is low

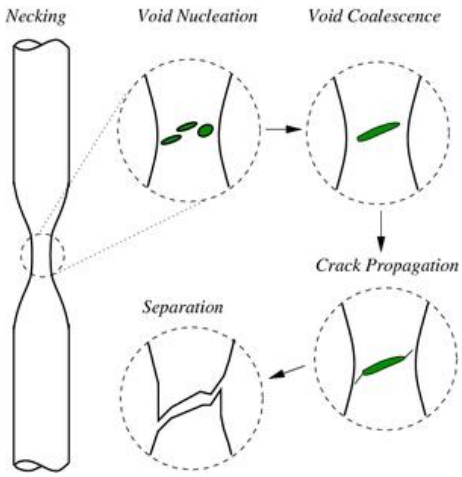

Figure 2.6: *Schematic representation of a ductile fracture (Wikipedia)*

(about 4 to 8% of the mean strength). In brittle material, the variation of strength can reach 100% of the material strength (Jayatilaka, 1979). This scatter is due to the fact that, in a brittle material, any defect can propagate and lead to failure. Moreover, the size and orientation of the flaw cannot be the same in two nominally identical materials.
According to Jayatilaka (1979), the probability of finding a bigger crack is higher for larger ice pieces. This results in the tensile strength decreasing as the volume of ice increases. This has been observed by other authors: Raraty and Tabor (1958), Chu et al. (1991), Xian et al. (1989), Loughborough and Haas (1946).
From the above, it is becoming clear that a statistical analysis is needed to explain the strength of the material. The Weibull distribution is commonly used to describe the behaviour of brittle materials. The Weibull analysis assumes that the material is isotropic and statistically homogeneous, and that the most critical flaw is responsible to the material fracture (Jayatilaka, 1979). The cumulative distributive function is

$$P_f = 1 - e^{\frac{\sigma - \sigma_u}{\lambda}^m} \tag{2.5}$$

where m is the Weibull modulus (also known as shape factor), σ_u is the threshold stress and λ is the scale factor. Table 2.1 presents the Weibull modulus for some brittle materials. It has been observed that a higher value of Weibull modulus lead to a less brittle material. During this study, values of the Weibull modulus were mainly found between 1 and 5.

material	m
glass	2-3
SiC	4-10
Si_3N_4	6-15
graphite	12
cast iron	38

Table 2.1: *Weibull modulus of some brittle materials (Jayatilaka, 1979)*

2.2.2 Fracture of ice on a substrate

When ice is removed from a substrate, three kinds of fracture could happen: adhesive, cohesive or cohesive-adhesive. With the adhesive breaks, the ice falls off the substrate and leaves the surface completely free of ice (figure 2.7). With

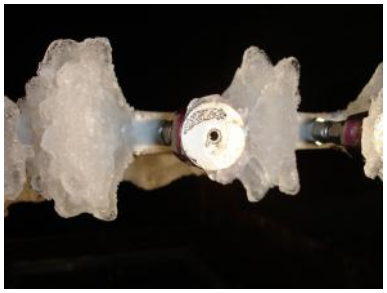

Figure 2.7: *Example of an adhesive failure where the surface of the substrate is clean of ice and shiny*

cohesive breaks, the crack propagates inside the ice and, when the ice falls off, the surface is still covered by a layer of ice (figure 2.8). A cohesive-adhesive

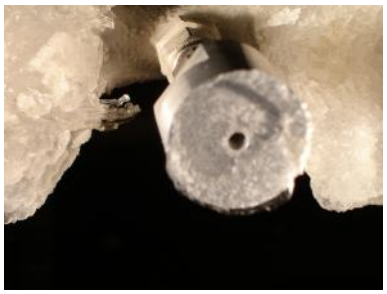

Figure 2.8: *Example of a cohesive failure where the surface of the substrate is still covered by ice*

break is a mix between an adhesive and a cohesive break; meaning that part

of the surface is completely free of ice while the other part is still covered by ice.

2.2.3 FEA and cohesive elements

Mostly used to model the delamination of composite materials, the cohesive elements are very useful to model the interface between two materials which are subject to separation from each other. The separation is simulated by two different steps: the delamination initiation and the delamination propagation. The initiation step is usually based on stress criteria and the propagation step on fracture energy criteria. The main advantage of using cohesive elements is that a prediction of initiation and propagation of delamination without any previous knowledge of crack location and propagation direction is possible. However cracks will only appear and propagate at the interface, through the cohesive elements.
Cohesive elements are based on a Dugdale-Barenblatt cohesive zone approach.

2.2.3.1 Single mode delamination

It is assumed that there is a process or cohesive zone ahead of the delamination tip. This concept was first proposed by Barenblatt and has the advantage to remove the singularity at the crack tip. For pure mode I, II or III loading, the

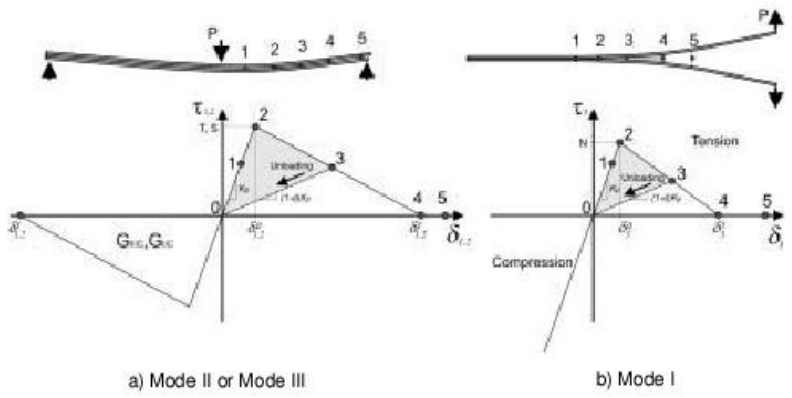

Figure 2.9: *Pure mode constitutive equation (Camanho and Davila, 2002)*

bi-linear constitutive behavior, presented in figure 2.9, is used. A high value of penalty stiffness (K) is used to hold the top and bottom face of the cohesive elements together in the linear elastic range (point 1 on figure 2.9). When the interfacial normal and shear tractions attain their respective interlaminar tensile and shear strengths (point 2 on figure 2.9), the stiffness is gradually

reduced to zero (point 4 on figure 2.9). Point 2 represents the initiation of damage. The relative displacement at this point can be obtained from the interlaminar tensile and shear strengths, ((noted)) respectively N, S and T for mode I, mode II and mode III loading, and from the penalty stiffness.

$$\delta_3^0 = N/K, \quad \delta_2^0 = S/K, \quad \delta_1^0 = T/K$$

The area under the traction-relative displacement curves is the critical fracture energy, $G_(Ic)$, $G(IIc)$, $G(IIIc)$, for each respective mode. Hence the final relative displacements can be obtained from

$$\delta_3^f = 2G_{Ic}/N, \quad \delta_2^f = 2G_{IIc}/S, \quad \delta_1^f = 2G_{IIIc}/T$$

At point 4 (figure 2.9), all the energy has been released, hence, for any further displacement, the interface will not transfer any load (point 5 on figure 2.9) and the penalty stiffness reverts to zero. In the case that the crack faces interpenetrate each other, the penalty stiffness would be reapplied (Camanho and Davila, 2002).

2.2.3.2 Mixed-mode delamination

In some applications and especially composites, delamination is more likely to grow under mix-mode loading. Under pure mode I, II or III loading, the onset of damage can be evaluated by comparing the traction components with their respective allowable value. Under mix-mode loading, delamination can occur before any of the traction components reach their respective allowable value. Therefore, the maximum stress criterion can give poor results. So a quadratic failure criterion has to be used:

$$\left(\frac{<\tau_3>}{N}\right)^2 + \left(\frac{\tau_2}{S}\right)^2 + \left(\frac{\tau_1}{T}\right)^2 = 1 \tag{2.6}$$

The total mix-mode displacement is defined has

$$\delta_m = \sqrt{\delta_1^2 + \delta_2^2 + <\delta_3>^2} \tag{2.7}$$

and, assuming that S=T, the single mode relative displacements are:

$$\delta_3^0 = \frac{N}{K} \tag{2.8}$$

$$\delta_1^0 = \delta_2^0 = \frac{S}{K} \tag{2.9}$$

where K is the penalty stiffness.
The delamination propagation can be predicted from the fracture energy. Interlaminar fracture energy can be obtained from test methods such as double

cantilever beam test (mode I), end notched flexure or end loaded split (mode II) and edge crack torsion (mode III).
Several criteria can be used to predict the delamination propagation under mix-mode loading:

- power law criterion

$$\left(\frac{G_I}{G_{Ic}}\right)^{\alpha} + \left(\frac{G_{II}}{G_{IIc}}\right)^{\alpha} = 1 \tag{2.10}$$

- Benzeggah and Kenane criterion (B-K criterion)

$$G_{Ic} + (G_{IIc} - G_{Ic}) \left(\frac{G_{II}}{G_T}\right)^{\eta} = G_c \qquad with\ G_T = G_I + G_{II} \tag{2.11}$$

The B-K criterion is using three parameters and, therefore, is capable of modeling the mix-mode fracture more accurately than the power law criterion (only two parameters) (Camanho and Davila, 2002).

2.2.3.3 Cohesive elements with Abaqus

Cohesive elements can be applied in both Abaqus/standard and Abaqus/explicit. In the standard analysis, the equations are solved using an implicit method. Most of the time, the Newton-Raphson method is used to converge the solution however the Riks method (arc-length algorithm) can also be used in case the tangent stiffness is 0. Abaqus/explicit solves the equations using an explicit method. It was originally developed to simulate high-speed impact events but can also be used to solve static problems. It is quite useful in cases of complicated contact problems in which the standard analysis is unlikely to produce a solution as the achievement of the convergence is not needed in the simulation (Hu et al., 2008).
In Abaqus, the traction-separation model is used in the case where the cohesive element layer is negligibly small. This model assumes a linear elastic behaviour of the cohesive elements until the initiation of the crack. The cohesive elements are used where cracks are expected to develop. Cracks are restricted to propagate in the cohesive elements layer and will not deflect into the surrounding material.
The damage initiation of the elements begins when the stresses or the strains satisfy a damage initiation criterion. Four different damage initiation criterion can be used in Abaqus:

- maximum nominal stress criterion (MAXS): damage is initiated when either the normal or shear stresses reaches a critical value

$$max\left\{\frac{< t_n >}{t_n^0}, \frac{t_s}{t_s^0}, \frac{t_t}{t_t^0}\right\} = 1$$

- maximum nominal strain criterion (MAXE): damage is initiated when either the normal or shear strains reaches a critical value

$$max\left\{\frac{< \epsilon_n >}{\epsilon_n^0}, \frac{\epsilon_s}{\epsilon_s^0}, \frac{\epsilon_t}{\epsilon_t^0}\right\} = 1$$

- quadratic nominal stress criterion (QUADS): damage is initiated when a quadratic interaction function involving the nominal stress ratios reaches a value of 1

$$\left\{\frac{< t_n >}{t_n^0}\right\}^2 + \left\{\frac{t_s}{t_s^0}\right\}^2 + \left\{\frac{t_t}{t_t^0}\right\}^2 = 1$$

- quadratic nominal strain criterion (QUADE): damage is initiated when a quadratic interaction function involving the nominal strain ratios reaches a value of 1

$$\left\{\frac{< \epsilon_n >}{\epsilon_n^0}\right\}^2 + \left\{\frac{\epsilon_s}{\epsilon_s^0}\right\}^2 + \left\{\frac{\epsilon_t}{\epsilon_t^0}\right\}^2 = 1$$

When damage is initiated, a damage evolution law is used to describe the rate at which the material stiffness is degraded. Evolution can be based on displacement or on energy. In the evolution based on displacement, the displacement at complete failure relative to the displacement at damage initiation has to be specified. The evolution based on energy required the energy dissipated during the damage process which is the fracture energy. The fracture energy is equal to the area under the traction-separation curve. Both displacement and energy based damage evolution can have a linear or a exponential softening. Under mix-mode loading, power law or Benzeggagh-Kenane criterion can be used.

Chapter 3

Calibrating the Cranfield Rig

3.1 Cranfield icing tunnel

The cranfield icing tunnel was completed in 2003. It is composed of a square test section of 760 mm in length , a fan driven by a diesel engine, a return duct, a heat exchanger and a spray rake (figure 3.1). The particularity of this

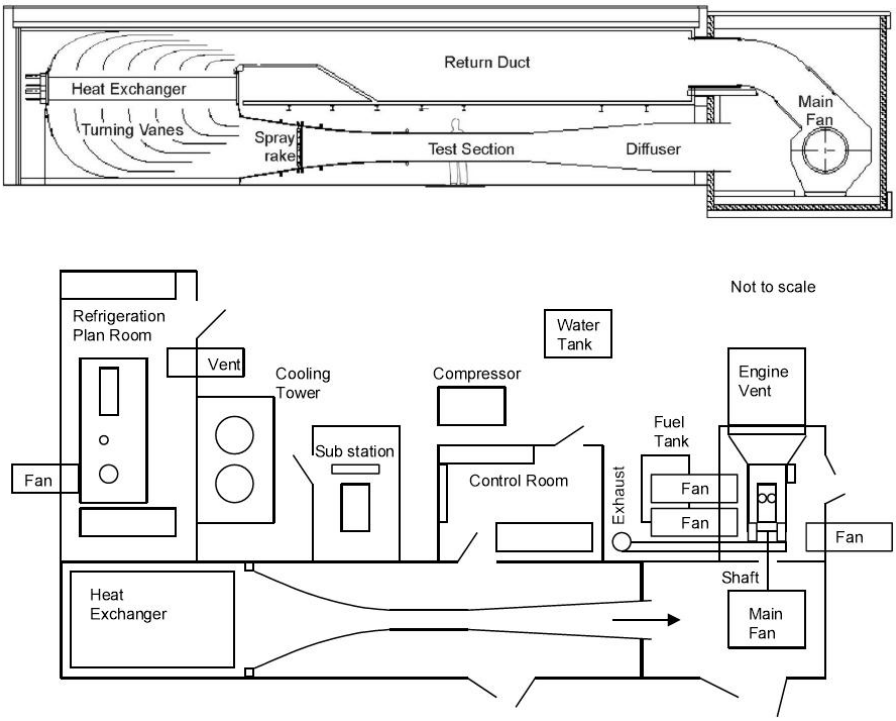

Figure 3.1: *Plane and side view of the Cranfield icing tunnel*

tunnel is that it is built on two floors: the working section is situated on the ground floor and the return leg on the upper floor.
The spray rake consists of 6 rows of nozzles with a total of 99 places for nozzles (figure 3.2), to allow the user to adapt the cloud. Depending on the model

Figure 3.2: *Cranfield icing tunnel spray rake (the distance between two rows of nozzle is 170 mm)*

tested, the configuration of nozzles used will differ in order to obtain a uniform spray which give a uniform thickness of ice on the model.
The nozzle bars include one pipe filled by air and, within it, one pipe filled by water. Both water and air are needed in order to make the water spray in fine droplets. When a nozzle is configured to be "sealed off", nothing happens; the water and the air stay in the pipe. When a nozzle is in configuration "open", the water flows through the hole in the center and the air flows through the holes at the edge. The values of the water and the air pressure determine the size of the droplets.
The cranfield icing tunnel has the capability of recreating atmospheric icing condition for supercooled water droplet from 16 to 300 microns at temperature between 0 and -25°C and for tunnel air speed between 30 to 100 $m.s^{-1}$.

3.2 Method to adjust the cloud uniformity

The cloud uniformity is obtained by opening or sealing off the nozzles at different positions in the spray rack. Unfortunately, the tunnel air flow is quite unpredictable and a large number of trials are needed to obtain the desired

cloud.
First of all, a grid was placed in the test section of the tunnel, perpendicular to the spray. The tunnel was set up to a very low temperature, -18°C, so we can assume that all the water sprayed was completely frozen as soon as it entered in contact with the grid surface. Water was sprayed on the grid for several minutes and the distribution of ice was observed. The nozzle configuration was then changed until a visually uniform layer of ice was obtained on the grid (figure 3.3).

Figure 3.3: *Repartition of ice on a grid placed in the test section (760 mm in width). The nozzle configuration has to be modified to avoid the big lump in the middle of the cloud*

Then the method of the icing blade was used to further refine the cloud uniformity. The principle of this method was to accrete ice on a blade at low temperature (-18°C) during a specified time of one or two minutes. After that time, the blade was taken out of the tunnel and the thickness of ice was measured carefully. A relation (Langmuir and Blodgett, 1946) allows the conversion of ice thickness to liquid water content (LWC):

$$LWC = \frac{h \times 1000 \times \rho_i}{V \times t \times E_M} \tag{3.1}$$

where h is the ice thickness in mm, ρ_i is the ice density in g.cm^{-3}, V is the velocity of air in m.s^{-1}, t is the time of accretion in s and E_M is the

total collection efficiency taken equal to 1. The factor 1000 is used for unity consistency.
For our test work, a large and highly uniform cloud was needed. A cloud uniform through the whole test section was impossible to obtain. However a reasonable uniformity can be obtained in most of the central part (figure 3.4). In the horizontal position between 1.5 and 5 most of the points had a LWC value in the range 0.6 to 0.8. The measurement uncertainty was about 0.1, so, in that typical case, the LWC was 0.7 in the central part between the horizontal position 1.5 to 5 and the vertical position -4 to 2.

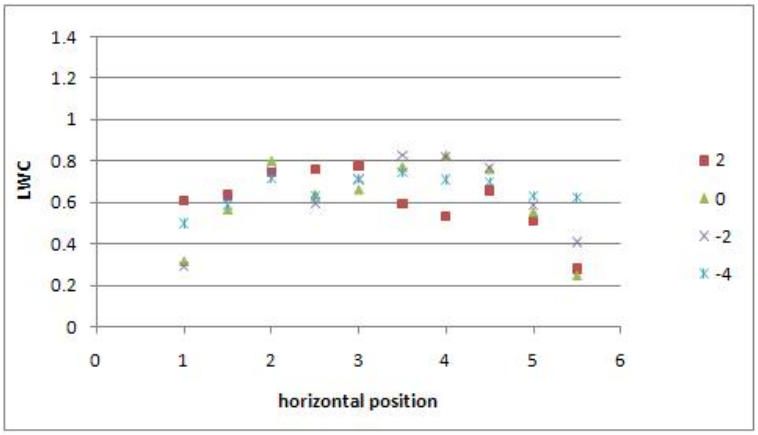

Figure 3.4: *LWC measurement at different vertical and horizontal position in the icing tunnel - wind speed 50* $\mathrm{m.s^{-1}}$ *, water pressure 18 PSI*

3.3 Results of the calibration and LWC measurement

The LWC of the cloud can be adjusted by changing the water pressure of the water sprayed. As the water pressure was increased, the LWC became higher. The air pressure needed to be adjusted together with the water pressure to keep the desired droplet size (figure 3.5). During our experiments, we wanted a droplet mean volume diameter (MVD) of 20 μm so we will choose the air pressure corresponding to the water pressure using the green curve.
The LWC had to be measured at different wind speeds and at different water pressures. Therefore a good map of the cloud LWC could be obtained. Knowing the LWC of the cloud is an essential step before carrying out any tests as it gives information on the cloud and, hence, on the ice attached on the substrate.

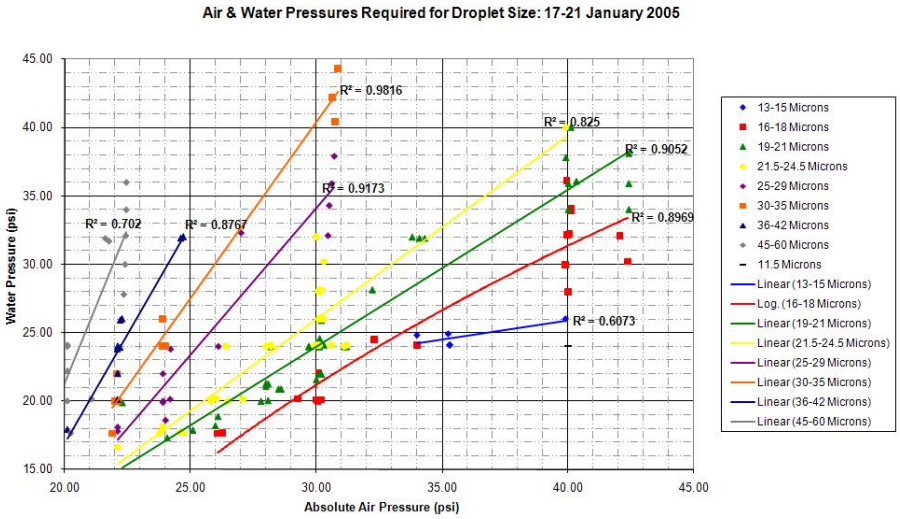

Figure 3.5: *Water pressure and air pressure for different droplets size*

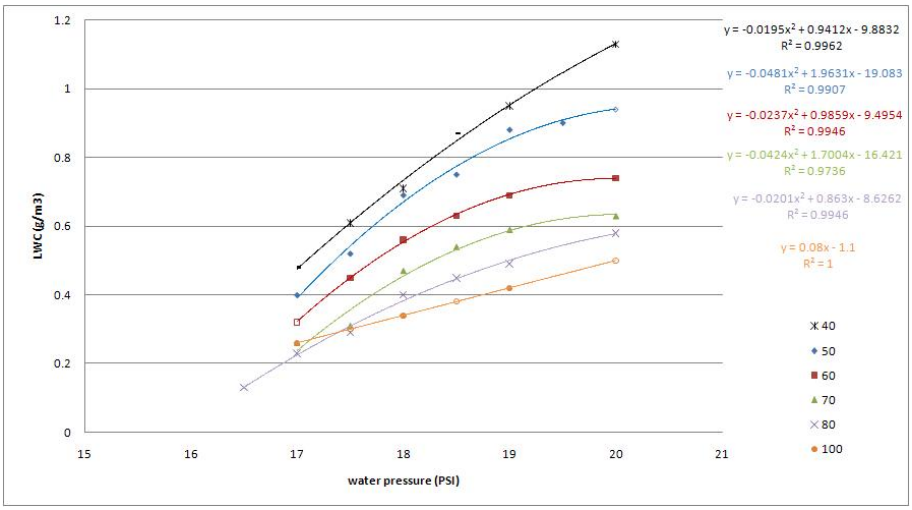

Figure 3.6: *Average Liquid Water Content of the cloud vs water pressure for various wind speed*

Figure 3.6 represents the average LWC of the cloud as a function of water pressure for different wind speeds. The unfilled points represent the values calculated using the equation of the curves on figure 3.7. Each value is an average of the values measured in different parts of the cloud in the testing area. The uncertainty in the measurement was estimated at 0.1 $g.m^{-3}$. Hence, especially at low water pressure, the values were not very accurate.

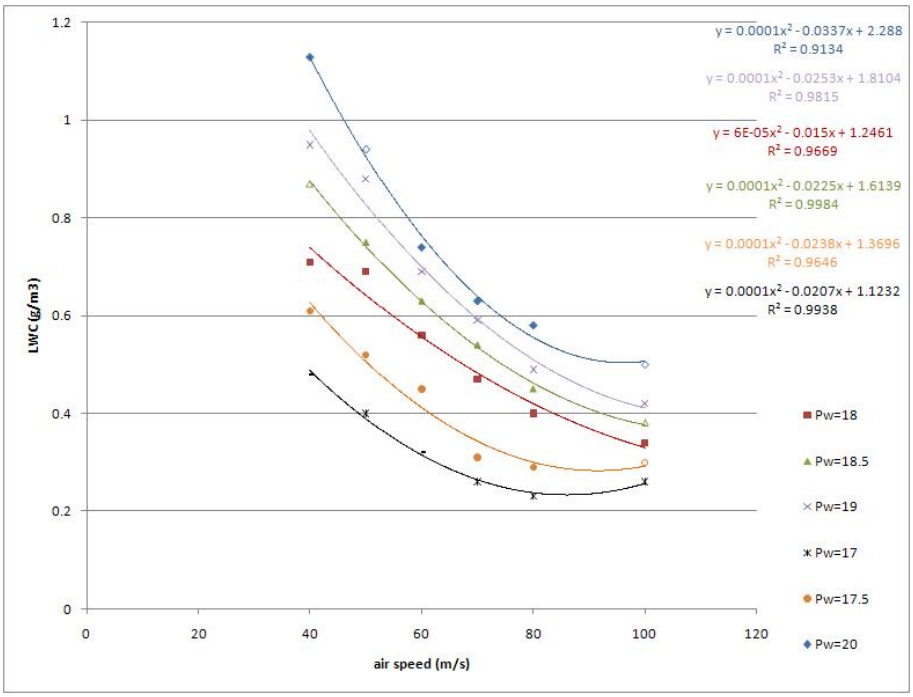

Figure 3.7: *Average Liquid Water Content of the cloud vs wind speed for various water pressure*

Chapter 4

Physical properties of ice

Some physical properties of impact ice have been measured during this project. Values of density, Young's modulus and average grain size have been reported for different ice growth conditions and have been compared with other author's values.
Work about the freezing fraction can also be found in this chapter. Although it is not considered as a property of ice, the freezing fraction determines the structure of ice and is known to have an influence on the ice properties.

4.1 Freezing fraction

The freezing fraction has been first introduced by Messinger. It represents the fraction of water which freeze initially when water droplets impinge on a surface. For rime ice, all the water impinging will freeze and the freezing fraction is 1 but for glaze or mixed ice only part of the water will freeze straight away, the remaining water will stay liquid and run back or soak into the ice. The freezing fraction for glaze ice is close to 0 and for mixed ice comprised between 0.3 and 1 (Ruff, 1985).
This parameter is thought to be very useful in order to provide a correlation of the properties of ice with ambient conditions. Indeed, the freezing fraction is a parameter which group together all the ambient conditions and the dimensions of the impacted object.
The rate at which the water freezes on a surface depends on the local heat balance. All the following analysis was based on the work done by Anderson (2004). His work was only valid in the case of glaze ice therefore terms were added to take into account rime and mixed ice ($T_s \neq 0$). An assumption was made that the object on which the ice accreted on, was a cylinder and that the analysis was conducted at the stagnation point.

When water impinges on the cold surface, heat is exchanged between the ice, the liquid water, the substrate and the surrounding.

4.1.1 Different terms of the mass and energy balance equation

In order to evaluate the freezing fraction, the heat terms need to be described:

4.1.1.1 Convection from the surface, q_c

By definition the convection from the surface to the boundary layer is

$$q_c = h_c(T_s - T_b l)$$

where h_c is the convective heat transfer coefficient , T_s is the surface temperature termed here as the temperature of the ice front surface and T_{bl} is the temperature in the boundary layer .
The convective heat transfer coefficient can be obtained from the Nusselt number, Nu_a (4.1)

$$h_c = \frac{Nu_a k_a}{d} \tag{4.1}$$

where k_a is the thermal conductivity of air and d is a characteristic length (here d is taken as the cylinder diameter). Kreith's correlation is used to calculate the Nusselt number (4.2). This relationship is specially used to calculate the Nusselt number at the stagnation line of a cylinder.

$$Nu_a = 1.14\, Pr_a^{0.4} Re_a^{0.5} \tag{4.2}$$

where Pr_a is the Prandtl number (4.3) and Re_a is the Reynolds number (4.4) .

$$Pr_a = \frac{Cp_a \mu_a}{k_a} \tag{4.3}$$

$$Re_a = \frac{V d \rho_a}{\mu_a} \tag{4.4}$$

where Cp_a is the specific heat of air , μ_a is the viscosity of air , V is the tunnel air velocity and ρ_a is the density of air . All these properties are evaluated at the film temperature, T_{film} , which is an average of the surface and the free-stream temperature, T_s and T respectively (4.5).

$$T_{film} = \frac{T_s + T}{2} \tag{4.5}$$

The boundary layer temperature, T_{bl} is obtained from

$$T_{bl} = T_{st} + \frac{r_f V^2}{2Cp_a}$$

where T_{st} is the static temperature and r_f is the recovery factor . For a cylinder in a flow at subsonic speed, the recovery factor is 1 at the stagnation point (Anderson, 2004). However a value of 0.85 for laminar flow and 0.87-0.88 for turbulent flow is usually used in case of flat plate. Some authors took an average value to cover most cases like Messinger who take 0.875. This analysis is made at the stagnation point so the recovery factor will be taken as 1 and the convection term becomes

$$q_c = h_c \left(T_s - T_{st} - \frac{V^2}{2Cp_a} \right) \tag{4.6}$$

4.1.1.2 Evaporation of water, q_e

The heat lost from the surface due to the evaporation of water is evaluated from the mass of water which evaporates, $\dot{m}_e$, and the latent heat of evaporation, Λ_v

$$q_e = \dot{m}_e \Lambda_v \tag{4.7}$$

The first term, $\dot{m}_e$, is obtained from (4.8). This equation developed by Ruff (Anderson, 2004) includes the compressible effect of the fluid.

$$\dot{m}_e = h_G \frac{\frac{p_{ww}}{T_{st}} - \frac{p_{tot}}{T_{tot}} \frac{p_w}{p_{st}}}{\frac{1}{0.622} \frac{p_{tot}}{T_{tot}} - \frac{p_{ww}}{T_{st}}} \tag{4.8}$$

h_G is called the gas-phase convective mass transfer coefficient and can be related to the convective heat transfer coefficient via the Schmidt and Prandtl number, Sc_a and Pr_a respectively.

$$h_G = \frac{h_c}{Cp_a} \left(\frac{Pr_a}{Sc_a} \right)^{0.67} \tag{4.9}$$

The Schmidt number is defined by

$$Sc_a = \frac{\mu_a}{\rho_a D_v}$$

where D_v is the diffusivity of water vapor in air . p_{ww} and p_w are the vapor pressure respectively at the surface and in the atmosphere.

4.1.1.3 Sublimation of ice, q_s

Similarly to the evaporation term, the heat lost from the surface by the sublimation of ice is obtained from the mass of ice which sublimes to vapor, $\dot{m}_s$, and the latent heat of sublimation, Λ_s

$$q_s = \dot{m}_s \Lambda_s \tag{4.10}$$

However, as the sublimation of ice is considerably smaller than the evaporation of water, this term is negligible in the energy balance equation.

4.1.1.4 Radiation from the surface, q_r

This term represent the heat lost from the surface by radiation.

$$q_r = \sigma_{SB} \epsilon (T_s^4 - T_{st}^4) \tag{4.11}$$

where σ_{SB} is the Stefan-Boltzmann constant ($\sigma_{SB} = 5.6703 \times 10^{-8}$ W.m^{-2}.K^{-4}) and ϵ is the emissivity of the object (number comprised between 0 and 1). As the surface temperature is close to the ambient temperature, this term is small compared to the convection term (in the order of 9 W.m^{-2} compared to 200 W.m^{-2} at an ambient temperature of -3°C and a tunnel air speed of 50 m.s^{-1}) and can be neglected.

4.1.1.5 Rise of temperature of impinging water to freezing point, q_w

The methodology assumes that the freezing takes place at a freezing temperature T_f . However, before impingement, water is at ambient temperature, T_{st}. Hence, heat from the surface is used to increase the temperature of impinging water from ambient to freezing temperature.

$$q_w = \dot{m}\, Cp_{ws} \,(T_f - T_{st}) \tag{4.12}$$

where $\dot{m}$ is the mass flux of water impinging the surface per unit of time and Cp_{ws} is the specific heat of water on model surface.
The total mass flux, $\dot{m}$, impinging the surface per unit of time is defined as $\dot{m} = LWC \times V \times \beta$ where LWC is the liquid water content of the cloud, V is the tunnel velocity and β is the local catch efficiency.

4.1.1.6 Runback water, q_{rb}

This term represents the heat lost from the surface by water flowing out of the control volume.

$$q_{rb} = [(1-n)\dot{m} - \dot{m}_e]\, Cp_{ws} \,(T_s - T_f) \tag{4.13}$$

where n is the freezing fraction .
The first term of equation (4.13) represent the mass flux of water which can flow out of the control volume. At the stagnation point there is no water inflow along the surface so the mass balance equation can be expressed as below :

$$\dot{m}\Delta S - \dot{m}_e\Delta S - \dot{m}_{rb} = \dot{m}_i\Delta S \tag{4.14}$$

where ΔS is the surface, $\dot{m}_{rb}$ is the mass flux of runback water and $\dot{m}_i$ is the mass flux of ice which forms on the surface. As the freezing fraction can be expressed by

$$n = \frac{\dot{m}_i}{\dot{m}} \tag{4.15}$$

the mass flow of runback water becomes

$$\dot{m}_{rb} = (1-n)\dot{m}\Delta S - \dot{m}_e\Delta S \tag{4.16}$$

In case of glaze ice, T_s is equal to T_f so the term q_{rb} is nil. In the other cases, the difference between the surface and the freezing temperature is quite small and the term could be neglected.

4.1.1.7 Conduction through the ice into the substrate, q_{cond}

The conduction term represents the heat lost by conduction in the model through the ice.

$$q_{cond} = k_i\frac{\Delta}{\xi l}\left(T_s - T_{st} - r\frac{V^2}{2Cp_a}\right) \tag{4.17}$$

Traditionally this term is neglected as it simplifies the equation however the conduction term, especially near the interface, might influence the grain size and could then have an influence on the ice growth.

4.1.1.8 Release of latent heat of fusion from the freezing water, q_f

This term represent the heat gained by the surface due to the release of latent heat of fusion from the freezing water.

$$q_f = \dot{m}\, n\, \Lambda_f \tag{4.18}$$

where Λ_f is the latent heat of fusion.
The water entering the control volume is $\dot{m} = LWC \times V \times \beta$. Except in the case of rime ice, only part of this water freezes on contact with the surface. This fraction is found by multiplying the impinging mass of water by the freezing fraction and the term q_f becomes

$$q_f = LWC \times V \times \beta \times n \times \Lambda_f \tag{4.19}$$

4.1.1.9 Decrease of temperature of ice from freezing temperature to surface temperature, q_i

When water is frozen, the ice has to be cooled from freezing temperature to the surface temperature. Therefore the heat gained by the surface is obtained from

$$q_i = \dot{m}\, n\, Cp_{is}(T_f - T_s) \tag{4.20}$$

where Cp_{is} is the specific heat of ice.
In the case of glaze ice, the surface temperature is equal to the freezing temperature and the term q_i disappears.

4.1.1.10 Kinetic energy of water drop impinging the surface, q_k

Due to the high velocity involved, the drops have a non-negligible kinetic energy which becomes heat when they hit the surface

$$q_k = \dot{m}\frac{V^2}{2} \tag{4.21}$$

4.1.1.11 Water flowing from neighbouring location

Water flowing from neighbour location to the control volume will transfer heat to the surface. However, at the stagnation point, water enters in the control volume only by impingement so this term is ignored in the energy balance equation.

4.1.2 Energy balance equation

If the terms q_s, q_r and q_{cond} are ignored, the energy balance equation obtained is

$$q_c + q_e + q_w + q_{rb} = q_f + q_i + q_k \tag{4.22}$$

After simplification, the freezing fraction is obtained from

$$n = \frac{Cp_{ws}}{\Lambda_f + Cp_{is}(T_f - T_s) + Cp_{ws}(T_s - T_f)}\left(\frac{\theta}{b} + \phi\right) \tag{4.23}$$

where

$$\begin{aligned} b &= \frac{LWC\, V\, \beta\, Cp_{ws}}{h_c} \\ \theta &= T_s - T_{st} - \frac{V^2}{2\, Cp_a} + \frac{h_G}{h_c}(\Delta P\, \Lambda_v) \\ \phi &= (T_f - T_{st}) + (T_s - T_f) - \frac{h_G}{\dot{m}}\, \Delta P\, (T_s - T_f) - \frac{V^2}{2\, Cp_{ws}} \end{aligned}$$

where

$$\Delta P = \frac{\frac{p_{ww}}{T_{st}} - \frac{p_{tot}}{T_{tot}}\frac{p_w}{p_{st}}}{\frac{1}{0.622}\frac{p_{tot}}{T_{tot}} - \frac{p_{ww}}{T_{st}}} \tag{4.24}$$

4.1.3 Air, water and ice properties

Most of the different properties introduced in the above equation are dependent on temperature and have to be determined either at the surface temperature or at the film temperature.The surface temperature is the temperature at the surface of the ice deposit and can be measured during experiments. However, for glaze ice, liquid water is present at the surface of the ice block, hence, the surface temperature is assumed to be equal to the freezing temperature. The film temperature is defined as the average between the ambient static temperature and the surface temperature (4.25).

$$T_{film} = \frac{T_s + T_{st}}{2} \tag{4.25}$$

4.1.3.1 Specific heat, Cp

The specific heat of air at atmospheric pressure varied very little with temperature in the range between -40°C and 0°C. Therefore a constant value is used in the equations

$$Cp_a = 1008 \quad \text{J.kg}^{-1}\text{.K}^{-1} \tag{4.26}$$

The specific heat of water over the range from -40°C to 0°C is obtained from the following equation given by Pruppacher and Klett as reference by Anderson (2004):

$$Cp_{ws} = [1.0074 + 8.29 \times 10^{-5} \times (T_s - 273.15)^2] \times 4200 \quad \text{J.kg}^{-1}\text{.K}^{-1} \tag{4.27}$$

where T_s is the surface temperature in K.

4.1.3.2 Thermal conductivity, k_a

In the temperature range from -40°C to 0°C and an ambient pressure of 1 bar, the thermal conductivity of air is given by the relation:

$$k_a = [-12.69 + 2.029\sqrt{T_{film}}] \times 1.2 \times 10^{-3} \quad \text{W.m}^{-1}\text{.K}^{-1} \tag{4.28}$$

A change in pressure of around 1 bar only influences the value of the thermal conductivity of air by 0.1%. Therefore the pressure variation will not be taken into account in the calculation of this value.

4.1.3.3 Diffusivity of water vapor, D_v

The diffusivity of water vapor is evaluated at the film temperature from a expression developed by Pruppacher and Klett (Anderson, 2004)

$$D_v = 0.211 \left(\frac{T_{film}}{273.15} \right)^{1.94} \left(\frac{1.0132 \times 10^5}{p_{st}} \right) \tag{4.29}$$

4.1.3.4 Vapor pressure of water, p_w

The vapor pressure of water is defined as the pressure at which the steam is saturated. Its value can be determined by a correlation developed by Pruppacher and Klett (Anderson, 2004) in the range of temperature from -50°C and 0°C.

$$p_w = a_0 + \Delta T(a_1 + \Delta T(a_2 + \Delta T(a_3 + \Delta T(a_4 + \Delta T(a_5 + \Delta T(a_6)))))) \, Pa \tag{4.30}$$

where

$$\begin{aligned} a_0 &= 610.78 \\ a_1 &= 44.365 \\ a_2 &= 1.4289 \\ a_3 &= 2.6506 \times 10^{-2} \\ a_4 &= 3.0312 \times 10^{-4} \\ a_5 &= 2.0341 \times 10^{-6} \\ a_6 &= 6.1368 \times 10^{-9} \end{aligned}$$

Equation 4.30 can be used for both the vapor pressure at the surface, $p_w w$, and the one in the atmosphere, pw by using the appropriate temperature, T.

4.1.3.5 Latent heat, Λ

The latent heat of fusion is obtained from Pruppacher and Klett's relation

$$\Lambda_f = [79.7 + 0.485 \times (T_s - 273.15) - 2.5 \times 10^{-3} \times (T_s - 273.15)^2] \times 4200 \quad \text{J.kg}^{-1} \tag{4.31}$$

The latent heat of vaporization is also obtained from an expression developed by Pruppacher and Klett

$$\Lambda_v = 597.3 \times \left(\frac{273.15}{T_s} \right)^E \times 4200 \quad \text{J.kg}^{-1} \tag{4.32}$$

where $E = 0.167 + 3.670 \times 10^{-4}$

4.1.3.6 Viscosity, μ

In the range from -40°C and 0°C, the viscosity of air varies following the relation

$$\mu_a = \frac{10^{-4}}{0.12764 + 124.38/T} \quad g.cm^{-2}.s^{-1} \tag{4.33}$$

The temperature used is the free stream temperature.

4.1.3.7 Density

The density of air is obtained from static pressure and temperature with the gas-law expression

$$\rho_a = \frac{p_s t}{R_a T_s t} \tag{4.34}$$

where R_a is the gas constant for air $R_a = 287\, J.kg^{-1}.K^{-1}$.
The density of ice varies with the type of ice formed. Because of the lack of data, as a first approximation, the density of ice will be taken as constant

$$\rho_i = 917\, kg.m^{-3} \tag{4.35}$$

The density of water is taken at the freezing point as

$$\rho_w = 999.87\, kg.m^{-3} \tag{4.36}$$

4.1.4 Mathematical study of the influence of the different terms of the energy balance equation

The freezing fraction depends on numbers of parameters (equation 4.23): the surface temperature (T_s), the tunnel velocity (V), the liquid water content of the cloud (LWC), the ambient pressure (p_{tot}), the droplet size (MVD) through the collection efficiency (β), the ambient temperature (T_a) and the size of the impinging surface.
The present section will show the influence of the different parameters on the freezing fraction and the ice thickness. The ice thickness, h, can be obtained from the freezing fraction (n), the collection efficiency (β) and the accumulation parameter A_{cp} by:

$$h = n \times A_{cp} \times \beta \times d \tag{4.37}$$

where

$$A_{cp} = \frac{LWC\, V\, t}{d\, \rho_i}$$

This study is only mathematical and does not contain any measurements. The freezing fraction was calculated with a matlab program (appendix B)

mainly using equation 4.23. The parameters were taken as realistic as possible according to observations of ice accretions in the icing tunnel. The main objective of this study was to determine which parameters have the most influence on the freezing fraction of ice and therefore on the quality of ice.

4.1.4.1 Influence of ambient temperature

The ambient temperature has a huge influence on the aspect of ice. As the temperature gets colder, the ice appears whiter. However the study of the influence of this parameter is difficult to make because the surface temperature is closely linked to the ambient temperature. Only at high ambient temperature, the surface temperature can be estimated to be 0°C which means the ice is mainly glaze. At lower temperature, the surface temperature starts to fall below 0°C and is dependent to other parameters like the tunnel velocity or the LWC. For that reason, only ambient temperature above -6°C have been represented on the following chart (the point at -8°C seems to follow the curve but may not be realistic) as at these temperatures the ice is mainly glaze and the surface temperature is most probably 0°C. The other parameters used are :

Surface temperature	0°C
Mean droplets diameter	20 μm
Tunnel air velocity	50 m.s^{-1}
Liquid Water Content	0.5 g.m^{-3}
Object diameter	3 cm
Accretion time	10 min
Total pressure	1 bar

Both the ice thickness and the freezing fraction are increasing as the temperature decreases. The rise is rather sharp which means that the ambient temperature is a major parameter in the ice freezing and is mainly responsible for the quality of ice obtained.

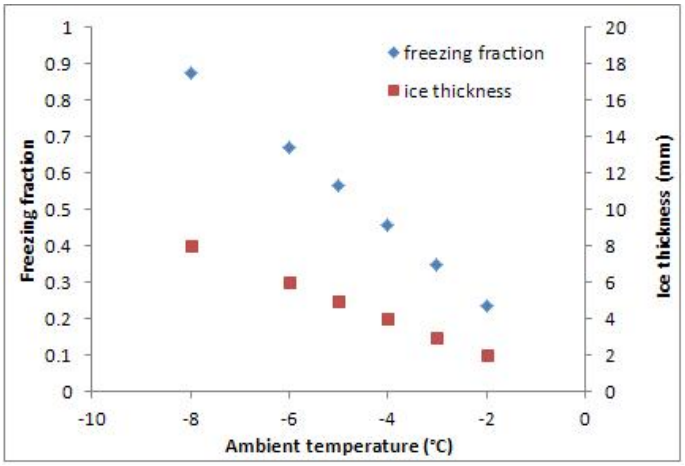

Figure 4.1: *Variation of freezing fraction and ice thickness as a function of ambient temperature*

4.1.4.2 Influence of surface temperature

The surface temperature (temperature of the ice front surface) is highly dependent on the ambient temperature, the tunnel air velocity, the LWC of the cloud, the droplet size and probably the material on which the ice is accreting. This means for each condition tested, a different value of the surface temperature could be obtained. However, for the purpose of this investigation, the surface temperature will be varied while all the other parameters are kept constant. The effects obtained will then be completely hypothetical but linked with the effect of the surface temperature with the other parameters can give us an indication of the physical effect of the surface temperature on the quality of ice.
In the case of glaze ice, the surface temperature is 0°C. Only in the case of mixed and rime ice, the surface temperature can be below 0°C. In this case study, the ambient temperature is fixed at -10°C which means the surface temperature can be realistically estimated between -2 and -5°C. The other parameters are:

Ambient temperature	-10°C
Mean droplets diameter	20 μm
Tunnel air velocity	50 m.s^{-1}
Liquid Water Content	0.5 g.m^{-3}
Object diameter	3 *cm*
Accretion time	10 *min*
Total pressure	1 *bar*

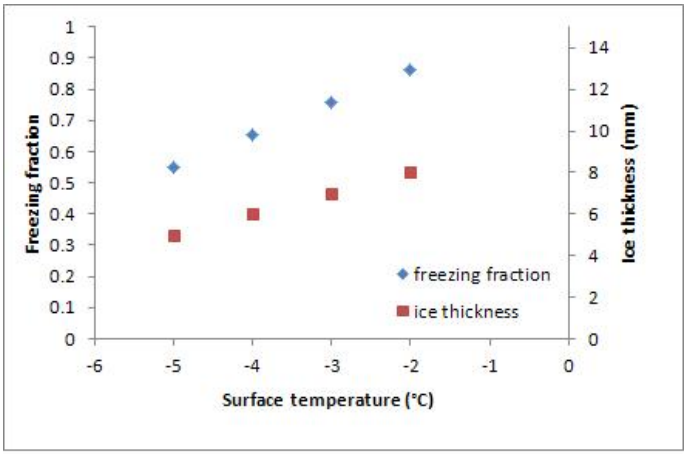

Figure 4.2: *Variation of freezing fraction and ice thickness as a function of the surface temperature*

The freezing fraction and the ice thickness are both sharply decreasing with the surface temperature. As the surface temperature is decreasing with the ambient temperature, it is reasonable to assume that the sharp increase of freezing fraction with ambient temperature will be lowered by the influence of the surface temperature.

4.1.4.3 Influence of tunnel air velocity

Even if the tunnel air velocity has an influence on the surface temperature it is reasonable to believe that at an ambient temperature of -3°C the surface temperature is 0°C whatever the air speed. In this study, the air velocity has been varied from 30 m.s^{-1} to 100 m.s^{-1} which represent the range of speed available in the icing tunnel. The other parameters are kept constant:

Ambient temperature	-3°C
Surface temperature	0°C
Mean droplets diameter	20 μm
Liquid Water Content	0.5 g.m^{-3}
Object diameter	3 *cm*
Accretion time	10 *min*
Total pressure	1 *bar*

The freezing fraction is globally decreasing with the air velocity. The decrease is more important at a lower speed than at a higher speed. Which means that at lower speed, the ice is more rime in aspect (in the case of V=30 m.s^{-1}, the hypothesis of Ts=0°C is probably not true and the freezing fraction is

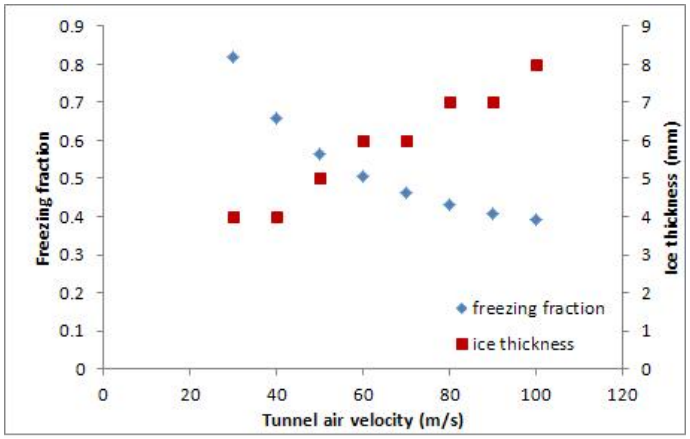

Figure 4.3: *Variation of freezing fraction and ice thickness as a function of tunnel velocity*

probably a bit lower) and more sticky whereas at higher speed, the ice is mainly glaze and will adhere less. The ice thickness is globally increasing with the air velocity from 4 *mm* at 30 m.s^{-1} to 8 *mm* at 100 m.s^{-1} .

4.1.4.4 Influence of LWC

The LWC represents the amount of liquid water in the cloud. If the number is higher the ice will appear more wet therefore more glaze. The LWC has a non negligible effect on the surface temperature as, if more liquid water impinges a surface, the surface temperature will be closer to 0°C. Therefore on the following figure, the value obtained for a LWC of 0.3 g.m^{-3} is probably over estimated as the surface temperature was assumed to be 0°C.

Ambient temperature	-3°C
Surface temperature	0°C
Mean droplets diameter	20 μm
Tunnel air velocity	50 m.s^{-1}
Object diameter	3 *cm*
Accretion time	10 *min*
Total pressure	1 *bar*

As expected the freezing fraction is decreasing with the LWC. At a low LWC, the ice obtained is rime whereas, at a higher LWC, glaze ice is obtained. The freezing fraction drops sharply at low LWC but the decrease is smoother for a moderate LWC.
However, the variation of LWC has no effect on the ice thickness.

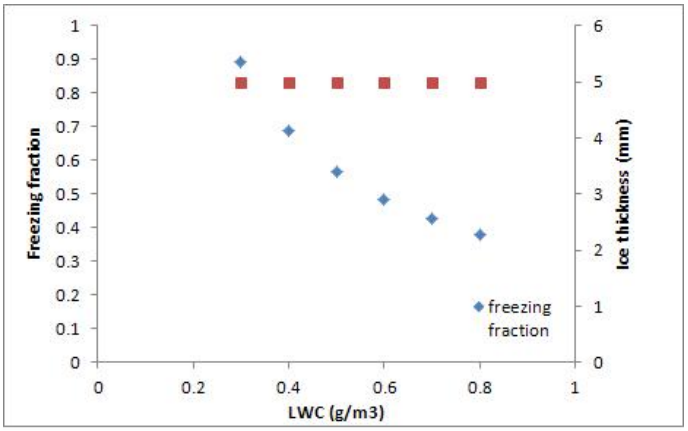

Figure 4.4: *Variation of freezing fraction and ice thickness in function of LWC*

4.1.4.5 Influence of object dimension

The dimension of the object where the droplets are impinging has an influence on the way the flow will hit the surface. In the above equations, the object is assumed to be a cylinder perpendicular to the flow (representing a wing). In our case, the object is a cylinder with its front surface perpendicular to the flow and the dimension is the diameter of this cylinder. A large object will deflect the flow more than a small object, resulting in a lower ice thickness.

Ambient temperature	-3°C
Surface temperature	0°C
Mean droplets diameter	20 μm
Tunnel air velocity	50 m.s^{-1}
LWC	0.5 g.m^{-3}
Accretion time	10 *min*
Total pressure	1 *bar*

Figure 4.5 shows that, as the object diameter increases, the freezing fraction sharply drops to a minimum value and then slowly increases. In the same time the ice thickness decreases, sharply at first and then more slowly.

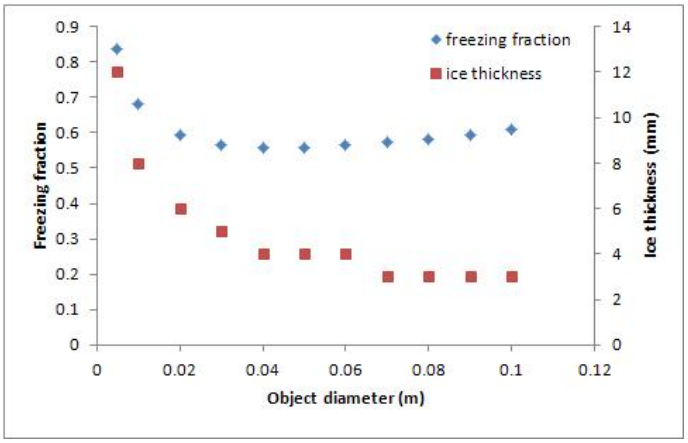

Figure 4.5: *Variation of freezing fraction and ice thickness as a function of impinging object dimension*

4.1.4.6 Influence of ambient total pressure

Ambient pressure has an effect on the freezing fraction through the compressibility of air (equation 4.24). However this effect is quite small in the case of our experiments conducted in the icing tunnel while the variation of ambient pressure is only due to meteorological conditions and could only vary slightly around 1 bar. At higher altitude, the pressure would be considerably lower and would have a much greater influence on the resulting freezing fraction. Nevertheless, the main objective of this investigation was to determine which parameter will have an influence on the quality of ice produced in the icing tunnel during our experiments to measure the mechanical properties of ice. Therefore, only values around 1 bar were investigated.
As it can be seen on the figure below, for ambient pressure in the range from 0.99 to 1.1 bar, there is only a slight variation in the freezing fraction. No variation can be seen on the ice thickness at all.

Ambient temperature	-3°C
Surface temperature	0°C
Mean droplets diameter	20 μm
Tunnel air velocity	50 m.s^{-1}
LWC	0.5 g.m^{-3}
Accretion time	10 *min*
Object diameter	3 *cm*

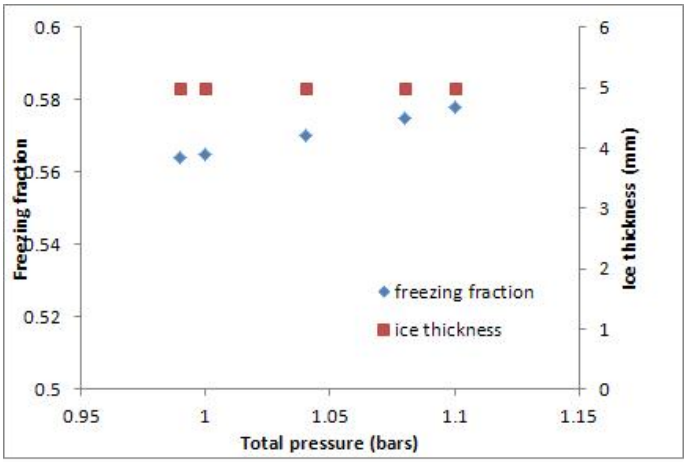

Figure 4.6: *Variation of freezing fraction and ice thickness as a function of ambient total pressure*

4.1.4.7 Influence of droplet size

The last parameter to be investigated was the droplet size. As the droplet size becomes bigger, more liquid water will hit the surface leading to ice more glaze and therefore a lower freezing fraction.

Ambient temperature	-5°C
Surface temperature	0°C
Tunnel air velocity	50 $m.s^{-1}$
Liquid Water Content	0.5 $g.m^{-3}$
Object diameter	3 *cm*
Accretion time	10 *min*
Total pressure	1 *bar*

The ice thickness is independent on the droplet size. The freezing fraction drops sharply for a small droplet size. When the droplet size increases, the decrease in freezing fraction becomes smoother. For each condition tested, parameters like the ambient temperature, the tunnel air speed, the cloud LWC, the droplet size, the total pressure and the size of the object were known. However the surface temperature may change depending on the set up conditions and, therefore, needed to be determined.
The following sections outline how the surface temperatures were measured and the freezing fractions calculated from temperature measurements.

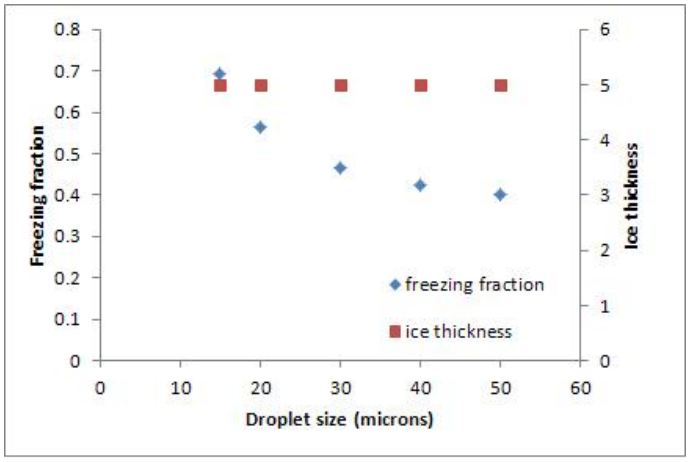

Figure 4.7: *Variation of freezing fraction and ice thickness as a function of droplet size*

4.1.5 Measurement of the surface temperature during the experiments

While the mechanical tests were conducted, the surface temperature, T_s, was measured using a laser gun (Milwaukee C12 LTGE). A hole has been made on the top of the tunnel to give access to the substrate surface when the tunnel is running. The gun was pointed at the substrate surface, through the hole, at the beginning of the ice accretion and the temperature was monitored. It is a very effective and non intrusive way of measuring the surface temperature however it is lacking in accuracy. To obtain a good measurement, the gun has to be perpendicular to the surface and at a certain distance from the surface so the sensing region is not larger than the substrate surface. One of the main problems was the side of the hole in the tunnel which sometimes interfere with the measurement, leading to high temperature readings. Another source of errors could be the presence of parasitic lights. Because the laser gun measure the surface temperature based on emission any other source of light could contribute to the measurement and leads to higher values of surface temperature. Anyway this method was giving a good indication of the surface temperature but, in order to get more accurate results, the whole installation needed to be redesigned and a comparison with the temperature read by a thermocouple placed at the interface ice/substrate needs to be done. In the current condition of measurement, the error on the reading of the surface temperature is estimated to be about 1°C.
In the future, this method could allow us to measure the surface temperature through the whole ice accretion as it is assumed to vary with time.

The surface temperature has been measured, with the laser gun, for different ambient total temperatures in the range from -3°C to -20°C. The LWC was kept constant either at 0.4 g.m^{-3} or at 0.7 g.m^{-3} and the tunnel air speed at 50 m.s^{-1} (figure 4.8). The values of surface temperature were found to be similar whichever LWC value was used. The surface temperature is 0°C down to an

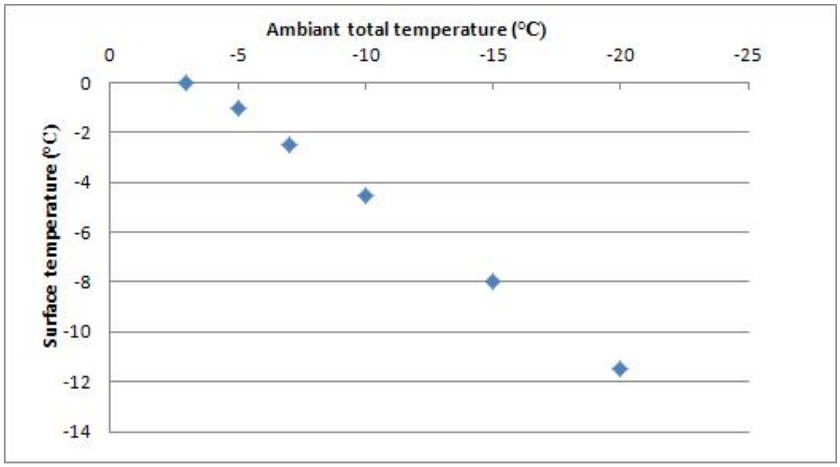

Figure 4.8: *Surface temperature at the beginning of the ice accretion for different ambient total temperature between -5 and -20° C - LWC=0.4* g.m^{-3} *and V=50* m.s^{-1}

ambient total temperature of -4°C and is , then, decreasing with the ambient temperature.
Further investigation of the influence of the LWC on the surface temperature has been carried out. The ambient total temperature was kept at -10°C and the tunnel air speed at 40 m.s^{-1} . The LWC was varied from 0.5 to 1.1 g.m^{-3} and, in this range, no difference was found on the surface temperature. Therefore an average of -4°C will be used for the freezing fraction calculation, which is the average temperature obtained during the measurement in this range of LWC.
The last parameter investigated was the tunnel air speed (figure 4.9). The ambient total temperature was kept at -10°C, the LWC at 0.5 g.m^{-3} and the tunnel air speed was varied from 40 to 80 m.s^{-1} . The surface temperature was found to decrease as the tunnel air speed increases. This trend is probably due to the fact that at higher tunnel air velocity, the convection term is higher resulting in a lower value of the temperature of the ice front surface (closer to the ambient temperature).

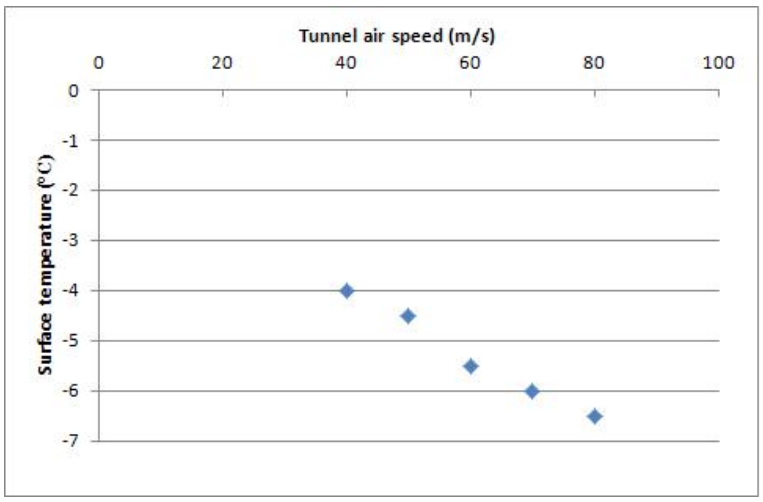

Figure 4.9: *Surface temperature at the beginning of the ice accretion for different tunnel air speeds between 40 and 80* $\mathrm{m.s^{-1}}$ *- Ta=-10°C and LWC=0.5* $\mathrm{g.m^{-3}}$

4.1.6 Freezing fraction

Using the surface temperatures from the previous paragraph, the freezing fraction was calculated using equation 4.23 for each of the conditions tested.
The freezing fraction is increasing as the temperature decreases (figure 4.10). This means that at a lower temperature, the ice is more like rime ice and at

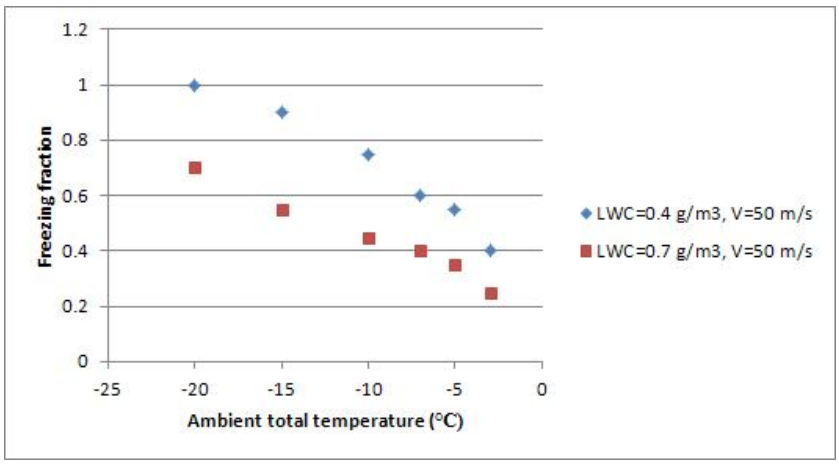

Figure 4.10: *Freezing fraction for different ambient temperature*

higher temperature the ice is more like glaze ice. This is confirmed by the visual observation of the ice samples (figure 4.11). The ice grown at -5°C has a

Figure 4.11: *Samples of impact ice grown at different temperatures (-5, -10, -15 and -20° C) with a LWC of 0.4* g.m^{-3} *and a speed of 50* m.s^{-1} *- the size of the -20° C sample is about 30 mm in diameter (the cubic shape of the samples at -10 and -15° C was obtained after polishing)*

clear aspect and has grown more on its side (perpendicularly to the oncoming air) which gives a sort of flower shape. On the other hand, the ice grown at -20°C is opaque and is more cylindrical in shape.
Even if the surface temperature is independent of the cloud LWC, the freezing fraction will vary (figure 4.12). After calculations, the freezing fraction has

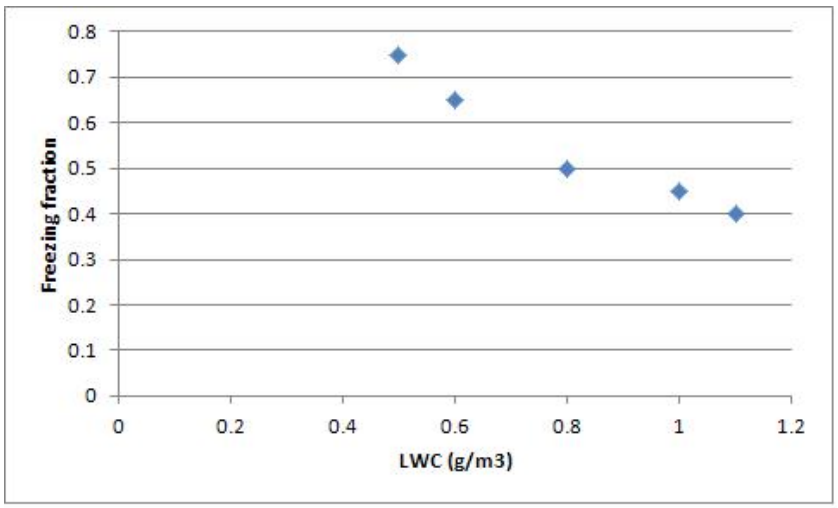

Figure 4.12: *Freezing fraction for different LWC - T=-10° C and V=40* m.s^{-1}

been found to decrease as the LWC increases. At high values of LWC, more liquid water is present in the cloud meaning that, at the same ambient temperature, a smaller amount of water is able to freeze on contact with the surface than at a low value of LWC. This results in a lower value of freezing fraction. Figure 4.13 show ice pieces grown with different LWC. It can be seen that the ice grown at LWC higher than 0.8 g.m^{-3} have a wider shape than the ice grown at lower LWC. The ice grown with a LWC of 0.5 and 0.6 g.m^{-3} are cylindrical

Figure 4.13: *Samples of impact ice grown with different LWC at a temperature of -10° C and a speed of 40* $\mathrm{m.s^{-1}}$ *- the size of the sample grown at a LWC of 0.5* $\mathrm{g.m^{-3}}$ *is about 3 mm in diameter*

in shape. However no real difference in the color can be made, meaning that all these pieces are mixed ice.
The decrease of air speed results in reducing the freezing fraction (figure 4.14). Indeed, as the cloud contacts the surface faster, the droplets are more prone

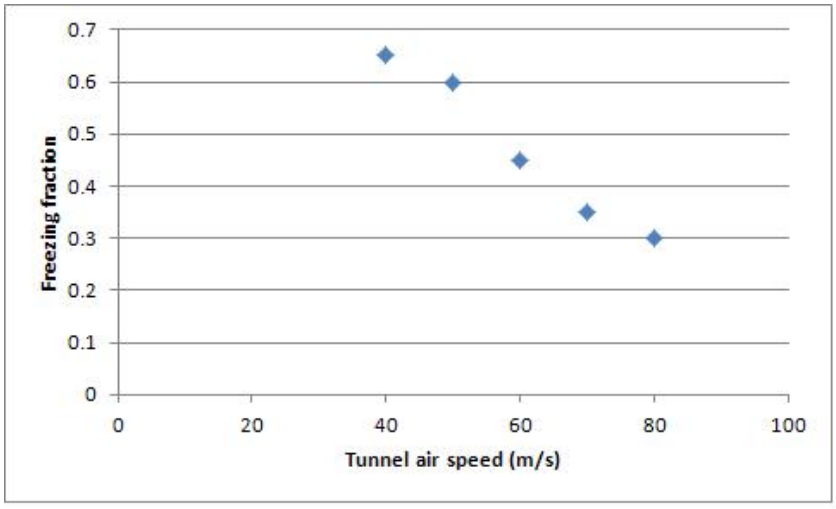

Figure 4.14: *Freezing fraction for different tunnel air speed - LWC=0.5* $\mathrm{g.m^{-3}}$ *and T=-10° C*

to splash around before freezing which will lower the freezing fraction value. Figure 4.15 shows three ice pieces grown with a different tunnel air speed. A small difference in the aspect of the ice can be noticed. The ice grown at 80 $\mathrm{m.s^{-1}}$ looks more transparent and has a wider shape than the others. The ice grown at 50 $\mathrm{m.s^{-1}}$ has a cylindrical shape and seems a little bit opaque.

Figure 4.15: *Samples of impact ice grown at different tunnel air speed with a LWC of 0.5* $\mathrm{g.m^{-3}}$ *and at a temperature of -10°C - the size of the sample obtained with a tunnel wind speed of 50* $\mathrm{m.s^{-1}}$ *is about 3 mm in diameter*

4.2 Density

4.2.1 Literature review

4.2.1.1 Measuring the ice density

By definition the density of a material is its mass per unit of volume. In the case of ice the volume is not always easy to determine or even, to define, especially with atmospheric ice, as it can take various and undetermined shapes. Therefore several techniques are used to determine the ice density.
The easiest technique would be to simply measure the mass and the volume of an ice sample. This technique is called mass/volume technique (Timco and Frederking, 1996). An ice block of regular shape has to be cut and trimmed from the ice sheet. The dimension of the block are measured and the volume (V_i) is calculated. Then the sample is weighted (m_i) and the density is obtained from

$$\rho_i = \frac{m_i}{V_i} \tag{4.38}$$

The main advantages of this method is the ease of application. However it can lead to errors due to the difficulties to obtain a sample with perfect regular shape (error on volume) and, in case of sea ice, significant brine drainage. In the latter case, if brine drainage occurs, the volume of brine is filled by air of lower density, resulting in a lower density ice sample.
In the displacement (submersion) technique (Timco and Frederking, 1996), the load (P) needed to submerge a block of ice of known volume (V_i) is measured. The ice density can be calculated from

$$\rho_i = \rho_w - \frac{P}{V_i} \tag{4.39}$$

where ρ_w is the density of water. This method allows the determination of the ice density accurately but a problem occurs if the ice is porous. Water in which the ice is submerged, can penetrate the block of ice and take place of the trapped air leading to higher density values.
With the specific gravity technique (Timco and Frederking, 1996), a sample of ice is placed in an air tight container and allowed to melt. A hydrometer is used to measure the specific gravity of ice which can be converted in density using international standard tables. Sometimes densities can be read directly with the hydrometer. This method is simple and very accurate however any air trapped in the ice will escape as ice melts and will not be taken into account in the density measurement. This method is mainly used to evaluate a maximum value of the ice density.
In the buoyancy technique (Tremblay, 1991) the Archimede's principle is used. The ice piece is first weighted using a scale (m_i). A thin film of formvar is coated on the ice surface and the piece of ice is weighted again (m_{i+f}) in order to remove the volume of formvar from the density calculation. The formvar film is used to avoid penetration of the submersion fluid into the porous ice. The ice piece is suspended by a copper wire of negligible mass and is immersed into a beaker filled with oil. The difference of mass before and after immersion is measured (m_{i+f2}).
The volume of ice covered by the film of formvar is calculated from

$$V_{i+f} = \frac{m_{i+f2}}{\rho_{oil}} \tag{4.40}$$

The volume of formvar is obtained from

$$V_f = \frac{m_{i+f} - m_i}{\rho_{formvar}} \tag{4.41}$$

All density values have to be taken at the temperature of measurement as density is highly dependent on temperature. The density of ice can finally be obtained from equation 4.42.

$$\rho_i = \frac{m_i}{V_{i+f} - V_f} \tag{4.42}$$

The main advantage of this method is that any air trapped in the ice is taken into account in the calculation. The use of formvar avoids the penetration by fluid and keeps the ice intact. However formvar is a dangerous product as the solvents used to prepare the solution is either ethylene dichloride or chloroform. Both these solvents are denser than air so all the work has to be done under an exhaust fan.

4.2.1.2 Results from previous authors

Measurements of the density of atmospheric ice have not been extensively reported through the literature. Examples of what is available is the work done in the sixties by Macklin and more recently by the university of Quebec in Chicoutimi. Macklin (1962) has thoroughly studied the ice in hailstones which is also produced from supercooled water droplets. He particularly studied the formation of ice deposits looking at microstructure and measuring density. The ice was built up around a brass cylinder rotating in an icing tunnel. The density is obtained from the mass and the volume of the ice piece. As the brass cylinder is rotating, the ice accretion is observed to be largely uniform and is taken to be so for the purpose of calculation of the volume. The density is thought to be dependent on ambient temperature, air speed, LWC, droplet size and cylinder diameter, therefore a wide range of these conditions were tested: temperature from -5 to -30°C, air speed from 2.5 to 11.8 $m.s^{-1}$, droplet size from 22 to 65 μm, LWC up to 6 or 7 $g.m^{-3}$ and cylinder diameter from 0.103 to 1.433 cm. After analysis of all the collected data, a correlation is proposed, function of the surface temperature, T_s, and the droplet impact velocity, v_0 (Macklin, 1962). The surface temperature is the temperature at the surface of the ice deposit. It is dependent on the ambient temperature, the cylinder diameter, the wind speed and other thermal characteristics of ice, water and air. The droplet impact velocity is the speed of impact of a droplet and is dependent on the droplet size, the cylinder diameter and the air speed. The correlation (equation 4.43) is valid for surface temperature between -5 and -20°C and for values of $\frac{rv_0}{T_s}$ between -0.8 and -10.

$$\rho_i = 0.110 \left(-\frac{r_d v_0}{T_s} \right)^{0.76} \tag{4.43}$$

where r_d is the radius of the droplets.
For surface temperatures close to 0°C, the relation is more complex particularly if the ambient temperature is close to 0°C. For surface temperatures below -20°C, the density has been found to be only dependent on the quantity rv_0 and not on the surface temperature (figure 4.16).

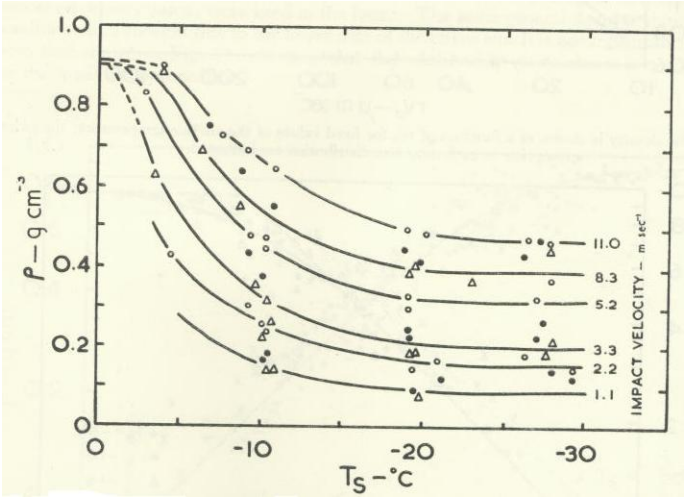

Figure 4.16: *Ice density measurement as a function of surface temperature (Macklin, 1962)*

At the university of Quebec in Chicoutimi, the ice density was measured using the buoyancy principle (Druez et al., 1986; Tremblay, 1991). Values for ice made at different temperature and wind speed for two combinations of LWC and MVD have been plotted on figures 4.17 and 4.18.

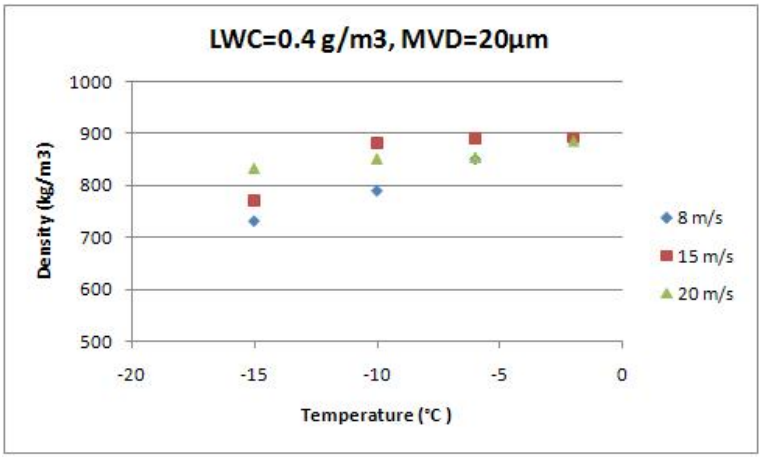

Figure 4.17: *Variation of the density of atmospheric ice with temperature and wind speed for ice grown in clouds with a liquid water content of 0.4* $\mathrm{g.m^{-3}}$ *and droplets of mean volume diameter of 20* μm *(Druez et al., 1986)*

It appears that density decreases with temperature and wind speed. The effect of LWC and MVD is not easy to determine but tend to reduce the decrease of

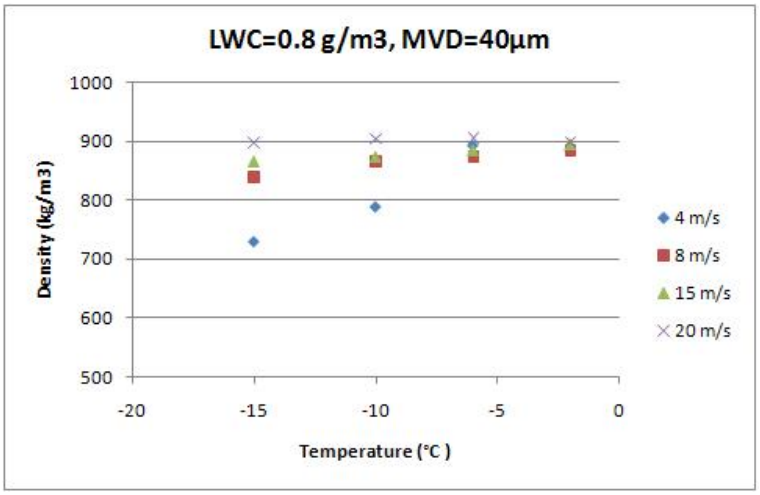

Figure 4.18: *Variation of the density of atmospheric ice with temperature and wind speed for ice grown in clouds with a liquid water content of 0.8* $\mathrm{g.m^{-3}}$ *and droplets of mean volume diameter of 40* μm *(Druez et al., 1986)*

density with temperature.
Ice density values measured by different authors have been plotted in the following graph (figure 4.19). Values obtained during the present study have

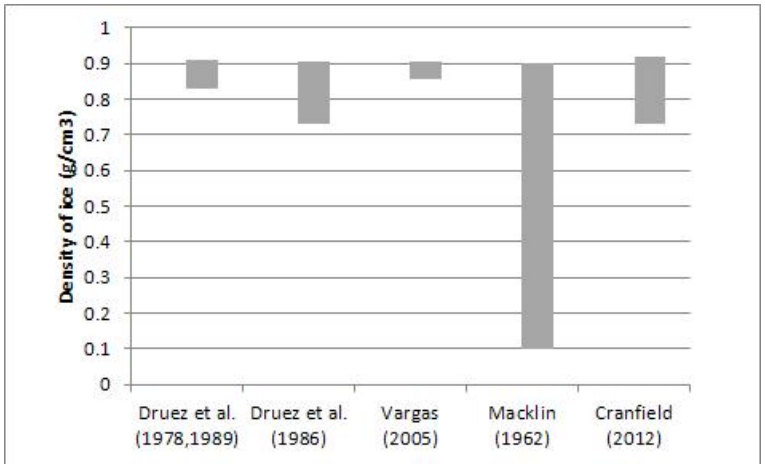

Figure 4.19: *Summary of the values found by different authors on the ice density*

been added to this graph for an easy comparison of the results. It appears that the results are in very good agreement with the other authors especially with Druez et al. (1986) despite the different method of measurement used.

Macklin (1962) results are wider as a wider range of temperature were used and at very slow air velocity resulting in all kind of ice produced from something very close to snow with a very low density to glaze ice with high density. The variation of density with temperature can be compared between different types of ice. The density of fresh freezing water ice increases as temperature decreases (figure 4.20). It is the complete opposite effect than the one found

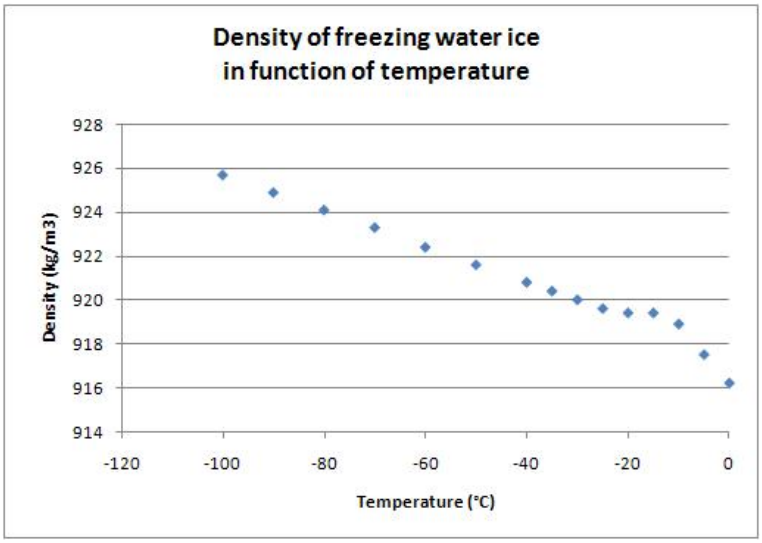

Figure 4.20: *Variation of the density of fresh freezing water ice with temperature (The engineering toolbox, 2011)*

for atmospheric ice. It could be explained by the amount of air trapped in the atmospheric ice which increases as temperature decreases. Indeed, at temperature near the melting point, the freezing fraction of water is very low meaning that water freezes very slowly and only a small amount of air can be trapped in the ice. At lower temperature, the freezing fraction is close to 1; all the water instantly freezes on contact with the surface trapping air. Therefore atmospheric ice is always made of solid ice and air but the amount of air is present in higher proportion at lower temperature resulting in a lower density.

4.2.2 Methodology

None of the technique presented in section 4.2.1.1 were completely satisfactory for our use. Indeed atmospheric ice contains trapped air, its shape is non uniform and we are not currently equipped to be able to work in a cold environment with fume extraction. Therefore a new technique had to be developed

for the determination of the volume. This technique involved a balance with good precision (0.01 g) and glass beads of small dimensions (200 μm).
Samples of ice were collected during the mechanical tests. Ice was grown in the icing tunnel at different conditions and then removed manually from the substrate and kept in a freezer at a temperature of -18°C. All measurements have been made in the icing tunnel at temperatures between -20°C and -10°C. The piece of ice was first weighted (m_i). Then a beaker was filled with glass beads and weighted (m_{gb}). Half of the glass beads were removed. The piece of ice was placed in the beaker which was filled again by the glass beads and weighted (m_{gb+i}). The second time, the volume of the glass beads used to fill the beaked was lower than the first time. The difference in volume represented the volume of the ice. By knowing the density of the pack of glass beads, the volume of ice can be obtained:

$$V_i = \frac{m_{gb} - (m_{gb+i} - m_i)}{\rho_{glass\,beads}} \tag{4.44}$$

The volume and the mass of the ice was known then the density can be calculated from

$$\rho_i = \frac{m_i}{V_i} \tag{4.45}$$

The error on the mass of ice was estimated as 0.05 g and the error on the volume as 1 cm^3, which gives an error on the ice density of 50 kg.m^{-3} . The volume especially was quite difficult to estimate as it depends greatly on the way the beaker was filled with glass beads. However this technique had the advantage to be very simple to use and to give an acceptable approximation of the ice density.

4.2.3 Results

Because of the small number of values reported in the literature and the difficulties to obtain exactly the same piece of impact ice than other authors, the technique was validated using a piece of ice made in the freezer. This piece of ice was supposed to contain no air and will be called in the following “bubble free ice”.

4.2.3.1 Bubble free ice

A large bowl of tap water was placed in the freezer for a couple of days. A warm plate was kept on the top of the bowl to give some heat and help the air to escape the ice. This results in a piece of ice with air bubbles in the middle but completely transparent on the outside. A sample from the bubble

free zone was cut and the density was measured. A value of 920 kg.m^{-3} has been found which is an expected value for bubble free ice grown in a freezer.

4.2.3.2 Impact ice

The density of pieces of impact ice grown under different conditions have been measured using the "glass beads" technique. The influence of ambient total temperature, cloud LWC and tunnel air speed were particularly investigated. For all the following results, ice was grown on mirror polished titanium alloy. As the previous authors (Macklin, 1962; Druez et al., 1986), the density has been found to decrease with decreasing temperature (table 4.1 and figure 4.21). This effect is easily understandable as, at lower temperature, the freezing

Temperature (°C)	Density (kg.m^{-3})
-5	916
-10	855
-15	821
-20	756

Table 4.1: *Density of impact ice grown at different temperature - LWC=0.4* g.m^{-3} *and V=50* m.s^{-1}

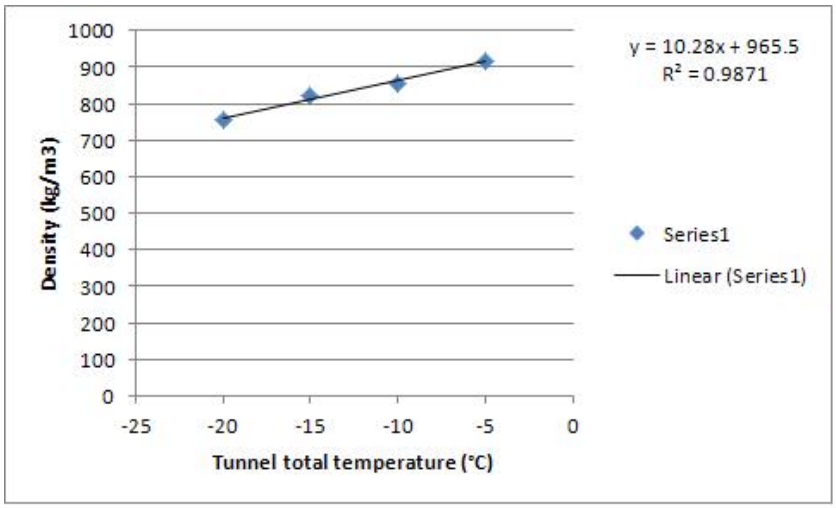

Figure 4.21: *Density of impact ice grown at different temperature with a LWC of 0.4* g.m^{-3} *and a tunnel air speed of 50* m.s^{-1}

fraction is higher, meaning that the quantity of water that froze on contact is higher. Therefore, pockets of air can be trapped into the ice which results

in a lower density as the density of air is much lower than the density of water. The results of Druez et al. are particularly interesting as only the tunnel wind speed differs from our conditions. The results they have obtained for the highest velocity (20 $m.s^{-1}$) are reasonably close to our results despite the fact that we were using different techniques.
The influence of the LWC has never been investigated clearly before. Druez et al. (1986) have conducted some measurement of the ice density grown from clouds at two different LWC and droplet size (0.4 $g.m^{-3}$ and 20 μm and 0.8 $g.m^{-3}$ and 40 μm). Their results show a significant increase of density at the higher LWC, especially at low temperature.
In this investigation, the density of ice grown at a temperature of -10°C, a tunnel air speed of 40 $m.s^{-1}$, a droplet size of 20 μm and five different values of LWC between 0.5 and 1.1 $g.m^{-3}$, has been measured using the same "glass beads" technique (table 4.2 and figure 4.22). The density of impact ice has

LWC ($g.m^{-3}$)	Density ($kg.m^{-3}$)
0.5	857
0.6	862
0.8	898
1.0	919
1.1	922

Table 4.2: *Density of impact ice grown at different LWC - T=-10° C and V=40* $m.s^{-1}$

been found to increase with the LWC. Looking at the influence of LWC on the freezing fraction, it can be observed that the freezing fraction of ice produced at a higher LWC is lower than the one produced at a lower LWC. This means that at high LWC, glaze ice is produced which contains fewer or no air inclusion and is expected to have a density closer to that of bubble free ice. On the contrary, at low LWC rime ice is produced which is assumed to contain lots of air pockets and, as a result, have a lower density.

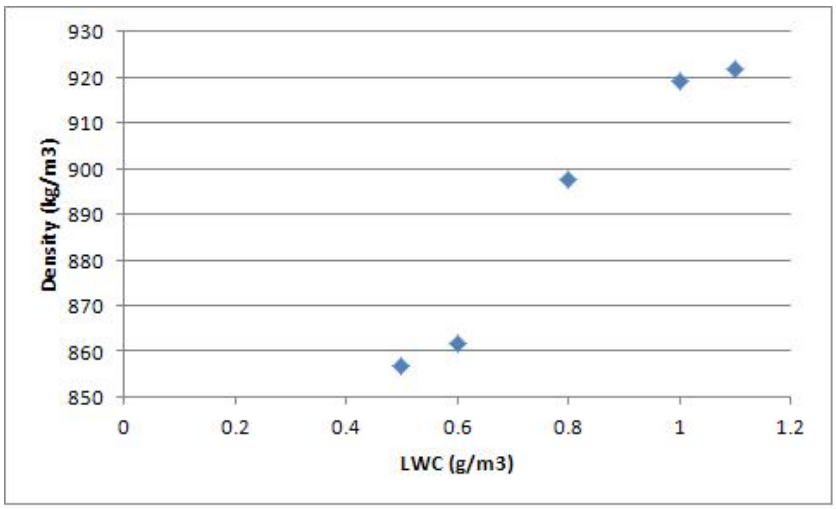

Figure 4.22: *Density of impact ice grown with different LWC at a temperature of -10° C and a tunnel air speed of 40* $\mathrm{m.s^{-1}}$

4.3 Stiffness

Young's modulus and Poisson's ratio are some of the main properties of a material. These numbers, characteristic of the stiffness of a material, are needed for the determination of the extension or the shrinkage of the material under load.
In this project, the Young's modulus and, to a lesser extent, the Poisson's ratio are of great importance in the calculation of the fracture energy in the mode I test and in all the finite elements analysis.

4.3.1 Previous work

From Hooke's elastic theory, a relationship can be obtained between stress and strain:

$$\sigma_{ij} = C_{ijkl}\epsilon_{kl} \quad or \quad \epsilon_{ij} = S_{ijkl}\sigma_{kl} \tag{4.46}$$

where σ is the stress, ϵ the strain, C the elastic or stiffness constants and S the compliance.
Because of symmetry relations in stress and strain ($\sigma_{ij} = \sigma_{ji}$ and $\epsilon_{ij} = \epsilon_{ji}$), the Hooke's relation can be simplified by

$$\sigma_i = C_{ij}\epsilon_j \quad or \quad \epsilon_i = S_{ij}\sigma_j \tag{4.47}$$

Due to the symmetry relation in the stiffness and the compliance ($C_{ij} = C_{ji}$ and $S_{ij} = S_{ji}$) and to crystallographic symmetry, the stiffness and the compliance

matrix have only five independent components (Schulson and Duval, 2009).

$$C_{ij} = \begin{bmatrix} C_{11} & C_{12} & C_{13} & 0 & 0 & 0 \\ C_{12} & C_{11} & C_{13} & 0 & 0 & 0 \\ C_{13} & C_{13} & C_{33} & 0 & 0 & 0 \\ 0 & 0 & 0 & C_{44} & 0 & 0 \\ 0 & 0 & 0 & 0 & C_{44} & 0 \\ 0 & 0 & 0 & 0 & 0 & 2(C_{11} - C_{12}) \end{bmatrix}$$

$$S_{ij} = \begin{bmatrix} S_{11} & S_{12} & S_{13} & 0 & 0 & 0 \\ S_{12} & S_{11} & S_{13} & 0 & 0 & 0 \\ S_{13} & S_{13} & S_{33} & 0 & 0 & 0 \\ 0 & 0 & 0 & S_{44} & 0 & 0 \\ 0 & 0 & 0 & 0 & S_{44} & 0 \\ 0 & 0 & 0 & 0 & 0 & 2(S_{11} - S_{12}) \end{bmatrix}$$

According to Sinha (1989), the Young's modulus can be obtained from

$$E_\Phi = \frac{1}{S_{11}(1-l^2)^2 + S_{33}l^4 + (2S_{13} + S_{44})l^2(1-l^2)} \tag{4.48}$$

and the shear modulus from

$$G_\Phi = \frac{1}{S_{44} + [S_{11} - S_{12} - (S_{44}/2)](1-l^2) + 2(S_{11} + S_{33} - 2S_{13} - S_{44})l^2(1-l^2)} \tag{4.49}$$

where $l = cos\Phi$ (Φ is the angle between the direction of the stress and the c-axis of the crystal).
The Poisson's ratio, for an isotropic material, can be obtained from the Young's modulus and the shear modulus by the relation

$$G = \frac{E}{2(1+\nu)} \tag{4.50}$$

Sinha (1989) calculated the Young's modulus, the shear modulus and the Poisson's ratio of four different type of polycrystalline ice using the above equations (4.48, 4.49, 4.50) and the compliance components determined by Dantl (1969) for single ice crystal.
Granular ice is isotropic and its elastic properties can be expressed by two independent constants (the superscript, e, indicates a derived quantity):

$$S_{11}^e = \frac{8S_{11} + 3S_{33} + 4S_{13} + 2S_{44}}{15} \tag{4.51}$$

$$S_{12}^e = \frac{S_{11} + S_{33} + 5S_{12} + 8S_{13} - S_{44}}{15} \tag{4.52}$$

The Young's modulus, the shear modulus and the Poisson's ratio can then be obtained from

$$E = 1/S^e_{11} \quad (4.53)$$
$$G = 1/(2(S^e_{11} - S^e_{12})) \quad (4.54)$$
$$\nu = -S^e_{12}/S^e_{11} \quad (4.55)$$

The Young's modulus of granular ice was found to vary from 8.93 to 9.39 GPa, depending on the temperature, and the Poisson's ratio was found to be around 0.31.
Columnar ice of type S1 has a texture with the c-axis oriented vertically. Which means that according to equations 4.48, 4.49 and 4.50, the elastic properties will vary with the angle Φ but will be isotropic in the horizontal plane (when the load is applied perpendicularly to the crystals' c-axis). In this latter plane, the angle Φ is equal to 90° which results in

$$E_{(h)} = 1/S_{11} \quad (4.56)$$
$$G_{(h)} = 1/[s_{44}/2 + S_{11} - S_{12}] \quad (4.57)$$
$$\nu_{(h)} = (S_{44} - 2S_{11} - 2S_{12})/S_{44} \quad (4.58)$$

Another particular direction is the vertical one (when the load is applied in the same direction as the c-axis). Therefore the angle Φ is equal to 0° and

$$E_{<v>} = 1/S_{33} \quad (4.59)$$
$$G_{<v>} = 1/S_{44} \quad (4.60)$$
$$\nu_{<v>} = (S_{44}/(2S_{33}) - 1 \quad (4.61)$$

At a temperature of -10°C, $E_{<v>}$ was found to be equal to 11.96 GPa and $E_{(h)}$ to 9.72 GPa (Sinha, 1989). The Poisson's ratio was found to be quite high with a value of 0.51 in the horizontal plane. According to the author, this value was probably overestimated and could show a limit in the application of equations 4.50 and 4.58 which are only correct for an isotropic material.
Columnar ice of type S2 has a texture with the c-axis in the horizontal plane and randomly oriented. In that case, for a vertical load, the angle Φ is equal to 90° and

$$E_{<v>} = 1/S_{11} \quad (4.62)$$
$$G_{<v>} = 1/[S_{44}/2 + S_{11} - S_{12}] \quad (4.63)$$
$$\nu_{<v>} = (S_{44} - 2S_{11} - 2S_{12})/S_{44} \quad (4.64)$$

In the horizontal plane, as the c-axis are randomly oriented, the equations are more complicated and will not be presented here. Values of Young's modulus

between 9.4 and 10 GPa were obtained for load in the horizontal plane while values between 9.6 and 10.2 GPa were obtained for vertical load (Sinha, 1989). In columnar ice of type S3, the c-axis are in the horizontal plane and are oriented. Therefore, for a vertical load, the results are identical to type S2 ice. In the horizontal plane, the results are close to type S2 ice, varying between 8.4 GPa and 12 GPa depending on the applied load direction and the orientation of the c-axis.

Sinha (1989) concluded by saying that the elastic properties of ice of different texture are very similar. He showed that type S2 ice is almost isotropic. Type S1 ice shows the maximum of anisotropy with a 23% difference between the Young's modulus calculated in the vertical direction and in the horizontal plane. Type S3 ice shows a slight anisotropy in the horizontal plane. The Young's modulus of granular ice appears to be lower than of columnar ice.

The stiffness components can be obtained by a "static" or a "dynamic" methods. The "static" method involves the measure of the displacement under an applied stress. The main problem of this method is that the stress needs to be applied and reverse very rapidly otherwise time-dependent deformation like creep will contribute to the deformation and the stiffness values will be underestimated.

Gold (1988) estimated the Young's modulus and the Poisson's ratio of two types of ice both cast in the shape of plate of different thicknesses. The first kind of plate measured 0.5 m in diameter and was made from freezing water (type S1). The second, measuring 1.22 m in diameter, was made using fine particles of ice to initiate the freezing, resulting in type S2 ice. Different loads were applied and withdrawn in cycles of 5 seconds to avoid creep and each time the deflection of ice was monitored by dial gauges. Values of Young's modulus and Poisson's ratio (table 4.3) were obtained using equations established by Roark (1965) and a correlation linking the Poisson's ratio to the Young's modulus, established by Gold for type S2 ice.

$$\nu = 0.88 - 0.59E/E_0 \tag{4.65}$$

where $E_0 = 10$ GPa.

Results are in general lower than Sinha which can be explained by the fact that Sinha's results have been obtained from the compliance matrix established for a single crystal and not for polycrystalline ice.

Traetteberg et al. (1975) studied the influence of temperature and strain rate on the elastic properties of two types of ice: naturally formed granular ice and laboratory grown columnar ice with the c-axis lying perpendicular to the long direction of the grains (probably type S2). Rectangular specimen of ice were loaded until a certain stress is reached and unloaded immediately. The load was measured using a load cell and the strain by an extensometer placed on

	h(mm)	T(°C)	E(GPa)	ν
0.5 m plate	10.7		9.65	0.32
	13.7		10.95	0.29
	16.8		11.16	0.29
1.22 m plate	32.5	-30	6.90	0.48
		-37	6.50	0.50
	33	-7	4.70	0.6
		-8	4.90	0.59
		-26	9.95	0.29
		-30	7.90	0.42
		-37	8.55	0.38
	40	-7	6.60	0.49
		-8	6.35	0.50
		-15	9.33	0.33
		-26	9.75	0.31
		-37	10.39	0.29

Table 4.3: *Young's modulus and Poisson's ratio of ice S1 and S2 for different ice thickness and temperature (Gold, 1988)*

the specimen. The Young's moduli were determined from the linear part of the stress-strain curve during loading. The dependence of the strain rate was investigated over a range of temperature from -10°C to -39.5°C. In overall, values of Young's modulus between 2.5 and 10.7 GPa have been found for granular ice whereas values between 3.7 and 9.7 GPa have been found for columnar ice. However at similar temperature and strain rate, like Sinha, Traetteberg et al.'s results are higher in case of columnar ice than in case of granular ice.
Koosheh (2007) measured the Young's modulus of impact ice by static loading using an extensometer attached to the ice specimens (table 4.4). The Young's modulus values where obtained from the first part of the stress-strain curve which is in theory linear. Koosheh reported problems to obtain a straight line and he also reported large scatter. This can be explained by the fact that static loading lack of accuracy and that only one extensometer could have been used (ASTM recommend the use of at least two extensometers). Values between 1.8 and 6.8 GPa were obtained which is much lower than the other authors.
The "dynamic" method involves the measurement of the speed of sound in the ice. The stiffness can be calculated using the relationship

$$C = \rho_i v_s^2 \tag{4.66}$$

where ρ_i is the density of ice and v_s is the speed of sound in ice.

accumulation temperature (°C)	test temperature (°C)	Young's modulus (GPa)
-6	-6	3.690 ± 1.532
-10	-3	5.014 ± 0.882
-10	-10	4.742 ± 1.899
-10	-20	4.903 ± 1.349
-20	-20	5.054 ± 1.777

Table 4.4: *Young's modulus of impact ice for different accumulation and test temperature (Koosheh, 2007)*

Gammon et al. (1983) determined the dynamic elastic moduli of four different kind of ice: artificially frozen ice from distilled water, ice from glacier, bubbly lake ice and sea ice. They used the Brillouin spectrometry technique which allow to obtain the sound velocity through a transparent medium by measuring the difference of frequency between a light entering and exiting the medium. The value of the sound velocity, v_s, is obtained from

$$v_s = \frac{\Omega\lambda}{2n\,sin(\alpha/2)} \tag{4.67}$$

where Ω is the Brillouin frequency shift, λ the wavelength of incident light, n the refractive index of the transparent medium and α the scattering angle.
Measurements in the longitudinal and the two transverse directions leads to an accurate determination of the elastic moduli (table 4.5). The values obtained

type of ice	artificial ice	glacier ice	lake ice	sea ice
c_{11}	13.96 ± 0.061	13.913 ± 0.061	13.876 ± 0.068	14.27 ± 0.68
c_{12}	7.153 ± 0.046	7.026 ± 0.058	6.979 ± 0.097	7.32 ± 0.51
c_{13}	5.765 ± 0.032	5.801 ± 0.037	5.657 ± 0.049	5.95 ± 0.15
c_{33}	15.013 ± 0.069	15.059 ± 0.075	15.071 ± 0.093	14.74 ± 0.2
c_{44}	3.021 ± 0.015	3.011 ± 0.018	3.024 ± 0.025	2.98 ± 0.03

Table 4.5: *Values of elastic moduli (in GPa) for different type of ice at a temperature of -16°C (Gammon et al., 1983)*

for the artificial ice, the glacier ice and the lake ice are similar. However the elastic moduli of sea ice are in general higher; except for c_{33} and c_{44} which are respectively lower and similar.
From the bulk modulus and the sound velocity in the longitudinal direction, Young's modulus and Poisson's ratio of granular ice at -16°C were obtained. Values of 9.332 GPa and 0.32521 were respectively found for the Young's modulus and the Poisson's ratio.

Attempts were made by Chu et al. (1991) to calculate the Young's modulus of laboratory grown ice using finite element analysis (table 4.6). Assumptions were made that the ice is an isotropic and a perfectly linear elastic material, and, that the applied load is uniformly distributed on the cross section of the specimen. The ice specimens were cast around an aluminium rod made of two parts. During the tensile test, the two aluminium parts are pulled out. The load was monitored by a load cell and the strain by an extensometer. A two dimensional axisymmetric model was used to simulate this experiment. As the Young's modulus of aluminium is known, the Young's modulus of ice was determined using the tensile force and the total strain from the experiments. The graph presented on figure 4.23 summarizes the values of Young's mod-

Temperature (°C)	-4	-7	-12	-18	-23
Young's modulus (GPa)	6.6	8.3	7.6	7.9	7.6

Table 4.6: *Young's modulus value for laboratory ice casted around an aluminium rod (Chu et al., 1991)*

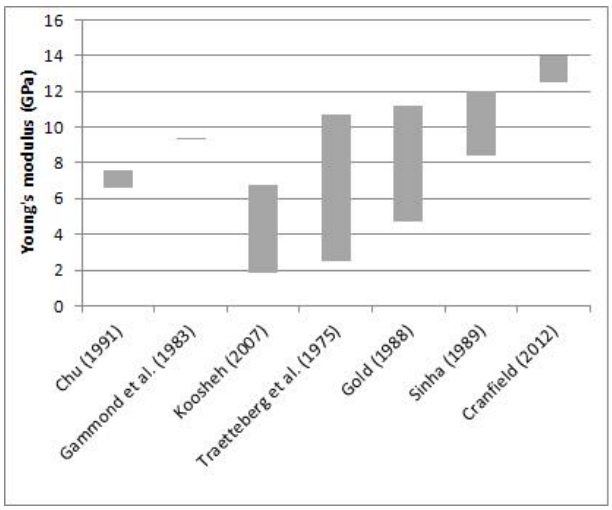

Figure 4.23: *Summary of the Young's modulus values obtained by different authors*

ulus obtained from different authors. It has been found, in general, that the Young's modulus of ice is comprised between 2.5 and 12 GPa depending on the type of ice (granular ice gives lower values than columnar ice) and the temperature of formation. However comparisons are not obvious as the methods used to obtain the Young's modulus of ice are very different between each authors: Chu et al. (1991) used a finite element method, Sinha (1989) theoretical

equations and values obtained from single crystal ice, Gold (1988), Traetteberg et al. (1975) and Koosheh (2007) a "static" method and Gammon et al. (1983) a "dynamic" method involving the speed of sound measured by Brillouin spectrometry. From all these authors, only Koosheh dealt with impact ice.

4.3.1.1 Influence of temperature

The investigation of the influence of ambient temperature on elastic properties is quite well documented. In his experiments on type S2 ice, Gold (1988) found that a decrease in ambient temperature leads to an increase of the Young's modulus of ice and a decrease in the Poisson's ratio. The same increase in Young's modulus was also found by Sinha (1989) for granular ice, type S1 ice and type S2 ice. The influence of temperature was not investigated for S3 ice. The influence on Poisson's ratio was only studied in case of granular ice and was found to slightly increase as the temperature decreases. Traetteberg et al. (1975) also confirmed the increase of Young's modulus with the decrease in temperature, in the range from -10°C to -39.5°C, for granular ice and S2 ice. For impact ice, Koosheh (2007) investigated the influence of both test temperature and accumulation temperature. The trend is not obvious for different test temperatures and similar accumulation temperatures, however, in the same way as for laboratory grown ice, the Young's modulus of impact ice increases as the temperature decreases (table 4.4).

4.3.1.2 Influence of ice thickness

Gold (1988) measured the elastic properties of type S1 and S2 ice of different thickness. For ice S1, the Young's modulus increases with the ice thickness while the Poisson's ratio decreases to a value of 0.29. For type S2 ice, the trend is not obvious but in general the same observation can be made (table 4.3).

4.3.1.3 Influence of strain rate

Traetteberg et al. (1975) measured the Young's modulus of ice by applying a force and immediately removing it. They studied the influence of strain rate on the Young's modulus of ice in the range from 10^{-8} to $5 \times 10^{-3}\,s^{-1}$. It appears that the Young's modulus increases with the strain rate (figure 4.24). It has been observed that in this range of strain rate, ice goes through a ductile to brittle transition. This observation could explain why the strain rate has such a dramatic effect on the Young's modulus of ice.

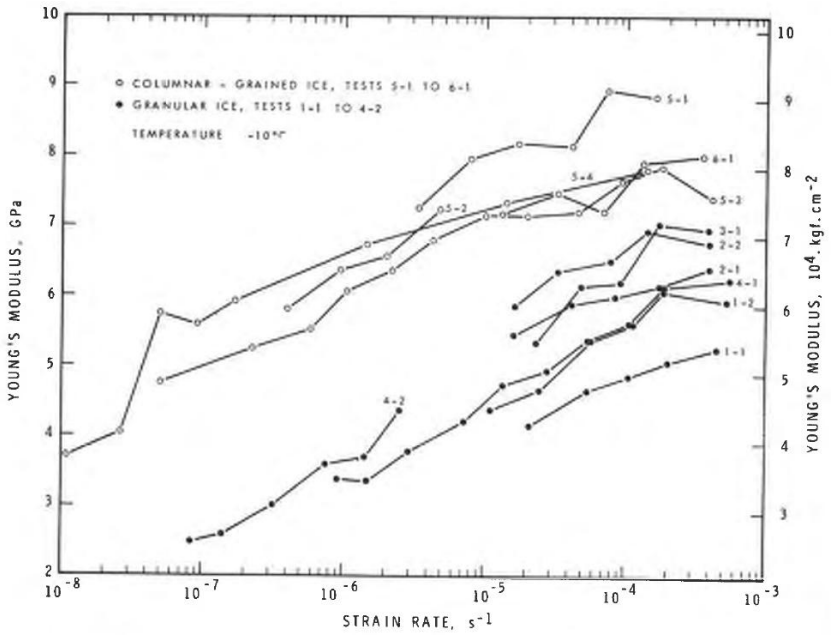

Figure 4.24: *Strain rate dependence of Young's modulus (Traetteberg et al., 1975)*

4.3.2 Methodology

In the present project, measurement of the Young's modulus has been made by measuring the speed of sound through a block of ice using an ultrasonic thickness measuring instrument (sonatest sitescan 120). Samples of ice have been collected after each series of mechanical tests. These samples were kept in a freezer and were then shaped in rectangular blocks using grinding paper. Care was taken to ensure that the opposite faces of the blocks were visually parallel.
Measurements were made in the three directions. The stiffness is calculated using the following equation:

$$C = \rho_i v_s^2 \tag{4.68}$$

The results show two identical values and a slightly lower one (table 4.7). An error of 10 $\mathrm{m.s^{-1}}$ was estimated on the sound speed measurement while the error on the density has been previously shown to be of 50 $\mathrm{kg.m^{-3}}$. Therefore the error on the stiffness measurement was of 0.9 GPa which means that the results can be assumed to be isotropic. The value obtained twice was taken as the Young's modulus which is also the highest of the three values. In order to get a more precise value of the Young's modulus, the whole compliance matrix would be needed however it involves a different type of probe to measure the

Temperature (°C)	Size (mm)	Speed of sound ($m.s^{-1}$)	Density ($kg.m^{-3}$)	Stiffness (GPa)	Young's modulus (GPa)
-5	17.7 22.95	3765 3916	916	13.0 14.0	14.0
-10	21.5 26.45 24.1	3963 3991 3990	855	13.4 13.6 13.6	13.6
-15	24.9 26.76 31.07	4013 4022 3972	821	13.2 13.3 13.0	13.2
-20	29.74 29.8 31.13	4067 4067 4010	756	12.5 12.5 12.2	12.5

Table 4.7: *Young's modulus of impact ice accreted at different temperature with a LWC of 0.4* $g.m^{-3}$ *and a tunnel air speed of 50* $m.s^{-1}$

speed of sound.

4.3.3 Results and discussion

The Young's modulus of impact ice was measured at four different temperatures between -5°C and -20°C. Young's modulus values were found to decrease as the ambient temperature at which the ice grown decreases which was the complete opposite trend than reported by the other authors (figure 4.25). Two

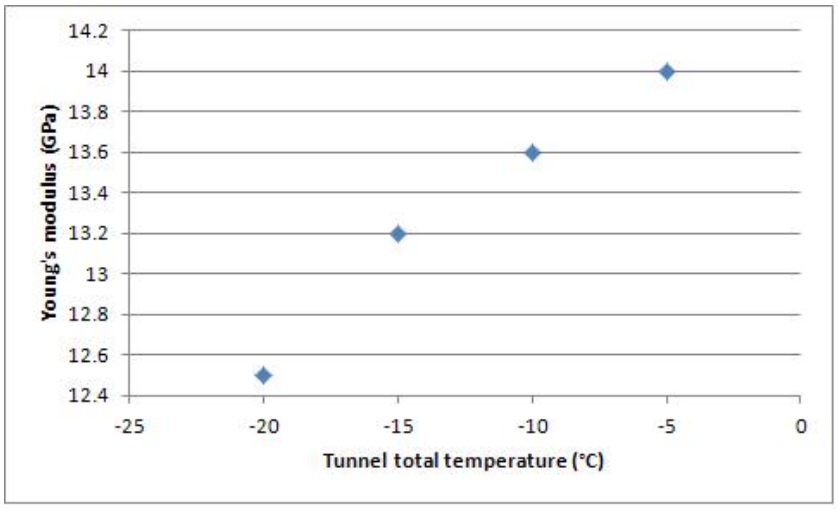

Figure 4.25: *Young's modulus values of impact ice accreted at different temperature with a LWC of 0.4* $g.m^{-3}$ *and a tunnel air speed of 50* $m.s^{-1}$

causes may explain this unexpected behaviour. First, most of the authors have measured the Young's modulus of laboratory grown ice or other types of ice grown very slowly instead of impact ice. The density of laboratory grown ice has been found to increase as the temperature decreases so, it is logical, as the speed of sound is increasing with decreasing temperature, that the stiffness will increase. However, in case of impact ice, due to the presence of air at lower temperature, the density decreases with decreasing temperature. Although the speed of sound is higher through ice grown at lower temperature, this results in a decrease of the Young's modulus with temperature. The second cause may be the difference in the thickness of the ice pieces used. Gold (1988) reported in his paper that the thickness of ice has an influence on the Young's modulus. Indeed it was found that the Young's modulus increases as the ice thickness increases. However, although this cause could produce some errors in the stiffness measurement, it was not thought to have a great impact on the trend found.
A third source of errors should also be raised: the ice is a porous material, hence, during the measurement, as the wave propagates, it can encounter or not air pockets. On the other side, the density is measured taking into account these air pockets. This observation and added to the fact that the equation used to calculate the stiffness (equation 4.68) has been defined in the case of an isotropic single phase elastic continuum material (which is generally not the case of impact ice) lead to the conclusion that the method used is not adequate. However, it was easy to put in place and it gives a good approximation of the Young's modulus of impact ice keeping in mind that there is very little data available in the literature.

4.4 Microstructure

Ice may be considered as a brittle material meaning that a rapid crack propagation leads to fracture of the material. As brittle fracture is mainly controlled by the presence of discontinuities within the material (defects, cracks, dislocations, pores, inclusions, segregations, grain boundaries, etc), a study of the ice microstructure can help to explain the behaviour of ice attached on a substrate.
When the material is subject to loading, the cracks are responsible for stress concentrations. The resulting stress fields cause the propagation of cracks, leading to brittle fracture (Jayatilaka, 1979). The crack propagates approximately perpendicular to the applied stress and can travel through the grains of the material or along its boundaries. The propagation through the grains is called transgranular fracture (figure 4.26). The cracks usually proceed along

crystallographic planes called cleavage planes (Hayden et al., 1965). The prop-

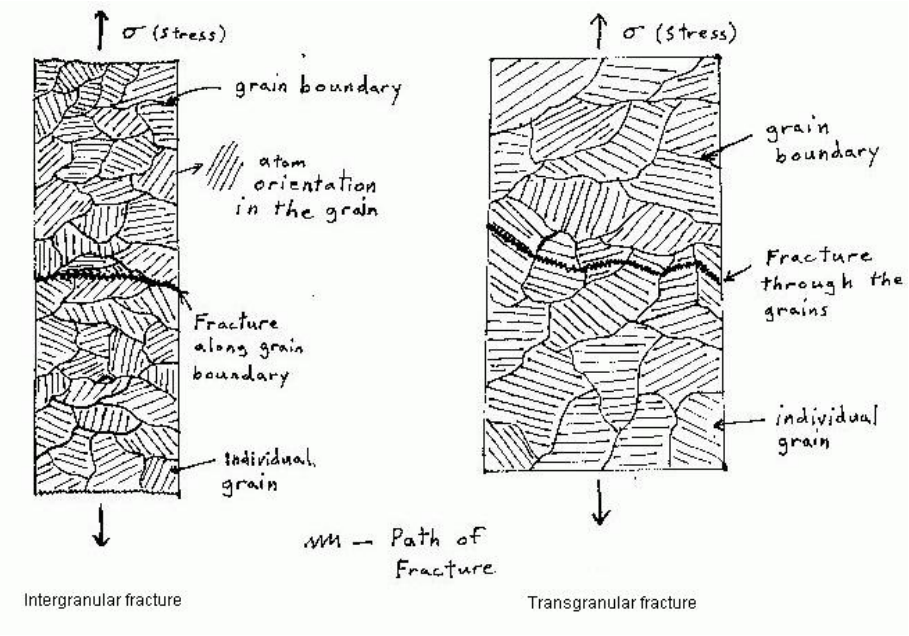

Figure 4.26: *Scheme of an intergranular (left) and a transgranular (right) fracture (Ballard, 2010)*

agation along the grain boundaries is called intergranular fracture (figure 4.26). In both case the crack changes direction at each grain and will always choose the path of least resistance, resulting in a slightly bumpy cracked surface.

4.4.1 Previous work

Only a limited number of authors have reported data about the microstructure of ice. Impact ice has been found to have smaller grain size, about one order of magnitude, compared to frozen bulk water ice. It also contains more air inclusions which would explain the lower density.
The characterising of the microstructure also requires that the size and amount of pores or bubbles be established.
The bubble structure was extensively studied on hailstones. Hail forms as an impact ice accretion, with a piece of ice colliding with supercooled droplets, in much the same way that ice can form on an aerodynamic component. The microstructure (including bubble distribution) of hail is discussed by Macklin et al. It mainly depends on the deposit temperature and therefore on the air temperature, the air velocity, the LWC and the droplet size (Carras and

Macklin, 1975).
Laforte et al. (1983) studied the microstructure of atmospheric ice accreted around electrical conductors. He reported that, in the dry regime, two kinds of air bubble can be observed: some tiny bubbles concentrically layered around the substrate (in their case a conductor) and some large bubbles elongated in the radial direction between the lobes.
The tiny bubbles appear at a deposit temperature below -3°C (figure 4.27). They form a distinct layer of ice corresponding to each cylinder revolution.

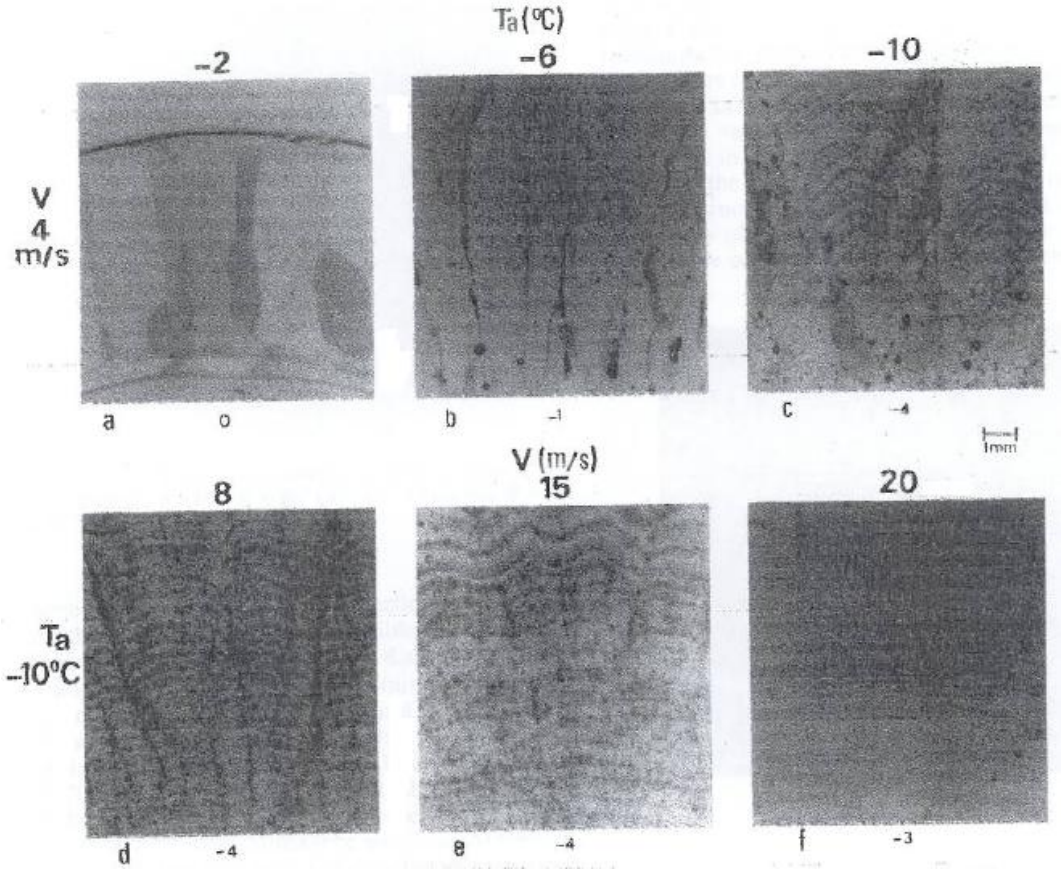

Figure 4.27: *Air bubble structure of ice accreted on aluminium conductors in function of ambient temperature and air velocity (Laforte et al., 1983) - The deposit temperature is indicated below each figures*

Their dependence with temperature and air speed is not obvious.
The large bubbles appear only when there is a rapid freezing and a local variation in the collection efficiency of the impinging droplets. This occurs particularly at low air velocity and low LWC both conditions required for a low accretion intensity. Their number varies with the LWC; for example,

with a droplet size of 12 μm , more bubbles can be observed at a LWC of 0.4 g.m^{-3} than at higher LWC. A similar trend has been found with a decreasing size of droplets (figure 4.28).

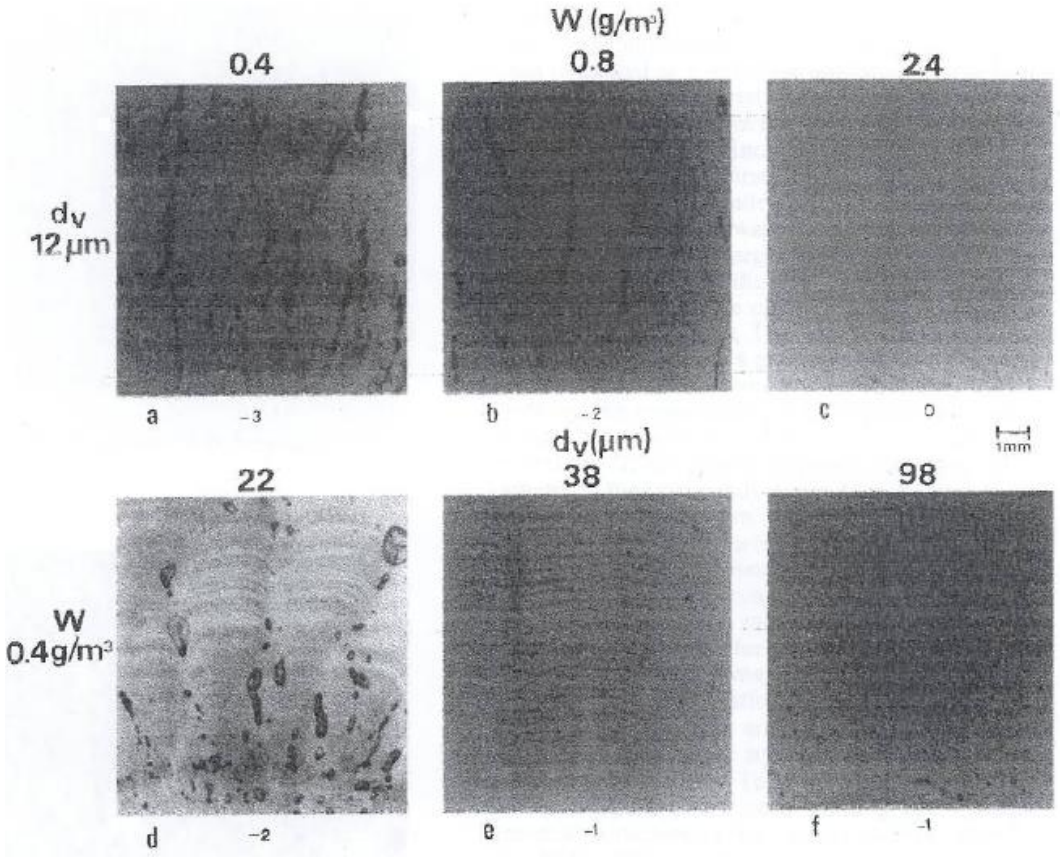

Figure 4.28: *Air bubble structure of ice accreted on aluminium conductors in function of LWC and droplet size (Laforte et al., 1983) - The deposit temperature is indicated below each figures*

In the wet growth regime, ice was reported to be almost transparent and to contain large quasi-spherical bubbles (Laforte et al., 1983). These bubbles seems to increase in number and in size with the LWC.
The form of the crystals was observed with a microscope under polarized light. The shape of the grains and their boundaries are clearly visualized at an air temperature above -6°C and a deposit temperature above -4°C. Below these values, the crystal structure becomes more complex: the grains boundaries are no longer smooth and subgrains can be observed inside the ice crystals (Laforte et al., 1983).
Figure 4.29 show the variation of the average grain size with the air tempera-

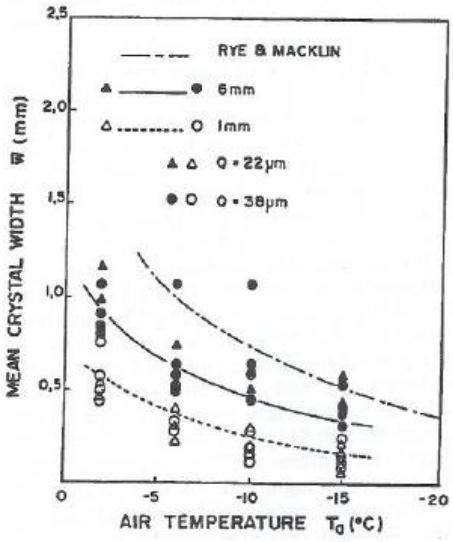

Figure 4.29: *Average grain size as a function of ambient temperature at 1 and 6 mm from the substrate surface (Laforte et al., 1983)*

ture at two different distances from the conductor surface (1 and 6 mm). At the same air temperature, the average grain size is larger at 6 mm than at 1 mm from the conductor surface. The dependence of crystal size with radial distance has been further investigated (Laforte et al., 1983). The average grain size increases rapidly in the first 2 *mm* of accretion and tend to a constant value after 6 mm (figure 4.30).
All authors have reported a decrease in the crystal size as the air temperature decreases (Laforte et al., 1983; Druez et al., 1978; Hammond, 1996; Rye and Macklin, 1975). Rye reported a fall of crystal dimension until -25°C then a tendency for the curves to flatten down (figure 4.31).
Koosheh (2007) has studied the ice microstructure at three different temperature: -6°C, -10°C and -20°C. The ice was produced by spraying water on a slowly rotating aluminium cylinder. The cloud LWC was 2.5 $g.m^{-3}$, the tunnel air speed was 10 $m.s^{-1}$ and the droplets MVD was 80 μm. A slice of ice was carefully cut from the ice accumulation and observed under a microscope. Koosheh found that the microstructure at -20°C is very different than at -6°C and -10°C. A more complex structure with more angular grain boundaries and distinctive cavities was reported. The grains near the substrate are finer which was attributed to the rapid heat transfer between the metal and the impinging droplets.
The dependence of the deposit temperature has been investigated by Laforte et al. (1983) by observing the microstructure of ice build at two different LWC

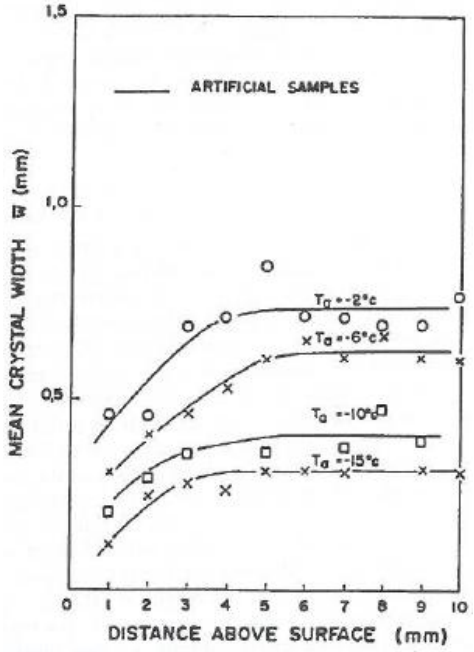

Figure 4.30: *Average grain size of ice grown at different ambient temperature in function of the distance from the substrate surface (Laforte et al., 1983)*

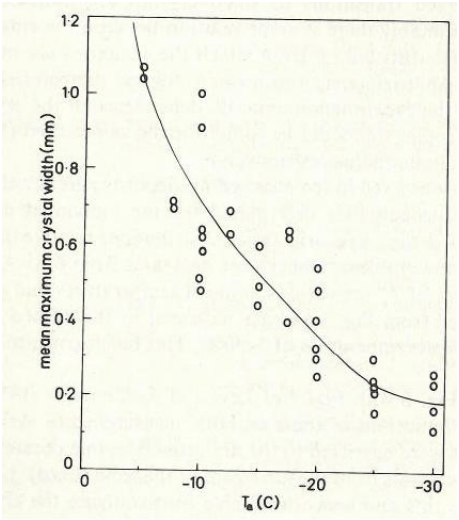

Figure 4.31: *Mean crystal width of ice grown at different ambient temperature (Rye and Macklin, 1975)*

and MVD. At the same air temperature the deposit temperature will be different however no variation has been found in the average grain size. Rye

and Macklin (1975) also investigated the dependence of grain size with deposit temperature over a larger ambient temperature range. As Laforte et al., they have found no dependence down to an ambient temperature of -15°C but for lower ambient temperatures, the deposit temperature appears to be an important factor for the crystal size. This dependence could be explained by the probability of crystal reorientation at these low temperatures. Under a certain temperature, when the freezing fraction is close to 1, the water droplets froze instantly when they came into contact with the surface (which can be the substrate or ice). In this case a new grain is nucleated with each droplet rather than contributing to the growth of an existing crystal. Figure 4.32 represents

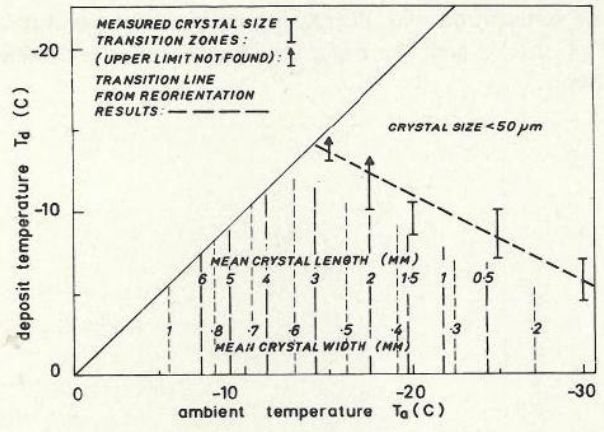

Figure 4.32: *Crystal size of ice grown at different ambient and deposit temperature (Rye and Macklin, 1975)*

the size of the crystals obtained at different ambient temperature and deposit temperature. A transition zone can be seen where the grain size drops from several millimeters to less than 50 μm which is in the order of the diameter of the supercooled droplets.

The crystal texture is also influenced by the air velocity (Laforte et al., 1983; Druez et al., 1978). Between 4 and 10 m.s^{-1} , the crystal size is decreasing as the velocity of air increases (figure 4.33). A constant grain size was found for larger air speed. The latter observation was confirmed by Rye and Macklin (1975) who found no real dependence on the grain size with air speed at 15 and 32 m.s^{-1} .

The grain size seems to not be dependent on the LWC or the droplet size (Rye and Macklin, 1975; Laforte et al., 1983). Indeed only a very small variation was found with the LWC while no variation at all could be observed with droplet size (figure 4.34).

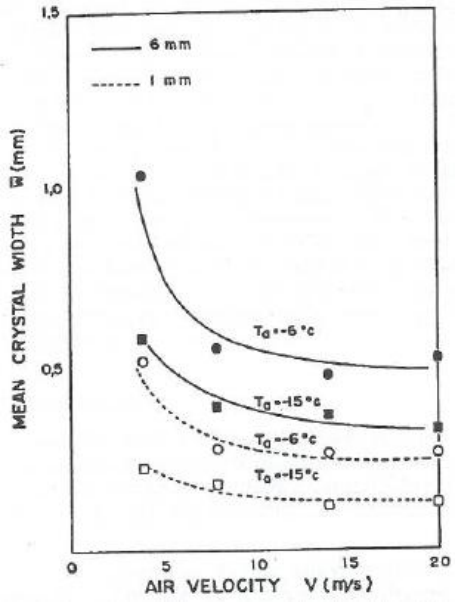

Figure 4.33: *Mean crystal width of ice grown at different tunnel wind speed (Laforte et al., 1983)*

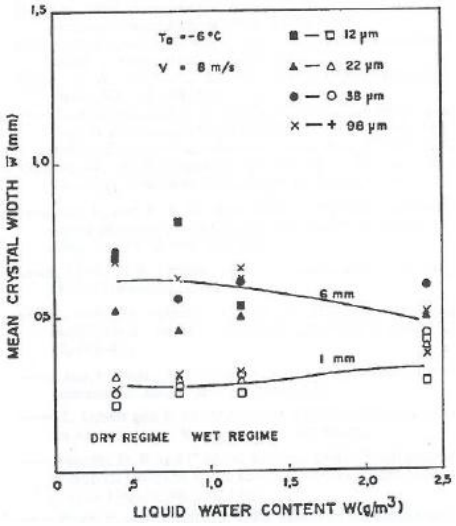

Figure 4.34: *Mean crystal width of ice grown at different LWC (Laforte et al., 1983)*

4.4.2 Obtaining the microstructure of ice

The most common method to study the microstructure of ice is to directly observe a thin slice of ice under a microscope. A slice of ice is first cut from the block of ice using a saw. Further thinning can be obtained by using grinding paper, a file, a sledge type microtome, by melting the ice or by allowing the ice to sublime. With these techniques (or a combination of some them) a slice of ice with a thickness of less than 0.5 mm can be obtained (Laforte et al., 1983; Hammond, 1996; Druez et al., 1978). Slices can be cut parallel or perpendicular (transverse section) to the substrate surface. Observations are made under a microscope with ordinary or polarized light.
This method is quite easy in principle but requires lot of care to achieve. The main drawback is the care needed to keep the ice in a frozen condition. All observations and manipulations need to be done in a cold room.
Direct observation of the grains structure can also be made (Laforte, 2001). After detachment of ice from a substrate, the surface of both the substrate and the detached piece of ice is observed under a microscope and pictures are taken.
Another method has been developed by the Anti-Icing Materials International Laboratory (Chicoutimi, Quebec) and the National Research Council Canada to study the grain size and their orientation as well as the ice structure (presence of air bubbles, defects, etc). The ice surface is first prepared to a mirror finish then it is coated by a solution of Formvar. After drying, a replica of the ice surface is obtained which could be observed under an optical microscope. This method has the advantage of providing a durable replica of the ice surface however, as discussed in section 4.2.1.1, the solution of Formvar is a toxic product and need some precaution to use.

4.4.3 Methodology

A similar method has been used in the present work by substituting the solution of Formvar for nail varnish. Samples of ice were produced during the mechanical tests. For each condition tested, one piece of accreted ice is left, untested, attached to the substrate. The ice piece was removed manually using a hammer and a chisel. The removal was completely adhesive, meaning that the substrate was visually free of ice. The ice pieces were kept in a freezer at a temperature of -18°C for several weeks before the surfaces were replicated using the nail varnish technique. Sublimation will occur revealing the grain boundaries as this process is faster along the grain boundaries than inside the crystal. A layer of nail varnish is coated on the ice surface and after drying, a

replica of this surface is obtained. The replica is observed under a microscope and pictures have been taken. Three different surfaces were replicated: the surface which was in contact with the substrate (called the interface), the surface at the other extremity (called the top surface) and a longitudinal surface which was obtain by cutting the ice piece normal to the substrate surface.
Each picture presented in this report has been obtained from several photos taken through the microscope. The photos are then stacked together using the software iMerge [1]. The average grain size was obtained, for each case, by using the mean linear intercept method on ten measurements. On a picture, a line of a known length is drawn (l_g) and the number of grains intersected by this line is counted (nb_g) . The average grain size is obtained by dividing the line's length by the number of grains: $d_g = l_g/nb_g$. For example, on figure 4.35, a red line representing 0.5 mm has been drawn. This line has crossed 11 grains. Hence the average size of a grain is $0.5/11 = 46\,\mu$m.
The grains of impact ice are columnar. Therefore, as represented on figure 4.36, the grain size can be assumed to be similar wherever the ice replica is made. This observation is true for ice accreted at low temperature where the grains grow in a straight forward direction. However, for ice accreted at high temperature the grains have a slightly conical shape. Therefore, if a replica is made on the side of the sample, the average grain size value calculated with the interlinear intercept method may be overestimated. Because of the difficulty of interpreting the actual difference in the results, an assumption is made that the grains are growing straight and no coefficient will be applied to correct the results.

[1] iMerge is an images stacking and mosaic-making software conceived primarily for astronomical purpose

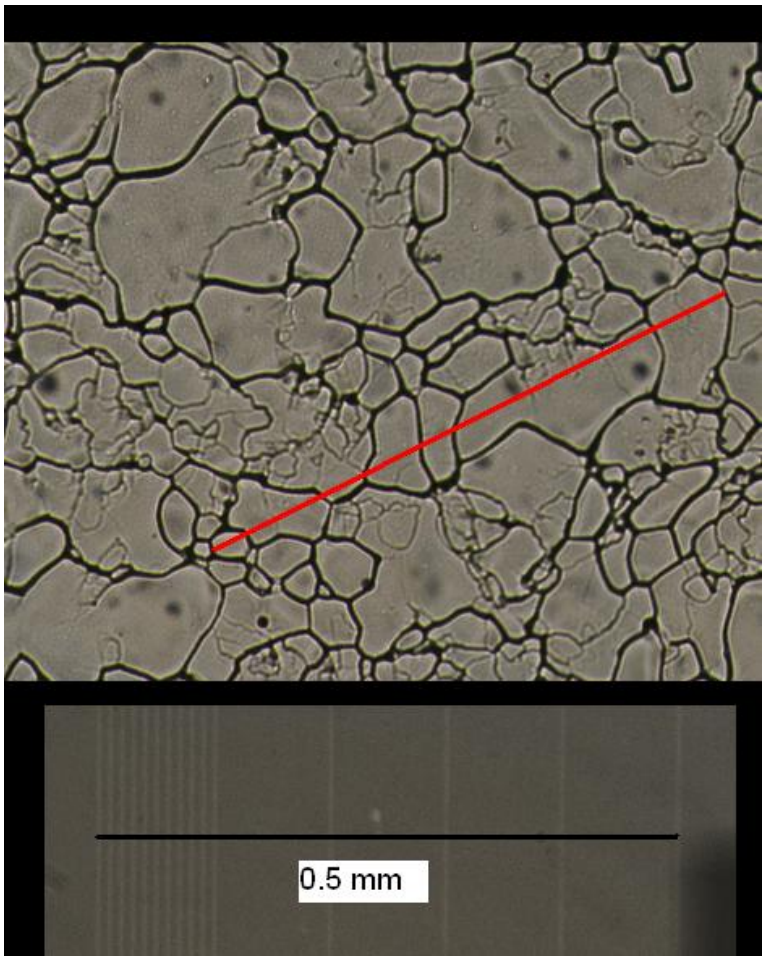

Figure 4.35: *Example of grain size calculation*

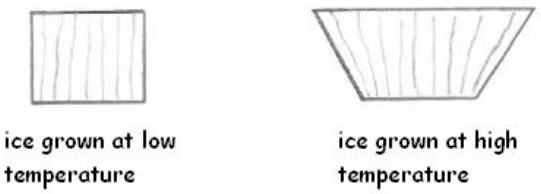

Figure 4.36: *Schematic drawing of the longitudinal view of ice samples*

4.4.4 Results of microstructure observations

As Laforte et al. (1983) reported in their paper, the grain sizes were found to be smaller at the interface than at the top surface. However, the difference between the two values is considerably higher in Laforte et al.'s results. A difference of about 200 μm and 300 μm has been found for ice grown at respectively low (-10 and -15°C) and high temperature (-2 and -6°C). In the present investigation, the difference between the grain size at the interface and at the top surface is only about 150 μm for the highest temperature (-5°C) and between 10 and 150 μm for the lowest temperature (-10, -15 and -20°C). This difference could come from the type of substrate used but also from the difference of LWC and air speed used to produce the ice. As it can be seen on figure 4.33, the difference of grain size measured at 1 mm and at 6 mm from the substrate surface is smaller when the ice has been made at a higher velocity.
The longitudinal surface showed elongated grains, typical of a columnar structure (figure 4.37).
The influence of ambient total temperature, cloud LWC and tunnel air speed have been investigated for ice accreted on mirror polished titanium. For comparison purpose, the microstructure of frozen bulk water ice (bubble free) was also investigated.

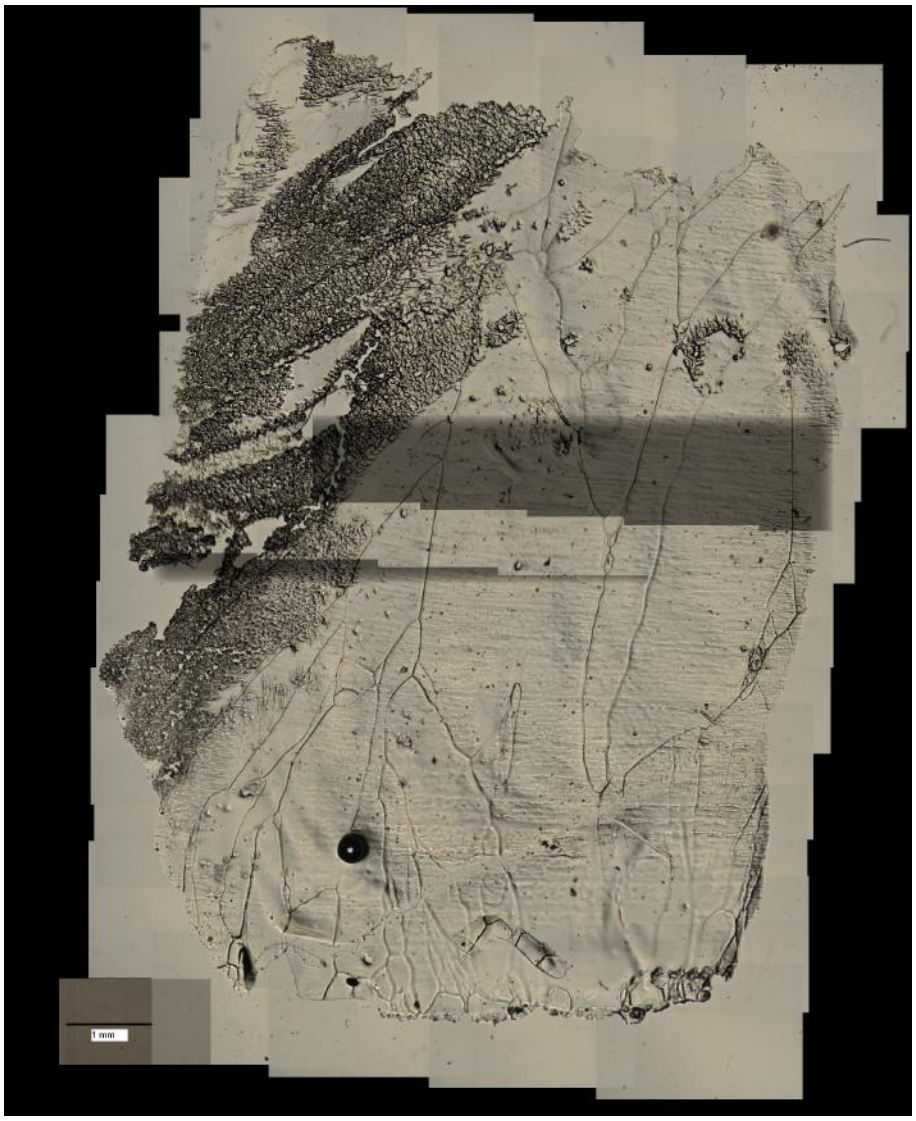

Figure 4.37: *Longitudinal cut of a piece of ice grown at a temperature of -5° C, a LWC of 0.4* $\mathrm{g.m^{-3}}$ *and a tunnel air speed of 50* $\mathrm{m.s^{-1}}$

4.4.4.1 Frozen bulk water ice

Frozen bulk water ice was left to sublime for a couple of weeks in the freezer, then a replica was made and observed under a microscope (figure 4.38). The

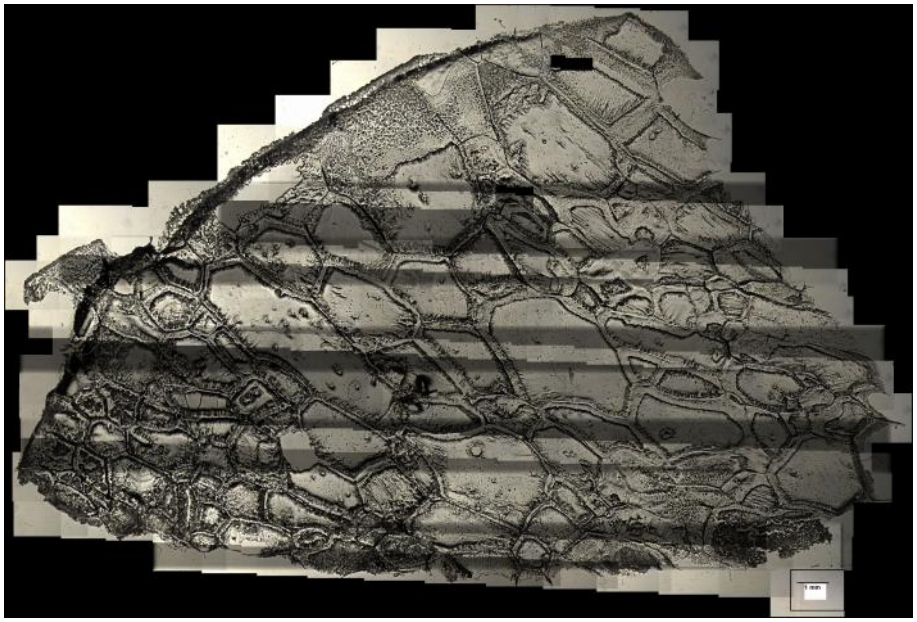

Figure 4.38: *Transversal cut of a piece of fresh freezing water ice grown in a freezer at a temperature of -18°C*

grains are very similar in shape and in dimension. Their average size was found to be of 1.5 mm.

4.4.4.2 Impact ice

The appearance of the microstructure of impact ice has been found to be different from that of frozen bulk water ice. The grains are in general much smaller: between 40 and 400 μm for impact ice against 1.5 mm for frozen bulk water ice. Their distribution is quite random. In some case they are similar in shape and dimension (figure 4.39) but in others small and bigger grains can be observed (figure 4.40). In the latter cases, measurements of the average grains size have been obtained taking into account the wide distribution of grain size. The mean linear intercept method has been used by drawing lines that include both small and big grains so the number obtained represent the average size of all the grains.
Ice has been grown at four different ambient total temperatures between -5 and -20°C, keeping the LWC constant at either 0.4 or 0.7 g.m^{-3} and the tunnel air

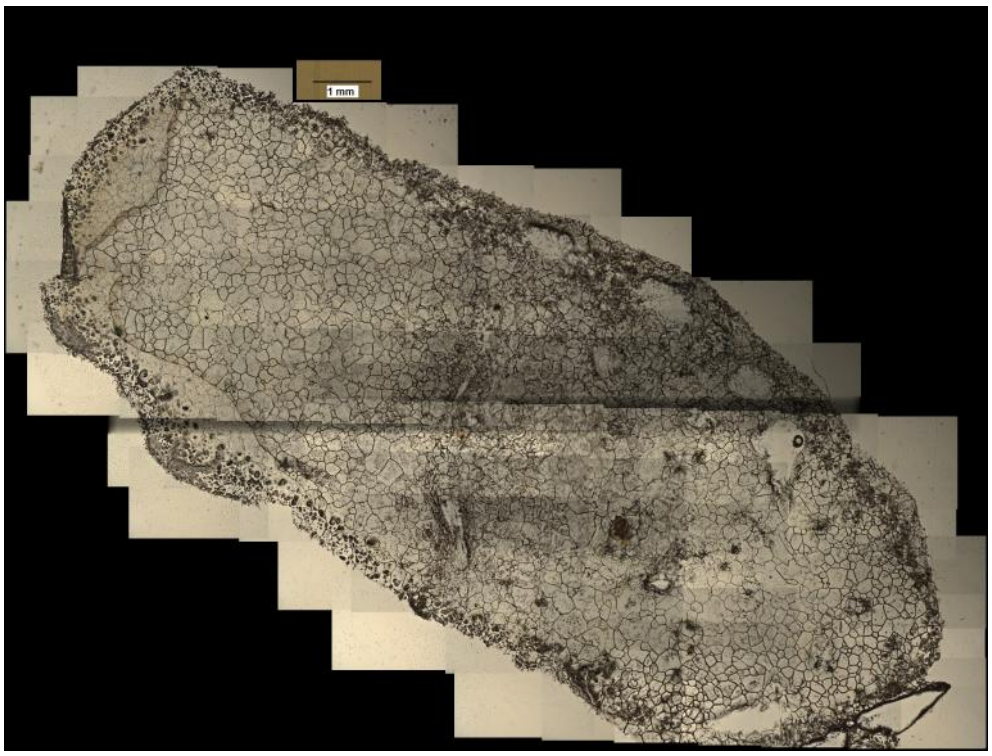

Figure 4.39: *Microstructure of ice showing similar grain structure - T=-10° C, LWC=1.1* g.m^{-3} *, V=40* m.s^{-1}

Figure 4.40: *Microstructure of ice showing a wide range of grain sizes - T=-10° C, LWC=0.5* g.m^{-3} *, V=70* m.s^{-1}

speed constant at 50 m.s^{-1} (tables 4.8 and 4.9 and figures 4.41 and 4.42).

LWC=0.4 g.m^{-3} , V=50 m.s^{-1}		
temperature (°C)	interface	top
-5	225	399
-10	110	135
-15	50	47
-20	36	49

Table 4.8: *Average grain size in* μm *for ice grown at different temperature with a LWC of 0.4* g.m^{-3} *and a tunnel air speed of 50* m.s^{-1}

LWC=0.7 g.m^{-3} , V=50 m.s^{-1}		
temperature (°C)	interface	top
-10	325	390
-15	400	146
-20	48	38

Table 4.9: *Average grain size in* μm *for ice grown at different temperature with a LWC of 0.7* g.m^{-3} *and a tunnel air speed of 50* m.s^{-1}

As the other authors have reported (Laforte et al., 1983; Druez et al., 1978; Hammond, 1996; Rye and Macklin, 1975; Koosheh, 2007), the grains have been found to be smaller at a lower temperature. The values obtained are at least half than the one obtained by Laforte et al.. At a temperature of -5°C, Laforte et al. and Rye and Macklin have respectively reported grain size of about 700 μm and 1 mm. In the present investigation, the grain size was found to be in average of 400 μm . At a temperature of -15°C, grain size of 400 μm and 600 μm were respectively reported by Laforte et al. and Rye and Macklin whereas in the present study, grain size was about 50 μm . Laforte et al.'s experiments were conducted with the same LWC and the same droplets MVD as ours; only the tunnel air speed was different. No additional details was given in the case of Rye and Macklin's experiments. However even if the LWC and the droplets MVD were similar to ours, the tunnel wind speed used was probably 30 m.s^{-1} so lower than ours. Hence the larger grains reported by these two authors could be explained by the difference in velocity. However, it could also be coming from the difference in the substrate material used (aluminium for Laforte et al., brass for Rye and Macklin and titanium for us). The different substrate materials present different grain structure which results in different nucleation site locations for the growing ice and could lead to a completely

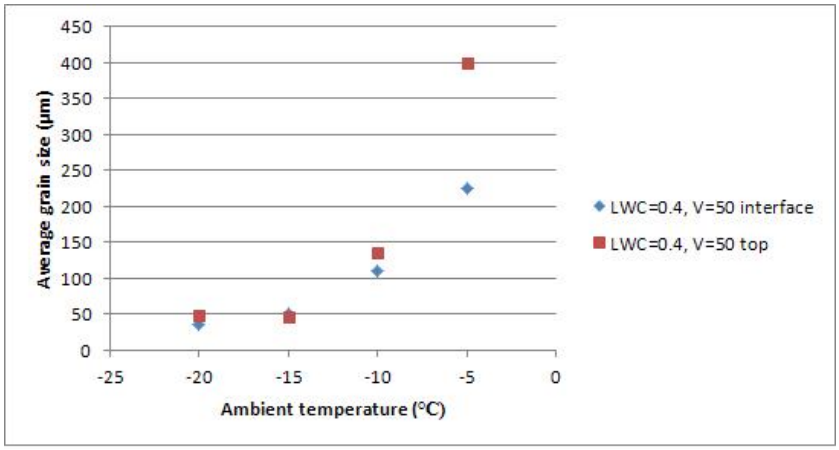

Figure 4.41: *Average grain size at the interface and at the top surface of ice grown at different temperature with a LWC of 0.4* $\mathrm{g.m^{-3}}$ *and a tunnel air speed of 50* $\mathrm{m.s^{-1}}$

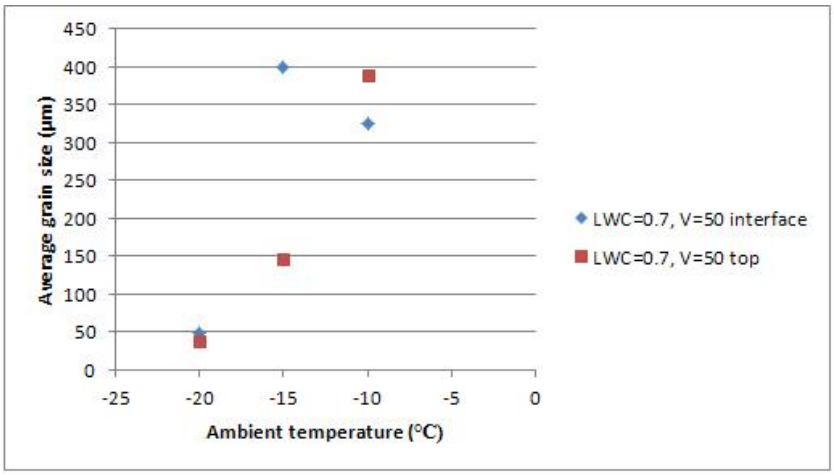

Figure 4.42: *Average grain size at the interface and at the top surface of ice grown at different temperature with a LWC of 0.7* $\mathrm{g.m^{-3}}$ *and a tunnel air speed of 50* $\mathrm{m.s^{-1}}$

different ice structure.
Two different LWC have been used for these results. It appears that the higher the LWC is, the larger are the grains. However at a temperature of -20°C, the grains have the same size despite of the difference in the LWC.
The influence of LWC has been further investigated. In these series of experiments, the ambient total temperature and the tunnel air speed have been kept constant at -10°C and 40 $\mathrm{m.s^{-1}}$ respectively. Results have been found to

T=-10°C, V=50 m.s^{-1}		
LWC (g.m^{-3})	interface	top
0.5	332	177
0.6	59	212
0.8	112	91
1.0	208	135
1.1	188	278

Table 4.10: *Average grain size in* μm *for ice grown at different LWC with a temperature of -10° C and a tunnel air speed of 40* m.s^{-1}

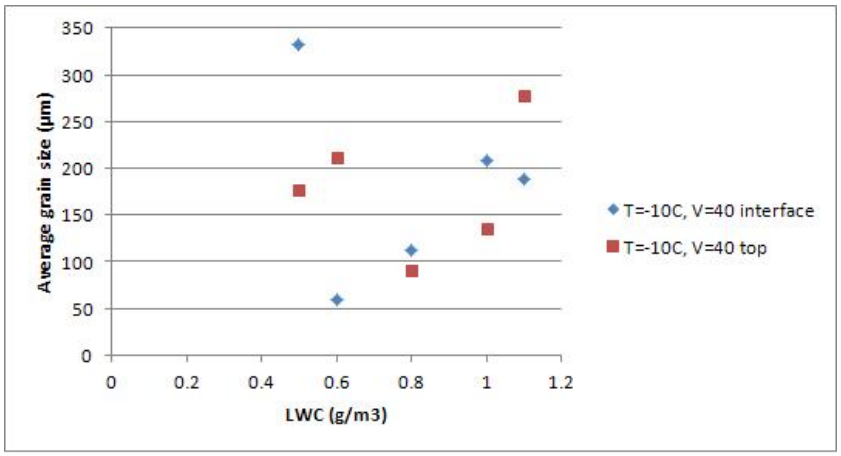

Figure 4.43: *Average grain size of ice grown with different LWC, a tunnel air speed of 40* m.s^{-1} *and a temperature of -10° C*

globally increase as the LWC increases (table 4.10 and figure 4.43). These results are in agreement with the freezing fraction which increases with the LWC, meaning that at high LWC the ice has a glazier aspect than at low LWC. It has been observed earlier, with the influence of ambient temperature, that glaze ice has bigger grains than rime ice, hence an increase of grain size with LWC is expected. However the trend is not so obvious and perhaps another effect is affecting the grain size especially at the interface. A higher LWC means that more liquid water is present in the cloud. As it impacts on the substrate surface, the local heat should be higher resulting in bigger grain size. However the state of the surface is expected to influence the size of the grain and even if the substrate surfaces have been carefully cleaned before each experiments, the presence of particles of dirt is always possible. Another ice specimen should be grown wherever a suspicious results is found (for example at the interface of the piece grown at a LWC of 0.5 g.m^{-3} and at the top surface of the one

grown at a LWC of 1.0 g.m^{-3}).
Other authors have investigated the influence of LWC (Laforte et al., 1983; Rye and Macklin, 1975) and have reported only a small or no dependence of the grain size with the LWC.
The influence of the tunnel air speed has been investigated by varying the speed while the temperature is kept at -10°C and the LWC at 0.5 g.m^{-3}. Results show that globally the size of the grains decreases as the tunnel air speed increases (table 4.11 and figure 4.44). Other authors have also reported an

T=-10°C, LWC=0.5 g.m^{-3}		
tunnel air speed (m.s^{-1})	interface	top
40	332	177
50	743	204
70	37	190
80	57	108

Table 4.11: *Average grain size in* μm *for ice grown at different tunnel air speed with a temperature of -10° C and a LWC of 0.5* g.m^{-3}

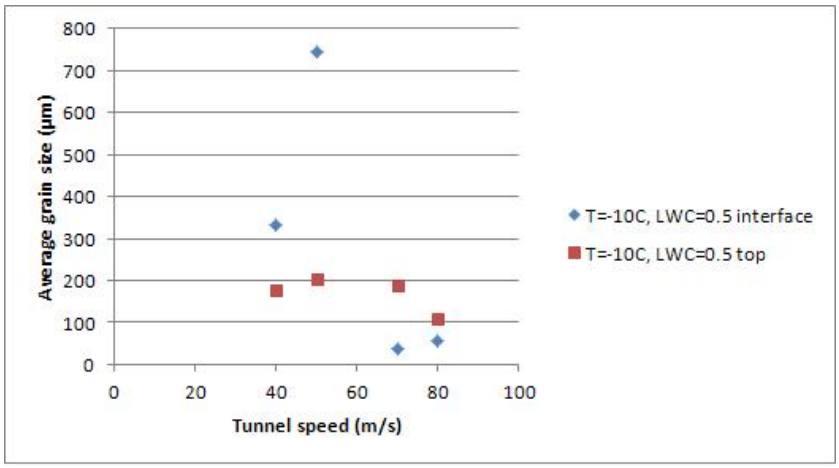

Figure 4.44: *Average grain size of impact ice grown for different tunnel air speed, at a temperature of -10° C and a LWC of 0.5* g.m^{-3}

influence of the air velocity to the grain size. Laforte et al. (1983) have found a decrease of grain size as the velocity increases from 4 to 10 m.s^{-1}. However the author has also found that at velocity higher than 10 m.s^{-1}, the grain size is constant. This latter observation is contradictory with the present investigation as it has been found that even at a velocity higher than 40 m.s^{-1}, the grain size is still decreasing. Rye and Macklin (1975) have produced ice at two

different speed (15 and 32 $m.s^{-1}$) and have found no difference in the size of the grains.
Looking at the variation of freezing fraction with air velocity (figure 4.3), it has been found that the freezing fraction is decreasing as the air velocity increases. It is expected that an ice piece made at a lower freezing fraction would have bigger grain. It is contradictory with the observation of the microstructure in the present investigation as the ice grown at 80 $m.s^{-1}$ presents the smaller grains.

Chapter 5

Mechanical properties of ice

As has been seen in the introduction, two "aspects of ice fracture" need to be determined in order to model the ice shedding from fan blades: the tensile and the shear strength. Associated with these, it can also be useful to calculate the fracture toughness and the fracture energy in both mode I and mode II especially in the case of modeling with cohesive elements.
As a first approximation, essentially because of the lack of published values about the physical properties of ice, the Young's modulus and the density were assumed to be constant at 8.5 GPa and 870 $kg.m^{-3}$ respectively. These values are an average of the values found in the literature for impact ice grown at -10°C. It has been shown in the previous chapter that the physical properties of ice are dependent on the ice growing conditions, however, these values were not available at the time of the writing.

5.1 Mode I/Tensile strength

5.1.1 Previous work

Only a few authors attempted to measure the tensile strength of impact (atmospheric) ice. The traditional method to measure the tensile strength, where a sample of the material is elongated until it breaks, is challenging in the case of impact ice. The difficulty is to have a good grip on the end of the ice specimens and to measure the deformation of the sample.
Druez et al. (1987, 1989) and Tremblay (1991) have studied the tensile strength of impact ice as a function of the ice growth parameters and test conditions. The ice is accumulated in a cold chamber around a cylinder. This cylinder is made of two parts which are held together by an internal screw. At the end of the accretion, the screw is removed and the cylinders are only held together

by the ice. The extremities of the cylinders are attached to a tensile machine which pull the ice at a certain strain rate. One hour is needed after the ice accretion to prepare the tensile test. Values between 0.7 and 5 MPa have been found for the tensile strength depending on the ice growing conditions and the strain rate. The highest values were obtained at a temperature of -14°C and a LWC of 1.2 $g.m^{-3}$ whereas the lowest values were obtained at temperature close to the melting point. Grains size were reported to be 1 mm at -3 °C and 0.5 mm at -8 °C. Comparing to the values measured in appendix A, the values of the grain size are similar to ours.
Xian et al. (1989) used a servo-hydraulic test machine to measure the tensile strength of ice accumulated on an aluminium rod. The load is measured by a load cell and the strain by an extensometer placed on the aluminium rod. The load-strain curve is recorded by an X-Y recorder. The discontinuity in the load/strain curve represents the instant of ice detachment. Tensile strength in the range from 0.8 to 1.4 MPa were obtained depending on the test temperature and ice thickness. Nothing was said about the conditions at which the ice was built, neither on its grain size or its density.
Laforte and Laforte (2009) accreted ice on aluminium bars. The bars were then pulled by a conventional traction machine until the ice broke off. A strain gauge was glued to the bare side of the aluminium bar to measure the deformation and the strain rate. A load cell was used to measure the tensile force applied to the iced substrate. The tensile strength was calculated from the strain at deicing and the Young's modulus of ice taken as 9.9 GPa. An assumption was made that the strain on the aluminium bar is the same as the strain at the ice interface. The ice was observed to either became detached from the substrate in one piece or to break into several pieces. In the last case, the cracks were perpendicular to the loading direction. Values between 2.8 and 5 MPa were found depending on the ice thickness. The droplets MVD was about 200 μm which is ten times larger than the one used in the present experiments. It resulted in a larger grain size: 1.6 mm at -10°C. After the ice accretion, the specimens were kept at the ice making temperature for one hour before the mechanical test was carried out allowing the internal stresses to relax.
Mohammed and Farzaneh (2011) have also grown ice around a rotating cylinder, however, they had cut an ice sample from the middle of the ice piece. The ice was grown from water sprayed, with a droplet MVD of 40 μm , a LWC of 2.5 $g.m^{-3}$ and a temperature of -10 °C, on an aluminium cylinder rotating at 1 RPM to ensure a uniform ice thickness. The average grain size was about 0.7 mm. A lathe was used to cut the ice to avoid any crack formation. Two cups are attached to the extremities of the ice sample using freezing water and the whole is let to rest for two to three hours. A closed loop electrohydraulic ma-

chine is used to pull on the ice specimen. This method gets rid of the influence of the metal, compared to the previous ones, but needs a lot of manipulations (cutting and machining the ice samples, positioning the extensometer, etc.) which could induce pre-cracks and lead to inaccurate results. Investigation of the influence of the test temperature, the wind speed and the strain rate were conducted. Strain rate was reported to be the parameter which has the most influence on the tensile strength. The tensile strength obtained was in the range from 0.9 to 1.6 MPa with the highest value obtained at a test temperature of -15°C, a wind speed of 15 $m.s^{-1}$ and a strain rate of $5 \times 10^{-5}\,s^{-1}$ (which correspond to the brittle zone where the tensile strength is independent of the strain rate).

To the author's knowledge, only Koosheh (2007) and Hammond (1996) reported values of fracture toughness or fracture energy of impact ice. Koosheh (2007) measured the fracture toughness using a three-point loading test. The ice was accreted in an icing tunnel and was then prepared using a microtome machine to introduce a crack. The ice was accreted and tested at three different temperatures, -6, -10 and -20°C, with a LWC of 2.5 $g.m^{-3}$, a tunnel wind speed of 10 $m.s^{-1}$ and a droplet MVD of 80 μm. Fracture toughness of 137.75, 111.17 and 108.04 $kPa\sqrt{m}$ were obtained for the accreted and testing temperature of -6, -10 and -20°C respectively; which correspond to a fracture energy of 2.0, 1.3 and 1.2 $J.m^{-2}$ using equation 5.4 with a Young's modulus of 8.5 GPa and a Poisson's ratio of 0.31. Hammond (1996) measured the fracture energy of impact ice attached to titanium alloy substrate using a blister test (described in more details later) in a running icing tunnel. The ice was accreted at a temperature of -5, -10 and -25°C with a LWC of 0.3 $g.m^{-3}$, a tunnel wind speed of 140 $m.s^{-1}$ and a droplet MVD of 20 μm. Values of 1.3, 3.9 and 4.0 $J.m^{-2}$ were obtained for the three temperatures in the respective order.

Taking into account the small amount of data available in the literature about the fracture toughness and the fracture energy of impact ice, comparisons with previous work will be mainly attempted in term of tensile strength. The latter will be calculated from the fracture toughness or the fracture energy using equation 5.4 and/or equation 5.6 (these equations will be presented in more detail in section 5.1.2).

Figure 5.1 presents the values of tensile strength obtained from the different authors cited above. Most of the values are in the same range between 1 and 2 MPa.

Laforte and Laforte (2009) have obtained higher values probably due to the fact that they have measured the tensile strength of ice accreted on an aluminium substrate while the authors have measured the tensile strength of a bulk of ice. They also have carried out their experiments with a thinner layer

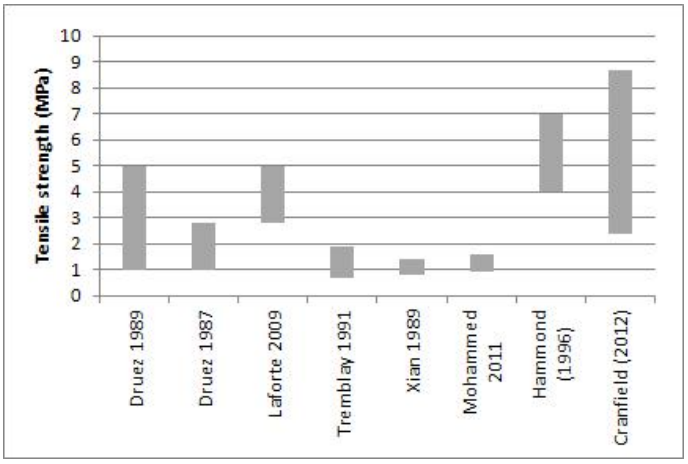

Figure 5.1: *Tensile strength values found by previous authors (Cranfield 2012 represent the present investigation)*

of ice (size effect) which could be responsible for higher tensile strength values. Another main difference was the large droplet size used by the authors to build the ice. Druez et al. (1989) have reported a wider range of values however they have investigated a wider range of experimental conditions. Hammond (1996) and the present investigation (Cranfield 2012) reported higher results because the method used was different from the other authors; the test was carried out in a running icing tunnel so the ice had no time to rest between the accretion and the actual mechanical test.
The traditional tensile test gives satisfactory results but is challenging to use in case of atmospheric ice. Moreover most of the tests are conducted a few hours after the ice has been made which could lead to some inconsistency due to the thermal stresses. The test presented and used here is adapted from Andrews and Lockington (1983)'s blister mechanical test. It allows for testing the ice fracture in mode I in a running icing tunnel.

5.1.2 Mode I test

The blister test first suggested by Andrews and Lockington (1983) is quite simple in principle. It consists of a hollow cylinder partly covered by a small plastic disc. Ice was cast on the surface with a significant thickness to allow the test to be undertaken in plane-strain conditions. Pressure was applied to the ice through the hole (figure 5.2). The pressure was increased until the ice breaks off at a value called critical pressure, P_c. The ice can break off in three different way: completely adhesive, completely cohesive or partly adhesive and partly cohesive (see section 2.2.2).

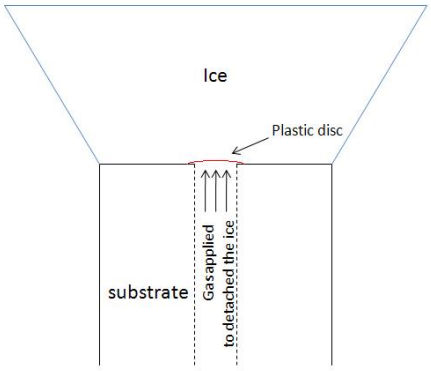

Figure 5.2: *Scheme of the mode I test rig - the cylinder has a diameter of 30 mm, the inner hole of 4 mm and the plastic disc of 6 mm*

Hammond (1996) has modified this test to allow its use in a running icing tunnel by connecting a vacuum pump in order to keep the plastic disc from falling. The surface of the cylinders was placed in the tunnel in a certain way so it was facing the oncoming flow. The applied pressure was provided by a nitrogen bottle and was measured using a pressure transducer.
This test has numerous advantages. It has proven to be reasonably reproducible taking into account the brittle properties of ice which can be responsible for large scatter. The plastic disc is initiating the crack meaning that the flaw dimension is known. The pressure rate can be modified so different load rates can be tested. Finally, an analytical solution is available allowing the calculation of the fracture energy needed to break the ice off the substrate and, from it, the fracture toughness and the tensile strength of ice.
The fracture energy, FE, of ice was calculated using the expressions established by Andrews and Lockington (1983) (equations 5.1 and 5.2) in which P_c is the critical pressure measured during the experiments, E_i is the Young's modulus of ice, ν_i is the Poisson's ratio of ice , c is the radius of the flaw and h is the thickness of ice above the flaw.

$$2\tau = \frac{P_c^2 c}{E f_1(h/c)} \tag{5.1}$$

$$\theta = \frac{P_c^2 c}{E f_2(h/c)} \tag{5.2}$$

where f_1 and f_2 are

$$f_1 = \frac{1}{1-\nu^2}\left(\frac{3}{32}\left[\left(\frac{c}{h}\right)^3 + \left(\frac{c}{h}\right)\frac{4}{1-\nu}\right] + \frac{1}{\pi}\right)^{-1}$$
$$f_2 = \frac{1}{1-\nu^2}\left(\frac{3}{32}\left[\left(\frac{c}{h}\right)^3 + \left(\frac{c}{h}\right)\frac{4}{1-\nu}\right] + \frac{2}{\pi}\right)^{-1}$$

Depending on the mode of fracture, cohesive or adhesive, equation 5.1 or 5.2 respectively, was used. In case of a mixed-mode fracture, the percentage of adhesive fracture, x, was visually estimated and the fracture energy was calculated in the following way

$$FE = \frac{100-x}{100} \times 2\tau + \frac{x}{100} \times \theta \tag{5.3}$$

By studying equation 5.1 and 5.2 for a defect radius of 3 mm and a critical pressure of 1 MPa, it appears that the influence of the ice thickness is negligible when the ice is thicker than 10 mm (figure 5.3). Hence during the experiments,

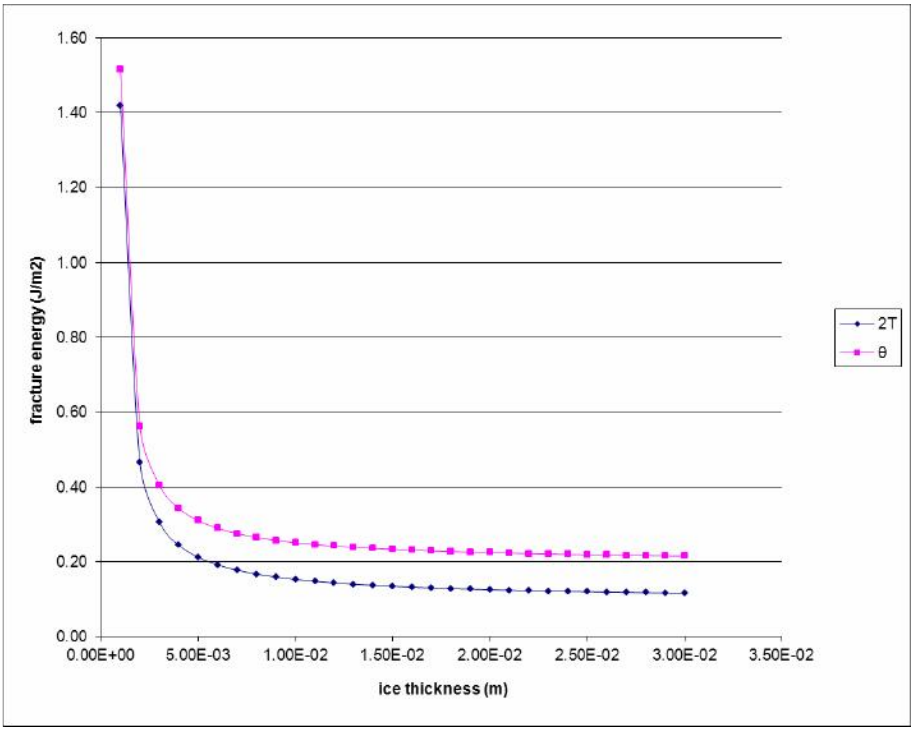

Figure 5.3: *Influence of the ice thickness in the fracture energy equations*

an ice thickness of at least 10 mm will be aimed before the start of the mechanical test.
The mode I fracture toughness, K_{Ic} , can be obtained from the fracture energy

$$K_{Ic} = \sqrt{\frac{FE \times E}{1 - \nu^2}} \tag{5.4}$$

From the fracture toughness, the tensile strength of a bulk of ice can be evaluated from the following equation (Tada et al., 2000),

$$\sigma_t = \frac{K_{Ic}}{\sqrt{\pi a}} \tag{5.5}$$

where σ_t is the tensile strength and a the size of the defect. The largest defect in ice is assumed to be smaller than the grain size. Therefore, the typical size of a defect will be taken as the average grain and the tensile strength equation becomes

$$\sigma_t = \frac{K_{Ic}}{\sqrt{\pi a_g}} \tag{5.6}$$

where a_g is the grain size.
The choice of the average grain size as a typical defect size can be surprising as a grain is not a real defect in a material. However, no defects can be seen on the microstructure pictures and, since no information is available to determine the defect size, it will be taken as an hypothesis that the grain size is the typical size of the defect for the strength calculation. A better knowledge of the microstructure would be needed in order to determine a more accurate value of the tensile strength.
For all the following calculations, assumptions are made that the Young's modulus and the Poisson's ratio are constant for all the conditions tested and are taken as 8.5 GPa, 0.31 respectively.

5.1.3 Test procedure

Before each test, the icing tunnel atomizer nozzles were checked to be sure that none of them were blocked. To ensure a good reproducibility of the mechanical test, the surface of each cylinder was carefully cleaned with ethanol and then dried with a hot air gun. Then the whole test rig was covered. Air was sprayed from the atomizer nozzles to make sure all the water remaining in and around the nozzles was sprayed anywhere but on the specimens surface. The specimens were then uncovered and the plastic discs put in place. Finally the tunnel window was closed and the main fan and cooling system were started. The different parameters were set (LWC, ambient temperature, tunnel air

speed, droplet size) and when the temperature in the tunnel was stable, the water was sprayed. When the thickness of 15 mm was reached (condition needed for the analytic solution from Andrews and Lockington), pressure was applied to the ice. The critical pressure needed to detach the ice as well as the mode of fracture and the estimated ice thickness above the flaw were noted.
Ice is a brittle material, hence, even if care has been taken to have a reproducible test, the results include scatter. It has been found that brittle fracture follow a Weibull distribution (Jayatilaka, 1979). A statistical analysis was carried out using the software Statistica [1]. A mean value and a standard deviation were calculated for each conditions.

5.1.4 Results and discussion

The influence of ambient temperature, cloud LWC and tunnel wind speed have been investigated. Tests have been carried out on a titanium alloy substrate with two surface finishes: a mirror polished finish and a more realistic surface finish. Between 6 and 38 values were obtained for each conditions. As the analytical solution of the mode I test is given in terms of fracture energy, the following results will be presented mainly in terms of fracture energy. As a matter of comparison with the work of previous authors, some results will be presented in terms of tensile strength.
In the following graphs, the symbols represent the mean values while the error bars represent one standard deviation. The results have been classified in three different categories depending on their mode of fracture:

- fracture predominantly adhesive: more than half of the specimens broke in an adhesive way (more than 60% adhesive)
- fracture predominantly cohesive: more than half of the specimens broke in an complete cohesive way (less than 40% adhesive)
- fracture cohesive and adhesive: no preference was observed in the mode of fracture

5.1.4.1 Influence of ambient total temperature

A tunnel velocity of 50 $m.s^{-1}$ has been chosen for this series of tests. Despite that this speed is a bit low for aeroengine application (typical speeds are about 60 $m.s^{-1}$ at the hub and 200 $m.s^{-1}$ at the tip of the fan blade), it is a comfortable speed for the tunnel and, hence, allows a good range of testing

[1] Statistica is a statistics and analytics software developed by StatSoft, `http://www.statsoft.com`

temperature. The mean volumetric diameter (MVD) of the droplet was set to 20 μm . Two different liquid water concentration have been chosen, one corresponding to a low rate (0.4 g.m^{-3}) and the other corresponding to a moderate rate (0.7 g.m^{-3}). For a droplet MVD of 20 μm , the in flight LWC is comprised between 0.15 and 2.5 g.m^{-3} (appendix C (Jeck, 2002)).

Mirror polished surface finish

In the first case (LWC=0.4 g.m^{-3}), the fracture energy increases from 0.6 J.m^{-2} to reach a value of 1.3 J.m^{-2} at a total temperature of -15°C which correspond to tensile strength of 1.83 to 9 MPa (figures 5.4 and 5.5).

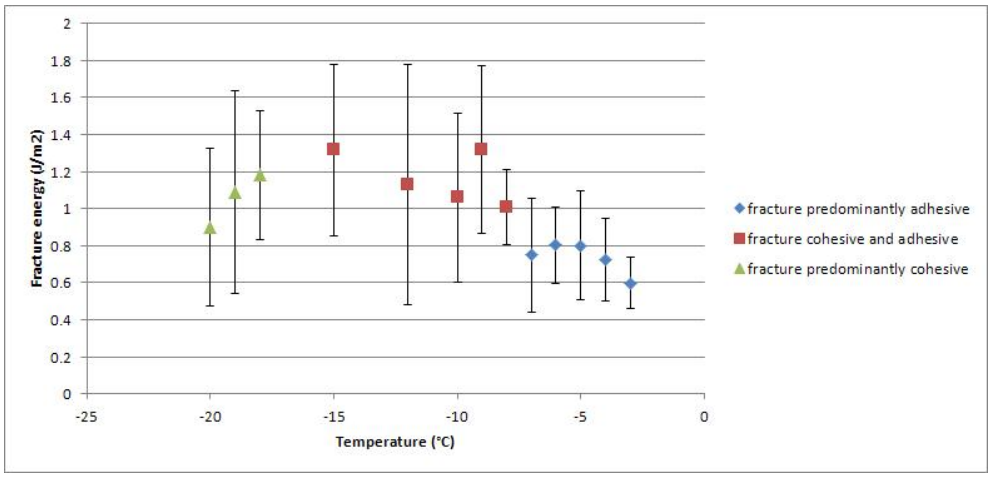

Figure 5.4: *Influence of ambient total temperature on fracture energy (LWC=0.4* g.m^{-3} *)*

At lower temperature (between -15 and -20°C), the fracture energy has been found to decrease. The type of fracture is either predominantly adhesive or a mix of cohesive and adhesive for temperature down to -15°C whereas for temperature below -15°C, the type of fracture was predominantly cohesive. This means that at a temperature below -15°C (where the freezing fraction is 1), the ice sticks to the metal so strongly that the easiest path of fracture is through the ice. The decrease of fracture energy (and tensile strength) at temperature below -15°C, could be explained by the probable presence of more pockets of air which would increase the number of possible defect in ice initiating a crack.

In the second case (LWC=0.7 g.m^{-3}), the fracture energy has been found to increase consistently through the whole range of temperature tested (figure 5.6).

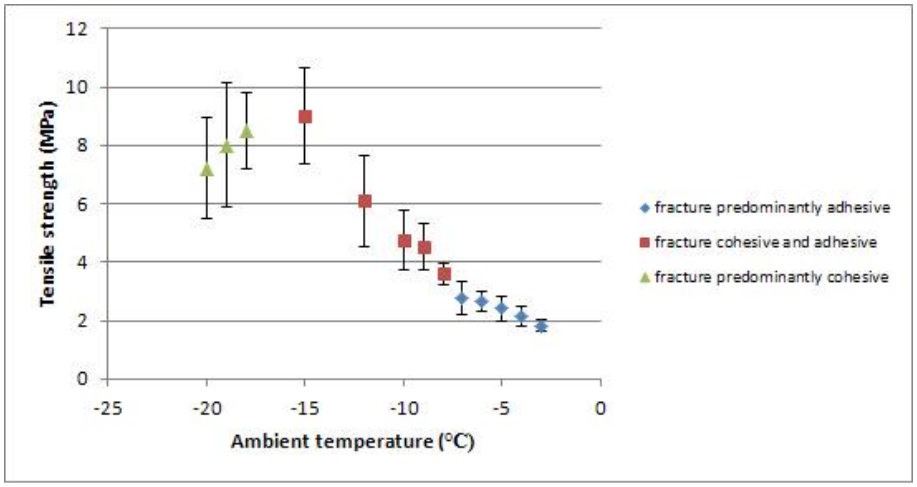

Figure 5.5: *Influence of ambient total temperature on tensile strength (LWC=0.4* $\mathrm{g.m^{-3}}$ *)*

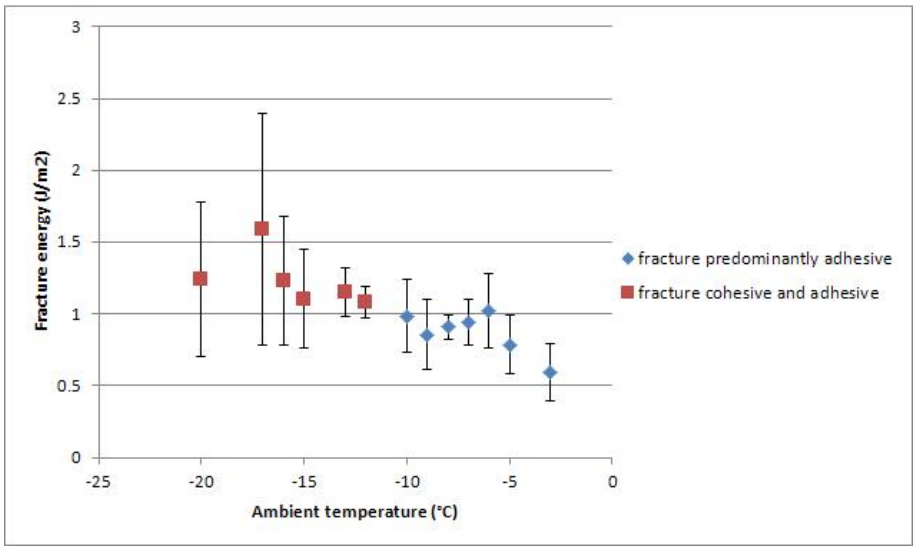

Figure 5.6: *Influence of ambient total temperature on fracture energy (LWC=0.7* $\mathrm{g.m^{-3}}$ *)*

Only the last value, obtained at a total temperature of -20°C, is slightly lower but taking into account the error bars it can still be seen as a global increase. Values obtained were between 0.6 $\mathrm{J.m^{-2}}$ and 1.5 $\mathrm{J.m^{-2}}$ which correspond to tensile strength from 1.83 to 9.7 MPa (figure 5.7). No fracture predominantly cohesive were observed in this case even at low temperature. The freezing fraction at -20°C is only 0.7.

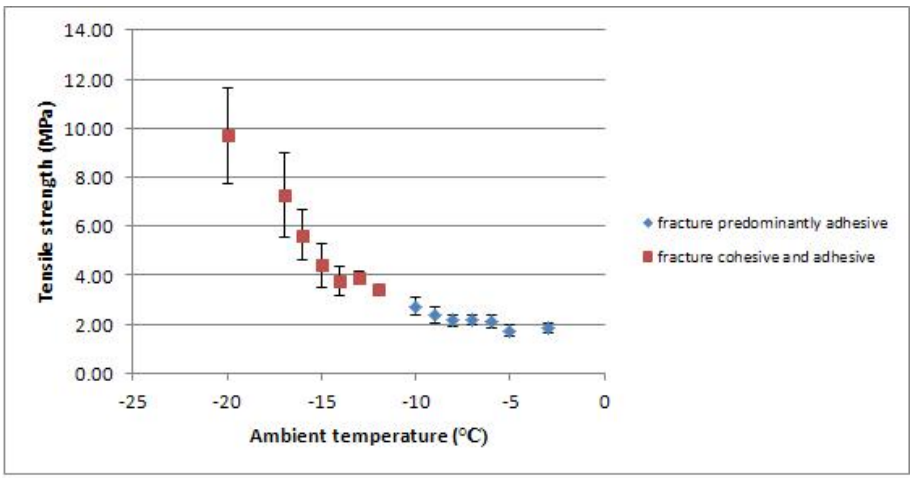

Figure 5.7: *Influence of ambient total temperature on tensile strength (LWC=0.7* $\mathrm{g.m^{-3}}$ *)*

In both cases (LWC=0.4 $\mathrm{g.m^{-3}}$ and LWC=0.7 $\mathrm{g.m^{-3}}$), scatter are generally larger (larger error bars) at lower temperature. This could be due to the fact that at low temperature, it is more difficult to maintain a constant temperature in the tunnel. The temperature could easily vary from 1 or 2°C around the temperature set. Another explanation could come from the mode of fracture. With a cohesive fracture, the tensile strength is more dependent on the presence of defects which are randomly distributed in the bulk of ice.
Previous authors have found a similar pattern. Druez et al. (1987, 1989) and Tremblay (1991) found, during their experiments, that the tensile strength goes through a maximum at -14°C as the ambient test temperature decreases while Xian et al. (1989) reported an increase of tensile strength with temperature until -12°C and then a constant value for lower temperatures. On the other hand, Mohammed and Farzaneh (2011) have only found a slight increase of tensile strength with decreasing temperature in the range from -5 to -15°C. All these authors have measured the tensile strength of impact ice within the ice whereas in this study the ice is accreted on a substrate and the force measured is the one to detached the ice from the substrate.
Hammond (1996) carried out experiments with the same blister test but with different experimental conditions. The liquid water content of the cloud was low (0.3 $\mathrm{g.m^{-3}}$) and the tunnel speed was high (140 $\mathrm{m.s^{-1}}$). Despite the higher values found (figure 5.8), the trend was similar to the present findings with an increase of fracture energy from -5 to -10°C then a constant value up to -25°C. Freezing fraction was probably in the order of 0.4 at -5°C, 0.7 at -10°C and 1.0 at -25°C. Higher values could be explained either by the difference in

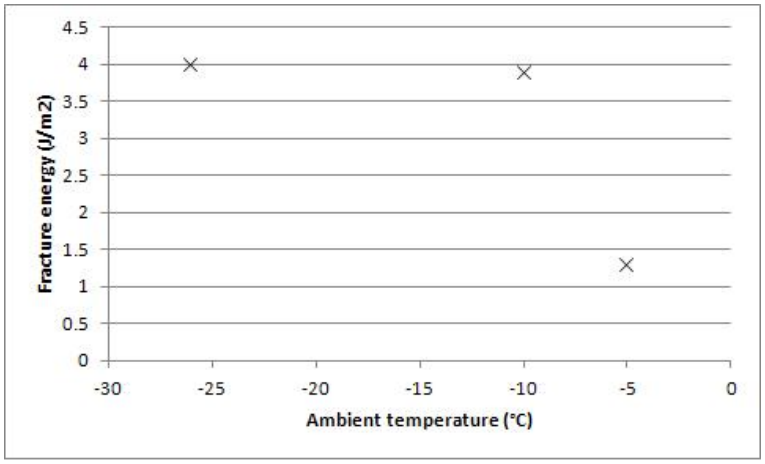

Figure 5.8: *Fracture energy of ice attached to titanium substrate for different temperatures (Hammond, 1996)*

the condition tested, especially the speed, or by the fact that, in the present experiment, the substrate surface is mirror polished whereas nothing was said about the surface of the titanium substrate in Hammond's experiments.
The values of tensile strength found with the blister test are generally higher than those reported by previous authors. In both the present and Hammond's experiments, the mechanical tests have been conducted while the icing tunnel was still running whereas in other authors' experiments, the ice was accreted first then it was let to rest before being tested. During the resting time, thermal stresses can change and partially break the ice leading to lower values.

Realistic surface finish

More testing has been conducted using a titanium substrate with a more realistic surface finish for the substrate. These latter specimens where provided by Rolls-Royce and were similar to the surface finish of a newly made clean blade. The tests were carried out as described before with the same cleaning process. Surprising results were obtained (figures 5.9 and 5.10).
The fracture mode was mainly cohesive even at temperature close to the melting point. Only at a temperature of -3 and -5°C for ice grown with a LWC of $0.4 g.m^{-3}$, was adhesive fracture obtained. This observation could easily be explained by the fact that, due to the roughness of the substrate, the ice is able to attach more strongly to the substrate surface and then, the easier path to break the ice is through the bulk and not along the interface.
On the contrary to the results obtained with the mirror polished titanium sub-

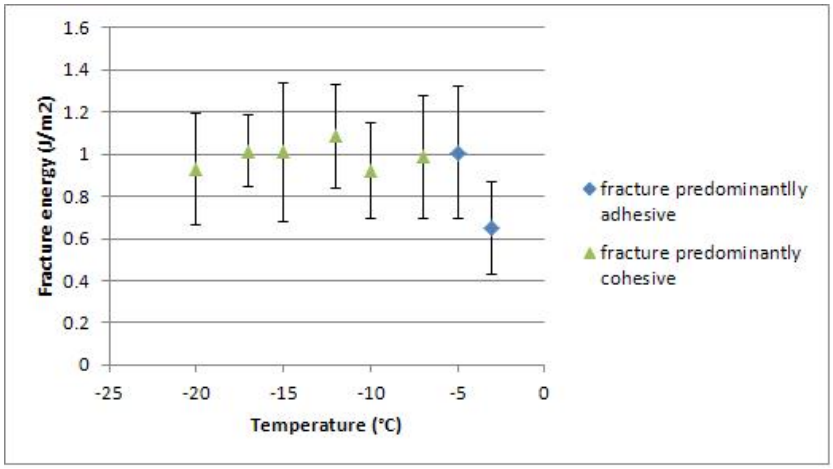

Figure 5.9: *Fracture energy of ice attached to more realistic surface finish titanium substrate for different ambient total temperature (LWC=0.4* $\mathrm{g.m^{-3}}$ *, V=50* $\mathrm{m.s^{-1}}$ *and MVD=20* μm *)*

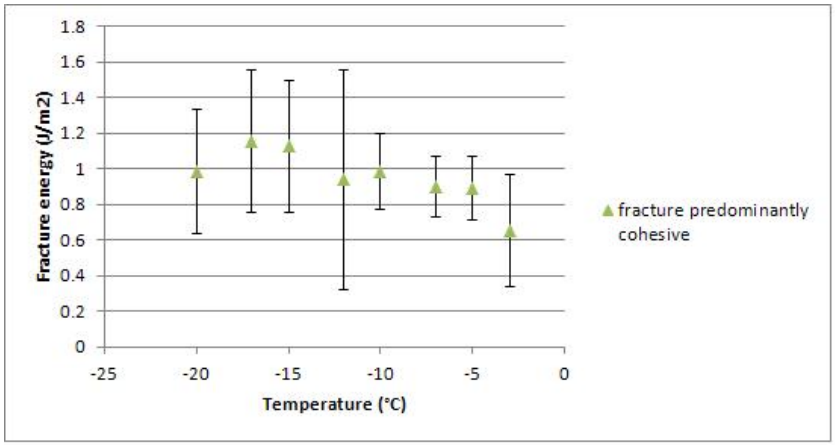

Figure 5.10: *Fracture energy of ice attached to more realistic surface finish titanium substrate for different ambient total temperature (LWC=0.7* $\mathrm{g.m^{-3}}$ *, V=50* $\mathrm{m.s^{-1}}$ *and MVD=20* μm *)*

strate, the main values of fracture energy were generally independent of the ambient total temperature. With the exception of the values obtained at a temperature of -3°C, all the others are around 1 $\mathrm{J.m^{-2}}$. The error bars are similar to those of the mirror polished titanium, being about a third of the mean value and usually larger at low temperature and smaller at temperature closer to the melting point.

5.1.4.2 Influence of LWC

A series of runs has been undertaken with a varying LWC while the tunnel speed, droplet diameter and ambient total temperature have been kept constant.

Mirror polished surface finish
A decrease of fracture energy can be observed as the LWC increases (figure 5.11).

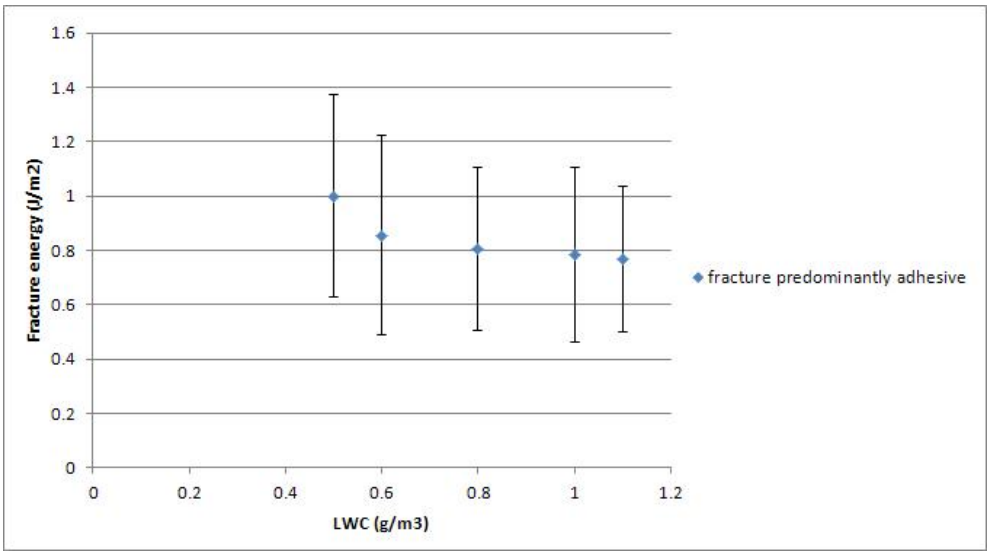

Figure 5.11: *Influence of LWC on fracture energy (T=-10° C, V=40* $\mathrm{m.s^{-1}}$ *)*

The mode of fracture was predominantly adhesive. Looking at the freezing fraction (see figure 4.12), it was found that a higher value of LWC reduces the freezing fraction meaning that the ice was more glaze like at higher LWC. In general, glaze ice was found to stick less than rime ice and is more prone to adhesive fracture. The results obtained seem to correlate well with the freezing fraction and the observation of the quality of ice, however, in the literature, the opposite was observed.
Druez et al. (1989) have conducted experiments with two different LWC values, 0.8 $\mathrm{g.m^{-3}}$ and 1.2 $\mathrm{g.m^{-3}}$, and found higher tensile strength for the highest value of LWC.

Realistic surface finish
As previously, more experiments were carried out with the more realistic surface finish. Again surprising results were obtained (figure 5.12), as, with the

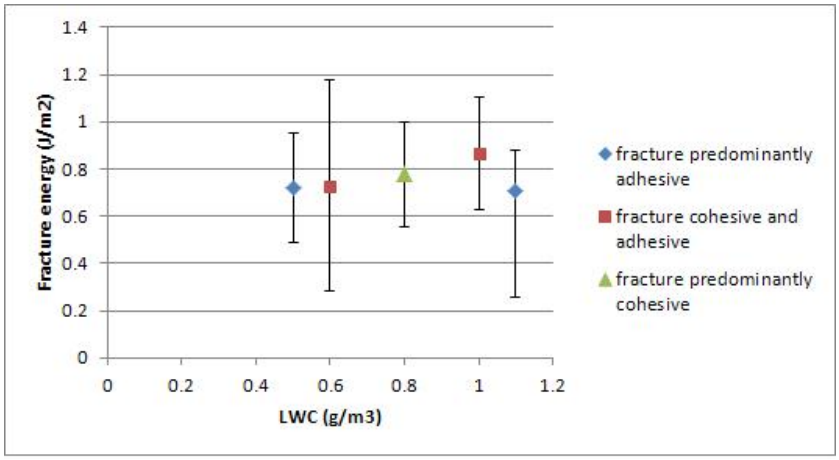

Figure 5.12: *Fracture energy of ice attached to more realistic surface finish titanium substrate for different LWC (T=-10°C, V=40* $\mathrm{m.s^{-1}}$ *and MVD=20* μm *)*

exception of the value obtained for the highest LWC, fracture energy were slightly increasing with LWC. No explanation of this behaviour has been found. A closer look at the roughness of the substrate surface needs to be done as well as observations of the ice microstructure.

5.1.4.3 Influence of speed

In the last series of runs, the tunnel speed has been varied while the tunnel total temperature, the LWC and the droplet diameter have been kept constant at respectively -10°C, 0.5 $\mathrm{g.m^{-3}}$ and 20 μm .

Mirror polished surface finish

The fracture energy of impact ice has been found to vary with most values being between 1 $\mathrm{J.m^{-2}}$ and 1.25 $\mathrm{J.m^{-2}}$ (figure 5.13). The curve is going through a maxima at a tunnel air speed of 60 $\mathrm{m.s^{-1}}$. The freezing fraction (see figure 4.14), for these conditions, has been found to be decreasing as the tunnel wind speed is increasing. Therefore, the freezing fraction by itself can not explain the behaviour of the fracture energy with the tunnel wind speed. The average grain size (see figure 4.44) seemed to go through a maximum at a tunnel wind speed between 40 and 80 $\mathrm{m.s^{-1}}$. The exact value at 60 $\mathrm{m.s^{-1}}$ was not available. However, ice with larger grain was usually shown to have a lower tensile strength and, hence, a lower value of fracture energy should have been obtained. The large scatter (between a third and half of the value) could be

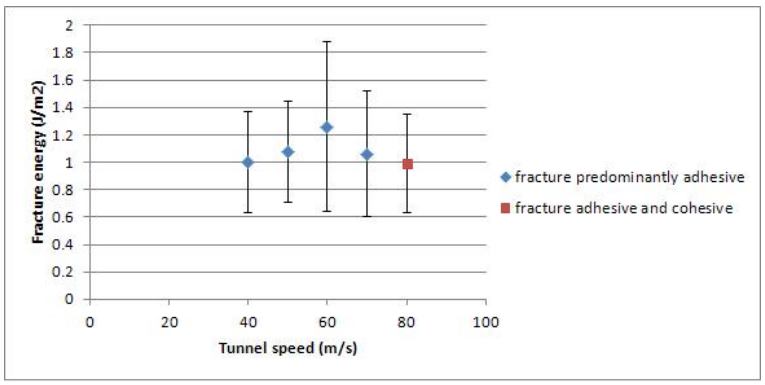

Figure 5.13: *Influence of tunnel speed on fracture energy (T=-10° C, LWC=0.5* $g.m^{-3}$ *)*

responsible to a misreading of the trend. More experiments should be carried out in order to reduce the scatter.
Other authors have carried out tests at much lower speed (lower than 30 $m.s^{-1}$) and have observed a maxima at 15 $m.s^{-1}$ (Mohammed and Farzaneh, 2011) or 16 $m.s^{-1}$ (Druez et al., 1986). However a decreasing of the tensile strength at high tunnel wind speed are not in agreement with the high values found by Hammond (1996).

Realistic surface finish
Results obtained with the more realistic surface finish are in agreement with those obtained with the mirror polished surface finish (figure 5.14). However, there are some disparities. The maximum was observed at a tunnel air speed of 70 $m.s^{-1}$ instead of 60 $m.s^{-1}$ and a wider range of fracture energy values have been obtained. Values as low as 0.7 $J.m^{-2}$ has been found and up to 1.6 $J.m^{-2}$. Such a dependence on the tunnel air speed is not explained yet. Investigation of the microstructure could help to understand the difference of ice structure when it is grown on a polished or on a rougher material.

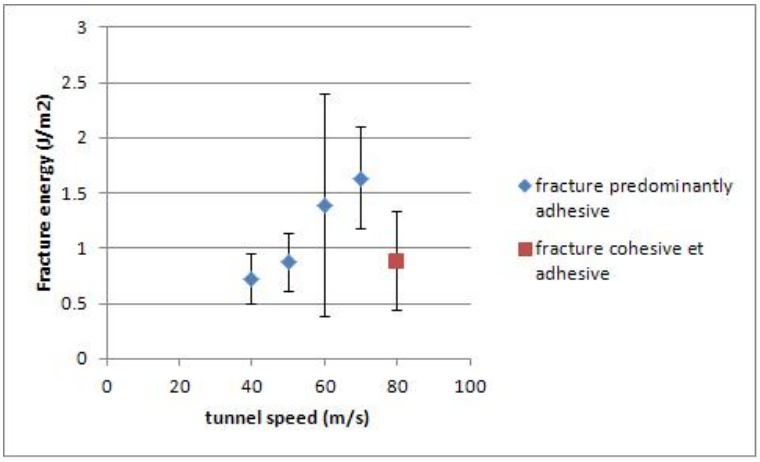

Figure 5.14: *Fracture energy of ice attached to more realistic surface finish titanium substrate for different tunnel air speed (T=-10° C, LWC=0.5* $\mathrm{g.m^{-3}}$ *and MVD=20* μm *)*

5.1.5 Finite elements models

Two finite elements models (FEM) were created to reproduce the mode I test. These two models were developed in order to compare the computational results against the experimental results with the objective to use a finite element analysis to postprocess the shear test results and to develop a model able to shed ice from a rotating blade.
The first model was a bonded nodes model where the ice piece was pushed by pressure and the resulting tensile stress distribution was calculated. The second one was a dynamic explicit model using cohesive elements to simulate the bond between the ice and the substrate.

5.1.5.1 Bonded nodes model

This finite element model was aimed to simulate the mode I test. In a given case, the value of the critical pressure was used as input. The results of the finite element analysis gave us the distribution of tensile stress through the model and a value of fracture toughness can be obtained. This value was then compared to the value obtained from the experiment.
The finite element model was a 3D static model. An axisymmetric model could have been used, however the brittle material properties in Abaqus can only be defined in a 3D model. The model was composed of 2 parts: ice and substrate (figure 5.15). The ice part was modeled as a brittle material with a density of 870 $\mathrm{kg.m^{-3}}$, a Young's modulus of 8.5 GPa and a Poisson's ratio of 0.31. The

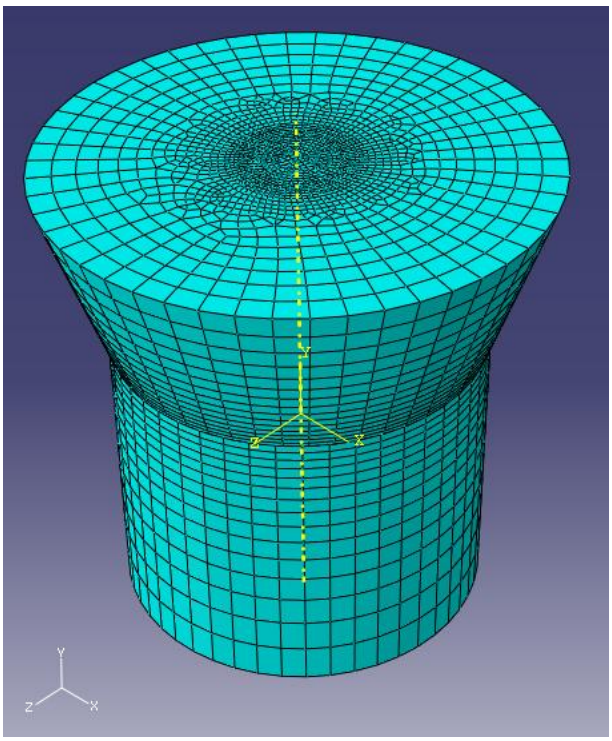

Figure 5.15: *Whole model with mesh*

substrate material used is titanium (E=116 GPa, $\nu = 0.32$, $\rho = 4506$ kg.cm^{-3}). A surface-to-surface contact interaction between the substrate and the ice was created using the option "kinematic contact method" and "finite sliding". The two surfaces were tied which means that the nodes cannot be separated during the simulation.
The lower surface of the cylinder was set as encastre so all the nodes of the face were constrained in translation and rotation. The load was applied through the hole, over the area covered by the plastic disc, to the ice in quasi-steady conditions using what is called in Abaqus "a smooth step amplitude" (figure 5.16).

The mesh has been particularly refined around the interface and at the crack tip (the crack tip is assumed to be the edge of the little plastic disc). The influence of the mesh has been studied (figure 5.17). Except for the coarsest mesh (dark blue curve), the stress distribution was pretty similar (red, purple and light blue curve). However the value at the crack tip was still quite different and an increase in the number of elements will increase this value further but with a huge increase in the computational time. For this reason, any further simulation will be run with the intermediate mesh (purple curve) as it presents

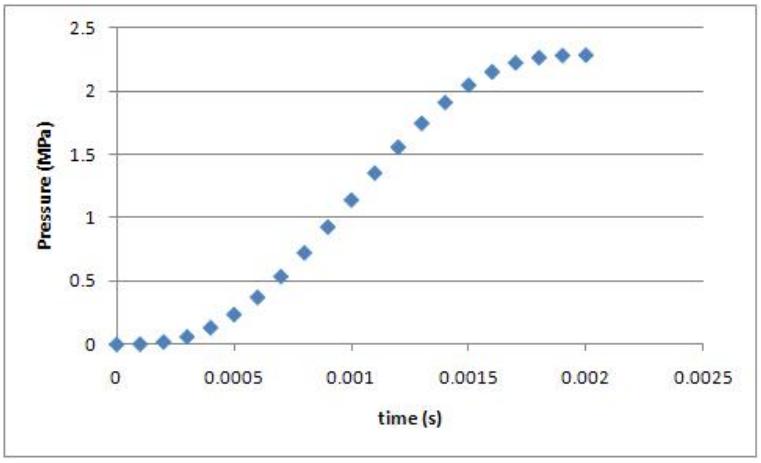

Figure 5.16: *Pressure applied on ice during the simulation*

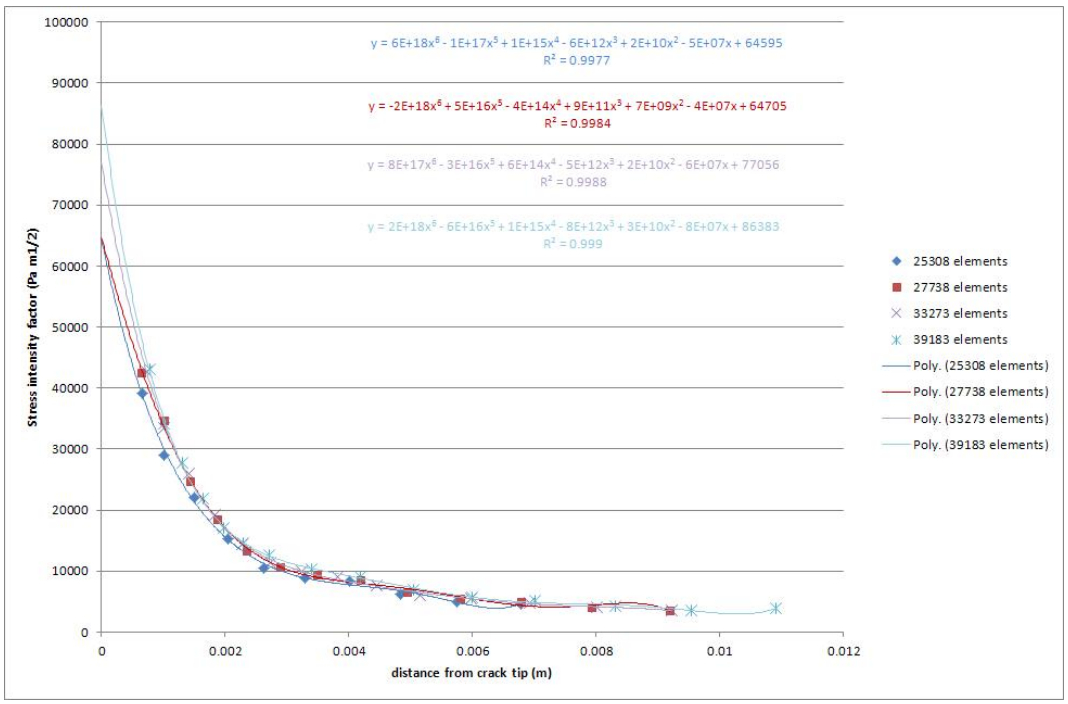

Figure 5.17: *Tensile stress distribution using different meshes*

a good compromise between results and computational time.
Figure 5.18 presents the tensile stress distribution in the ice part and especially at the interface. The blue part represents the section in which the pressure is applied. The crack tip is at the junction between the red part and the green part. Figure 5.19 shows the stress variation along the path drawn on

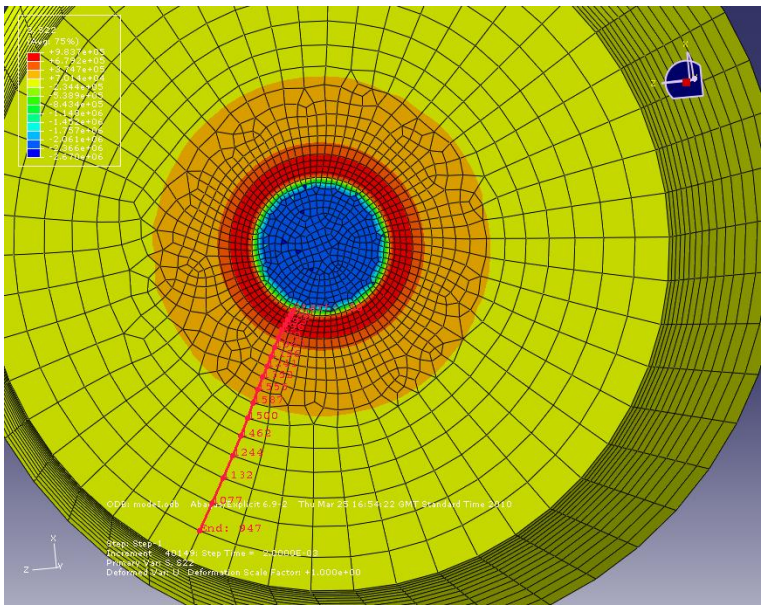

Figure 5.18: *Stress along y axis in ice and path*

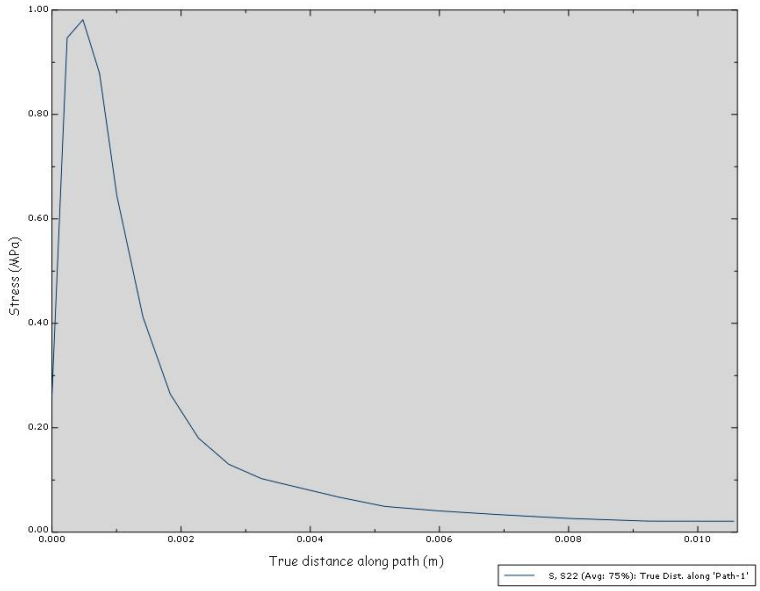

Figure 5.19: *Tensile stress (y axis) along the path*

figure 5.18. The path starts at the crack tip and finishes almost at the edge of the ice piece. From the crack tip, the calculated tensile stress increases quite sharply, then drops until it reaches a value almost constant. The mathematical

equation used to calculate the stress around a crack leads to singularity at the crack tip (r=0):

$$\sigma_y = \frac{K_I}{\sqrt{2\pi r}} cos\frac{\theta}{2}(1 + sin\frac{\theta}{2} sin\frac{3\theta}{2}) \tag{5.7}$$

To get the value of the fracture toughness, K_{Ic}, the stress intensity factor, K_I, is calculated from the stress values obtained when the load applied is the critical pressure, using equation 5.8.

$$K_I = \sigma\sqrt{2\pi r} \tag{5.8}$$

The values of the stress intensity factor are then plotted against the distance from the crack tip, r. A graph like in figure 5.20 can be obtained. The curve

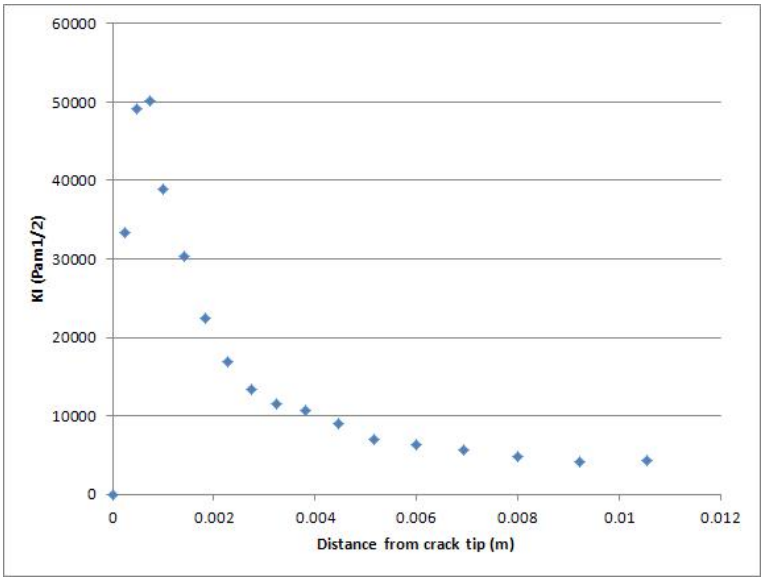

Figure 5.20: *Values of K_I along the crack path*

is initially increasing and start to decrease several milimeters from the crack tip. The first few points of this curve were deleted to keep only the decreasing part of it (figure 5.21). The curve can now be fitted with a polynomial curve of degree 6. The extrapolation of this curve to the crack tip (r=0) gives a value of K_{Ic} corresponding to the critical pressure applied. This value can be compared to the one obtained from the experiments using the analytical expression developed by Andrews and Lockington (1983). For example, a test ran at an ambient temperature of -10°C with a cloud LWC of 0.7 g.m^{-3} and a tunnel wind speed of 50 m.s^{-1} gave a critical pressure of 1.91 MPa producing a fracture toughness of 90.801 kPa$\sqrt{\text{m}}$ according to Andrews and Lockington's formulations. The fracture mode was 100% adhesive. The finite element model

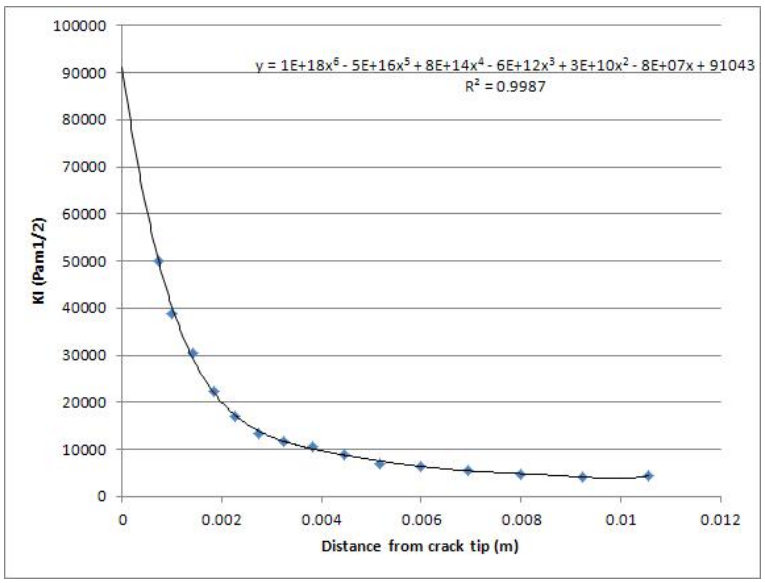

Figure 5.21: *Values of K_I along the crack path - decreasing part*

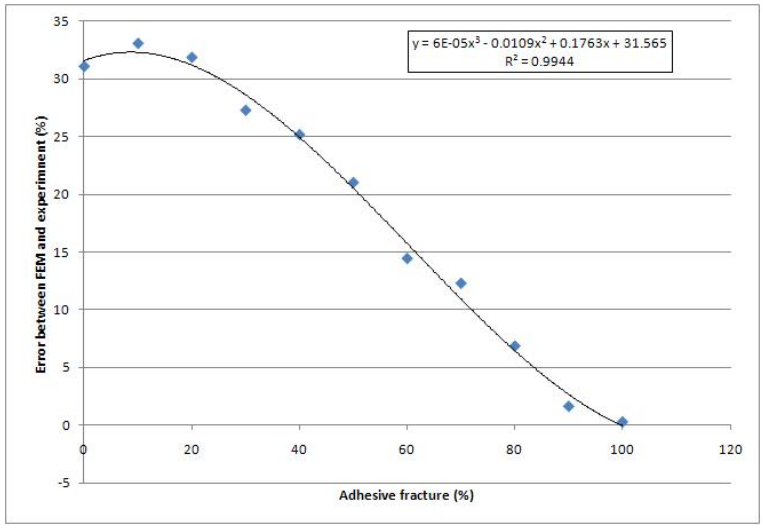

Figure 5.22: *Difference between the fracture toughness value obtained from experiments and from FEM vs percentage of adhesive fracture*

predicted a fracture toughness of 91.043 kPa$\sqrt{\text{m}}$ (figure 5.21) which means that the difference between the two values was only of 0.26%.
In the finite element model, the path was drawn at the interface between ice and the substrate. Hence, the stress values are taken at the interface. During the experiments, both cohesive and adhesive fracture are observed (and

most of the time a mix between the two types of fracture). For different types of fracture (percentage of adhesive break), the fracture toughness values obtained from the experiments, analysed by the analytical and the numerical methods have been compared. The difference between the two values was plotted against the percentage of adhesive fracture on figure 5.22. A fit has been obtained which can allow us to estimate the value of fracture toughness from the finite element results even if the failure does not happen at the interface.

5.1.5.2 Model with cohesive elements

This second model was similar to the previous one in respect of geometry and mesh. The only difference was the presence of a layer of cohesive elements at the interface between the ice and the substrate.
This model was created in order to determine the appropriate values to choose for the different parameters used to characterise the cohesive elements in order to model ice adhesion and fracture and achievesimilar results to the experiment. The cohesive elements are usually used as a sort of glue between two materials. If the stress (or the strain) at the interface reaches a certain value given as a material property, the cohesive elements are deleted and the materials are not glued together anymore at that point. In the present model, four parameters are needed to describe the material properties of the cohesive elements: the density, the penalty stiffness, the tensile and the shear strength and the fracture energy. The last two parameters are obtained from the experiments whereas the first ones are completely non physical. The density was chosen to be close to the ice density at about 1000 $kg.m^{-3}$. The penalty stiffness should be the highest value possible that does not lead to numerical problems (Camanho and Davila, 2002). As a first approximation, a value of 2000 GPa was set. This value was then reconsidered in order to match the experimental results.
As it was said before, this model was created to match experimental results using a layer of cohesive elements between the ice and the substrate. A test case was chosen where the ice was removed from the substrate in an adhesive way. The temperature was -10°C, the tunnel air speed 50 $m.s^{-1}$ and the LWC 0.4 $g.m^{-3}$. The critical pressure needed to remove the ice was 2.05 MPa which gives a fracture energy of 1 $J.m^{-2}$ (using Andrews and Lockington analytical approach), a fracture toughness of 97 $kPa\sqrt{m}$ and a tensile strength of 4.71 MPa taking into account an average grain size of 135 μm, a Young's modulus of 8.5 GPa and a Poisson's ratio of 0.31.
The model was then constituted of two parts:

- a 3D deformable solid part representing the substrate. The material was titanium with a density of 4430 $kg.m^{-3}$, a Young's modulus of 113

GPa and a Poisson's ratio of 0.34. An 8-node linear brick mesh with reduced integration and hourless control (C3D8R) was used and it was particularly refined near the hole and near the interface ice/substrate (figure 5.23).

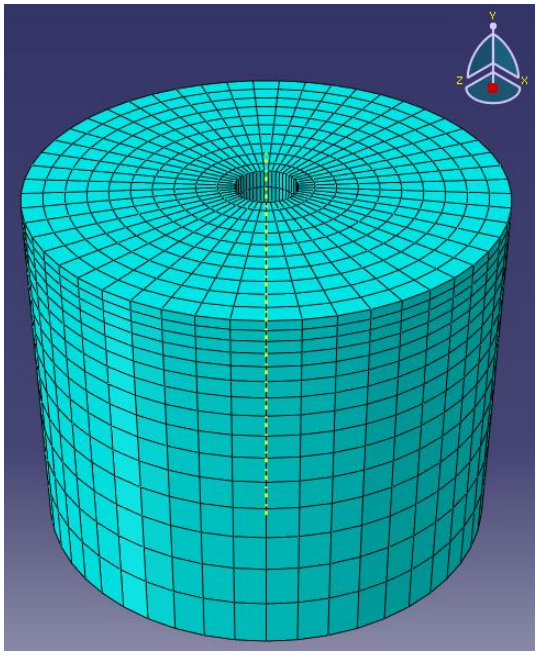

Figure 5.23: *Part representing the substrate*

- a mesh, called "orphan mesh" in the software, obtained from the replicate of the mesh of a 3D deformable part representing the ice. The ice was modeled as a cone with a diameter of 30 mm at the base, 40 mm at the top and a thickness of 15 mm. The ice density was set as 870 $kg.m^{-3}$, the Young's modulus to 8.5 GPa and the Poisson's ratio to 0.31. The mesh was particularly refined at the interface ice/substrate and at the center of the ice piece (figure 5.24).
  A layer of cohesive elements of 0 thickness was embedded in the bottom face of the ice (at the ice/substrate interface). An 8-node linear brick mesh with reduced integration and hourglass control (C3D8R) was used for the mesh of the ice part while an 8-node three dimensional cohesive elements was used for the cohesive layer.
  As the cohesive layer was very thin, a traction-separation based model was chosen. The problem was only mode I (load applied perpendicular to crack opening) so there were no coupling effects between normal and shear components and the elastic matrix (penalty stiffness) can be

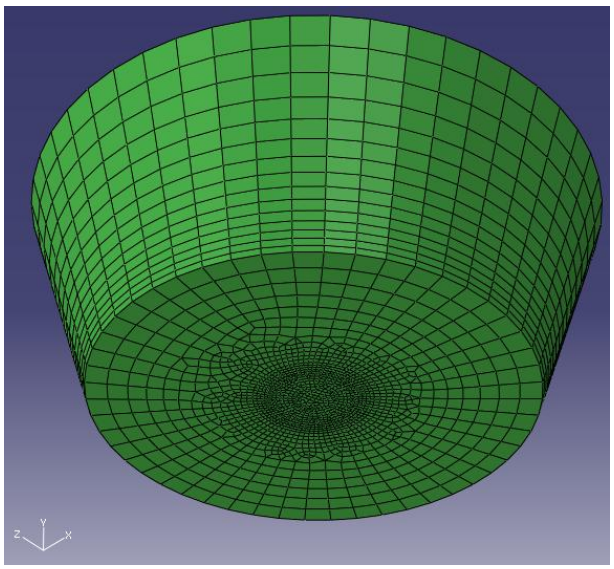

Figure 5.24: *Part representing the ice*

described with the traction option. Two criterions were needed to described the initiation and the propagation of a crack. The maximum nominal stress criterion ("Maxs damage" option in the software) was chosen for the damage initiation criterion. This criterion assumes that when the stress in one direction reaches the maximum value set, damage initiate. A nominal stress value of 4.71 MPa in the normal mode and 1 MPa in the first and the second direction was set. A damage evolution criterion based on energy was chosen with a linear softening and a mode independent mixed-mode behaviour. The fracture energy value was set to 1 $J.m^{-2}$.

The contact between these two parts was defined by a tied constraint between the substrate and the cohesive elements layer. During the simulation, the cohesive elements will be removed and the ice will be free to detach away from the substrate.
During the mechanical test in the icing tunnel, gas pressure was applied to the plastic disc through the hole in the cylinder. The plastic disc was not represented in this model as a seperate entity as it only acted as a crack initiator, therefore the pressure (load) was directly applied to the ice on a surface equivalent to the plastic disc (figure 5.25). A uniform pressure of 5 MPa was set with a smooth step amplitude to ensure a quasi-static simulation. A boundary condition to restrict the substrate from any movements (encastre) was set to the bottom face of the substrate.
Several attempts have been made in order to match the experimental results

Damage initiation criterion "Maxs Damage"	normal only mode first direction second direction	4.7 MPa 1 MPa 1 MPa
Damage evolution type=energy softening=linear degradation=maximum mixed mode behaviour=mode independent mode mix ratio=energy	fracture energy	1 J.m^{-2}
Density	mass density	1000 kg.m^{-3}
Elastic type=traction	K_{nn} K_{ss} K_{tt}	2000 GPa 2000 GPa 2000 GPa

Table 5.1: *Summary of the cohesive elements properties*

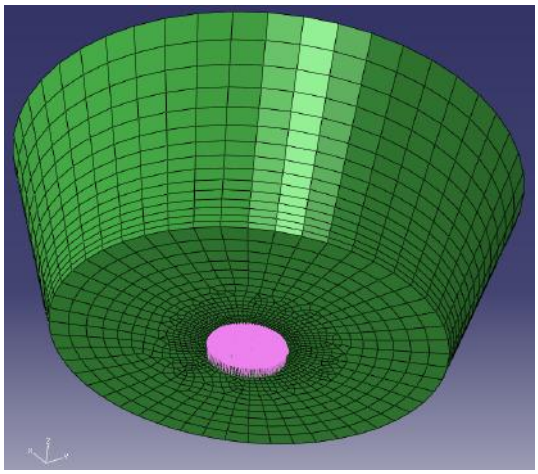

Figure 5.25: *Load applied to the ice part*

of the study case. By increasing the value of the penalty stiffness to 25000 GPa, the critical pressure needed to initiate the crack was reduced. However the initiation of the crack became more difficult to estimate. At a low value of penalty stiffness (about 2000 GPa), the initiation of the crack was defined by the delamination of the cohesive elements. For a high value of penalty stiffness (25000GPa), it was defined by a change in the stress distribution: some values at the crack tip start to decrease instead of increasing (figure 5.26). By choosing this very high value, a critical pressure of 2.03 MPa instead of 4.4 MPa can be obtained which is very close to the experimental value (2.05 MPa).

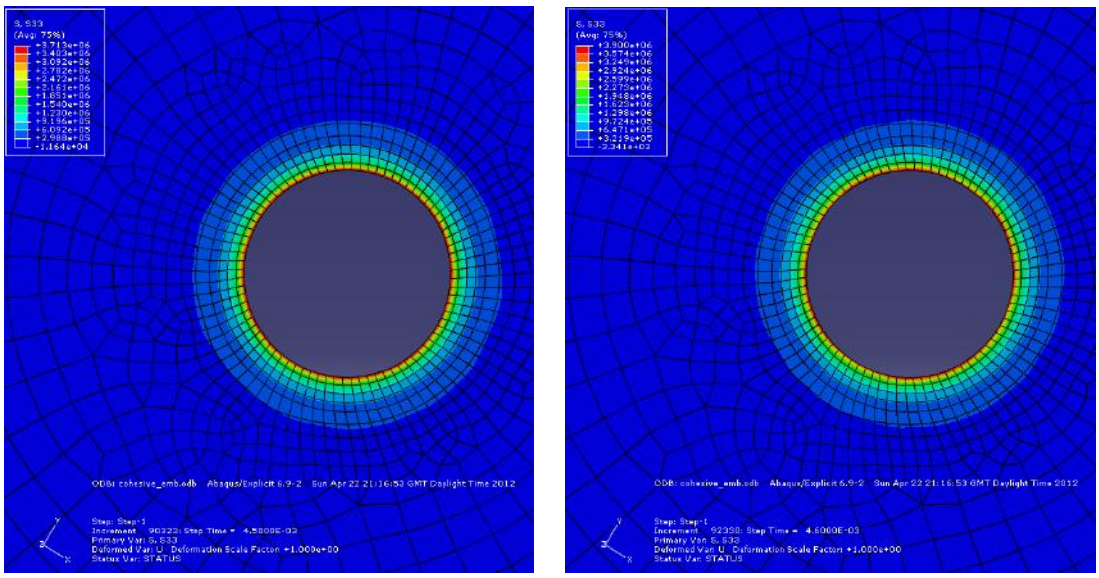

Figure 5.26: *Stress distribution before (left) and after (right) the crack initiation*

The simulation of the mode I test using a layer of cohesive elements seems to have been successful. However the penalty stiffness used needed to be increased to the value of 25000 GPa in order to obtain a value of the critical pressure which can match the experimental value. By increasing the penalty stiffness, the instant of crack initiation became more difficult to determine and, between the crack initiation and the delamination of the first cohesive elements, unexpected behaviour were obtained in term of stress distribution (figure 5.27). The highest values of the tensile stress are not obtained near the crack tip but four elements further.
This method seems then very useful to determine the instant at which the crack was initiated as well as the critical pressure needed to shed the ice but seems very doubtful to provide an accurate stress distribution during the shedding process.

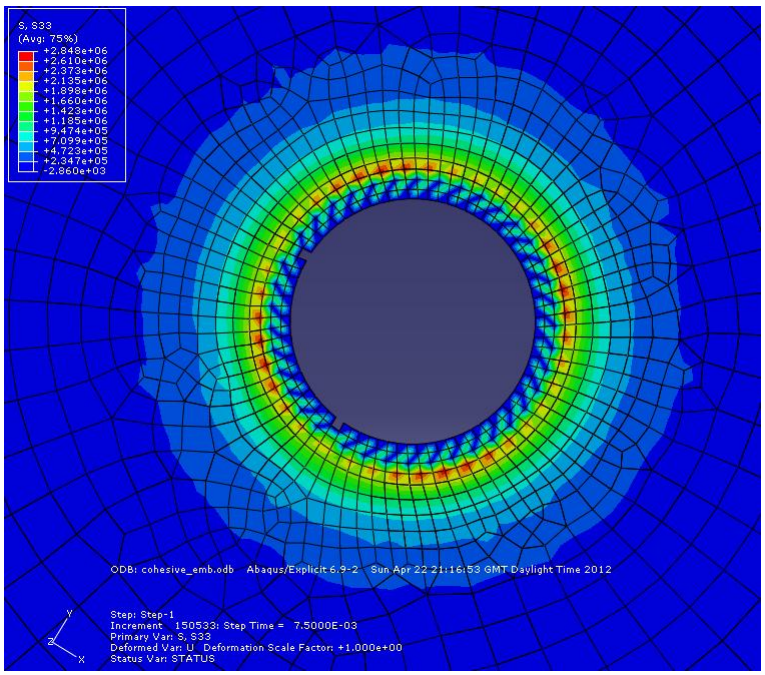

Figure 5.27: *Stress distribution at the first cohesive element delamination*

5.2 Shear strength

5.2.1 Previous studies

Two types of shear tests have been described for impact ice: "static" tests where the ice is pushed or pulled to separate it from the body it has grown on, and rotational tests where the ice is removed due to the centrifugal force.
The first rotational test was carried out by Stallabrass and Price (1962). A cylindrical specimen was mounted on a helicopter rotor blade. Ice was formed by spraying water in a cold room. The blades were rotating at a constant speed of 500 RPM. The centrifugal load was determined using strain gauge measurements. As ice built up, the centrifugal load increased until the adhesive or cohesive strength of ice was reached and ice shed. Five different materials were tested (aluminium, stainless steel, titanium, Teflon and Viton) through a range of temperature between -7°C and -18°C. The adhesive shear strength of aluminium and titanium were found to be in the range from 30 to 130 kPa and from 20 to 250 kPa respectively. Whilst this method is realistic for application to spinning components in using centrifugal force to apply the load, it does not force the fracture to follow the interface between the ice and the substrate. Furthermore, it is not always possible to see whether the fracture

event was confined to the interface (adhesive) or whether the ice broke within itself (cohesive). The authors reported significant cohesive ice fracture with viton and reported that it was difficult to determine the presence or absence of ice on the metal substrate surface. Therefore, the results do not tell us with certainty what the ice bond strength was.
Fortin and Perron (2009) used a similar method but the ice was accreted directly on the blades of a helicopter rotor. The rotating speed was kept constant around 3230 RPM and, as the ice build up, the power needed to rotate the blades increased. An ice shedding event was recorded as a sudden drop in power. The blades were made of aluminium alloy and four temperatures between -5°C and -20°C have been tested. The adhesive strength is calculated from the balance of the centrifugal, cohesive and adhesive force. The assumption made was that the ice thickness has a linear increase from hub to tip. Values between 70 and 260 kPa were found for the shear strength of ice on aluminium.
Laforte and Beisswenger (2005) used a slightly different system. Icing is built up at the extremity of beams by spraying water and the beams are then placed in a centrifuge. The speed of the centrifuge is increased from 0, at a rate of 300 RPM/s, until ice shedding occurs. The shedding event is picked up by two piezzoelectric cells which can detect vibrations, placed on the side of the centrifuge casing. The shear strength is calculated by dividing the centrifugal force by the iced area. An average value of 350 kPa was obtained for ice on aluminium at a temperature of -10°C. Like for the test rig used by Stallabrass and Price, the two test rigs described previously do not guarantee that an adhesive break can be made. The crack responsible for the fracture will take the easiest path to propagate, either within the ice or at the interface. In case of cohesive failure, the rotational test rigs will then provide lower values for what is taken as the shear strength compared to purely adhesive shear test rigs. Furthermore, rotational test rigs are subject to additional forces like vibrations or aerodynamic forces which are not taken into consideration in static test rigs.
Druez et al. (1978, 1986), Chu and Scavuzzo (1991), Scavuzzo et al. (1996) and Scavuzzo and Chu (1987) used a test apparatus which pushes the ice accreted around a metallic cylinder. In both cases the ice was formed in an icing tunnel by spraying water on the cold metal surface, then the mechanical test was carried out. In Druez et al.'s experiments, a metal disc pushed the ice until it was removed from the surface and the force was recorded by four strain gauges. The shear strength was calculated by dividing the force applied by the contact area between the ice and the substrate. Each adhesion measurement was made at the same temperature as the icing formation but a delay of 20 minutes was observed before any measurement. Values in the

range from 40 to 450 kPa were obtained on aluminium. Chu and Scavuzzo's specimens were made of two concentric cylinders between which the ice was built up. The adhesive shear force was measured by pushing the inner cylinder until ice became detached. A load cell was used to record the force and a linear variable displacement transducer to determine the instant of shedding. The test temperature was obtained by heating the interface ice/substrate using a heating element placed at the center of the inner cylinder. Values between 100 and 500 kPa have been obtained depending on the icing conditions. In all these tests, only purely adhesive shear strength values were reported. The authors reported some cohesive failure especially with rime ice but the values were discarded. In these tests the ice was allowed to rest after being built up, so the thermal stresses have time to redistribute and be only residual stresses. Chu and Scavuzzo even used a different temperature for growing and testing the ice. As the thermal coefficient of expansion of ice is relatively high compared to the thermal coefficient of metal, a small variation in temperature will induce high thermal stresses which could partially break the ice prior to the mechanical test. This might be expected to result in an underestimation of the adhesive shear strength.

Millar (1970) has studied the adhesion of ice on a wing. After accretion, a piece of ice was isolated by removing the neighboring ice and then it was pushed using a hydraulic ram device. Values between 100 and 2500 kPa were obtained depending on the material tested. The adhesive strength can also be obtained by bending a beam of material which ice was accreted on.

Blackburn et al. (2000) have shown that, for a specific thickness of ice, when the neutral axis was positioned at the interface ice/substrate, the ice was debonded adhesively and therefore the adhesive shear strength can be obtained. This test was conducted in two steps: the first one where the ice was accreted on aluminium beams in a cold chamber at -10°C and the second one where the iced beams were tested. Several tests have been conducted and an average value of 230 kPa have been obtained. No information on LWC, tunnel wind speed or droplet size have been given hence comparison with other values is a bit difficult. Again the tests were not conducted in the same conditions as the ice accretion (different static temperature, ice allowed to rest after accretion, etc).

Javan-Mashmool (2006) also used the bending properties of an aluminium bar to measure the shear strength of ice attached to them. Prior to the ice accretion, piezoelectric film sensors were attached on the aluminium beams. The iced aluminium beams were clamped onto an electric shaker and the ice adhesion was measured by monitoring bending vibrations. The test temperature was set at -10°C and the wind speed at 3.3 $m.s^{-1}$. An average value of 285 kPa was obtained.

Laforte and Laforte (2009) reported, in a recent paper, about other tests to

measure the adhesion of ice on an aluminium substrate. They use tests where the ice was only constrained at the interface ice/substrate and the force was applied to the substrate and not to the ice. Due to the applied force, the substrate was strained and the strain propagated into the ice. The force was applied in three different ways: tension, torsion and bending. In all tests, the adhesion of ice was measured in terms of deicing strain directly measured by strain gauges placed on the aluminium bar. Normal stress or shear stress at the instant of shedding can then be calculated from the strain value. Only the torsion test gives a value for pure shear strength. Average values of 2300, 1000 and 400 kPa were obtained for ice thicknesses of 2, 5 and 10 mm respectively. The strength of ice was lower for a larger piece of ice which could be expected as a larger piece of material will contain more defects statistically and therefore has a higher probability to initiate a crack. Furthermore, two different materials, aluminium and nylon, have been tested with different surface finish and results show an absence of influence from the material but an increase in the shear strength with roughness. Here again time is allowed between ice formation and mechanical test for relaxing the internal stresses.
The only static experiment carried out in a running icing tunnel was done by Petrenko (2006). Stainless steel wires were placed on a surface and, as ice accumulates, the wires were pulled out. The force needed to pull the wires was measured using a force sensor. The time at which the wire was pulled and the tensile force were recorded. The adhesive shear strength of ice was obtained from the measured tensile force and the iced surface of the wires. A curve of adhesive strength variation through time was obtained. For ice made at a temperature of -10°C and a tunnel speed of 20 $m.s^{-1}$, values between 150 and 350 kPa were obtained depending on the LWC of the cloud. Despite the fact that these values have been measured in a running icing tunnel, they were probably under evaluated due to the way they were obtained. The adhesive shear strength was calculated from the force needed to pull the wire and the wire surface area covered by ice. This under represents the shear force in the case that the wire stretches. In practice the shear stress will diminish along the wire depending on its stiffness relative to the ice and its size.
Through all literature, the authors seems to agree that the adhesive shear strength of impact ice falls in the range from 50 to 500 kPa (figure 5.28). This range of values may seem wide but the authors have all used different sorts of tests and even if the ice was mainly tested at a temperature of -10°C, different conditions have been used (MVD, ice thickness, LWC, wind speed). All these conditions have an effect on the physical properties of ice, especially grain size and porosity, hence they affect the mechanical properties and especially the adhesive properties of ice attached on a substrate. Finally the substrate properties and state of the surface might also be supposed to explain the variation

in the adhesive shear strength values. Some authors worked with a highly cleaned, polished surface whereas others did not pay real attention to the surface state. This difference could also explain the wide range of values obtained.

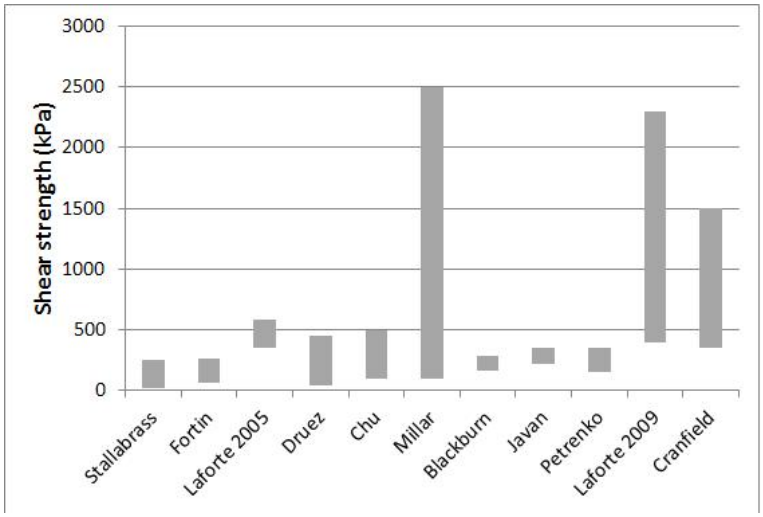

Figure 5.28: *Range of adhesive shear strength values found by the different authors*

5.2.2 The new ice shear test

As most of the results found in the literature were obtained from ice which has rested for some time, a new test rig has been designed and built at Cranfield University to allow a measurement of the shear strength in a running icing tunnel (Lou, 2010). The principle was very simple: when a certain thickness of ice was reached, a plunger was moved, under the action of pressure, to push the ice off the surface. The pressure needed to move the ice was measured and then converted to a shear strength value through a finite element analysis.
Each test device included a substrate, a plunger, a rubber tube and a supporting structure (figure 5.29). The substrate can be changed easily so different materials can be tested. The plunger was the movable part. Its role was to push the ice off the substrate. Nitrogen gas under pressure passed into the rubber tube which, by inflating, pushed the plunger.
The test rig was placed in the tunnel at an angle of 45°with respect to the flow stream. In that way both the substrate surface and the plunger wall were uniformly covered by ice. Adhesion on top and bottom part of the test rig were mainly avoided by the presence of two shields which catch the supercooled

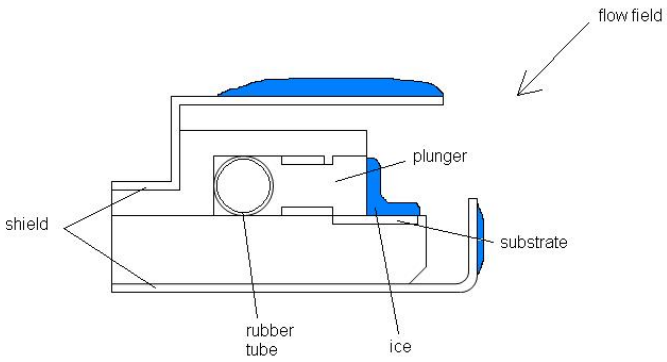

Figure 5.29: *Schematic diagram of the cross section of the shear test*

water droplets before they impinged on surfaces which were best kept clear. In the same way, the enlarged shape of the plunger was designed to avoid any

Figure 5.30: *Test rig*

unwanted accretion on both side of the apparatus (figure 5.30).
The rubber tube was connected to a nitrogen bottle through a pressurization system. The pressurization system consisted of a whole system of valves allowing a complete independence of each test device, a needle valve was employed to select the flow rate of the gas and an electronic valve to allow gas to enter the system. Due to the gas pressure, the rubber tube tried to inflate but was blocked by the plunger (and the ice). A force was therefore applied to the plunger to push the ice. When the shear strength of ice was overcome the plunger moved and the rubber tube was able to inflate. This inflation can be seen on the pressure graph as a tiny drop in pressure (figure 5.31). The pressure was measured using a pressure transducer and a recording of one value

each ms was made by a signal recording system controlled by Labview [2].

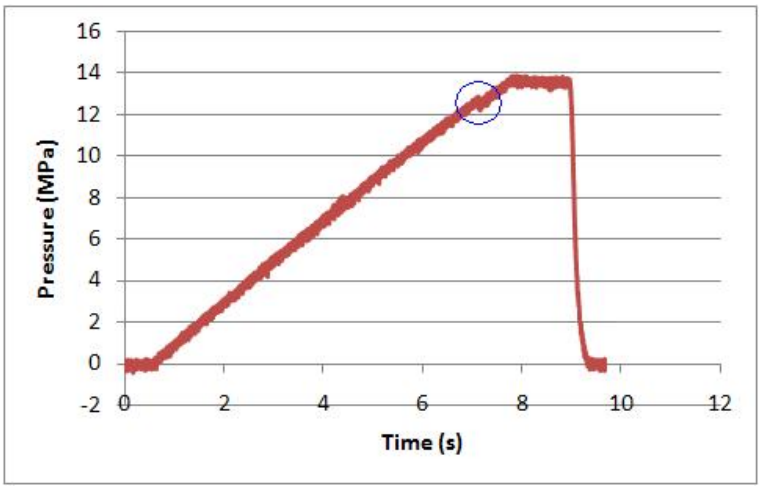

Figure 5.31: *Example of the pressure recording during the test*

5.2.3 Methodology and test procedure

The test rigs were placed in the tunnel on two support bars. Attention was taken to constrain the rubber tubes well so they can only expand inside the test rig and not on the outside (which can lead to a bursting of the rubber tube). The substrate was then cleaned with ethanol and dried using a hot air gun. Special care was made to remove all the water which might have gone under the plunger. The test rigs were covered and the air supply to the tunnel atomising system was switched on so any water still in the nozzles can be purged to prevent it landing on the test rigs before the experiment was started. The test rigs were then uncovered, the tunnel was closed and the main fan and the cooling system were started. The different parameters (LWC, temperature, tunnel speed) were set and when the tunnel was in stable condition, the water was sprayed.
After 5 minutes, depending on the tunnel conditions, a thickness of about 3 mm was reached and the mechanical test can start. The tunnel was kept running with the water still being sprayed. Each test device was operated in turn by selecting the individual valve and switching on the electrical valve until the ice sheds. The pressure of the gas passing through the rubber tube was recorded by a pressure transducer. The pressure applied to the plunger was

[2]Labview is the trade name of software produced by National Instruments, `http://www.ni.com`

assumed to be identical to the pressure measured by the pressure transducer taking into account the thickness of the rubber pipe walls. The rate at which the test fixture was pressurized was controlled to approximately 10 bars per second. This typically gave fracture in one to two seconds. The strain rate was of the order of 10^{-4}s^{-1}.
A post-processing task consisted of determining the instant of shedding and noting the value of pressure needed to shed the ice. This latter was called critical pressure (P_c). As ice is a brittle material, the experimental results will include some scatter, even when a lot of care is taken to reproduce the same conditions exactly . To deal with this, several values of critical pressure were obtained for each condition (between 6 and 17). It has been proved previously that the strength of brittle materials follow a Weibull distribution (Jayatilaka, 1979), hence, a statistical analysis was run.The software Statistica [3] was used and at the end of the process a mean value and a standard deviation were obtained.
A finite element analysis using the commercial software Abaqus 9.2 [4] has been used for the determination of the correlation between the critical pressure and the stress intensity at the junction between the ice, the interface and the plunger. The local shear strength was then calculated from the latter using the average grain size as a typical default size. More details about the model and the methodology will be discussed in the following section. The use of finite element analysis allowed us to get the value of adhesive shear strength at the location where the force was applied (at the bottom right corner of the ice piece). Therefore, the value obtained will not be an average value along the substrate surface but the exact value of shear stress needed to detach the ice at the point where the fracture initiates.
In parallel, an average value of the shear strength was calculated in order to compare the values obtained during the present study to the values obtained by the previous authors. This average value was obtained by dividing the force applied to the ice by the surface of contact between the ice and the substrate

$$\tau_{av} = \frac{P_c \times A_p}{A_c} \tag{5.9}$$

where P_c is the critical pressure with the rubber tube thickness correction, A_p is the surface of the plunger applying the force to the ice and A_c is the surface of contact between the ice and the substrate.

[3]Statistica is a statistics and analytics software developed by StatSoft, `http://www.statsoft.com`

[4]Abaqus is the name of a finite element analysis software developed by Simulia, `http://www.simulia.com`

5.2.4 Finite Elements Analysis

During this test, a crack was assumed to be initiated from the edge where the plunger apply on the ice and to propagate along the interface ice/substrate. That is why, even if the crack is not physically present at the beginning of the simulation, an analysis similar to the LEFM will be applied to the edge.

5.2.4.1 Model

The finite elements model of the shear test was composed of three parts:

- a 3D deformable solid part representing the plunger. A round shape was modeled where the rubber tube will apply some pressure after inflation (figure 5.32). The material is aluminium with a density of 2700 kg.m^{-3} ,

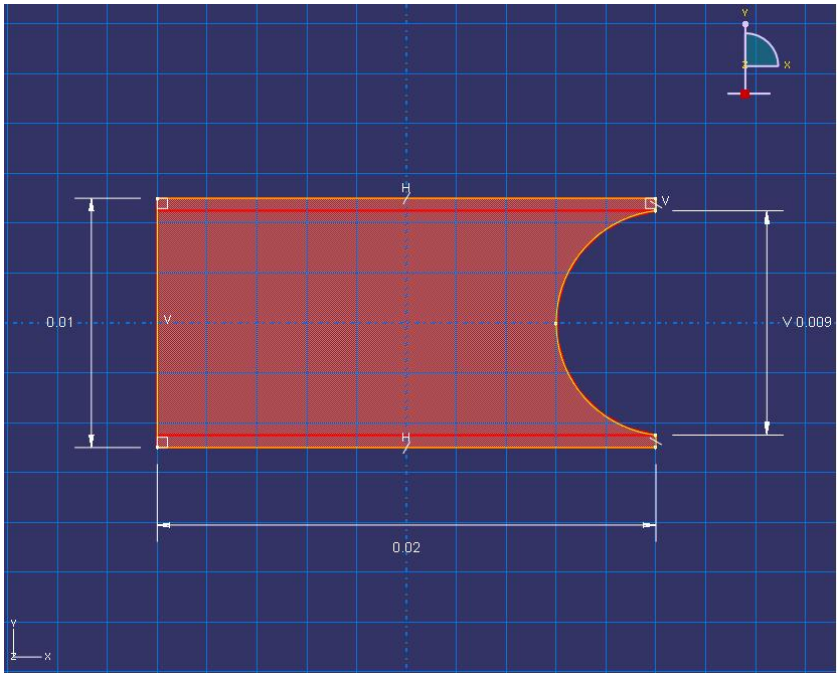

Figure 5.32: *Sketch of the plunger part*

  a Young's modulus of 70 GPa and a Poisson's ratio of 0.35. An 8-node linear brick mesh with reduced integration and hourglass control (C3D8R) was used. The mesh was particularly refined near the interface with the substrate and near the side attached to the ice (figure 5.33).

- a 3D deformable solid part representing the substrate (figure 5.34). The material was titanium with a density of 4430 kg.m^{-3} , a Young's modulus

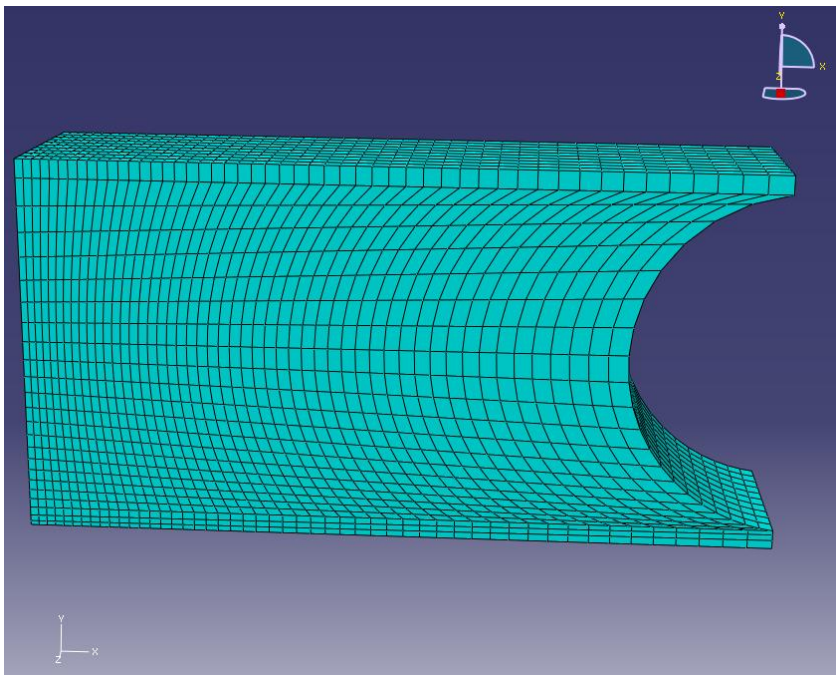

Figure 5.33: *Mesh of the plunger part*

of 113 GPa and a Poisson's ratio of 0.34. The same type of elements as in the plunger was used (C3D8R). The mesh was particularly refined at the interface ice/substrate and plunger/substrate and near the location where the ice is attached to the plunger (figure 5.35).

- a 3D deformable solid part reprensenting the ice (figure 5.36). The ice was modeled with an "L" shape of constant thickness of 3 mm. The ice density is set to 870 $kg.m^{-3}$, the Young's modulus to 13.2 GPa and the Poisson's ratio to 0.31. These values have been chosen as they are an average of the values found during the density and stiffness measurements (see section 4.2 and 4.3) The mesh was particularly refined at the interface ice/substrate and near the side attached to the plunger.
  Like for the two other parts, an 8-node linear brick mesh with reduced integration and hourglass control (C3D8R) was used (figure 5.37).

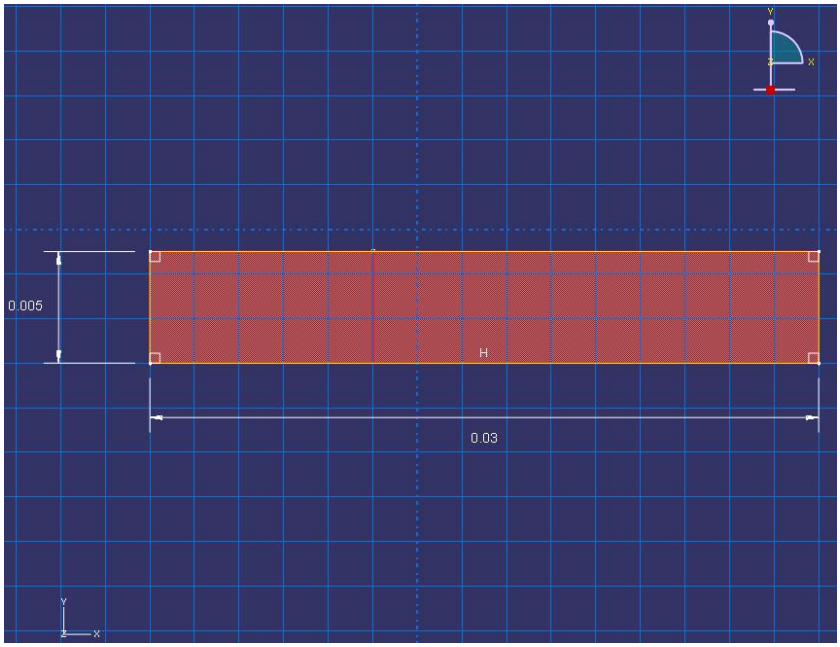

Figure 5.34: *Sketch of the substrate part*

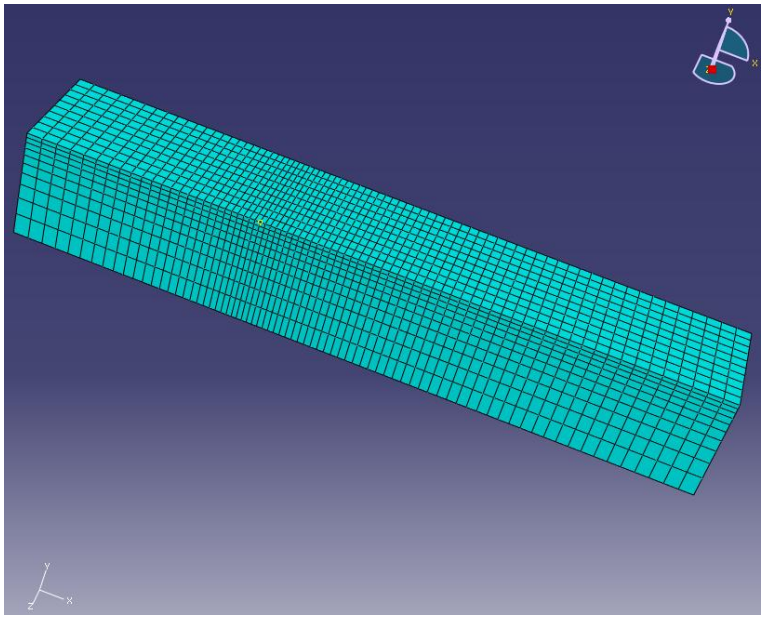

Figure 5.35: *Mesh of the substrate part*

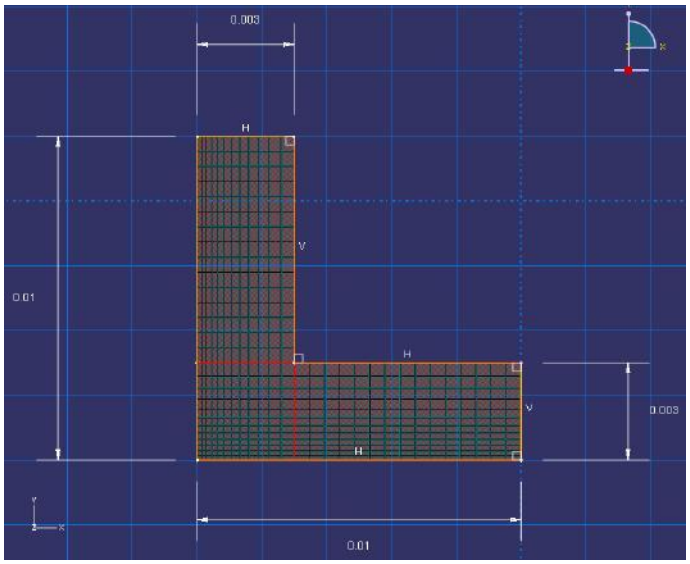

Figure 5.36: *Sketch of the ice part*

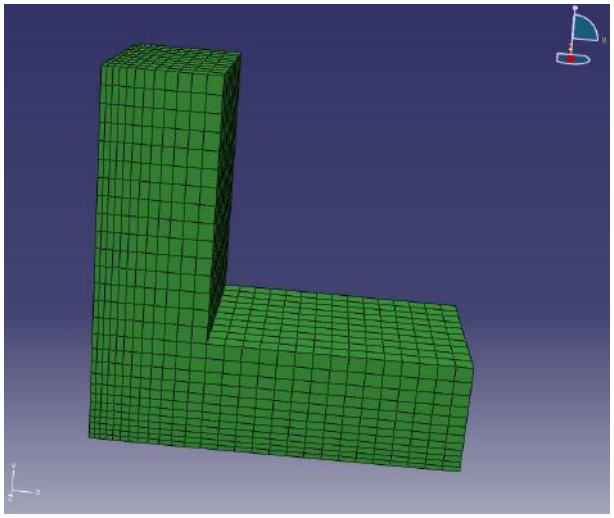

Figure 5.37: *Mesh of the ice part*

The contact between these three parts was defined by one interaction and two constraints. A surface-to-surface contact interaction was set between the plunger and the substrate. These two surfaces were in contact for all the simulation and the plunger was only allowed to slide along the substrate surface. For simplification, no friction was defined between these two surface.
A tied constraint was set between the plunger and the ice. These two parts will stay stuck together throughout the whole simulation.
Another tied constraint was set between the substrate and the ice. This simulation was made to calculate the shear strength of ice corresponding to the pressure needed to remove the ice. The ice was not supposed to be removed until this pressure was reached, hence the ice can be assumed to be completely attached to the substrate for the whole simulation.
During the mechanical test, the gas pressure was inflated the rubber tube which will apply some pressure on the plunger. To simplify the model, the rubber tube was not represented as a separate part and the gas presssure was applied directly on the plunger curved wall. The pressure was assumed to be uniform and a magnitude of 1 MPa was set with a smooth step amplitude to ensure a quasi-static simulation.
Two boundary conditions were set: one to restrict the substrate from any movement (encastre boundary condition on the bottom surface of the substrate) and the other to restrict the plunger movements to only translation in the horizontal direction x (figure 5.38).

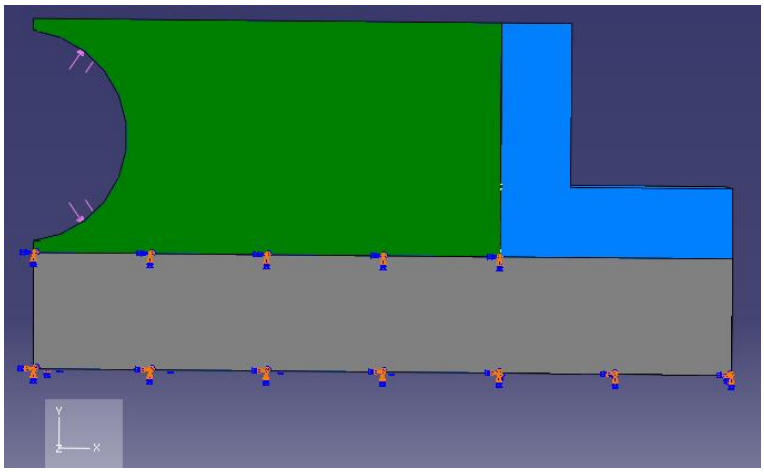

Figure 5.38: *Load and boundary conditions applied on the model*

This whole model was a 3D model but as the width did not have a huge effect on the shear stress distribution, this dimension has been reduced and only a quarter of the piece has been modeled. Figure 5.39 shows that at the middle of

the modeled piece, no effect from the side can be observed on the shear stress distribution.

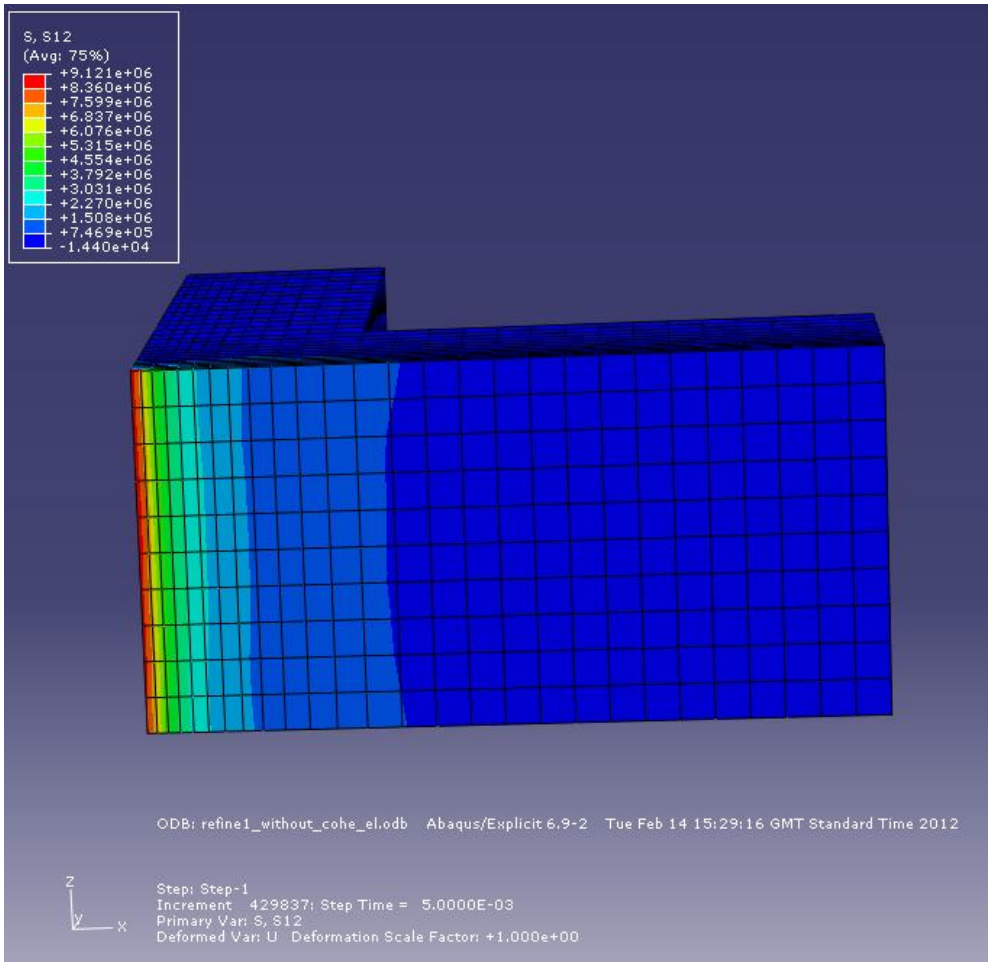

Figure 5.39: *Shear stress distribution at the ice/substrate interface*

5.2.4.2 Finite elements results

As the pressure value increased, the shear stress built up. The shear stress was higher at the edge and gradually decreased along the interface (figure 5.39). A path was set at the middle of the ice's interface (figure 5.40). The values

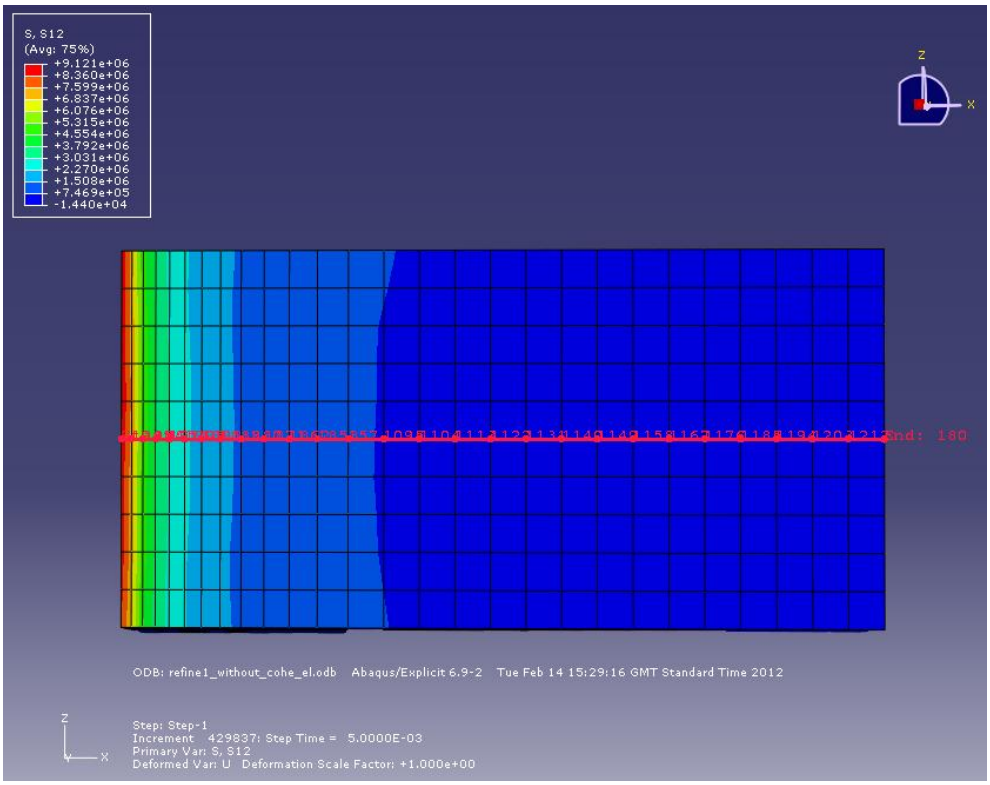

Figure 5.40: *Path at the ice/substrate interface*

of the shear stress along the path were taken. The value similar to the stress intensity factor, K^*_{II}, was calculated from these values by using equation 5.10.

$$K^*_{II} = \tau\sqrt{2\pi r} \tag{5.10}$$

where τ is the shear stress and r is the distance from the edge.
A curve, like the one presented on figure 5.41, was obtained. This curve can be approximated by a polynomial equation. The value for r=0, reprensenting the critical stress intensity at the junction for a crack to grow, is shorthand K^*_{IIc} . This latter can be seen as a material characteristic independent of any external conditions, hence a correlation can be obtained for different critical pressure applied (figure 5.42):

$$K^*_{IIc} = 183727 \times P_c - 1641.8 \tag{5.11}$$

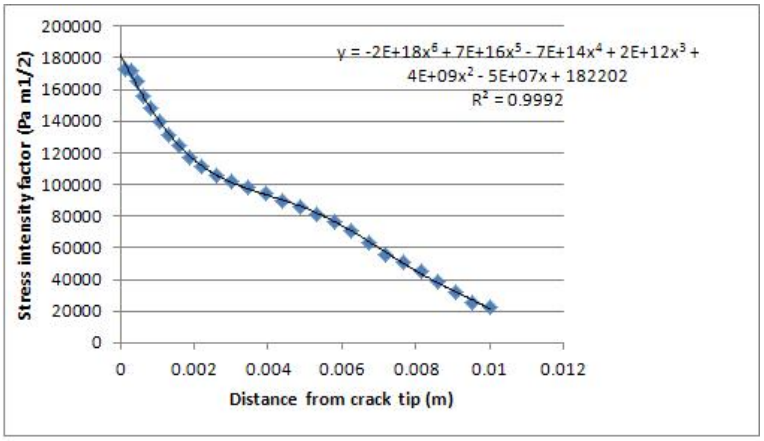

Figure 5.41: *"Stress intensity factor" (K^*_{II}) along the interface*

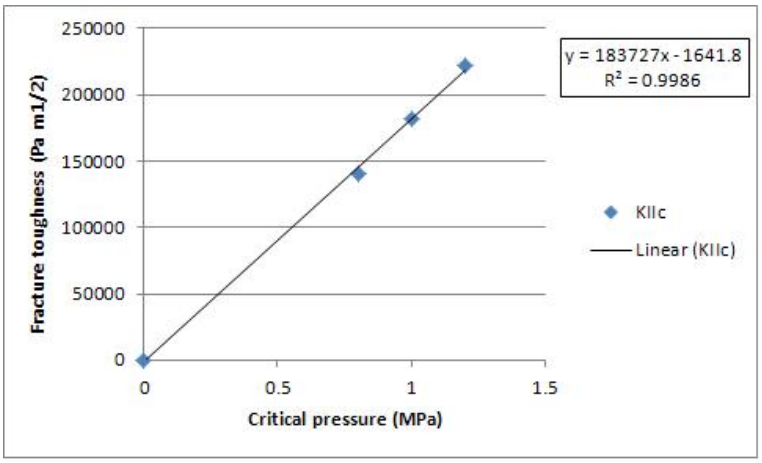

Figure 5.42: *Critical stress intensity at the junction for a crack to grow in function of critical pressure*

From the value of the critical stress intensity and taking the grain size as an indication of material inherent defect size, a shear strength in a bulk of ice can be calculated :

$$\tau = \frac{K^*_{IIc}}{\sqrt{\pi a_g}} \tag{5.12}$$

where a_g is the grain size.

5.2.4.3 Mesh analysis

Different meshes, more or less refined, have been used to check their influence on the results obtained. A more refined mesh will give more accurate results but at the expense of computational time. Figure 5.43 presents the shear stress distribution along a path drawn on the ice part at the ice/substrate interface. The three curves are quite similar to each others. They only

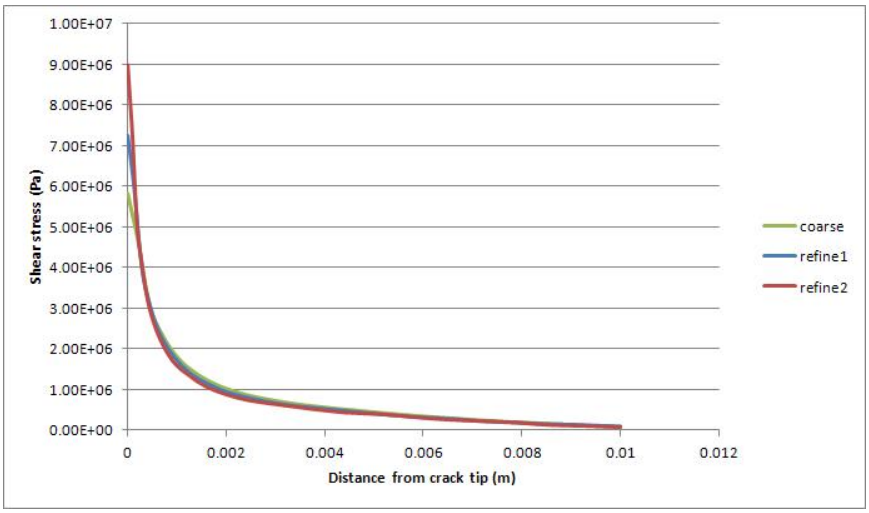

Figure 5.43: *Shear stress distribution along the interface for different meshes*

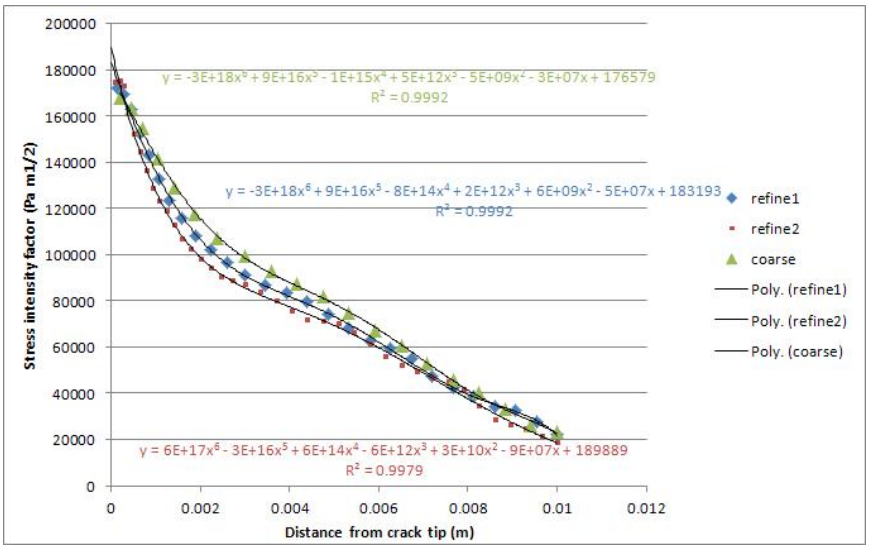

Figure 5.44: *Stress intensity factor along the interface for different meshes*

differs at the edge with the more refined curve showing a higher value at the singularity. However, the graph of figure 5.44 shows that, at the edge, the difference in term of "stress intensity factor" is not so large. The three curves are extremely close to each others. Any of these meshes seems to be good enough for our analysis, therefore the intermediate mesh will be chosen and used for the following.

5.2.5 Results

Each result presented was derived statistically from five or more shear tests performed in the same condition. Shear strength was obtained using the correlation presented in the previous section and the average grain size measured during the microstructure observations. Assumptions have been made that the Young modulus, the Poisson ratio and the density of the ice did not vary significantly with tunnel temperature, tunnel wind speed or LWC. The values used were 13.2 GPa, 0.31 and 870 $kg.m^{-3}$ respectively.

5.2.5.1 Influence of temperature

The temperature referred to is the ambient total temperature inside the tunnel. It was set prior to the ice accretion process and was kept constant during the formation and the mechanical testing of the ice. The runs made to investigate the influence of temperature have been made using a low and a moderate value of the LWC (respectively 0.4 $g.m^{-3}$ and 0.7 $g.m^{-3}$). The tunnel wind speed and the droplet size were kept constant at 50 $m.s^{-1}$ and 20 μm respectively for the whole series of experiments. Two different substrates have been tested. Both were made of titanium, one had a mirror polished finish and the other had a more realistic finish (comparable to the state of newly made, clean fan blades). However, no information about the microstructure of the ice grown on the more realistic surface finish titanium substrate were available at the present time. Hence, only the results on the mirror polished surface will be presented here.
In both cases, the shear strength has been found to increase as the temperature decreases in the range of temperature from -2°C to -12°C (figures 5.45 and 5.46).
The values obtained in these tests lied in a range between 2 and 13.6 MPa which is a lot higher than the values found in the literature. At a temperature of -10°C, values less than 500 kPa were usually reported by previous authors. In the present study, the ice was sheded from its substrate in exactly the same conditions as during its formation; meaning that no redistribution of thermal stresses has been involved within the ice. Also the shear force reported relates

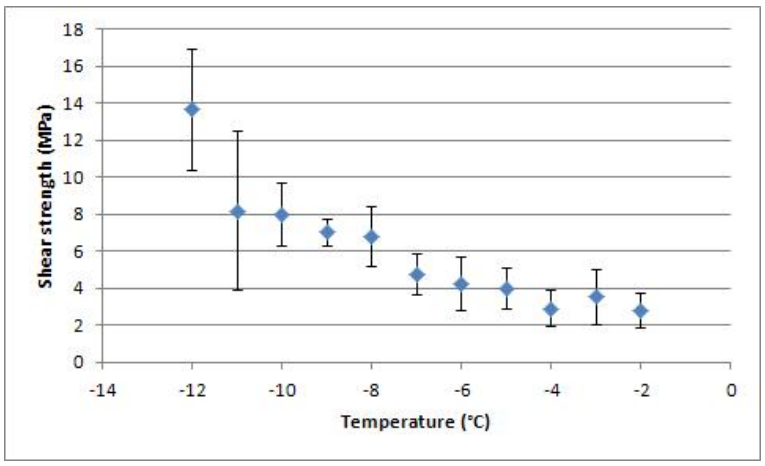

Figure 5.45: *Effect of temperature on the shear strength of ice (LWC=0.7*g.m^{-3} *)*

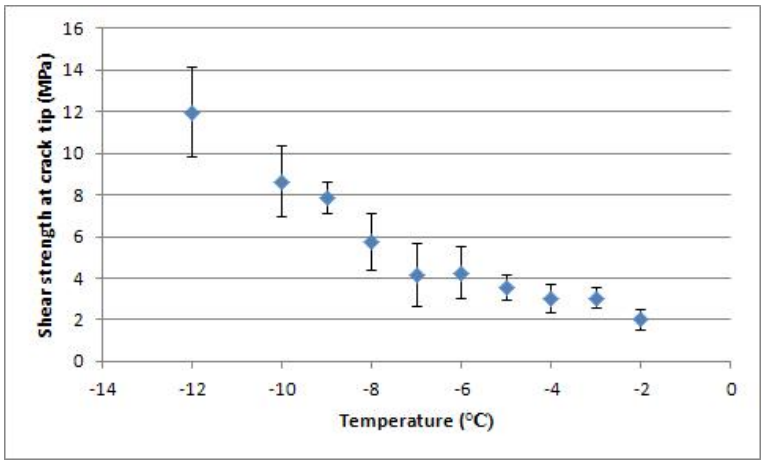

Figure 5.46: *Effect of temperature on the shear strength of ice (LWC=0.4*g.m^{-3} *)*

to the peak shear force where fracture initiates (edge), not the mean force/area factor usually used. Shear stress is decreasing as the distance from the edge increases meaning that an average value would be lower than the value at the edge. An average value of the shear strength has actually been calculated using equation 5.9. Values obtained lied in the range between 0.4 to 1.6 MPa which were closer to the values obtained by the previous authors.
The trend of adhesive shear strength to increase with decreasing temperature is relatively comparable with the previous studies. Druez et al. (1978, 1986), Chu and Scavuzzo (1991), Scavuzzo et al. (1996), Scavuzzo and Chu (1987),

Stallabrass and Price (1962) and Fortin and Perron (2009) reported an increase in shear strength as the temperature decreases with either a constant or a maximum value reached at a certain temperature.

5.2.5.2 Influence of Liquid Water Content (LWC)

A series of tests has been conducted where the LWC of the cloud has been modified while keeping the tunnel total temperature, wind speed and droplet size constant at respectively -5°C, 50 m.s^{-1} and 20 μm. Five different values of LWC have been tested from 0.4 to 0.8 g.m^{-3} (figure 5.47). In this range of LWC, a general increase of the shear strength has been observed as the LWC increases. Druez et al. (1986) conducted experiments with two different

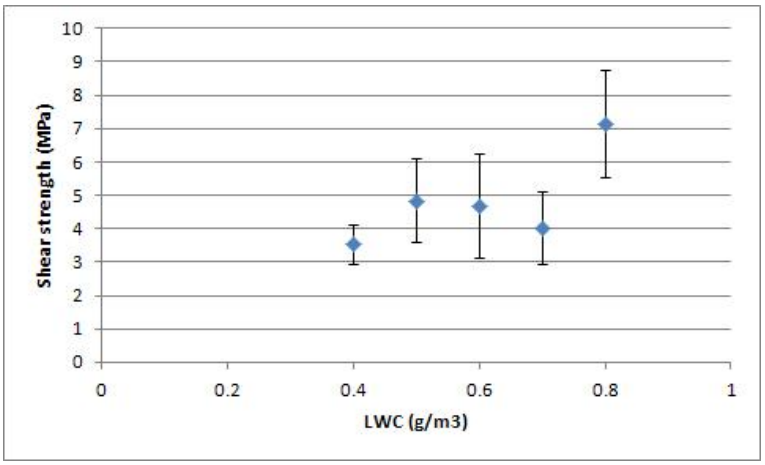

Figure 5.47: *Effect of LWC on the shear strength of ice (T=-5° C, V=50* m.s^{-1} *, MVD=20* μm *)*

LWC and droplet sizes. He reported that an increase in this combination of parameters results in an increase in the adhesive shear strength. The same kind of observation was made by Petrenko (2006) who concluded that adhesive shear strength increases with LWC in the range from 0.3 to 2.4 g.m^{-3}. In these two studies, the wind velocity used was much lower than in the present experiments (between 8 and 20 m.s^{-1} for Druez, 20 m.s^{-1} for Petrenko and 50 m.s^{-1} for this study).

5.2.5.3 Influence of tunnel wind speed

In the same way as for the previous parameters, the tunnel wind speed has been modified while the temperature, the LWC and the droplet size are kept

constant at respectively -5°C, 0.4 g.m^{-3} and 20 μm . Different values have been tested from 50 to 80 m.s^{-1} with the mirror polished surface finish (figure 5.48). In this range, the adhesive shear strength of ice is increasing as the tunnel

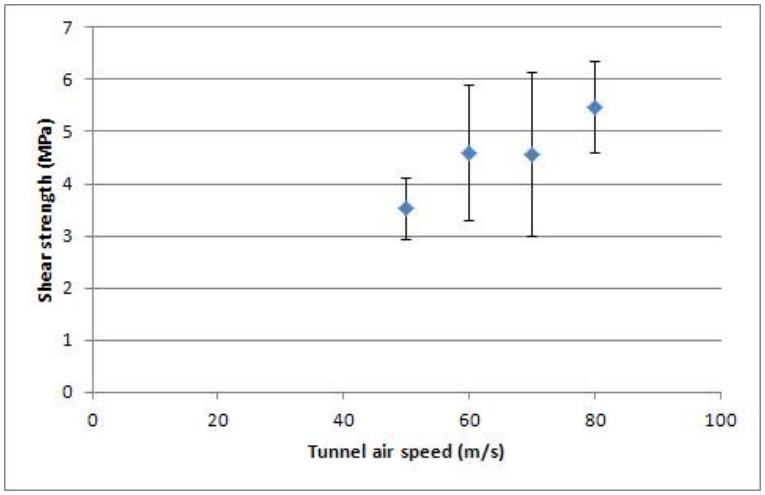

Figure 5.48: *Effect of tunnel wind speed on the shear strength of ice*

wind speed is increasing.
Druez et al. (1978) reported an increase of shear strength with speed from 4 to 16 m.s^{-1} which level up until 20 m.s^{-1} . Chu and Scavuzzo (1991) also found a small increase of shear strength with speed between 20 and 90 m.s^{-1} but the trend is not obvious due to scatter.

5.2.5.4 Influence of surface roughness

The afore mentioned results have been obtained from mechanical tests carried out on well polished titanium. Some preliminary work on the effect of the substrate surface finish has been made by finishing the titanium surface with coarse grinding paper. This resulted in the appearance of groves in the horizontal or vertical direction (figure 5.49). No microstructure observations have been made for the ice accreted on these surface so, in order to compare the influence of substrate surface roughness, the average adhesive shear strength will be calculated in this section.
In general, the average shear strength is seen to increase as the roughness increases and higher values have been found for the horizontal stripes rather than with the vertical stripes. On figure 5.50, the numbers “500“ and “800“ represent the grit of the silicone carbide paper and the letters, V and H, stands for vertical and horizontal respectively as shown in figure 5.49.

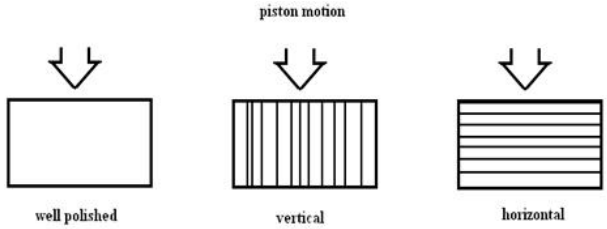

Figure 5.49: *Representation of the different roughness on the substrate surface*

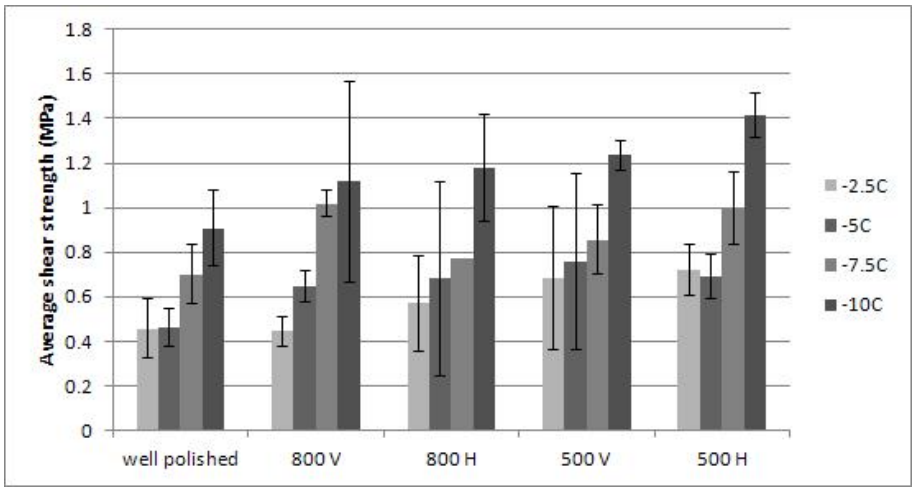

Figure 5.50: *Effect of substrate roughness on the adhesive shear strength of ice*

The increase in shear strength with the roughness was expected as the ice is assumed to stick more to a rough surface than a smooth surface. In the case of shear especially, ice is thought to slide more easily when accreted on a smoother surface.
The authors who have studied the effect of surface roughness reported an increase in adhesive shear strength as the roughness increases up to a certain value at which further increase in roughness has no influence on the adhesive shear strength (Druez et al., 1978; Chu and Scavuzzo, 1991; Scavuzzo et al., 1996; Scavuzzo and Chu, 1987; Laforte and Beisswenger, 2005).
Further study should be conducted with a better knowledge of the surface roughness.

5.2.6 Further analysis with finite elements

Another finite elements model has been built using a layer of cohesive elements to simulate the attachment of ice on the substrate. This model is very useful

to determine the instant of ice detachment however the results, especially in the shear stress distribution, are totally different.

5.2.6.1 Model

The model with the cohesive elements is similar to the model with the bonded nodes presented previously (section 5.2.4.3). It is composed of three parts:

- a 3D deformable solid part representing the plunger which is identical to the previous model
- a 3D deformable solid part representing the substrate (also identical to the previous model)
- a replicate of the mesh (called orphan mesh in the software) of a 3D deformable solid part reprensenting the ice (figure 5.51). The ice is modeled

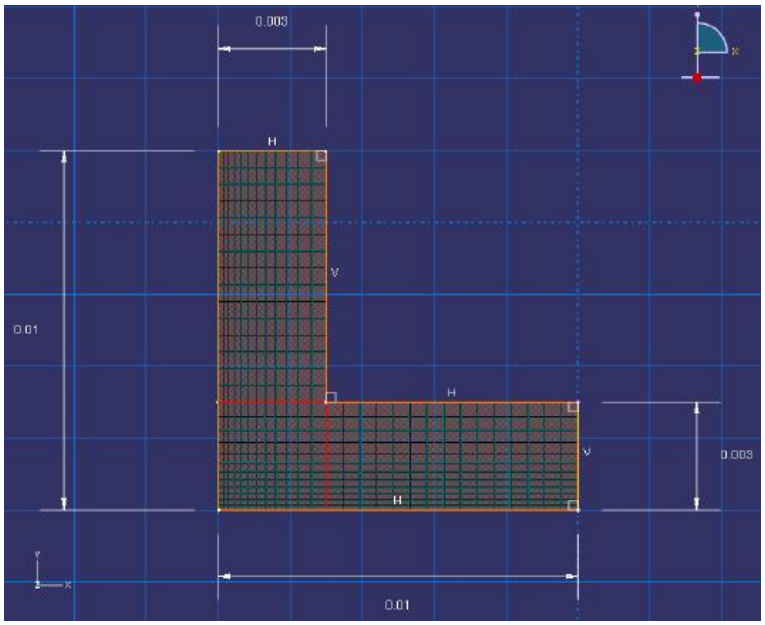

Figure 5.51: *Sketch of the ice part*

with a "L" shape of constant thickness of 3 mm. The ice density is set to 870 kg.m^{-3}, the Young's modulus to 9 GPa and the Poisson's ratio to 0.31. The mesh is particularly refined at the interface ice/substrate and near the side attached to the plunger.
A layer of cohesive element of zero thickness was embedded in the bottom face of the ice (at the ice/substrate interface). This layer is non-physical

but is acting like a glue between the ice and the substrate. During the simulation, if the shear stress between the ice and the substrate is greater that the value set in the cohesive element material properties, the corresponding cohesive element is removed and the ice is not attached to the substrate anymore.
Like for the two other parts, an 8-node linear brick mesh with reduced integration and hourglass control (C3D8R) was used for the mesh representing the ice and an 8-nodes three dimensional cohesive element was used for the cohesive layer (figure 5.52).

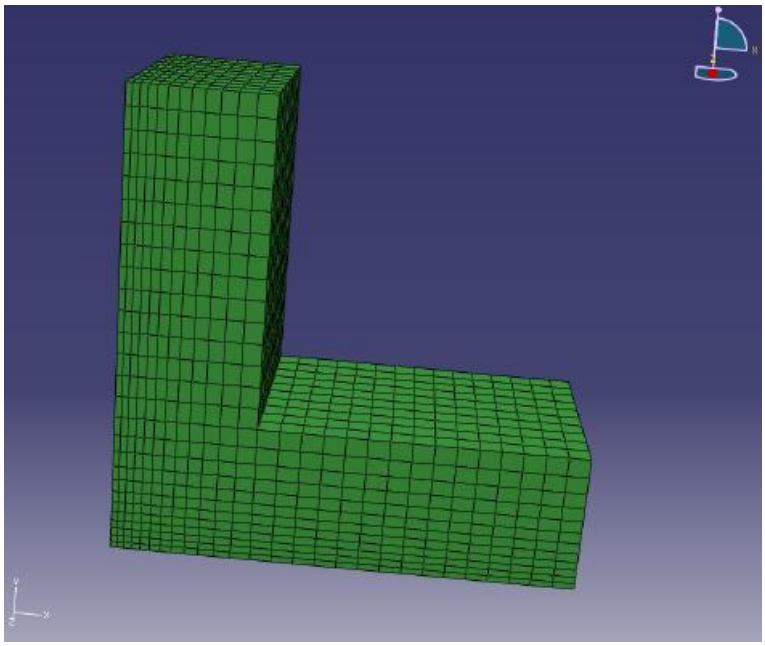

Figure 5.52: *Mesh of the ice part*

As the cohesive layer is very thin, a traction-separation based model was chosen. The problem is only shear so there are no coupling effects between the normal and shear components and the elastic matrix can be described with the traction option. A value of 100 GPa is set for the three components of the penalty stiffness which represents ten times the stiffness of the ice.
The maximum nominal stress criterion (Maxs damage) was chosen for the damage initiation criterion. This criterion assumes that when the stress in one direction reaches the maximum value set, damage initiates. As this problem is purely about shear stress, this criterion is sufficient. In case of a more complex problem involving normal and shear stresses, the quadratic nominal stress condition would have been chosen (Quads damage). A nominal stress value

of 1.5 MPa in the normal mode and 1 MPa in the first and second direction was set. A damage evolution criterion based on energy was chosen with a linear softening and a mode-independent mixed mode behaviour. The fracture energy value was set to 1 $J.m^{-2}$.
The density of the cohesive elements was set to 1000 $kg.m^{-3}$ which is a density value close to the one of the ice.
The contact between these three parts was defined by one interaction and two constraints. A surface-to-surface contact interaction was set between the plunger and the substrate. These two surface are in contact for all the simulation and the plunger is only allowed to slide along the substrate surface. For simplification, no friction was defined between these two surfaces.
A tied constraint was set between the plunger and the ice. These two parts will stay stuck together throughout the whole simulation.
Another tied constraint was set between the substrate and the cohesive element layer. As the elements of the cohesive layer disappear during the simulation, this constraint will be removed and the ice will be free to slide over the substrate surface.
During the mechanical test, the gas pressure inflates the rubber tube which will apply some pressure on the plunger. To simplify the model, the rubber tube is not represented and the gas presssure is applied directly on the plunger curved wall. The pressure is assumed to be uniform and a magnitude of 2 MPa is set with a smooth step amplitude to ensure a quasi-static simulation.
Two boundary conditions were set: one to restrict the substrate from any movement (encastre boundary condition on the bottom surface of the substrate) and the other to restrict the plunger movements to only translation in the horizontal direction x (figure 5.53).
Like in the bonded nodes model (see section 5.2.4.3), only a quarter of the piece has been modeled.

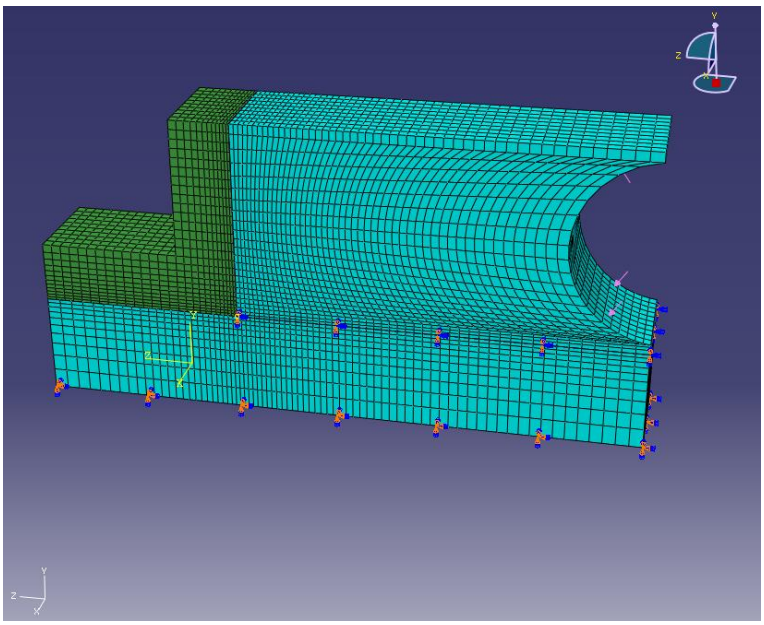

Figure 5.53: *Load and boundary conditions applied on the model*

5.2.6.2 Finite elements results

As the pressure value increases, the shear stress builds up. The shear stress is higher at the crack tip and gradually decreases along the interface. When a value of 1 MPa (value set in the cohesive elements material properties) is reached, the cohesive elements break and disappear. A crack as been initiated. As the crack propagates, the peak of shear stress moves to the end opposite from the crack tip and the cohesive elements become removed. The ice piece is then free to move and slide along the substrate as the pressure is still applied to the ice.
The quasi-static condition during the simulation is checked by visualizing the kinetic and internal energy. During a quasi-static simulation, the kinetic energy should be less than 5% of the internal energy (Riahi, 2007). Figure 5.54 shows that before the ice debounding the kinetic energy is much smaller than the internal energy.

5.2.6.3 Mesh sensitivity analysis

Different meshes, more or less refined, have been used to check the influence of mesh density on the results obtained. A more refined mesh will give more accurate results but at the expense of computational time. Figure 5.55 presents the shear stress distribution along a path drawn on the ice part at the ice/substrate

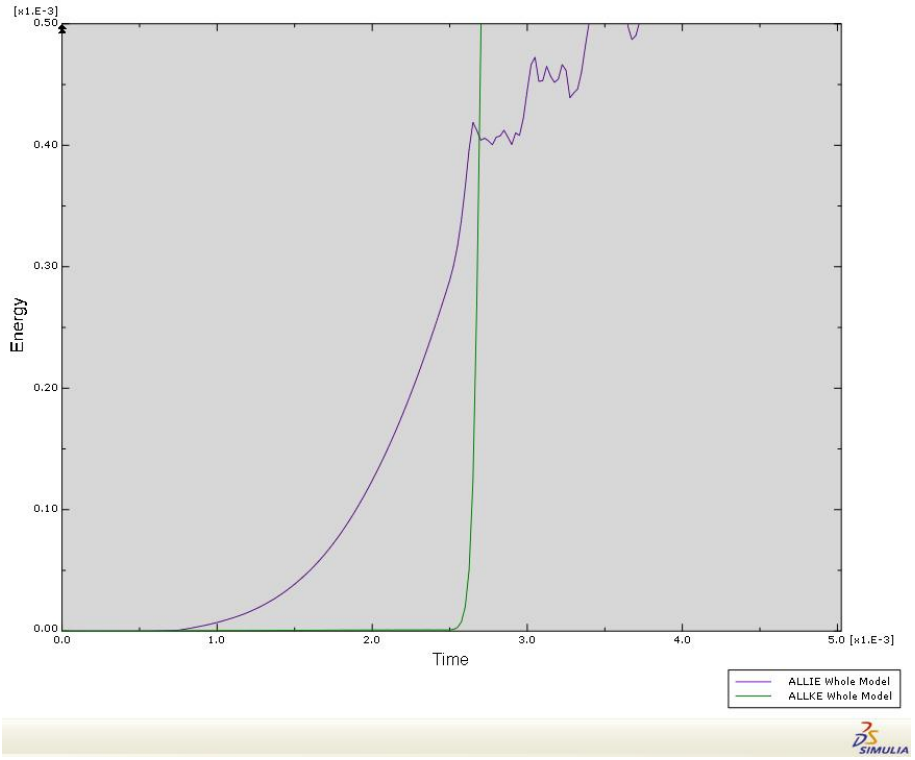

Figure 5.54: *Kinetic (ALLKE) and internal (ALLIE) energy throughout the whole simulation*

interface. The three curves are quite similar to each others. The coarse mesh gives results slightly lower than the two others however the instant of shedding and the critical pressure are identical with the three meshes. The intermediate mesh seems to be the best compromise results/computational time. Therefore the intermediate mesh will be used in the following analysis.

5.2.6.4 Investigation of the influence of input parameters

Different parameters are used for the finite element analysis. Some of them are known and are well defined like the material properties of the substrate (in our case titanium), others, like the ice properties, are less well known. Indeed the ice properties of atmospheric ice are dependent on the growth condition of the ice and are not extensively discussed in the literature. This investigation will show which parameters have an influence on the finite element results and which have none.
In this model, the initiation of the crack is determined by the delamination of the first cohesive elements. This means that, looking at the simulation frame

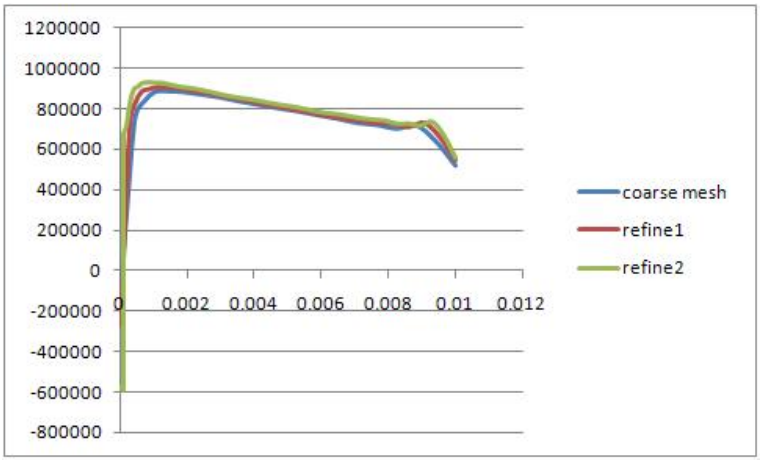

Figure 5.55: *Shear stress distribution along the interface for different meshes*

by frame, the initiation is assumed to happen in the frame previous to the one showing the first deleted cohesive element. The critical pressure and the time to break related to this specific frame are recorded.
The variation of the Young's modulus of ice has been found to result in a variation of both the critical pressure and the time to break (figure 5.56). These two quantities increase, respectively, by 15% and 9% while the Young's

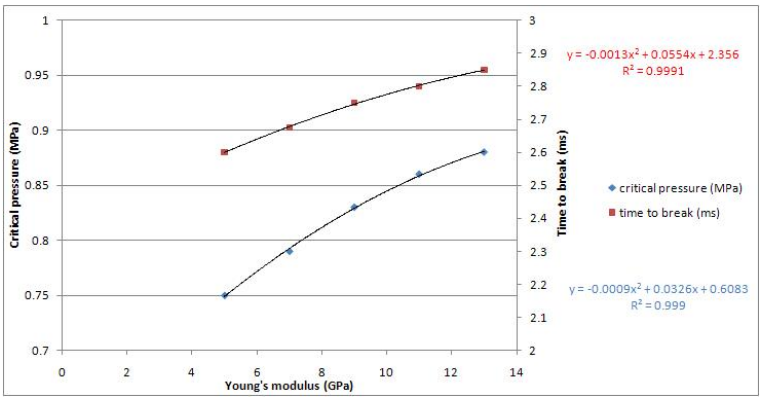

Figure 5.56: *Influence of the Young's modulus of ice on the critical pressure and the time needed to break the ice*

modulus increases by 6% in the range from 5 to 13 GPa.
The variation of either the ice density or the fracture energy (parameter defined in the cohesive elements material properties) have been found to have no effect at all on the critical pressure or on the time to break.
On the other hand, the penalty stiffness (another parameter of the cohesive

elements material properties) have been found to have a massive influence on the overall results. Figure 5.57 shows the variation of critical pressure with the penalty stiffness. It can be seen that at high value of penalty stiffness,

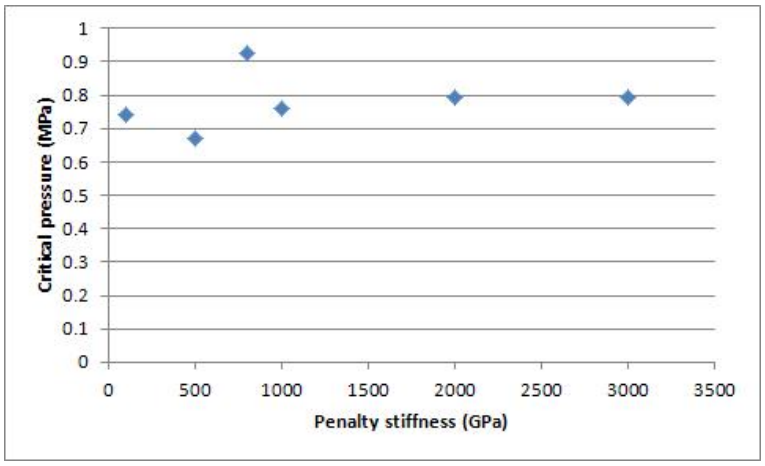

Figure 5.57: *Influence of the penalty stiffness value on the critical pressure*

the critical pressure becomes independent of this quantity. However, looking at the shear stress distribution along the interface, the highest values of shear stress have been obtained in the middle of the ice piece and not at the edge as it would be expected (figure 5.58). Even by using the highest value of the penalty stiffness allowing the highest value of the shear stress to be near the crack tip, a comparison of the shear stress distribution along a path at the ice/substrate interface, obtained from the bonded-nodes model with those obtained from the cohesive elements model shows a great discrepency (figure 5.59). The use of cohesive elements is a way to get rid of the singularity at the edge, therefore, values near the edge are lower with the cohesive elements model. As we go further from the edge, the bonded-nodes model presents a significant decrease of shear stress while, for the cohesive elements model, the decrease is very small and even seems to be a constant value.
Even if the cohesive elements model seems really useful to model shedding, this model is difficult to be trusted to determine the value of shear strength at the edge. That is why the model with the bonded nodes was chosen for the analysis of the results from the shear test experiments.

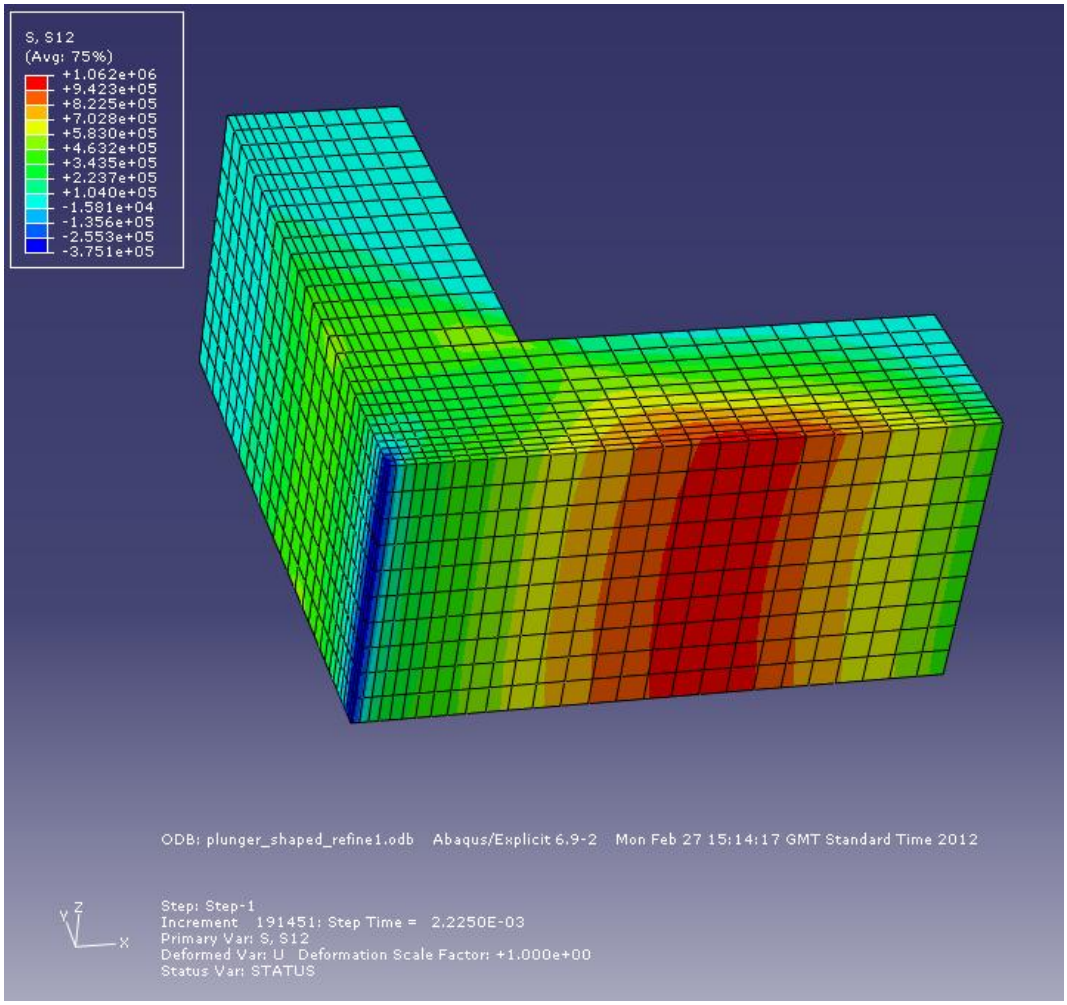

Figure 5.58: *Shear stress distribution at the ice interface for a high value of penalty stiffness*

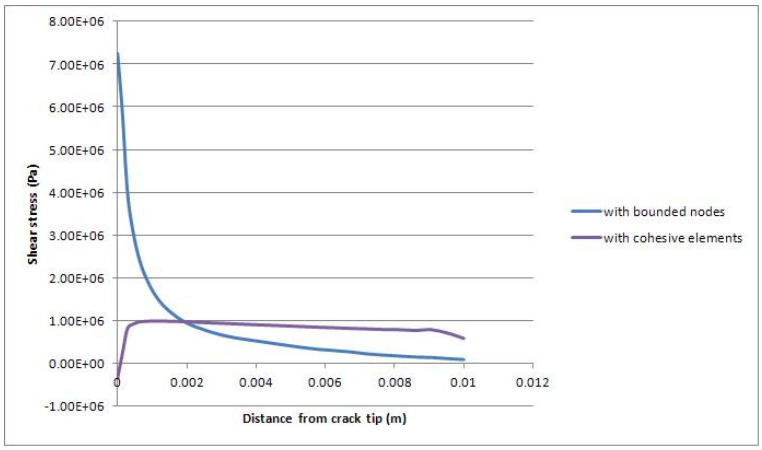

Figure 5.59: *Comparison of the shear stress distribution at the ice interface between the bounded nodes and the cohesive elements model*

Chapter 6

Ice shedding

The following work was based on an ice shedding mechanism due to centrifugal loading in a two steps process. First, the loading is inducing shear stress with higher values at the tip than at the hub. Then, after initiation and propagation of a crack at the interface ice/blade, tensile stress is increasing until a crack initiates and propagates through the ice (figure 1.2 in chapter 1). Several authors have also studied the process of ice shedding from a rotating blade either for aircraft or helicopter applications. Their work has been described in the following section.

6.1 Previous work

Itagaki (1983) carried out an analysis on the balance of forces involved in the shelf-shedding process of ice on a rotor blade. He assumed that both normal tensile stresses and interface shear stresses are acting on ice accreted on blades. According to him the ice will fall off the blade when the stress due to the centrifugal force is higher than the addition of tensile and shear strength. Assuming that the accreted ice has a uniform cross-sectional area along the rotor blade, expression of the tensile strength and adhesive shear strength can be obtained.

$$Ts = \frac{\omega^2 \rho_i \, (R - r)^2}{2} \tag{6.1}$$

$$\tau = \omega^2 \rho_i \, h \, r \tag{6.2}$$

where Ts is the tensile strength, ω the rotational speed, ρ_i the density of ice, R the rotor's radius, r a radial position on the airfoil, τ the adhesive shear strength and h the ice thickness (Itagaki, 1983).

These expressions are for the minimum tensile and shear strength needed to shed the ice from the rotor blades. Laboratory experiments were conducted where self-shedding was observed and tensile and adhesive shear strengths calculated using equation 6.1 and 6.2. Their results show that the tensile strength is higher for slow accreted ice (1 to 2 MPa) compared to more rapidly grown ice (400 to 600 kPa). On the contrary, they report that adhesive shear strength is higher for rapidly grown ice.
Itagaki has also found from experiments that the ice thickness varies with radial position. A maximum thickness is obtained at 2/3 of the radial length of the rotor and then the thickness decreases to the tip. This non uniformity of the ice layer could explain the difference between the values found with equations 6.1 and 6.2, and the previous experiments.
Scavuzzo et al. (1994) carried out some finite element analysis to determine the importance of aerodynamic loads compared to shear strength experimental values. They have modeled an NACA0012 airfoil with a typical accretion of glaze ice. They reported that when the air velocity is less than a Mach number of 0.45, the stresses are insignificant. At a Mach number of 0.6, the maximum shear stress due to aerodynamic forces represents 20% of the shear ultimate debonding strength. Shear stresses due to aerodynamic forces also increase with angle of attack. Hence at high speeds and high angle of attack aerodynamic loads have to be considered in the calculation of ice shedding prediction.
Scavuzzo et al. (1996) have used a finite element analysis and a statistical structural analysis to predict the ice shedding from a rotating beam. Their finite element analysis is based on the basic assumption that the strains in the rotating airfoil are developed before ice accretes on the beam. The airfoil has been considered rigid as the stiffness of the airfoil is greater than the one of the ice. The results show a stresses distribution different from Itagaki. For a uniform layer of ice on a rigid spinning airfoil, there are no normal stresses in the ice layer. Only the shear stress is present and its value increases from the hub to the tip with a maximum value at the ice/substrate interface.The shear stress, τ, increases linearly with the radial position on the airfoil, r, and the ice thickness, h (equation 6.3).

$$\tau = \rho_i \omega^2 r h \tag{6.3}$$

As long as there is continuous adhesion of ice with the blade, the shear strength is the dominating factor. When a crack appears, between the ice and the substrate, and increases in length, adhesive shear stress increases as well as the tensile stress. The tensile stress increases faster than the adhesive shear stress and is responsible for the failure, according to Scavuzzo et al. (1996), after a propagation of approximately one inch of the shear crack.

To sum up, according to Scavuzzo et al.'s finite element analysis, the shear strength is responsible for the initiation and propagation of the crack and the tensile strength is responsible for the failure and the shedding of the ice.
Miller and Bond (1989) carried out experiments on a helicopter tail rotor in an icing tunnel. The shaft of the rotor was driven by an electric motor which allows the rotational speed to be controlled. The incidence of shedding events where determined by the vibration output and rotor torque records. Ice thickness has been measured at various chord locations.
The tunnel controls were first set to the desired parameters. Then the tail rotor was brought to a nominal operating rotational speed and the tunnel was started up. Finally water was sprayed on the rotor blades. At the end of the run, the tunnel wind speed was brought to idle and then the tail rotor speed was reduced to zero.
In all cases, ice accretion on the blades produce a torque rise which was linear with time for a fixed set of conditions. Figure 6.1 presents the variation of the torque with time in case of multiple shedding. The torque increased when ice

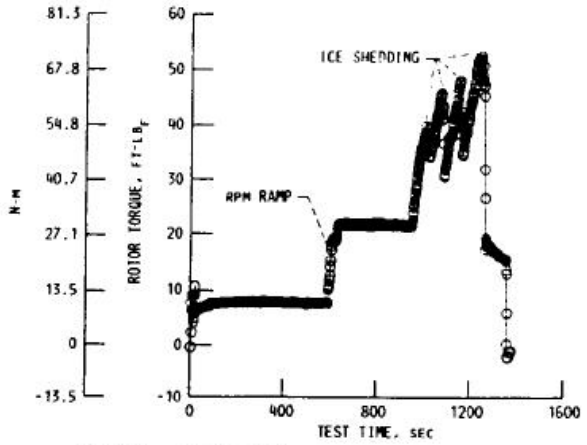

FIGURE 6. - ROTOR TORQUE VERSUS TEST TIME. 2100 RPM, T = 5.4 MIN. 15 μM. 31.3 M/S. -9.4 ^{0}C. .5 g/m^3, θ_{75} = 4^0.

Figure 6.1: *Variation of torque during one run - T_a=-9.4°C, MVD=15 μm, LWC=0.5* g.m^{-3} *, V=31.3* m.s^{-1} *, ω=2100 RPM, run lasted 5.4 min (Miller and Bond, 1989)*

accretes on the rotor blades. When shedding occurred, the torque dropped, then, as ice continue to accrete, it rose again until the next shedding event occurred. According to Miller and Bond, if the accretion was allowed to continue long enough, shedding and accretion would roughly balanced each other out and torque would reach an equilibrium value.

The presence of ice on rotor blades increases vibration due to addition of uneven mass on the blades and distortion of the flow around the blades' leading edge. Accretion is always symmetrical, so, at the beginning, vibrations rise gradually. When shedding occurs, vibrations can either decrease if the ice shed symmetrically or increase if shedding occurs only in one blade.
At the coldest temperature tested (-26.1°C), no shedding occurred. At the warmest temperature and most dense cloud condition (T_a=-6.7°C, MVD=10 μm , LWC=0.25 g.m^{-3}), ice shed, outboard of 85% of the blade length, several times during the run. At a temperature of -15°C, a LWC of 0.5 g.m^{-3} and a MVD of 15 μm , ice accreted over the entire blade leading edge and shed from the outer 30% of the blade length. At the same temperature but lightest cloud conditions (0.25 g.m^{-3} and 10 μm), no shedding was reported as the mass of ice accreted was not enough for the centrifugal force to be higher than the adhesive force of ice.
Temperature, LWC and MVD have a significant effect on ice accretion and shedding as they influence the ice type and the transition location from glaze to rime ice. The rotor rotational speed has also an important effect on the type of ice accreted on the blades. As the rotational speed was increased, the local velocity at some radial part of the blade increased and more glaze ice was formed. Therefore the transition rime to glaze ice was shifted further inboard on the blade. At a temperature of -15°C, a LWC of 0.5 g.m^{-3} and a MVD of 15 μm , no shedding was observed at rotational speed of 1200 and 1700 RPM. At 2100 RPM, shedding began to occur but only at the end of the run when the spray was switched off and the air turbulence changed.
Visual observations show that striae were present in most of the ice shapes. These lines were vertical in the inboard part (30 to 50%) of the blade and become more spanwise orientated in the outboard part. According to Miller and Bond, a chordwise crack would form in the ice at the radial position and once that crack has fully developed, the tensile strength decrease to zero. If the centrifugal force on the outboard ice piece was high enough to overcome the ice bond force, the ice would exit the blade in the radial direction (figure 6.2).
Fortin and Perron (2009) have set a series of experiments in order to understand the physics of ice adhesion and shedding and to study hydrophobic and icephobic materials. Their apparatus, called the Spinning Rotor Blade (SRB) apparatus, is a sub-scale model of the main and tail rotor of an helicopter. This model placed in an icing wind tunnel will be able to provide useful information on ice shedding and its effect of ice on power, RPM, torque, trust variation, etc.
The SRB is composed of two blades, NACA0012 profile, made of aluminium alloy 6066-T6, with a chord of 69.64 mm and a length of 315 mm. Before each

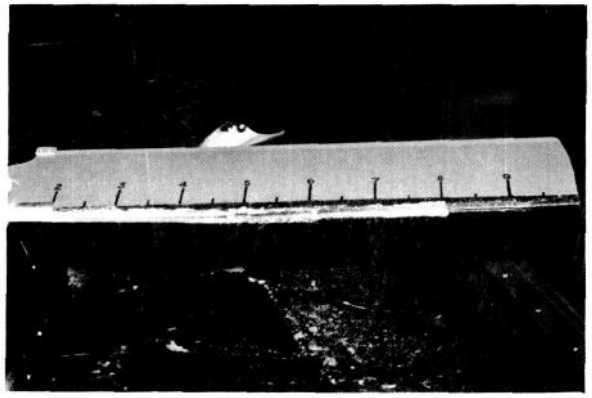

Figure 6.2: *Helicopter blade leading edge after ice accretion and shedding - T_a = -9.4°C, 0.5* $\mathrm{g.m^{-3}}$ *, 15* μm *, 2100 RPM, 31.3* $\mathrm{m.s^{-1}}$ *, run last 5.4 min (Miller and Bond, 1989)*

test the blade surface was resurfaced using 3M scotch brite. The LWC was set at 0.842 $\mathrm{g.m^{-3}}$, the droplets MVD at 26.7 μm and the air speed at 15 $\mathrm{m.s^{-1}}$. The blade was placed with a pitch angle of 6 ° and the rotational speed was set at 3240 RPM. Shedding event was determined by monitoring the power needed to rotate the blades at the same speed. As ice builds up on the blades, the power increases and when a piece of ice shed, the power suddenly decreases. The test was then stopped and measurements were taken on the length and the position of the piece of ice which had shed.
Pictures were taken through the duration of the test to analyse the ice accretion along the blade. The ice thickness at the stagnation point was found to grow almost linearly from the hub to the tip. The shape of the ice at the hub was reported to be stream wise and to have a milky appearance which is characteristic of rime ice. While at the tip, the ice was described as trapezoidal in shape with small double horns which is characteristic of glaze ice (figure 6.3).

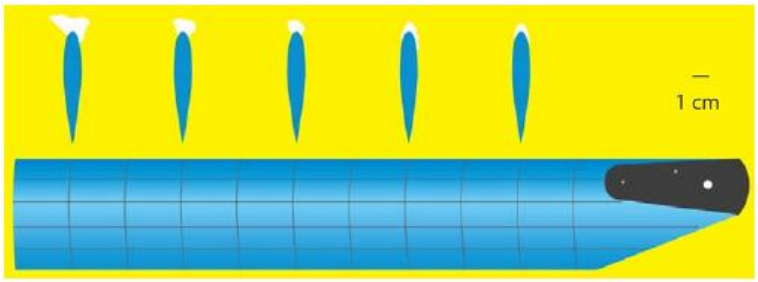

Figure 6.3: *Ice section along the span (Fortin and Perron, 2009)*

Experiments were conducted at four different temperatures between -5 and -20°C and on a coated blade (with icephobic coating) at -15°C. Results are presented in table 6.1. The ice thickness at the tip was reported to increase

Parameters	-5°C	-10°C	-15°C	-20°C	Coating A (-15°C)
Power at shedding (W)	2492	4704	5085	4081	3216
Shedding time (s)	82	105	130	163	74
Ice shedding length (mm)	123	111	70	36	64
Ice thickness at tip (mm)	2.9	4.6	7.9	11.3	3.7
Adhesive shear stress (MPa)	0.07	0.12	0.21	0.26	0.10

Table 6.1: *Shedding results of the SRB tests (Fortin and Perron, 2009)*

dramatically as the temperature was decreased. This effect is due to the freezing fraction of ice which is low at -5°C and about 1 at -20°C. At -5°C, only part of the water impinging the blade freeze whereas at -20°C all the water become ice. The shedding time was found to double between the ice accreted at -5°C and the ice accreted at -20°C which indicates a stronger ice at lower temperatures. This observation is reinforced by the adhesive shear stress values which are higher at lower temperatures and the ice shedding length which is smaller at lower temperatures. Figure 6.4 illustrates these observations where it can

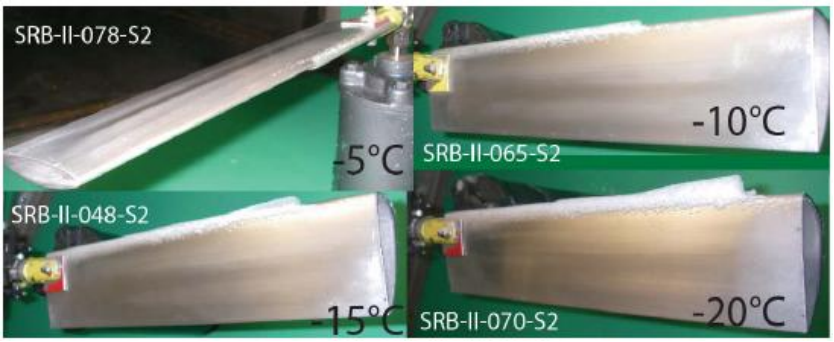

Figure 6.4: *View of the iced blade at different test temperatures (Fortin and Perron, 2009)*

be seen that at -5°C almost all the ice on the blade has shed whereas at -20°C only a small portion of the ice has been removed.

6.2 Rolls-Royce development test

Rolls-Royce certification tests were carried out in Manitoba (Canada) on the Trent XWB. This engine has a fan tip radius of 1499 mm and a fan hub radius of 399 mm. For a Rolls-Royce three shafts engine the range of speed critical for icing conditions is between 100 and 200 rad.s^{-1}.
The certification tests are undertaken to make sure that even if an aircraft is flying under icing conditions nothing hazardous will affect the engine. The ice shedding from the fan was then carefully monitored and, after the tests, the fan blades and the engine core section stator were carefully inspected as well as the casing. It appears that there is more threat for the bypass duct than for the core as the centrifugal force is ejecting the pieces of ice which have shed on the external part of the engine. However icing on the engine core section stator would be more critical because of the presence of the first rotor just behind which rotate at a much higher speed.
Certification tests have been conducted to simulate ground icing, icing in hold and during the descent. A typical certification test consists of 30 minutes of ice accretion followed by a slam acceleration after the water supply has been switched off.
Ground icing tests have been carried out at a temperature of -15, -9 and -6°C. The engine was in idle condition (22-25% of maximum power) and the LWC is 0.3 g.m^{-3} . At -15°C, cohesive shedding has been observed on the pressure side after about 27 minutes whereas ice from the leading edge started to shed only after 40 minutes of accretion. Even after 1 hour of accretion, the ice near the hub has never shed. At -9°C, the ice from the leading edge started to shed after 26 minutes. The test carried out at -6°C was a development test. It consisted of 30 minutes of accretion, an engine shut down followed by another cycle of 30 minutes of ice accretion and a slam acceleration. The ice started to shed from the leading edge after 17 minutes of accretion. When the engine was stopped, the ice on the pressure surface had not shed and the ice on the leading edge had shed up to mid span. During the second cycle, more ice is accreting, meaning that the ice thickness was non uniform especially on the pressure surface. After the slam acceleration, all the ice had been removed from the blades.
This series of tests conducted at different temperature confirmed the fact that ice is stronger at low temperature and stick more to the blades as it takes more time to shed. However more complicated effects seem to appear as, during the test done at -15°C, the ice shed first from the pressure surface then from the leading edge which is the opposite of what had been observed at -6°C.
Hold condition tests have been conducted at two different temperatures: -12.5°C which simulates a temperature of -20°C at altitude and -17°C. The LWC

was cycling between 0.4 and 2 g.m^{-3}. At -12.5°C, the first shedding occurred after 5 minutes of accretion, from the pressure surface and in big patches. The second cycle of shedding was very random and ice even shed near the hub. The ice on the pressure surface was observed to shed particularly when the LWC was high. A high LWC was found to produce ice which was more glazed and therefore weaker. However, the fact that the LWC continuously varied from low to high values prevented from drawing any conclusion about the particular shedding observed during this test. The type of ice accumulated was a random collection of glaze, mixed and rime ice. On certain part of the blade it was even possible that the ice was made of layer of ice of different freezing fraction some of which were weaker than others. At the end of the test, the slam acceleration was not as efficient as in the previous case. Indeed, significant quantities of ice were still present on the blades and on the spinner after the engine was switched off.
The test carried out at -17°C showed no shedding in some parts of the blades (especially near the hub) where a maximum thickness of about 4 cm could be observed. More ice was observed on the fan OGV resulting in the centrifugation of the droplets not caught by the fan.
The descent was simulated with the engine on idle condition (25% of maximum power). The temperature was kept constant during the test but the pressure was increased to simulate the decrease of altitude. The LWC was 1.3 g.m^{-3} and the temperature was -8°C to represent a temperature of -15°C at altitude. The ice shed randomly during the test however no ice shed near the hub. The centrifugal force which is a function of the position along the blade, was probably too small to induce shedding. Indeed, after the slam acceleration (the centrifugal force is increased due to the increase in rotational speed), almost all the ice have shed from the blades. The last test probably simulates the most critical condition for the engine, in term of ice accretion and shedding, as the rotational speed was very low and cannot be increased due to the descent of the aircraft.

6.3 FEA on rotating arm

This preliminary model has been created to evaluate the possibilities of using Abaqus to simulate ice shedding from a fan blade. It consists of two parts:

- a 3D deformable solid part representing the blade. The shape is rectangular with a length of 1.2 m, a width of 0.05 m and a thickness of 0.002 m. An 8-node linear brick mesh with reduced integration and hourless control (C3D8R) was used (figure 6.5). The material was titanium with

a density of 4430 kg.m^{-3} , a Young's modulus of 113 GPa and a Poisson's ratio of 0.34.

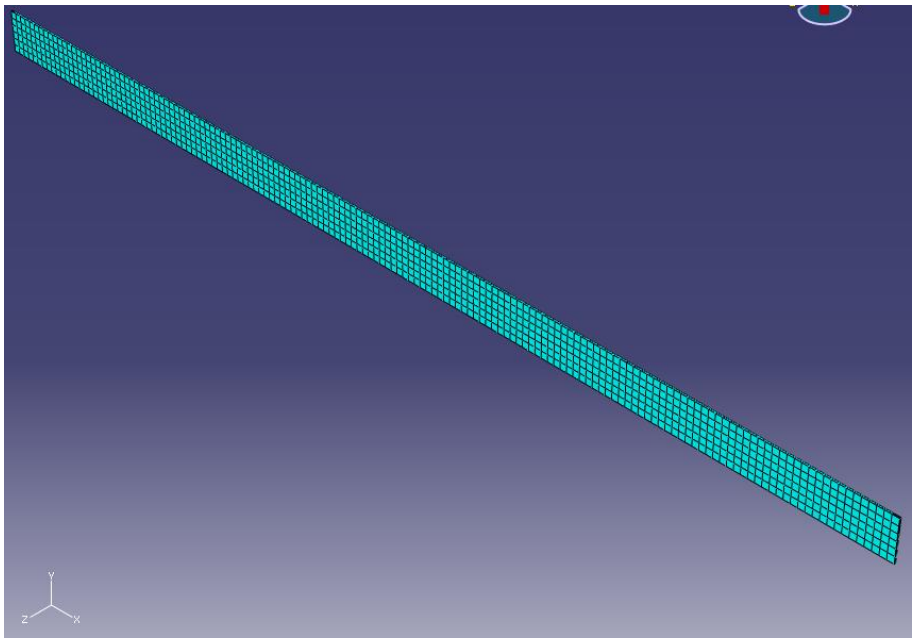

Figure 6.5: *Mesh of the bar part*

- a replicate of a mesh of a 3D deformable part representing the ice (called orphan mesh in the software). The shape was also rectangular with a length of 1.05 m, a width of 0.05 m and a thickness of 0.01 m (figure 6.6). These dimensions were representative of a typical fan in a civil aircraft engine. A zero thickness layer of cohesive elements was embedded at the ice/substrate interface. The ice was defined with a density of 917 kg.m^{-3} , a Young's modulus of 9 GPa and a Poisson's ratio of 0.31. The cohesive elements were defined with a density of 1000 kg.m^{-3} , a penalty stiffness of 100 GPa (traction type), a MAXS Damage of 1.2 MPa in the normal mode and 1.5 MPa in the first and second direction, and a damage evolution of 1 J.m^{-2} . It has been shown previously that both shear stress and tensile stress are responsible for self-shedding of ice on fan blades. However, it is a two steps mechanism and the first is govern by the shear stress. Therefore as a first approximation and in order to simplify the model, a damage evolution of type energy with a mode-independent behaviour was chosen. In the future, to take into account both the shear strength and the tensile strength, a mix-mode delamination criterion, like power law or BK option, should be chosen.

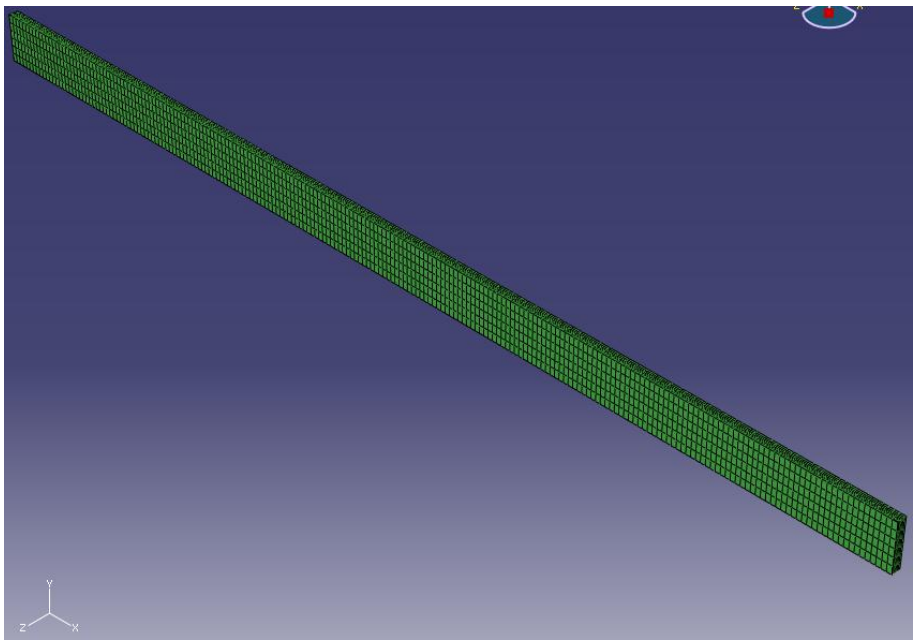

Figure 6.6: *Mesh of the ice part*

The values set for the tensile and shear strength can be considered as low compared to the mode I and shear test results. However at the time this model was built, the results were not all known and an average value, considering the experimental values and the values reported by previous authors in the literature, was chosen. It is believed that the shear strength should be higher that the tensile strength hence therefore, as a value of 1.2 MPa was chosen for the tensile strength, a value of 1.5 MPa was chosen for the shear strength.
The mesh was particularly refined at the interface ice/substrate (figure 6.7). An 8-node linear brick mesh with reduced integration and hourglass control (C3D8R) was used for the ice whereas an 8-node three dimensional cohesive element mesh (COHD8) was used for the cohesive elements layer.

A tied constraint between the cohesive elements layer and the substrate was set. The load was modeled as a body force and was applied on the ice part with a smooth amplitude to have a quasi static simulation. The body force was defined with an analytical field such as

$$F_b = \rho_i \times \omega^2 \times x \tag{6.4}$$

where F_b is the body force , ρ_i is the density of ice taken as 870 kg.m^{-3} , ω is the rotational speed taken as 167 rad.s^{-1} and x is the radial distance from the

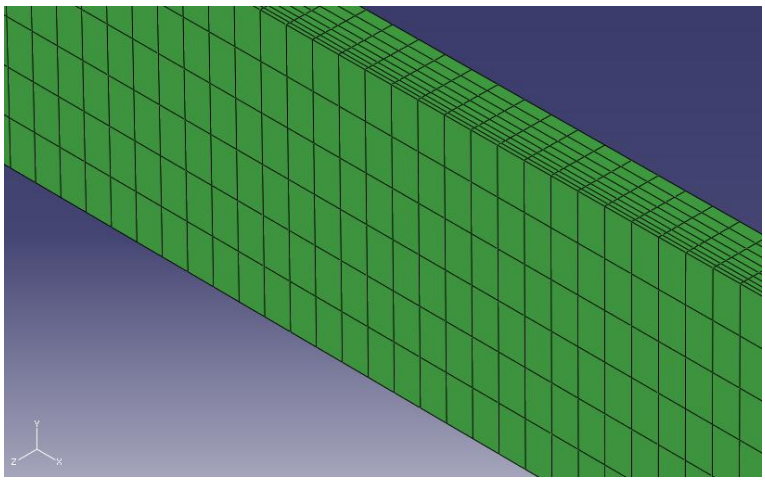

Figure 6.7: *Zoom on the mesh of the ice part*

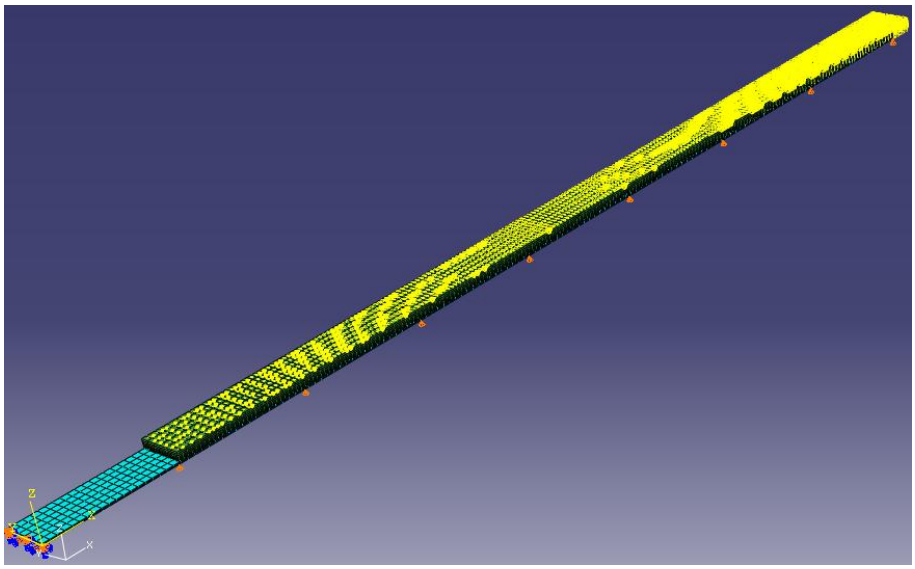

Figure 6.8: *Load and boundary conditions applied to the model*

hub. The end of the substrate, modeling the hub, was encastred to restrain the blade from any movements. The lower face of the blade was restrained from any movements in the vertical direction (z) so the blade was not able to bend (figure 6.8).
This model was simulating a rotating blade on which a constant thickness of ice was accreted. The rotational speed, and therefore the body force, was slowly increased from zero to full power (figure 6.9). This type of load application was chosen to facilitate the convergence of the solution. Sudden loading can

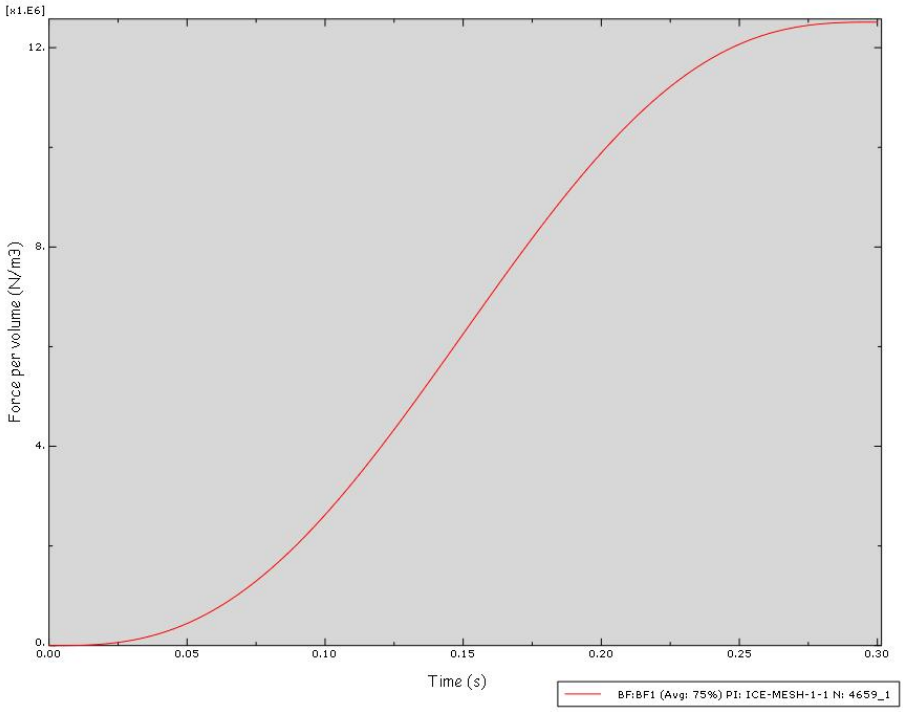

Figure 6.9: *Evolution of the load at a specific point in the ice part during the simulation*

induce noise or inaccurate solutions (Riahi, 2007).
The cohesive elements started to be deleted after 0.249 s and the piece of ice was shed after 0.258 s. The whole simulation was designed to last 0.3 s and was computed with Abaqus/explicit. At the end of the simulation, the ice part was completely detached from the substrate (figure 6.10).
The model seemed to work well however looking at the shear stress distribution (figure 6.11), a peak of shear stress can be observed near the hub. This peak seems unlikely as the centrifugal force is the lowest in this part of the blade (figure 6.12). This peak is probably due to the stretching of the bar. In this model, the ice is attached to the bar and, then, the whole is made to rotate at an increasing speed which cause both ice and the bar to stretch. The stretching of the bar which is restrain by the ice, causes a shear stress in the ice, responsible of the peak observed on figure 6.11. In the real world, when the engine is started, the blades are completely free of ice. Therefore they are able to stretch and twist before ice start to accrete on them. A realistic finite elements model is far beyond the objective of this thesis and will not be attempted here. However, a model with a bar restraints from any movements in the x and z directions has been attempted. The shear stress distribution

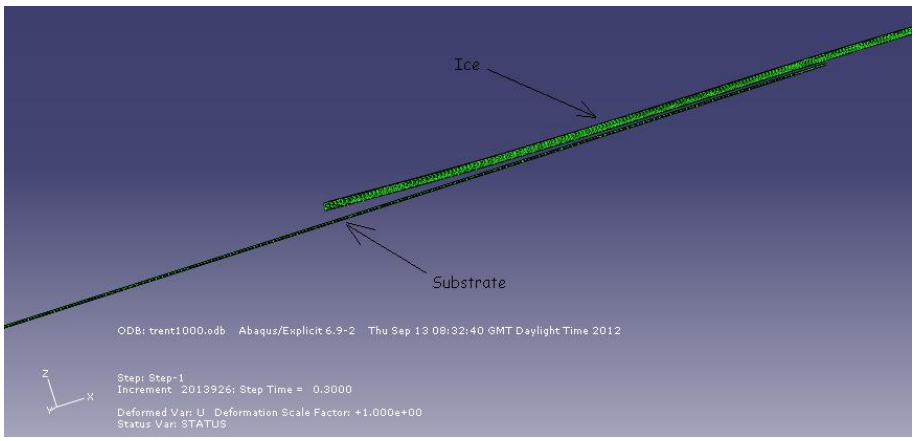

Figure 6.10: *Ice detached from the substrate at the end of the simulation*

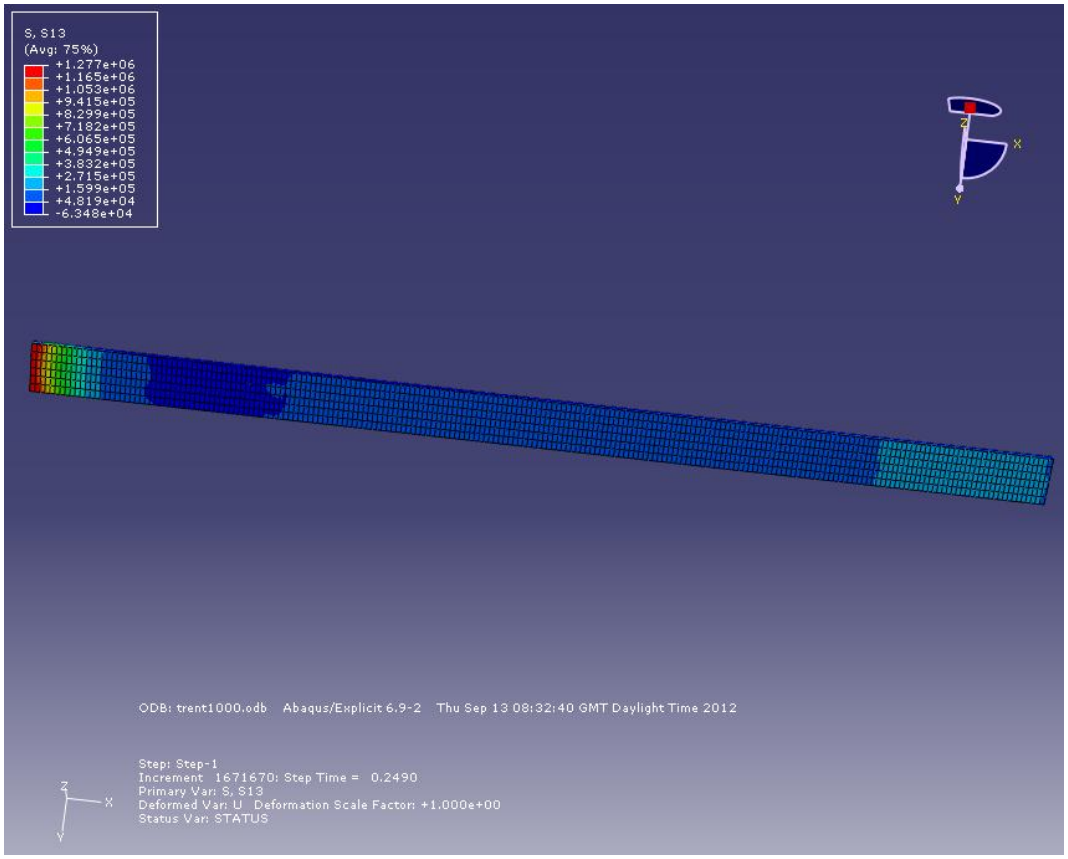

Figure 6.11: *Shear stress distribution at the ice/substrate interface (ice part)*

seemed more realistic, with the highest values near the tip, however the values

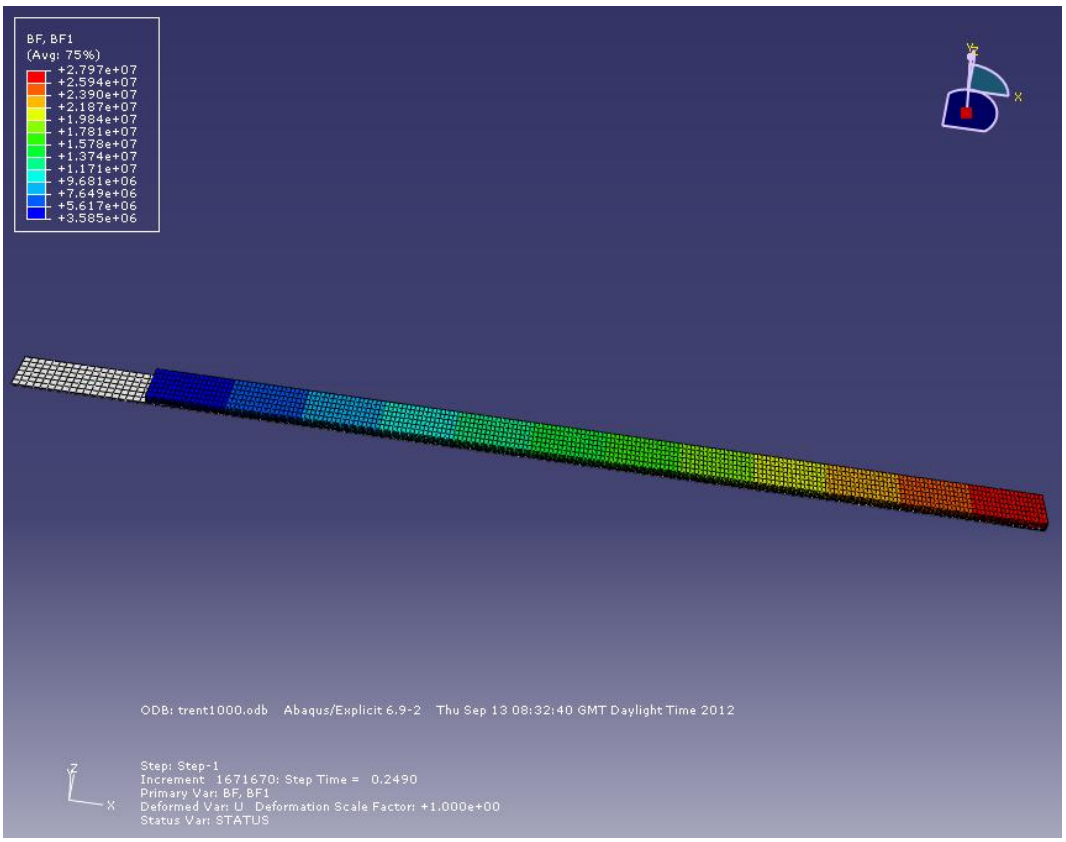

Figure 6.12: *Load distribution at the initiation of the "crack"*

obtained were too low to induced shedding.
A model simulating ice shedding from a rotating bar has been developed. This model was able to shed the ice however the shedding started from the hub while experiments show shedding starting from the tip. The model was improved by restraining the bar from any movements in the x and z directions. The model could be improved even more by using a more realistic shape for the blade and by developing a two steps simulation: a first step with the blade only and a load increasing until the rotational speed was reached and a second step with the ice accretion on the blade and the load kept constant. Another improvement could be made on the material properties used for the cohesive elements. The tensile stress needs to be taken into account as well as the shear strength using a mix-mode delamination criterion such as the QUADS damage option for the crack initiation and the power law or BK option for the crack propagation.

Chapter 7

Conclusion and further work

The objective of this project was to provide impact ice property values in order for Rolls-Royce to build a finite elements model to enable them to predict ice shedding from fan blades. This included experimental work with the measurement of the density, the stiffness, the grain size, the tensile strength and the shear strength of ice, and computational work with the development of different finite elements models.
Two mechanical tests have been developed: the mode I test rig to measure the fracture energy and the associated fracture toughness and tensile strength, and the shear test rig to measure the shear strength. Both tensile strength and shear strength have been calculated from the fracture energy and the critical stress intensity, respectively, by making the hypothesis that the grain size can be used as the material inherent defect size. The results obtained with that hypothesis were coherent with values reported by previous authors.
The influence of ambient total temperature, tunnel wind velocity, cloud LWC and substrate surface roughness were investigated. The ambient total temperature has been found to be the parameter which probably has the strongest influence on the mechanical and the physical properties of ice. As the temperature reduces the impact ice is stronger. Both tensile strength and shear strength have been found to increase as the temperature decreases. The microstructure presents smaller grains at lower temperature (in the order of the droplets diameter at -20°C). The density and the stiffness have also been found to decrease as the temperature is decreasing.
The influence of the LWC and the tunnel air velocity have been found to be smaller but not negligible. Fracture energy is decreasing as the LWC increases while shear strength, density and grain size are increasing with LWC. Both fracture energy and grain size have been found to go through a maximum as the tunnel velocity increases. Shear strength increases with the tunnel wind speed.

The trend obtained has been found, in general, to be relatively close to the one reported by the other authors. However the experimental values obtained for the tensile and shear strength have been found to be, in general, higher than those reported by previous authors. The main reason is probably the method used to conduct the test: in the present experimentation, the mechanical tests are carried out in a running icing tunnel while ice is still accreting. The shear strength measured with the shear test rig is the actual shear strength at the edge between the ice, the plunger and the substrate and not an average value of the shear strength along the surface of contact which is the value measured in general by previous authors.
Density, stiffness and grain size of impact ice have not been reported widely in the literature. Values of density measured have been found to be relatively close to the ones reported by previous authors especially Druez et al. (1986). Stiffness has been found to decrease as the temperature is decreasing whereas the opposite trend has been reported by previous authors. The values are also higher than the one found in the literature. However previous authors have used an ice which has grown very slowly compared to impact ice. An error could have been made during the measurement as the porosity of ice has not been taken into account.
Only few measurements were carried out with different substrate roughness and, as reported by previous authors, the roughness has been found to have a certain influence on the results. In the present experiments, only shear strength has been measured with substrate of different roughness and an increase of shear strength has been obtained for a rougher substrate.
Finite element models have been built using the commercial software Abaqus. Two models have been built to simulate each of the mechanical tests. The difference is in the way ice is attached to the substrate: one is using bonded nodes, the other cohesive elements. The cohesive element model has been found to be less reliable as one of the cohesive elements material properties, the penalty stiffness, is difficult to determine and leads to unrealistic stress distributions. Therefore a bonded nodes model was used to postprocess the results of the shear test.
A preliminary model, modeling the ice shedding from a rotating bar was created. This model was very basic and was successful to remove the ice from the bar. However the shear stress distribution was unrealistic with the highest values at the hub instead of the tip.

The freezing fraction has been introduced in this report but not fully used to process the results. This parameter should provide interesting ways of comparing the results as it can be considered as a global parameter representing the quality of ice produced.

The hypothesis made to calculate the tensile strength and the shear strength need to be investigated further. Size of real defects needs to be determined and more accurate values of tensile strength and shear strength need to be calculated.
The influence of the droplet MVD and the strain rate should be investigated. The strain rate, in particular, has been found by previous authors to have a certain influence on the tensile and the shear strength. At low strain rate, the ice was reported to have a ductile behaviour and effect due to creep could influence the mechanical as well as the physical properties of ice.
More quantitative measurements of the substrate roughness need to be done as well as a deeper investigation of its influence on the ice microstructure, density and stiffness and on the results of the mode I test. Substrate roughness is believed to have a strong influence on the microstructure of ice and to increase the bond between the ice and the substrate. Therefore higher values of tensile and shear strength are expected. The ice produced on a rougher surface is expected to have larger grain and more inclusion of air pockets. Hence a lower density could be obtained compared to a mirror polished surface finish.
A more realistic finite element rotating model should be developed in the future including a more realistic geometry for the blade and the ice. A model in two steps should be developed with the first step where the blade is made rotating and the second where the ice is accreting. The material properties of the cohesive elements need to be investigated to have a better understanding of their function. A mix-mode delamination criterion needs to be used in order to take into account the tensile strength as well as the shear strength in the crack initiation and in the crack propagation criterion.

Bibliography

D.N. Anderson. Manual of scaling methods. *NASA CR-2004-212875*, 2004.

D.N. Anderson and J.C. Tsao. Evaluation and validation of the messinger freezing fraction. *NASA CR-2005-213852*, 2005.

E.H. Andrews and N.A. Lockington. The cohesive and adhesive strength of ice. *Journal of materials science*, 8:1455–1465, 1983.

J. Ballard. Brittle fracture, may 2010. URL `http://www.sv.vt.edu/classes/MSE2094-Notebook/97ClassProj/exper/ballard/www/ballard.html`.

C. Blackburn, C. Laforte, and J.L. Laforte. Apparatus for measuring the adhesion force of a thin ice sheet on a substrate. *th international workshop of atmospheric icing structures*, 2000.

P.P. Camanho and C.G. Davila. Mixed-mode decohesion finite element for the simulation of delamination. *NASA TM-2002-211737*, 2002.

J.N. Carras and W.C. Macklin. The opacity of accreted ice. *Quaterly journal of the royal meteorological society*, 101:203–206, 1975.

M.C. Chu and R.J. Scavuzzo. Adhesive shear strength of impact ice. *AIAA journal*, 29:1921–1926, 1991.

M.L. Chu, R.J. Scavuzzo, and T.S. Srivatsan. An experimental technique for the evaluation of properties of ice. *Journal mater. res.*, 6(9), 1991.

G. Dantl. *Elastic moduli of ice.* Plenum Press, New York, 1969.

J. Druez, C.L. Phan, J.L. Laforte, and D.D. Nguyen. Adhesion of glaze and rime on aluminium electrical conductors. *Transaction of canadian society for mechanical engineering*, 5(4):215–220, 1978.

J. Druez, D.D. Nguyen, and Y. Lavoie. Mechanical properties of atmospheric ice. *Cold regions science and technology*, 13(1):67–74, 1986.

J. Druez, J. Cloutier, and L. Claveau. Etude comparative de la résistance à la traction et à la compression de la glace atmospherique. *Journal de physique, colloque C1, tome 48*, pages 337–343, 1987.

J. Druez, J.L. Laforte, and C. Tremblay. Experimental results on the tensile strength of atmospheric ice. *Proc. 8th intn conference offshore, mechanics and arctic engineering*, 4:405–410, 1989.

M. Eskandarian. *Ice shedding from overhead electrical lines by mechanical breaking*. PhD thesis, Université du Québec (Chicoutimi), 2005.

G. Fortin and J. Perron. Spinning rotor blade tests in icing wind tunnel. *AIAA 2009-4260*, 2009.

P.H. Gammon, H. Kiefte, M.J. Cloutier, and W.W. Denner. Elastic constants of artificial and natural ice samples by Brillouin spectroscopy. *Journal of glaciology*, 29(103):433–460, 1983.

L.W. Gold. On the elasticity of ice plates. *Canadian journal of civil engineering*, 15:1080–1084, 1988.

D.W. Hammond. Microstructure and mechanical properties of some small impact ice accretions. *7th international workshop on atmospheric icing structures*, 1996.

H.W. Hayden, W.G. Moffatt, and J. Wulff. *The structure and properties of materials; vol.III: Mechanical behavior*. John Wiley Sons, 1965.

Y. Hu, B. Davison, and R. Planck. Modelling of flexible end plate connections in fire using cohesive elements. *Fifth international workshop 'structure in fire '*, 2008.

K. Itagaki. Self-shedding of accreted ice from high-speed rotors. *ASME paper 83-WA/HT-68*, 1983.

M. Javan-Mashmool. A new method for measuring ice adhesion strength at an ice-substrate interface. *Hydrol. Process.*, 20:645–655, 2006.

A. Jayatilaka. *Fracture of engineering brittle materials*. Applied science publishers, London, 1979.

R.K. Jeck. Icing design envelopes (14 cfr parts 25 and 29, appendix c) converted to a distance-based format. *DOT/FAA/AR-00/30*, 2002.

M. Kermani Koosheh. *Ice shedding from cables and conductors - a cracking model of atmospheric ice*. PhD thesis, Université du Québec (Chicoutimi), 2007.

C. Laforte. Etude de l'adhérence de la glace sur des solides à caractère glaciophobe. Master's thesis, Université du Québec (Chicoutimi), 2001.

C. Laforte. *Deformation à la rupture adhésive par traction, flexion et tension d'un substrat givré*. PhD thesis, Université du Québec (Chicoutimi), 2007.

C. Laforte and A. Beisswenger. Icephobic material centrifuge adhesion test. *IWAIS XI*, 2005.

C. Laforte and J.L. Laforte. Tensile, torsional and bending strain at the adhesive rupture of an iced substrat. *Proceedings of the ASME 2009 28th international conference on ocean, offshore and arctic engineering*, pages 79–86, 2009.

J.L. Laforte, L.C. Phan, and B. Felin. Microstructure of ice accretions grown on aluminium conductors. *Journal of climate and applied meteorology*, 22 (7):1175–1189, 1983.

I. Langmuir and K. Blodgett. A mathematical investigation of water droplet trajectories. *Army air forces technical report no.5418*, 1946.

D. Lou. The development, production, demonstration and analysis of the ice shear rig of the study of engine icing. Master's thesis, Cranfield University, SoE, 2010.

D.L. Loughborough and E.G. Haas. Reduction of the adhesion of ice to de-icer surfaces. *Journal of the aeronautical sciences*, 13:126–134, 1946.

W.C. Macklin. The density and structure of ice formed by accretion. *Quaterly journal of the royal meteorological society*, 88:30–50, 1962.

D.M. Millar. Investigation of ice accretion characteristics of hydrophobic materials. *report no. FAA-DS-70-11*, 1970.

T.L. Miller and T.H. Bond. Icing research tunnel test of a model helicopter rotor. *NASA TM-101978*, 1989.

A.M.A. Mohammed and M. Farzaneh. An experimental study on the tensile properties of atmospheric ice. *Cold regions science and technology*, 2011.

V.F. Petrenko. In-situ study of physical properties and structure of atmospheric ice. *report no.45042-EV*, 2006.

L.E. Raraty and D. Tabor. The adhesion and strength properties of ice. *Proceedings of the Royal Society of London*, 245A:184–201, 1958.

M.M. Riahi. Numerical and experimental studies of the mechanical behaviour at the ice/aluminium interface. Master's thesis, Université du Québec (Chicoutimi), 2007.

R.J. Roark. *Formulas for stress and strain*. McGraw-Hill Book Company, New York, 1965.

G.A. Ruff. Analysis and verification of the icing scaling equations. *AEDC-TR-85-30*, 1, 1985.

P.J. Rye and W.C. Macklin. Crystal size in accreted ice. *Quaterly journal of the royal meteorological society*, 101:207–215, 1975.

R.J. Scavuzzo and M.L. Chu. Structural properties of impact ices accreted on aircraft structures. *NASA CR-179580*, 1987.

R.J. Scavuzzo, M.L. Chu, and J. Kellackey. Impact ice stresses in rotating airfoils. *AIAA 90-0198*, 1990.

R.J. Scavuzzo, M.L. Chu, and V. Ananthaswamy. Influence of aerodynamic forces in ice shedding. *Journal of Aircraft*, 31(3), 1994.

R.J. Scavuzzo, M.L. Chu, and C.J. Kellackey. Structural analysis and properties of impact ices accreted on aircraft structures. *NASA CR-198473*, 1996.

E.M. Schulson. *Ice: mechanical properties*. Encyclopedia of Materials - Science and Technology. Elsevier, 2001.

E.M. Schulson and P. Duval. *Creep and fracture of ice*. Cambridge university press, 2009.

N.K. Sinha. Elasticity of natural types of polycrystalline ice. *Cold regions science and technology*, 17(2):127–135, 1989.

J.R. Stallabrass and R.D. Price. On the adhesion of ice to various materials. *National research laboratories LR-350*, 1962.

H. Tada, P.C. Paris, and G. Irwin. *The stress analysis of cracks handbook*. ASME, 2000.

The engineering toolbox, march 2011. URL `http://www.engineeringtoolbox.com/ice-thermal-properties-d_576.html`.

G.W. Timco and R.M.W. Frederking. A review of sea ice density. *Cold regions science and technology*, 24:1–6, 1996.

G.W. Timco and W.F.Weeks. A review of the engineering properties of sea ice. *Cold regions science and technology*, 60:107–129, 2010.

A. Traetteberg, L.W. Gold, and R. Frederking. The strain rate and temperature dependence of Young's modulus of ice. *Third international symposium on ice problems*, pages 479–486, 1975.

C. Tremblay. Détermination de la résistance à la traction de la glace atmosphérique. Master's thesis, Université du Québec (Chicoutimi), 1991.

X. Xian, M.L. Chu, R.J. Scavuzzo, and T.S. Srivatsan. An experimental evaluation of the tensile strength of impact ice. *Journal of materials science letter*, 8:1205–1208, 1989.

Appendix A

Results

All values obtained from the experimental analysis have been presented in the following tables.
The first table (table A.1) shows the conditions at which the ice was accreted, the surface temperature and the related freezing fraction. A reference number was assigned in order to relate each condition to other properties in the following tables. This number was designed in the following way: temperature-LWC-speed-MVD-material-roughness where "temperature" represents the ambient total temperature, "LWC" the liquid water content of the cloud, "speed" the tunnel wind speed, "MVD" the mean volume diameter of the droplets, "material" the substrate material and "roughness" the state of the substrate's surface. A distinction was made for the surface temperature between the "measured" and "estimated" surface temperature. The "measured" surface temperature is the accurate temperature of the front surface of the ice measured during the first few second of accretion using the laser gun. The incertitude of the measurement was estimated at 1°C. The "estimated" surface temperature was obtained by interpolation using the curve ploted with the "measured" values of the surface temperature. The freezing fraction was calculated using equation 4.23 and the surface temperature "measured" or "calculated" during the experiments.
Table A.2 presents the results obtained during the measurements of the physical properties of ice: density, stiffness and average grain size. From each property, a "measured" and/or a "used" value is given. The "measured" value is the actual value measured during the experiments whereas the "used" value is the value used for the calculation of the meachanical properties related to mode I and mode II (presented in table A.3 and A.4). An incertitude of 50 $kg.m^{-3}$ and 0.9 GPa was estimated for the measurements of the density and the Young's modulus respectively. For the grain size, both the values obtained at the interface ice/substrate (noted "interface") and at the front surface of the

ice (noted "top") were given. These values were obtained from an arithmetic average of 10 values themselves obtained with a linear intercept method. The "used" value of the grain size was taken as the "top" value. This value was, indeed, used for the calculation of the tensile and shear strength and should be taken as an estimation of a size defect in a bulk of ice. The "interface" values were thought to be different because of the presence of the substrate which initiate the crystal growth and therefore do not represent the size of the defects in the bulk.
Table A.3 presents the mechanical properties related to mode I: fracture energy, fracture toughness and tensile strength. For each properties, a mean value and a standard deviation were given. These values were obtained using a Weibull distribution. The number of values used at each condition is given in the column named "number of samples". The preferential type of fracture was reported in the first column. "Adhesive" means that most of the ice sample were detached from the substrate at the interface ice/substrate. "Cohesive" means that most of the samples were detached in a complete or almost complete cohesive way. "Mixed" means that the samples were detached from the substrate in either a cohesive or adhesive way with no real preference within the two types of fracture.
Table A.4 presents the mechanical properties related to mode II: the equivalent of the fracture toughness and the shear strength. In addition to these, an average shear strength was calculated using the critical pressure needed to remove the ice and the surface of contact between the ice and the substrate. Similarly to the mode I properties, a statistical analysis with a Weibull distribution was performed to provide a mean value and a standard deviation. The first column reports the number of samples used for the statistical analysis.

Table A.1: *Conditions tested and aspect of ice*

Condition Reference Number	**Ice growth conditions**				**Substrate**		**Type of ice**		
	Ambient total temperature (°C)	LWC ($g.m^{-3}$)	Tunnel wind speed ($m.s^{-1}$)	Droplets MVD (μm)	Material	Roughness	Surface temperature (°C)		Freezing fraction
							measured	estimated	
2-04-50-20-ti-mp	-2	0.4	50	20	titanium alloy	mirror polished		0.0	0.30
2-07-50-20-ti-mp	-2	0.7	50	20	titanium alloy	mirror polished		0.0	0.20
3-04-50-20-ti-mp	-3	0.4	50	20	titanium alloy	mirror polished	0.0		0.45
3-04-50-20-ti-rf	-3	0.4	50	20	titanium alloy	realistic finish		0.0	0.45
3-07-50-20-ti-mp	-3	0.7	50	20	titanium alloy	mirror polished	0.0		0.25
4-04-50-20-ti-mp	-4	0.4	50	20	titanium alloy	mirror polished		-0.3	0.50
4-07-50-20-ti-mp	-4	0.7	50	20	titanium alloy	mirror polished		-0.3	0.30
5-04-50-20-ti-mp	-5	0.4	50	20	titanium alloy	mirror polished	-1.0		0.55
5-04-50-20-ti-rf	-5	0.4	50	20	titanium alloy	realistic finish	-1.0		0.55
5-04-60-20-ti-mp	-5	0.4	60	20	titanium alloy	mirror polished			
5-04-70-20-ti-mp	-5	0.4	70	20	titanium alloy	mirror polished			
5-04-80-20-ti-mp	-5	0.4	80	20	titanium alloy	mirror polished			
5-07-50-20-ti-mp	-5	0.7	50	20	titanium alloy	mirror polished	-1.0		0.35
6-04-50-20-ti-mp	-6	0.4	50	20	titanium alloy	mirror polished		-1.7	0.60
6-07-50-20-ti-mp	-6	0.7	50	20	titanium alloy	mirror polished		-1.7	0.35
7-04-50-20-ti-mp	-7	0.4	50	20	titanium alloy	mirror polished	-2.5		0.65
7-07-50-20-ti-mp	-7	0.7	50	20	titanium alloy	mirror polished	-2.5		0.40
8-04-50-20-ti-mp	-8	0.4	50	20	titanium alloy	mirror polished		-3.1	0.65
8-07-50-20-ti-mp	-8	0.7	50	20	titanium alloy	mirror polished		-3.1	0.40
9-04-50-20-ti-mp	-9	0.4	50	20	titanium alloy	mirror polished		-3.8	0.70
9-07-50-20-ti-mp	-9	0.7	50	20	titanium alloy	mirror polished		-3.8	0.45
10-04-50-20-ti-mp	-10	0.4	50	20	titanium alloy	mirror polished	-4.5		0.75

continued on next page

continued from previous page

Condition Reference Number	Ice growth conditions				Substrate		Type of ice		
	Ambient total temperature (°C)	LWC (g.m^{-3})	Tunnel wind speed (m.s^{-1})	Droplets MVD (μm)	Material	Roughness	Surface temperature (°C) measured	Surface temperature (°C) estimated	Freezing fraction
10-05-40-20-ti-mp	-10	0.5	40	20	titanium alloy	mirror polished			
10-05-50-20-ti-mp	-10	0.5	50	20	titanium alloy	mirror polished			
10-05-60-20-ti-mp	-10	0.5	60	20	titanium alloy	mirror polished			
10-05-70-20-ti-mp	-10	0.5	70	20	titanium alloy	mirror polished			
10-05-80-20-ti-mp	-10	0.5	80	20	titanium alloy	mirror polished			
10-06-40-20-ti-mp	-10	0.6	40	20	titanium alloy	mirror polished			
10-07-50-20-ti-mp	-10	0.7	50	20	titanium alloy	mirror polished	-4.5		0.45
10-08-40-20-ti-mp	-10	0.8	40	20	titanium alloy	mirror polished			
10-10-40-20-ti-mp	-10	1.0	40	20	titanium alloy	mirror polished			
10-11-40-20-ti-mp	-10	1.1	40	20	titanium alloy	mirror polished			
11-07-50-20-ti-mp	-11	0.7	50	20	titanium alloy	mirror polished		-5.2	0.50
12-04-50-20-ti-mp	-12	0.4	50	20	titanium alloy	mirror polished		-5.9	0.80
12-07-50-20-ti-mp	-12	0.7	50	20	titanium alloy	mirror polished		-5.9	0.50
13-07-50-20-ti-mp	-13	0.7	50	20	titanium alloy	mirror polished		-6.6	0.50
14-07-50-20-ti-mp	-14	0.7	50	20	titanium alloy	mirror polished		-7.3	0.55
15-04-50-20-ti-mp	-15	0.4	50	20	titanium alloy	mirror polished		-8.0	0.90
15-07-50-20-ti-mp	-15	0.7	50	20	titanium alloy	mirror polished		-8.0	0.55
16-07-50-20-ti-mp	-16	0.7	50	20	titanium alloy	mirror polished		-8.7	0.60
17-04-50-20-ti-mp	-17	0.4	50	20	titanium alloy	mirror polished		-9.4	1.00
17-07-50-20-ti-mp	-17	0.7	50	20	titanium alloy	mirror polished		-9.4	0.60
18-04-50-20-ti-mp	-18	0.4	50	20	titanium alloy	mirror polished		-10.1	1.00
19-04-50-20-ti-mp	-19	0.4	50	20	titanium alloy	mirror polished		-10.8	1.00
20-04-50-20-ti-mp	-20	0.4	50	20	titanium alloy	mirror polished		-11.5	1.00
20-07-50-20-ti-mp	-20	0.7	50	20	titanium alloy	mirror polished		-11.5	0.70

Table A.2: *Physical properties of impact ice: Density, stiffness and average grains size*

Condition Reference Number	**Physical properties**								
	Density ($kg.m^{-3}$)		Young's modulus (GPa)			Grain size "a_g" (μm)			
	measured	used	measured	used mode I	used mode II	interface	top	used mode I	used mode II
2-04-50-20-ti-mp		870		8.5	13.2			600	600
2-07-50-20-ti-mp		870		8.5	13.2			1063	1063
3-04-50-20-ti-mp		870		8.5	13.2			530	530
3-04-50-20-ti-rf		870		8.5	13.2				
3-07-50-20-ti-mp		870		8.5	13.2			960	960
4-04-50-20-ti-mp		870		8.5	13.2			460	460
4-07-50-20-ti-mp		870			13.2				862
5-04-50-20-ti-mp	916	870	14	8.5	13.2	225	400	400	400
5-04-50-20-ti-rf		870		8.5	13.2				
5-04-60-20-ti-mp		870		8.5	13.2				200
5-04-70-20-ti-mp		870		8.5	13.2				200
5-04-80-20-ti-mp		870		8.5	13.2				100
5-07-50-20-ti-mp		870		8.5	13.2			770	770
6-04-50-20-ti-mp		870		8.5	13.2			335	335
6-07-50-20-ti-mp		870		8.5	13.2			683	683
7-04-50-20-ti-mp		870		8.5	13.2			280	280
7-07-50-20-ti-mp		870		8.5	13.2			602	602
8-04-50-20-ti-mp		870		8.5	13.2			231	231
8-07-50-20-ti-mp		870		8.5	13.2			526	526
9-04-50-20-ti-mp		870		8.5	13.2			187	187
9-07-50-20-ti-mp		870		8.5	13.2			455	455
10-04-50-20-ti-mp	855	870	13.6	8.5	13.2	110	135	135	135
10-05-40-20-ti-mp	857	870		8.5	13.2	332	177	177	

continued on next page

continued from previous page

Condition Reference Number	Physical properties								
	Density ($kg.m^{-3}$)		Young's modulus (GPa)			Grain size "a_g" (μm)			
	measured	used	measured	used mode I	used mode II	interface	top	used mode I	used mode II
10-05-50-20-ti-mp		870		8.5	13.2	743	204	204	
10-05-60-20-ti-mp		870		8.5	13.2			220	
10-05-70-20-ti-mp		870		8.5	13.2	37	190	190	
10-05-80-20-ti-mp		870		8.5	13.2	57	108	108	
10-06-40-20-ti-mp	862	870		8.5	13.2	59	212	212	
10-07-50-20-ti-mp		870		8.5	13.2	325	390	390	390
10-08-40-20-ti-mp	898	870		8.5	13.2	112	91	91	
10-10-40-20-ti-mp	919	870		8.5	13.2	208	135	135	
10-11-40-20-ti-mp	922	870		8.5	13.2	188	278	278	
11-07-50-20-ti-mp		870		8.5	13.2			330	330
12-04-50-20-ti-mp		870		8.5	13.2			86	86
12-07-50-20-ti-mp		870		8.5	13.2			276	276
13-07-50-20-ti-mp		870		8.5	13.2			227	
14-07-50-20-ti-mp		870		8.5	13.2			184	
15-04-50-20-ti-mp	821	870	13.2	8.5	13.2	47	50	50	
15-07-50-20-ti-mp		870		8.5	13.2			400	146
16-07-50-20-ti-mp		870		8.5	13.2			114	
17-04-50-20-ti-mp		870		8.5	13.2			48	
17-07-50-20-ti-mp		870		8.5	13.2			86	
18-04-50-20-ti-mp		870		8.5	13.2			48	
19-04-50-20-ti-mp		870		8.5	13.2			48	
20-04-50-20-ti-mp	756	870	12.5	8.5	13.2	36	49	49	
20-07-50-20-ti-mp		870		8.5	13.2	48	38	38	

Table A.3: *Mechanical properties of impact ice: mode I*

Condition Reference Number	**Mechanical properties: mode I**							
	Preferential type of fracture	Number of samples	Fracture energy ($J.m^{-2}$)		Fracture toughness K_{Ic} ($kPa\sqrt{m}$)		Tensile strength (MPa) based on observed a_g	
			mean	standard dev.	mean	standard dev.	mean	standard dev.
2-04-50-20-ti-mp								
2-07-50-20-ti-mp								
3-04-50-20-ti-mp	adhesive	9	0.599	0.140	74591	8497	1.83	0.21
3-04-50-20-ti-rf								
3-07-50-20-ti-mp	adhesive	7	0.591	0.201	73752	11633	1.34	0.21
4-04-50-20-ti-mp	adhesive	9	0.726	0.225	81744	12900	2.15	0.34
4-07-50-20-ti-mp								
5-04-50-20-ti-mp	adhesive	16	0.802	0.292	85510	15748	2.41	0.44
5-04-50-20-ti-rf								
5-04-60-20-ti-mp								
5-04-70-20-ti-mp								
5-04-80-20-ti-mp								
5-07-50-20-ti-mp	adhesive	13	0.787	0.206	85298	11546	1.73	0.23
6-04-50-20-ti-mp	adhesive	10	0.803	0.207	86180	11747	2.66	0.36
6-07-50-20-ti-mp	adhesive	9	1.032	0.247	97882	11709	2.11	0.25
7-04-50-20-ti-mp	adhesive	9	0.750	0.306	82400	17206	2.78	0.58
7-07-50-20-ti-mp	adhesive	7	0.943	0.162	93895	8351	2.16	0.19
8-04-50-20-ti-mp	mixed	8	1.011	0.203	97062	9976	3.60	0.37
8-07-50-20-ti-mp	adhesive	9	0.832	0.173	87954	9680	2.16	0.24
9-04-50-20-ti-mp	mixed	8	1.318	0.451	109850	19392	4.53	0.80
9-07-50-20-ti-mp	adhesive	9	0.857	0.246	88920	13035	2.35	0.34
10-04-50-20-ti-mp	mixed	26	1.061	0.457	97749	20999	4.75	1.02
10-05-40-20-ti-mp	adhesive	12	1.000	0.371	95460	17878	4.05	0.76

continued on next page

continued from previous page

Condition Reference Number	Mechanical properties: mode I							
	Preferential type of fracture	Number of samples	Fracture energy ($J.m^{-2}$)		Fracture toughness K_{Ic} ($kPa\sqrt{m}$)		Tensile strength (MPa) based on observed a_g	
			mean	standard dev.	mean	standard dev.	mean	standard dev.
10-05-50-20-ti-mp	adhesive	18	0.808	0.361	85233	18734	3.37	0.74
10-05-60-20-ti-mp	adhesive	6	1.258	0.617	105986	26666	4.03	1.01
10-05-70-20-ti-mp	adhesive	6	1.125	0.441	101351	19124	4.15	0.78
10-05-80-20-ti-mp	mixed	13	0.993	0.356	95295	16809	5.17	0.91
10-06-40-20-ti-mp	adhesive	6	0.856	0.365	88373	17073	3.43	0.66
10-07-50-20-ti-mp	adhesive	38	0.985	0.251	95421	12671	2.73	0.36
10-08-40-20-ti-mp	adhesive	6	0.814	0.293	86343	15591	5.11	0.92
10-10-40-20-ti-mp	adhesive	14	0.859	0.411	87899	19456	4.27	0.94
10-11-40-20-ti-mp	adhesive	7	0.716	0.279	80783	15622	2.73	0.53
11-07-50-20-ti-mp								
12-04-50-20-ti-mp	mixed	9	1.131	0.651	100273	25561	6.10	1.56
12-07-50-20-ti-mp	mixed	6	1.082	0.106	100757	4945	3.42	0.17
13-07-50-20-ti-mp	cohesive	6	1.150	0.168	103776	7612	3.89	0.29
14-07-50-20-ti-mp	mixed	15	0.898	0.302	90838	14441	3.78	0.60
15-04-50-20-ti-mp	mixed	13	1.317	0.465	109624	19954	9.02	1.64
15-07-50-20-ti-mp	mixed	31	0.975	0.380	94001	18596	4.39	0.87
16-07-50-20-ti-mp	mixed	9	1.239	0.450	106399	19419	5.62	1.03
17-04-50-20-ti-mp	adhesive	8	0.944	0.386	92657	18188	7.55	1.48
17-07-50-20-ti-mp	mixed	10	1.587	0.806	119143	28385	7.25	1.73
18-04-50-20-ti-mp	cohesive	6	1.182	0.348	104431	15673	8.5	1.28
19-04-50-20-ti-mp	cohesive	6	1.091	0.549	98372	26335	8.01	2.14
20-04-50-20-ti-mp	cohesive	12	0.899	0.427	89569	21726	7.22	1.75
20-07-50-20-ti-mp	mixed	13	1.239	0.536	105993	21199	9.7	1.94

Table A.4: *Mechanical properties of impact ice: mode II*

Condition Reference Number	**Mechanical properties: mode II**						
	Number of samples	Average shear strength (MPa)		Critical stress intensity K^*_{IIc} (kPa$\sqrt{\text{m}}$)		Shear strength (MPa) based on observed a_g	
		mean	standard dev.	mean	standard dev.	mean	standard dev.
2-04-50-20-ti-mp	5	0.486	0.118	87699	21713	2.02	0.50
2-07-50-20-ti-mp	6	0.670	0.223	121353	41037	2.10	0.71
3-04-50-20-ti-mp	6	0.666	0.100	120802	18326	3.05	0.46
3-04-50-20-ti-rf							
3-07-50-20-ti-mp	5	0.769	0.318	139559	58379	2.54	1.06
4-04-50-20-ti-mp	5	0.631	0.142	114278	26241	3.01	0.69
4-07-50-20-ti-mp	5	0.613	0.197	110942	36164	2.13	0.69
5-04-50-20-ti-mp	10	0.688	0.115	124811	21106	3.52	0.60
5-04-50-20-ti-rf							
5-04-60-20-ti-mp	5	0.636	0.177	115258	32613	4.60	1.30
5-04-70-20-ti-mp	5	0.631	0.214	114229	39232	4.56	1.57
5-04-80-20-ti-mp	5	0.537	0.084	96958	15524	5,47	0.88
5-07-50-20-ti-mp	17	0.783	0.211	142191	38856	2.89	0.79
6-04-50-20-ti-mp	5	0.761	0.218	138260	39997	4.26	1.23
6-07-50-20-ti-mp	8	0.756	0.251	137210	46101	2.96	1.00
7-04-50-20-ti-mp	5	0.680	0.243	123219	44673	4.15	1.51
7-07-50-20-ti-mp	4	0.781	0.177	141880	32581	3.26	0.75
8-04-50-20-ti-mp	5	0.849	0.198	154379	36348	5.74	1.35
8-07-50-20-ti-mp	5	1.001	0.237	182281	43493	4.48	1.07
9-04-50-20-ti-mp	5	1.042	0.102	189802	18779	7.83	0.77
9-07-50-20-ti-mp	5	0.937	0.096	170572	17707	4.51	0.47
10-04-50-20-ti-mp	5	0.977	0.192	177823	35294	8.63	1.71
10-05-40-20-ti-mp							

continued on next page

continued from previous page

Condition Reference Number	**Mechanical properties: mode II**						
	Number of samples	Average shear strength (MPa)		Critical stress intensity K^*_{IIc} (kPa$\sqrt{\text{m}}$)		Shear strength (MPa) based on observed a_g	
		mean	standard dev.	mean	standard dev.	mean	standard dev.
10-05-50-20-ti-mp							
10-05-60-20-ti-mp							
10-05-70-20-ti-mp							
10-05-80-20-ti-mp							
10-06-40-20-ti-mp							
10-07-50-20-ti-mp	4	0.900	0.190	163713	34913	4.68	1.00
10-08-40-20-ti-mp							
10-10-40-20-ti-mp							
10-11-40-20-ti-mp							
11-07-50-20-ti-mp	9	0.910	0.327	165564	60059	5.14	1.87
12-04-50-20-ti-mp	4	1.079	0.194	196646	35602	11.97	2.17
12-07-50-20-ti-mp	5	1.230	0.292	224343	53626	7.62	1.82
13-07-50-20-ti-mp							
14-07-50-20-ti-mp							
15-04-50-20-ti-mp							
15-07-50-20-ti-mp							
16-07-50-20-ti-mp							
17-04-50-20-ti-mp							
17-07-50-20-ti-mp							
18-04-50-20-ti-mp							
19-04-50-20-ti-mp							
20-04-50-20-ti-mp							
20-07-50-20-ti-mp							

Appendix B

Matlab program for calculation of freezing fraction

```
function varargout = freezing_frac(varargin)

    % FREEZING_FRAC M-file for freezing_frac.fig
    %       FREEZING_FRAC, by itself, creates a new FREEZING_FRAC or
    %       raises the existing singleton*.
    %
    %       H = FREEZING_FRAC returns the handle to a new FREEZING_FRAC
    %       or the handle to the existing singleton*.
    %
    %       FREEZING_FRAC('CALLBACK',hObject,eventData,handles,...) calls
    %       the local function named CALLBACK in FREEZING_FRAC.M with
    %       the given input arguments.
    %
    %       FREEZING_FRAC('Property','Value',...) creates a new FREEZING_
    %       FRAC or raises the existing singleton*. Starting from the left,
    %       property value pairs are applied to the GUI before freezing_frac_OpeningFcn
    %       gets called. An unrecognized property name or invalid value makes
    %       property application stop. All inputs are passed to freezing_frac_OpeningFcn
    %       via varargin.
    %
    %       *See GUI Options on GUIDE's Tools menu. Choose "GUI allows
    %       only one instance to run (singleton)".

    % See also: GUIDE, GUIDATA, GUIHANDLES

    % Edit the above text to modify the response to help freezing_frac

    % Last Modified by GUIDE v2.5 09-May-2011 09:47:39

    % Begin initialization code - DO NOT EDIT
    gui_Singleton = 1;
    gui_State = struct('gui_Name', mfilename, ...
    'gui_Singleton', gui_Singleton, ...
```

```
'gui_OpeningFcn', @freezing_frac_OpeningFcn, ...
'gui_OutputFcn', @freezing_frac_OutputFcn, ...
'gui_LayoutFcn', [] , ...
'gui_Callback', []);
if nargin && ischar(varargin1)
gui_State.gui_Callback = str2func(varargin{1});
end

if nargout
[varargout{1:nargout}] = gui_mainfcn(gui_State, varargin{:});
else
gui_mainfcn(gui_State, varargin{:});
end
% End initialization code - DO NOT EDIT

% — Executes just before freezing_frac is made visible.
function freezing_frac_OpeningFcn(hObject, eventdata, handles, varargin)
% This function has no output args, see OutputFcn.
% hObject handle to figure
% eventdata reserved - to be defined in a future version of MATLAB
% handles structure with handles and user data (see GUIDATA)
% varargin command line arguments to freezing_frac (see VARARGIN)

% Choose default command line output for freezing_frac
handles.output = hObject;

% Update handles structure
guidata(hObject, handles);

% UIWAIT makes freezing_frac wait for user response (see UIRESUME)
% uiwait(handles.figure1);


% — Outputs from this function are returned to the command line.
function varargout = freezing_frac_OutputFcn(hObject, eventdata, handles)
% varargout cell array for returning output args (see VARARGOUT);
% hObject handle to figure
% eventdata reserved - to be defined in a future version of MATLAB
% handles structure with handles and user data (see GUIDATA)

% Get default command line output from handles structure
varargout{1} = handles.output;


function T_Callback(hObject, eventdata, handles)
% hObject handle to T (see GCBO)
% eventdata reserved - to be defined in a future version of MATLAB
% handles structure with handles and user data (see GUIDATA)
% Hints: get(hObject,'String') returns contents of T as text
% str2double(get(hObject,'String')) returns contents of T as a double


% — Executes during object creation, after setting all properties.
function T_CreateFcn(hObject, eventdata, handles)
```

```
% hObject handle to T (see GCBO)
% eventdata reserved - to be defined in a future version of MATLAB
% handles empty - handles not created until after all CreateFcns called

% Hint: edit controls usually have a white background on Windows.
% See ISPC and COMPUTER.
if ispc && isequal(get(hObject,'BackgroundColor'), get(0,'defaultUicontrolBackgroundColor'))
set(hObject,'BackgroundColor','white');
end

function MVD_Callback(hObject, eventdata, handles)
% hObject handle to MVD (see GCBO)
% eventdata reserved - to be defined in a future version of MATLAB
% handles structure with handles and user data (see GUIDATA)

% Hints: get(hObject,'String') returns contents of MVD as text
% str2double(get(hObject,'String')) returns contents of MVD as a double


% --- Executes during object creation, after setting all properties.
function MVD_CreateFcn(hObject, eventdata, handles)
% hObject handle to MVD (see GCBO)
% eventdata reserved - to be defined in a future version of MATLAB
% handles empty - handles not created until after all CreateFcns called

% Hint: edit controls usually have a white background on Windows.
% See ISPC and COMPUTER.
if ispc && isequal(get(hObject,'BackgroundColor'), get(0,'defaultUicontrolBackgroundColor'))
set(hObject,'BackgroundColor','white');
end

function V_Callback(hObject, eventdata, handles)
% hObject handle to V (see GCBO)
% eventdata reserved - to be defined in a future version of MATLAB
% handles structure with handles and user data (see GUIDATA)

% Hints: get(hObject,'String') returns contents of V as text
% str2double(get(hObject,'String')) returns contents of V as a double


% — Executes during object creation, after setting all properties.
function V_CreateFcn(hObject, eventdata, handles)
% hObject handle to V (see GCBO)
% eventdata reserved - to be defined in a future version of MATLAB
% handles empty - handles not created until after all CreateFcns called

% Hint: edit controls usually have a white background on Windows.
% See ISPC and COMPUTER.
if ispc && isequal(get(hObject,'BackgroundColor'), get(0,'defaultUicontrolBackgroundColor'))
set(hObject,'BackgroundColor','white');
end

function d_Callback(hObject, eventdata, handles)
```

```
% hObject handle to d (see GCBO)
% eventdata reserved - to be defined in a future version of MATLAB
% handles structure with handles and user data (see GUIDATA)

% Hints: get(hObject,'String') returns contents of d as text
% str2double(get(hObject,'String')) returns contents of d as a double


% --- Executes during object creation, after setting all properties.
function d_CreateFcn(hObject, eventdata, handles)
% hObject handle to d (see GCBO)
% eventdata reserved - to be defined in a future version of MATLAB
% handles empty - handles not created until after all CreateFcns called

% Hint: edit controls usually have a white background on Windows.
% See ISPC and COMPUTER.
if ispc && isequal(get(hObject,'BackgroundColor'), get(0,'defaultUicontrolBackgroundColor'))
set(hObject,'BackgroundColor','white');
end

function tau_Callback(hObject, eventdata, handles)
% hObject handle to tau (see GCBO)
% eventdata reserved - to be defined in a future version of MATLAB
% handles structure with handles and user data (see GUIDATA)

% Hints: get(hObject,'String') returns contents of tau as text
% str2double(get(hObject,'String')) returns contents of tau as a double


% --- Executes during object creation, after setting all properties.
function tau_CreateFcn(hObject, eventdata, handles)
% hObject handle to tau (see GCBO)
% eventdata reserved - to be defined in a future version of MATLAB
% handles empty - handles not created until after all CreateFcns called

% Hint: edit controls usually have a white background on Windows.
% See ISPC and COMPUTER.
if ispc && isequal(get(hObject,'BackgroundColor'), get(0,'defaultUicontrolBackgroundColor'))
set(hObject,'BackgroundColor','white');
end

function LWC_Callback(hObject, eventdata, handles)
% hObject handle to LWC (see GCBO)
% eventdata reserved - to be defined in a future version of MATLAB
% handles structure with handles and user data (see GUIDATA)

% Hints: get(hObject,'String') returns contents of LWC as text
% str2double(get(hObject,'String')) returns contents of LWC as a double


% --- Executes during object creation, after setting all properties.
function LWC_CreateFcn(hObject, eventdata, handles)
% hObject handle to LWC (see GCBO)
% eventdata reserved - to be defined in a future version of MATLAB
```

```
% handles empty - handles not created until after all CreateFcns called

% Hint: edit controls usually have a white background on Windows.
% See ISPC and COMPUTER.
if ispc && isequal(get(hObject,'BackgroundColor'), get(0,'defaultUicontrolBackgroundColor'))
set(hObject,'BackgroundColor','white');
end

function p_Callback(hObject, eventdata, handles)
% hObject handle to p (see GCBO)
% eventdata reserved - to be defined in a future version of MATLAB
% handles structure with handles and user data (see GUIDATA)

% Hints: get(hObject,'String') returns contents of p as text
% str2double(get(hObject,'String')) returns contents of p as a double


% — Executes during object creation, after setting all properties.
function p_CreateFcn(hObject, eventdata, handles)
% hObject handle to p (see GCBO)
% eventdata reserved - to be defined in a future version of MATLAB
% handles empty - handles not created until after all CreateFcns called

% Hint: edit controls usually have a white background on Windows.
% See ISPC and COMPUTER.
if ispc && isequal(get(hObject,'BackgroundColor'), get(0,'defaultUicontrolBackgroundColor'))
set(hObject,'BackgroundColor','white');
end

function ts_Callback(hObject, eventdata, handles)
% hObject handle to ts (see GCBO)
% eventdata reserved - to be defined in a future version of MATLAB
% handles structure with handles and user data (see GUIDATA)

% Hints: get(hObject,'String') returns contents of ts as text
% str2double(get(hObject,'String')) returns contents of ts as a double


% — Executes during object creation, after setting all properties.
function ts_CreateFcn(hObject, eventdata, handles)
% hObject handle to ts (see GCBO)
% eventdata reserved - to be defined in a future version of MATLAB
% handles empty - handles not created until after all CreateFcns called

% Hint: edit controls usually have a white background on Windows.
% See ISPC and COMPUTER.
if ispc && isequal(get(hObject,'BackgroundColor'), get(0,'defaultUicontrolBackgroundColor'))
set(hObject,'BackgroundColor','white');
end

% — Executes on button press in pushbutton1.
function pushbutton1_Callback(hObject, eventdata, handles)
% hObject handle to pushbutton1 (see GCBO)
```

```
% eventdata reserved - to be defined in a future version of MATLAB
% handles structure with handles and user data (see GUIDATA)

file=fopen('freezing_fraction.txt','w');
date_time=clock;
fprintf(file,'%d/%d/%d %dh%d\n',date_time(3),date_time(2),date_time(1),date_time(4),date_time(5))
fprintf(file,'\n');
t=str2num(get(handles.T,'string')); %free-stream temperature (C)
T=273.15+t; %free-stream temperature (K)
ts=str2num(get(handles.ts,'string')); %surface temperature (C)
Ts=273.15+ts; %surface temperature (K)
tf=0.5*(ts+t); %film temperature (C)
Tf=273.15+tf; %film temperature (K)
fprintf(file, 'ambiant temperature: %3.1f C \n',t);
fprintf(file, 'surface temperature: %3.1f C \n',ts);
MVD=str2num(get(handles.MVD,'string'));
fprintf(file, 'droplet size: %d e-6 m \n',MVD);
MVD=MVD*1e-6;
V=str2num(get(handles.V,'string'));
fprintf(file, 'tunnel air speed: %4.2f m/s \n',V);
d=str2num(get(handles.d,'string'));
fprintf(file, 'object size: %4.2e m \n',d);
LWC=str2num(get(handles.LWC,'string'));
fprintf(file, 'Liquid Water Content: %4.2f g/m3 \n',LWC);
tau=str2num(get(handles.tau,'string')); %accretion time (s)
fprintf(file, 'accretion time: %d s \n',tau);
[cpa,cpw]=specific_heat(Ts);
cpi=2000; %specific heat of ice
p=str2num(get(handles.p,'string'));

aa=input('static (s) or total (t) pressure ? ','s');
ab=input('static (s) or total (t) temperature ? ','s');
if (aa=='s' && ab=='s')
pst=p;
Tst=T;
[ptot,Ttot]=static2total(pst,Tst,cpa,V);
elseif (aa=='t' && ab=='t')
ptot=p;
Ttot=T;
[pst,Tst]=total2static(ptot,Ttot,cpa,V);
elseif (aa=='s' && ab=='t')
pst=p;
ptot_dum=1;
Ttot=T;
[pst_dum,Tst]=total2static(ptot_dum,Ttot,cpa,V);
[ptot,Ttot_dum]=static2total(pst,Tst,cpa,V);
elseif (aa=='t' && ab=='s')
ptot=p;
pst_dum=1;
Tst=T;
```

```
[ptot_dum,Ttot]=static2total(pst_dum,Tst,cpa,V);
[pst,Tst_dum]=total2static(ptot,Ttot,cpa,V);
end
fprintf(file, 'static pressure: %8.2f Pa \n',pst);
fprintf(file, 'total pressure: %8.2f Pa \n',ptot);
fprintf(file, 'static temperature: %5.2f K \n',Tst);
fprintf(file, 'total temperature: %5.2f K \n',Ttot);

[rhow,rhoa,rhoi]=density(Tst,pst);
fprintf(file,'\n');
fprintf(file, 'density of water at %3.1f C: %5.3f kg/m3 \n',t,rhow);
fprintf(file, 'density of air at %3.1f C: %5.3f kg/m3 \n',t,rhoa);
fprintf(file, 'density of ice at %3.1f C: %5.3f kg/m3 \n',t,rhoi);
mu=viscosity_air(T);
fprintf(file, 'viscosity of air at %3.1f C: %6.3e kg/m.s \n',t,mu);
fprintf(file, 'specific heat of air: %4.3f J/kg.K \n',cpa);
fprintf(file, 'specific heat of ice: %4.3f J/kg.K \n',cpi);
fprintf(file, 'specific heat of water at %3.1f C: %5.3f J/kg.K \n',ts,cpw);
ka=thermal_conductivity(Tf);
fprintf(file, 'thermal conductivity of air at %3.1f C: %5.3f W/m.K \n',tf,ka);
Dv=vp_diffusivity(Tf,pst);
fprintf(file, 'water vapor diffusivity in air at %3.1f C: %5.3e m2/s \n',tf,Dv);
pw=vapor_press(T);
pww=vapor_press(Ts);
fprintf(file, 'vapor pressure of water in atmosphere at %3.1f C: %5.2f Pa \n',t,pw);
fprintf(file, 'vapor pressure of water at the icing surface (%3.1f C): %5.2f Pa \n',ts,pww);
[Lf,Lv]=latent_heat(Ts);
fprintf(file, 'latent heat of fusion at %3.1f C: %5.2f J/kg \n' ,ts,Lf);
fprintf(file, 'latent heat of vaporization at %3.1f C: %5.2f J/kg \n' ,ts,Lv);
fprintf(file,'\n');

[rhow_tf,rhoa_tf,rhoi_tf]=density(Tf,pst);
mu_tf=viscosity_air(Tf)
Rea=V*d*rhoa_tf/mu_tf
Pra=cpa*mu_tf/ka
Sca=mu/(rhoa*Dv)
Nua=1.14*Pra^0.4*Rea^0.5
hc=ka*Nua/d
hG=hc/cpa*(Pra/Sca)^0.67

Red=V*MVD*rhoa/mu;
fprintf(file, 'droplet Reynolds number: %6.2f \n',Red);
lambda_lambdaStokes=(0.8388+0.001483*Red+0.1847*Red^0.5)^(-1)
K=(rhow*MVD^2*V)/(18*d*mu);
fprintf(file, 'inertia parameter: %4.2f \n',K);
K0=1/8+lambda_lambdaStokes*(K-1/8)
fprintf(file, 'modified inertia parameter: %4.2f \n',K0);
beta0=(1.4*(K0-1/8)^0.84)/(1+1.4*(K0-1/8)^0.84)
fprintf(file, 'stagnation point collection efficiency: %5.3f \n',beta0);
Ac=(LWC*1e-3*V*tau)/(rhoi*d)
```

```
fprintf(file, 'accumulation parameter: %4.2f \n',Ac)

deltap=(pww/Tst-ptot/Ttot*pw/pst)/(1/0.622*ptot/Ttot-pww/Tst)
phi=(273.15-Tst)+(Ts-273.15)-hG/(LWC*1e-3*V*beta0)*deltap*(Ts-273.15)-V^2/(2*cpw)
fprintf(file, 'water droplet energy transfer parameter: %5.2f K \n',phi);
b=LWC*1e-3*V*beta0*cpw/hc;
fprintf(file, 'relative heat factor: %5.3f \n',b);
theta=Ts-Tst-V^2/(2*cpa)+hG/hc*Lv*deltap;
fprintf(file, 'air energy transfer parameter: %5.2f K \n',theta);
n=cpw/(Lf+cpi*(273.15-Ts)+cpw*(Ts-273.15))*(phi+theta/b)
fprintf(file, ' \n')
fprintf(file, 'freezing fraction %5.3f \n',n);
Delta=n*Ac*beta0;
fprintf(file, ' \n')
fprintf(file, 'non-dimentional thickness: %5.3f \n',Delta);
Delta_i=Delta*d;
fprintf(file, 'ice thickness: %5.3f \n',Delta_i);

fclose(file);
delete(handles.figure1)
```